SERS & Efficacy Assessment of Anti-Cancer Drug-Nanoparticle Conjugates

Rachael Yvonne Cameron

Thesis presented for a joint degree of Doctor of Philosophy.

The University of Strathclyde, Pure & Applied Chemistry and
The University of Edinburgh, College of Medicine & Veterinary Medicine.

April 2019

Supervisors: *Professor Duncan Graham*
Professor Margaret Frame
Doctor Alastair Wark
Professor Karen Faulds

Declaration of Authenticity and Authorship

This thesis is the result of the author's original research. It has been composed by the author and has not been previously submitted for examination which has led to the award of a degree. The copyright of this thesis belongs to the author under the terms of the United Kingdom Copyright Acts as qualified by University of Strathclyde Regulation 3.50. Due acknowledgement must always be made of the use of any material contained in, or derived from, this thesis.

Rachael Cameron
University of Strathclyde
April 2019

Signed: _____

Date: _____

Acknowledgements

This PhD would not have been possible without opportunities and support provided by many people both academically and otherwise. Primarily thanks are extended to the administrators and management of the Optima PhD programme at the University of Edinburgh and Strathclyde, who created the PhD with EPSRC and MRC funds. Many thanks to my supervisors: Professors Duncan Graham, Karen Faulds and Margaret Frame, and Dr Alastair Wark- for taking a gamble on me with no prior knowledge of cancer or chemistry, for your encouragement, for the opportunities given and for your trust in giving me the freedom to work independently.

Thanks to my science families during the PhD. The Ramanators- I will always have time for you crazies. The memories I take from my time with you all are second to none: the Ark, Sheffield beer hall dancing, San Fran closed check-in fiasco (and bikini rescue with Matlab-Face Frame), de Polo s-drops (Mr Ward), gin eyeballs (Miss Spilligan!), *etc.*. Continue celebrating one another's successes, learn from them and be inspired to pave the way for your own accolades. My Optima cohort- I am proud to have been in the year of the guinea pig with you. We were afforded many opportunities and I'm glad I shared all those with you. Those conferences and summer schools brought the class of 2014 together, long live Optimal Optima. My 2015 Strathclyde Optima Girls- you're the best little sisters I never had.

Thanks are given to both institution's business schools for including us in the Business Masters of Healthcare Innovation and Entrepreneurship, it provided business nous to transition from academia to industry. I thank Dr Rabinder Buttar for the opportunity to intern in her clinical research organisation, Clintec, and for creating a part-time job for me during the final years of my PhD.

My appreciation is given to the funding agencies enabling me to attend conferences. The Athena Swan lecture and "Swing it!" comment that instigated my applications require credit and thanks to Duncan for his endorsements. My sincere thanks for enabling travel to international and national events go to: The Company of Biologists, The ABS Trust, The Analytical Chemistry Fund, The RSC, The GRC Fund. My gratitude for the prizes awarded on my work go to: TransMed, SAS, and IRDG.

Final academic thanks are extended to all the collaborators. A million thanks to Lauren for giving massive moral and scientific support, proud of you for 'Daring to Dream' and running away to the circus. Thanks to the Strathclyde staff: Corinna Wetherill for cell lab help, to all the post-docs from the Graham/Faulds Groups who have guided me through the PhD- special thanks to Dr Samuel Mabbott and Dr Lauren

Jamieson for support and Matlab 'techers', to Dr Alastair Wark for his technical demonstrations and scientific discussions, to Patricia Keating at the Mass Spec for guidance on drug quantification. Thanks to the Edinburgh staff: to members of the Frame/Brunton Groups, special thanks to Dr John Dawson for cell based assay advice, to Dr William Tipping for discussions on erlotinib, to Dr Kenneth McLeod for the RPPA study, to Dr Adam Byron for advice on RPPA software, to Dr Jimi Wills for your Mass Spec facility skills on drug loading of the nanoparticles, and to Stephen Mitchell of the TEM facility for help with samples and demonstrating microscope usage. Thanks to our external collaborators: Dr Marjorie Willner of Virginia Tech University for the microfluidic work, and Heidi Goenaga-Infante and Susana Nunez at the London Government Laboratories for their ICP-MS work on silver in cells.

On a personal level, thanks to the Cameron-Martin's for welcoming us into their home for 3 months, whilst we moved house to enable me to do this twin-city PhD. You contributed more than you know. Special credits to the delicious Friday French Martinis, the family games and selecting me as your subject of 'My Hero' to present to your class. Thanks to my biggest Cameron fan, 'wee Ruthie'. Your not-so-humble brags to your pals were entertaining and flattering throughout my PhD. The Tuesday night visits brought the PhD into perspective and restored the work-life balance.

Thank you to the Orr's, my family, for encouraging this 'nerd' over the years. You have been my motivation throughout. Thanks: to Mum for tolerating my incessant "But why?!" questions as a child, to Dad for keeping me abreast of the most recent cures and discoveries, to both parents for giving me the best start in life with a happy childhood on the farm, to big bro J-H for keeping me grounded over the years and for the lifts after late nights at the Cancer Centre in his fancy motors, to big bro MCO for showing his pride by asking 'Raj- what is it you do again?' so he can tell Jamie her auntie will be a doctor, to big sis Lisa for being a great cheer leader, along with her 3 Wason amigos- who like to proclaim their aunt's an author.

Finally and most importantly- I dedicate this work to my husband, Ali. I appreciate the emotional, financial, and physical support that you have provided throughout. You knew when to deliver tough love, gentle encouragement or a bottle of wine. Your selflessness knows no bounds in all that you do for us, I am forever grateful. Not only did you raise my spirits with an occasional sing-song, ahem every Friday, you held me up when my foot could no longer take the strain. Thank you for being my barista, chef, nurse and all the roles you fulfil, whilst I recover from the surgery. Now I almost forgive you that I will be Dr Cameron, and not Dr Orr, almost.
Ali- I dedicate this to you… *"My angel in disguise."*

Abstract

Non-small cell lung cancer (NSCLC) is the result of tumour development from genetically-mutated epithelial cells lining the surface of the lung. Clinical response to treatments is generally gauged by comparing tumour sizes pre- and post-treatment on computerised tomography. If no response is observed, it is difficult to understand why the patient is not responding to treatement. Measuring the success of the drug at the intracellular level, for example: drug entry, accumulation and binding to its active site, can be difficult to observe directly when the drug is not labelled. Being able to determine the intracellular accumulation (concentration), biological effect and fate (metabolism or degradation) of the drug could inform pre-clinical development of future generations of drugs.

The purpose of this study was to functionalise a nanoparticle (NP) with an anti-cancer drug to be intracellularly imaged without the use of a dye. The aim was to track the uptake, distribution and release kinetics of the small molecule drug from the NP conjugate within the cell at clinically relevant levels. Here, the inherent chemical signature of the small molecule tyrosine kinase inhibitor (SM-TKI) erlotinib (EL) that targets a mutant epidermal growth factor receptor (EGFR), was selected as a proof of concept for optical imaging in cancerous cells. The alkyne bond within EL was detected with the vibrational spectroscopy technique, Raman microspectroscopy. Raman scattered signals can be enhanced when the analyte is associated with the surface of a NP (surface enhanced Raman spectroscopy (SERS)). Two metals were compared for signal detection, namely gold and silver NPs. Once EL conjugate imaging was achieved, the anti-proliferative efficacy and cytotoxicity of the NP conjugated erlotinib to the free drug was assessed.

EL-NP conjugates were characterised in solution and mapped in fixed cells by SERS at 300 nM EL. This was a high resolution time-lapsed intracellular localisation study. The alkyne signal from silver conjugates were found to occupy more of the cell volume over time 32.6% *versus* gold 0.2% of the cell volume at 24 hours. The dynamic release of EL from the silver NP was observed from 4 hours by tracking a Raman shift of the alkyne vibration from bound to free-EL. The intracellular uptake was confirmed *via* correlative dark-field (DF) microscopy, single particle inductively coupled plasma- mass spectrometry (spICP-MS) and TEM. Conjugates were present at 1-10,000 particles per cell and a final concentration of 39 nM EL was delivered. The fate of gold NPs were illustrated by TEM to be different when compared to the silver, as they tend to accumulate more in membrane bound organelles than the silver NPs. This is likely to have consequences for the efficacy of drug responses. A

microfluidics device was also employed to demonstrate the potential for 3D SERS imaging at physiological conditions to monitor conjugated EL in real-time. This is the first example of a dye-free SERS approach for drug detection within cells using 3D mapping and a microfluidic device for live cell imaging.

Cell viability was assessed during a fluorescent image time-course study to evaluate the cytotoxicity and efficacy of the nano-delivery method employed *versus* parent (free) drug formulation. It was found that the silver NP conjugate was almost as effective as the free drug. In contrast, the gold NP conjugate was completely ineffective on EL-sensitive cells. It was shown that that NP toxicity on cells must be determined empirically per NP and per cell type, as the EL-insensitive cell line was far more susceptible to silver NP toxicity than the EL-sensitive cell line.

Examining the inhibition of EGFR phosphorylation elucidated reduced expression levels in EL-silver NP conjugate treated cells, the gold counterpart had no effect on inhibiting activation of EGFR. This was demonstrated by immunofluorescent imaging for localisation and Western immunoblots for quantitation (of phosphorylated/total EGFR (p/tEGFR) protein). Functional proteomics in the form of reverse phase protein array (RPPA) analysis was carried out to assess the downstream effects of the conjugates compared with unconjugated (free) EL on drug-sensitive cells. Hierarchical cluster analysis (HCA) and interactive network maps of RPPA for downstream signal transduction phosphorylation studies confirmed the earlier efficacy results from cell viability studies. EGFR and associated signalling events were similarly disrupted in free-EL and silver conjugate but were unaffected in the gold conjugate samples. Interestingly, RPPA highlighted another key difference in that free-EL induced more of a DNA damage response than in the conjugate-treated EL-sensitive cells.

In conclusion, it was determined that nanoparticles could be useful as the next generation of dye-label-free theranostics for multiple purposes, for example: as diagnostic, treatment and prognostic markers. To enable this, the NPs must be rendered safe enough for use in humans, specifically targeted to the cancerous cells and loaded with a drug moiety that can be released near the active site. Although these studies have revealed potential utility in drug imaging, there are clearly a number of key hurdles to be overcome if NP-drug conjugates are to be used in a clinical setting for cancer treatment. However, their potential to aid in the tracking the intracellular fate of the drug could help in nanoformulation drug discovery pipelines.

Contents

Abbreviations

ADME	Adsorption, Distribution, Metabolism and Elimination
AgHA	Hydroxylamine Reduced Silver
ATCC	American Type Culture Collection
ATP	Adenosine Triphosphate
AuCt	Citrate Reduced Gold
BSA	Bovine Serum Albumin
DFT	Density Functional Theory
DLS	Dynamic Light Scattering
DMEM	Dulbecco's Modified Eagles Medium
DNA	Dioxyribonucleic Acid
EGF	Epidermal Growth Factor
EGFR	Epidermal Growth Factor Receptor
EGFRm+	Mutation positive EGFR gene
EGFRwt	Wild type EGFR gene
EPR	Enhanced Permeability Retention
ESF	European Science Foundation
GSH	Glutathione
HCA	Hierarchical Cluster Analysis
HGU	Human Genetics Unit
ICP-MS	Inductively Coupled Plasma - Mass Spectrometry
IFA	Immunofluorescence Assay
IGMM	Institute for Genetics and Molecular Medicine
IR	Infrared spectroscopy
FBS	Foetal Bovine Serum
fps	Frames per second
FWHM	Full Width Half Maximum
LC-MS	Liquid Chromatography – Mass Spectroscopy
LGC	Laboratory of the Government Chemists
LOB	Limit of Blank
LOD	Limit of Detection
LOQ	Limit of Quantitation
MRC	Medical Research Council
MTS	3-(4,5-dimethylthiazol-2-yl)-5-(3-carboxymethoxyphenyl)-2-(4-sulfophenyl)-2H-tetrazolium)
MTT	3-(4,5-Dimethylthiazol-2-yl)-2,5-diphenyltetrazolium bromide

NP	Nanoparticle
NSCLC	Non-Small Cell Lung Cancer
NTA	Nanoparticle Tracking Analysis
OR	Ordinary Raman
pEGFR	Phosphorylated EGFR
PBS	Phosphate Buffered Saline
PBST	Phosphate Buffered Saline Tween
PCA	Principle Component Analysis
PCR	Polymerase Chain Reaction
PEG	Polyethylene Glycol
PFA	Paraformaldehyde
PDMS	Polydimethylsiloxane
PMMA	Poly (methyl methacrylate)
RES	Reticuloendothelial System
RIPA	Radio-Immune Precipitation Assay
ROS	Reactive Oxygen Species
RPPA	Reverse Phase Protein Array
RTK	Receptor Tyrosine Kinase
SD	Standard Deviation
SEM	Scanning Electron Microscopy
SERS	Surface Enhanced Raman Spectroscopy
SERRS	Surface Enhanced Resonance Raman Spectrocopy
SM-TKI	Small Molecule-Tyrosine Kinase Inhibitor
STR	Short Tandem Repeat
spICP-MS	Single Particle ICP-MS
SPR	Surface Plasmon Resonance
SRS	Stimulated Raman Spectroscopy
tEGFR	Total EGFR
TEM	Transmission Electron Microscopy
TKD	Tyrosine Kinase Domain
UV	Ultra Violet
UV-Vis	UV-visible

Thesis Motivation

There is a need to expedite the translation of drugs from development into the clinic from the usual 10-15 years, to reduce the 95% failure rate of those entering phase I clinical trials to reaching the patient. Furthermore, it is a necessity to understand why current treatments become unsuccessful in the therapy of patients' cancerous tumours. Recent attention has turned to repurposing of drugs in clinical trials *e.g.* to treat another condition or reformulate as a nanoformulation, to increase efficacy and reduce systemic toxicity. On a cellular level it is difficult to detect drugs *via* direct imaging, and mis-localisation or lack of uptake may contribute to why resistance or lack of response to a drug arises. Here, Raman imaging was investigated and proved a useful tool in detecting a frequently used anti-cancer drug erlotinib (EL) within cells and nanoparticles (NP) were used to explore increasing the efficacy of the parent drug, due to a higher drug payload being delivered and released.

Aims & Novelty

Chapter 3: to characterise the NPs and conjugates to determine the optimum concentrations for cell-based studies

Chapter 4: to characterise cell lines and determine whether erlotinib-nanoparticle (EL-NP) conjugates can improve the efficacy and toxicity of *in vitro* cancer cell treatment compared to free erlotinib.

Chapter 5: to characterise the spatio-temporal distribution of EL when bound to NPs and detect dynamic release events within *in vitro* fixed and live cells within a microfluidic device by SERS and correlative uptake studies.

Chapter 6: to explore the mechanisms of action of conjugated EL on NPs and whether they differ from free-EL. Furthemore, cellular stress, cell death or toxicity signalling associated with bare NPs is investigated by Reverse Phase Protein Arrays (RPPA).

Project Contributions

Matlab support was provided by Dr Lauren Jamieson who wrote the script for the map ratios and foundation skills were taught by Dr Samuel Mabbott, University of Strathclyde. The final stages of TEM fixation and microtoming was carried out by Stephen Mitchell at the University of Edinburgh, all further imaging and analyses were performed by the author. Inductively Coupled Plasma- Mass Spectrometry

(ICP-MS) and single particle ICP-MS (spICP-MS) samples were prepared and interpreted by the author and experiments were carried out at the Laboratory of the Government Chemist group (LGC), Teddington, UK. Patricia Keating at the University of Strathclyde advised on preliminary Liquid Chromatography- Mass Spectrometry (LC-MS). Dr Jimi Wills at the University of Edinburgh advised and created the protocol on the LC-MS instrument (jointly run with Dr Andy Finch) and he ran some of the samples prepared by the author and advised on preliminary data analysis. The microfluidics devices were prepared by Marjorie Willner from Virginia Tech, VA, USA. The RPPA assay was carried out in collaboration with Dr Kenneth McLeod at the University of Edinburgh; sample preparation and analyses were by the author. Dr Adam Byron advised on selecting software packages to use for analyses of RPPA data.

Conference Proceedings & Awards

2018

"Multi-modal imaging of erlotinib-nanoparticle conjugates in lung cancer cells"
R. Cameron, A. W. Wark, K. Faulds, M. C. Frame and D. Graham, Oral Presentation at Spring SciX, Glasgow, UK.

2017

"Multi-modal imaging of erlotinib-nanoparticle conjugates in lung cancer cells"
R. Cameron, A. W. Wark, K. Faulds, M. C. Frame and D. Graham, Invited Oral Presentation at SciX, Reno, USA.

- **IRDG Chalmers and Dent Student Travel Award for Outstanding PhD Student in Vibrational Spectroscopy £500 and Invited Talk to SciX**
- **Royal Society of Chemistry Travel Grant £800**

"Multi-modal imaging of erlotinib-nanoparticle conjugates in lung cancer cells"
R. Cameron, A. W. Wark, K. Faulds, M. C. Frame and D. Graham, Poster Presentation at SciX, Reno, USA.

- **Outstanding Student Research Poster, Society for Applied Spectroscopy**

"Multi-modal imaging of erlotinib-nanoparticle conjugates in lung cancer cells"
R. Cameron, A. W. Wark, K. Faulds, M. C. Frame and D. Graham, Poster Presentation at Gordon esearch Symposium and Conference, Vermont, USA.

- **Overseas Conference Travel Grant from Analytical Chemistry Fund £500**
- **Association of British Spectroscopy Trust Travel Bursary £250**

2016

"SERS anti-cancer drug-nanoparticle conjugate assessment"
R. Cameron, A. W. Wark, K. Faulds, M. C. Frame and D. Graham, Oral Presentation at TransMed Conference, Edinburgh, UK.

- **Best Oral Presentation Award £100**

"Re-Thinking Cancer Workshop" Company of Biologists, London, UK.

- **Competitive Fully Funded Early Career Research Award to Attend £500**

"SERS anti-cancer drug-nanoparticle assessment"
R. Cameron, A. W. Wark, K. Faulds, M. C. Frame and D. Graham, Oral Presentation at IRDG Martin and Willis Meeting, Sheffield, UK.

Chapter 1 Introduction

"Don't be afraid of hard work. Nothing worthwhile comes easily"
Gertrude B Elion, Nobel Prize for Physiology or Medicine 1988.

1.1 Cancer

Cancer is responsible for nearly a quarter of deaths worldwide, claiming 8.8 million lives in 2015.[1] Bronchus, lung and tracheal cancers were responsible for the greatest portion of lives taken by cancer, with 1.7 million people dying globally in 2015.[1] Cancer develops when mutations arise in cells or an imbalance in cell cycle regulation occurs, allowing exponential unmoderated growth. Cancer is an umbrella term covering hundreds of subtypes of the disease and has been described as having 10 hallmarks, which are a displayed in Figure 1.[2] Combined, these 10 hallmarks allow cancerous cells to grow in an uncontrolled manner, with increased angiogenesis, resisting cell death and evading the immune system. Carcinogenic factors can be based on environmental, lifestyle or genetics.[3-5] Around 30 % of cancers are deemed preventable through avoidance of tobacco and alcohol and with an active lifestyle and eating a balanced diet.[5] During this study the focus is on lung cancer and more specifically, non-small cell lung cancer (NSCLC).

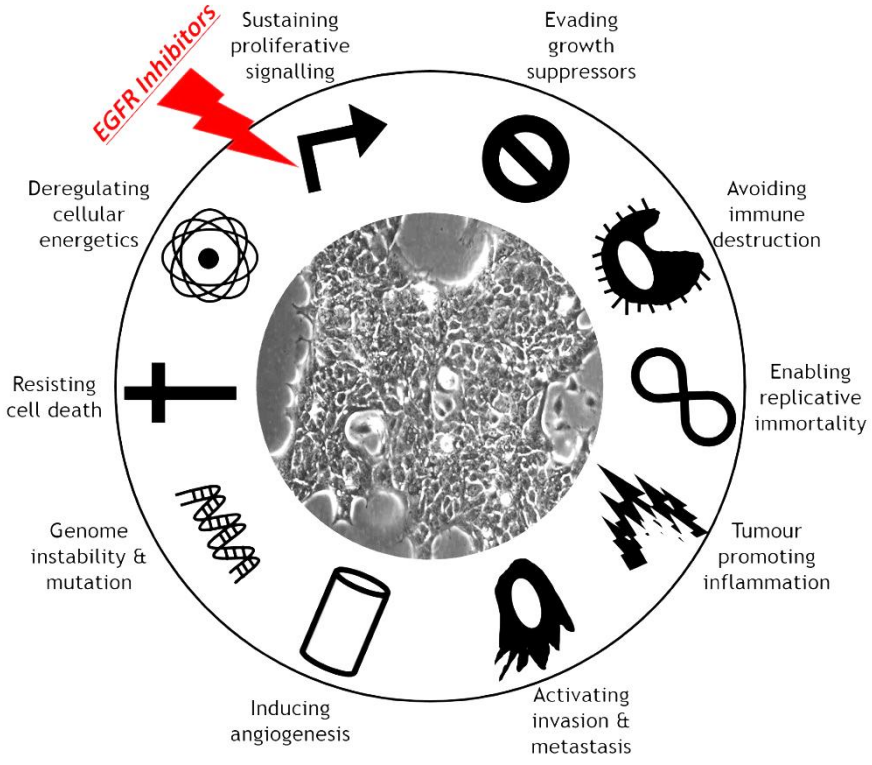

***Figure 1 Ten hallmarks of cancer. Adapted from D. Hanahan, et al.*[2].**

1.1.1 Non-Small Cell Lung Cancer

Lung cancer is the most fatal of malignancies amongst men and second most fatal in women, only exceeded by breast cancer deaths.[1] There are two types of lung cancer, small cell and NSCLC. NSCLC is a group of three subtypes of the disease, which are categorised together due to their similar prognoses and treatment, and are responsible for up to 80% of lung cancers.[6] Large cell carcinoma, squamous cell carcinoma and adenocarcinoma are the three subtypes.[7] Adenocarcinoma is found in cells that normally secrete mucus and accounts for the largest portion of NSCLCs.[7] Non-small cell cancer can also be found in the prostate of men as a result of similar cell types. Treatment for cancers vary depending on its location, advancement, metastatic status and other factors. However, the scale of the problem faced by clinicians diagnosing and treating patients, with the hope of curing the cancer, is immense.

It is imperative to minimise preventable cancers but also to provide more rapid diagnostics and effective treatments that result in a better prognosis and quality of life for cancer patients. The clinicians tasked with this, note that there are many issues surrounding treatment selection and monitoring. For example, cardiomyopathy can result from chemotherapies, and therefore serum levels of drugs must be monitored which can be invasive, *e.g.* lung biopsy, blood collection, since a sample is required for testing.[8] This does not inform clinicians if the cancerous cells have been targeted, only that the drug is still in circulation.

On a cellular level, doctors or researchers have no way of visualising or quantifying the drug content within the malignant cancer cells. If this could be achieved, it could be considered the key to unlocking the possibility of treatment tailored to each patient. In future, optical fibre imaging could probe cellular response to a drug *in situ*, but much work is required to obtain this precision oncology goal. If observations of a drug's localisation, retention time in cells, metabolites and cellular response can be made, then a decision can be reached on whether the treatment being prescribed is the most efficacious. Furthermore, it may unlock key biological modes of action that are unclear in bulk or overall responses observed *in vitro* by studying the effects of the drug at a single cell level, thus aiding future drug development routes in the pharmaceutical industry.

One of the ten hallmarks of cancer discussed earlier was sustaining proliferative signalling, this is achieved through cell surface receptors binding ligands to be activated. This can occur through elevated expression of the receptors or mutations

that make them constitutively active. One such example is the epidermal growth factor receptor (EGFR) which is a focus of this study.

1.1.2 Epidermal Growth Factor Receptor Signalling

EGFR is generally located on the cell surface and is composed of; an extracellular ligand binding domain, a transmembrane domain, a tyrosine kinase domain (TKD) and a c-terminal.[6] A diagrammatic representation can be seen in Figure 2, demonstrating where small molecule tyrosine kinase inhibitors (SM-TKI) could prevent the activation of EGFR by binding to the auto-phosphorylation site, the ATP-binding pocket.[9]

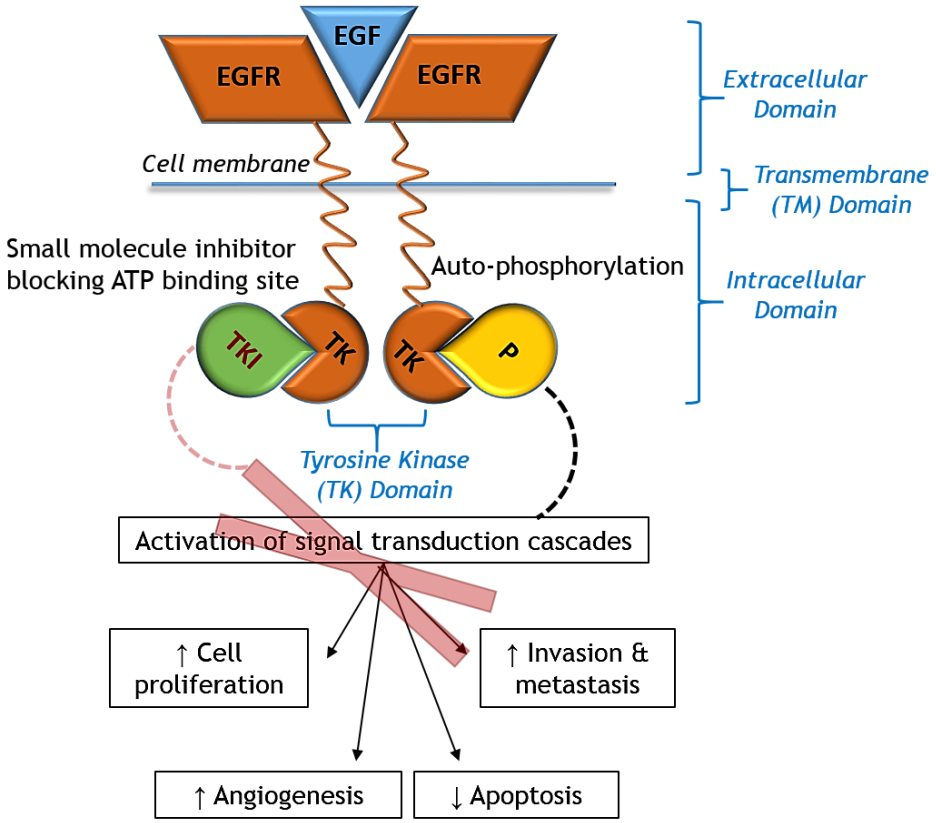

Figure 2 EGFR and its downstream signal cascade stimulated upon activation, and TKD where SM-TKI can block auto-phosphorylation.

EGFR is a member of the ErbB family of four receptor tyrosine kinases (RTKs) and can form homo- or hetero-dimers upon activation by its ligand, epidermal growth factor (EGF). Cancer can result from mutations in, or overexpression of, these growth factors resulting in unregulated proliferation. This can also occur by having a constitutively active EGFR through which no ligand is required for stimulation. EGFR is classed as a proto-oncogene, mutations can convert this receptor into a carcinogenic oncogene and therefore tumour promoting if it is rendered constitutively active.[10]

The TKD is the catalytic portion of the receptor and is responsible for transferring a phosphate from ATP to proteins in the cell, in a process called phosphorylation. This in turn induces further protein modifications and signal cascades. The activation occurs after EGF binds to the receptor, resulting in dimerisation with another receptor. This conformational change internalises EGF, inducing auto-phosphorylation. The activated EGFR distribution is provided in Figure 3 displaying an immunofluorescence image labelled with α-phospho-EGFR antibody in red and co-staining for the nucleus with DAPI in blue. The intracellular punctate distribution demonstrates the internalisation into endosomes where the EGFR is either recycled to the surface or destroyed.

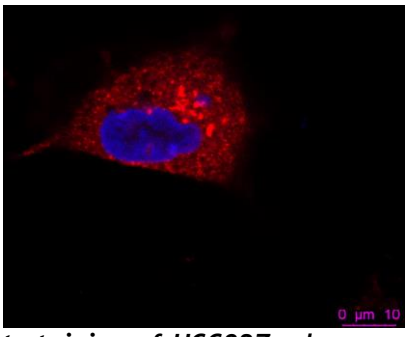

Figure 3 Immunofluorescent staining of HCC827 adenocarcinoma lung cell stimulated with 50 ng/mL EGF ligand for 15 minutes, showing a punctate distribution of activated phospho-EGFR (red) and the nucleus (DAPI, blue), scale bar 10 µm.

Cells can become cancerous when the expression level of the EGFR is elevated or mutated.[11] This EGFR overexpression is found in 62% of NSCLC cases and can be to the extent of 200 fold greater receptor expression on tumour cells *versus* normal cells.[11,12] The elements of the EGFR that result in proliferative activity are now discussed together with tyrosine kinase inhibitors.

1.1.3 Small Molecule Tyrosine Kinase Inhibitor - Erlotinib

SM-TKIs including EL, amongst others including gefitinib, are treatments for cancers bearing EGFR mutations.[13] Response to EL is elevated from 7% in all NSCLC patients to 77% in the presence of these EL-sensitising mutations in the EGFR-TKD.[6] A summary of the statistics associated with NSCLC prevalence, EGFR expression, mutation rate and response to EL is found in Figure 4.[3,6,14]

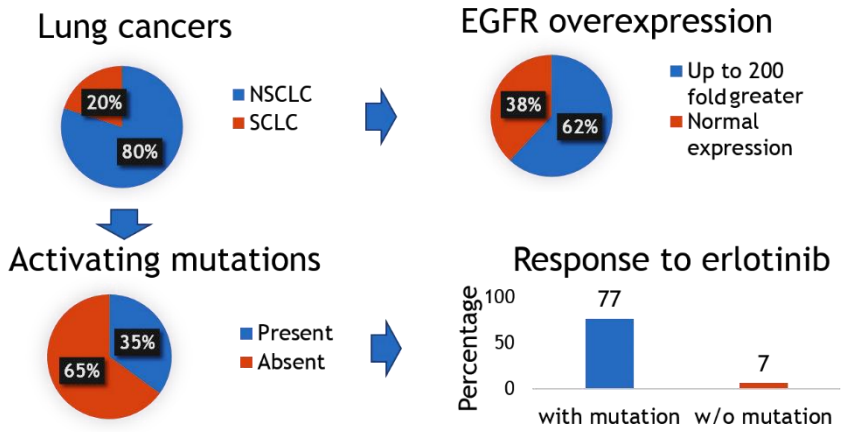

Figure 4 Summary of NSCLC prevalence, EGFR overexpression, activating mutation rates and response to EL statistics.[3,6,14]

A summary of the sensitising and de-sensitising mutations introduced in Figure 4 is presented in Figure 5, adapted from Sharma *et al.*[6] The domains of the gene are outlined including introns (non-gene coding deoxyribonucleic acid (DNA) regions) and exons (gene-coding regions of the DNA). It is known that 1 in 7 NSCLC patients have the activating mutations affecting the EGFR protein, known collectively as *EGFRm+*, which make them more likely to respond to EL. The patients who are *EGFRm+* have a 90% chance of possessing one of two mutations responsible, which are exon 19 deletions and an exon 21 (L858R) substitution (Figure 5).[6]

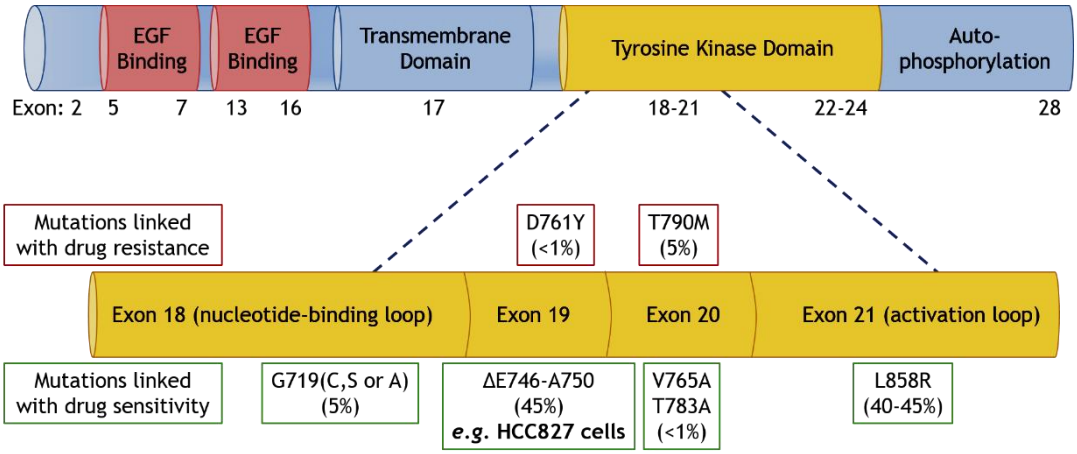

Figure 5 EL-sensitising mutations of EGFR in NSCLC. Adapted from Sharma, S. V. et al.[6] ***A diagrammatic representation of EGFR with exons in the extracellular domain (EGF binding), transmembrane domain (TM) and intracellular domain (containing the TKD and auto-phosphorylation regions with ATP-binding pocket). The cysteine-rich regions in the extracellular domain (EGF binding; pink area) and the TKD region in the intracellular domain (yellow area) are also represented. Exons 18-21 in the TKD region where the relevant mutations are located are expanded in the yellow bar below. A list of EGFR mutations in these exons that are associated with sensitivity (green outlined boxes) or resistance (red outlined boxes) to EL is shown with the % occurrence in brackets. The most prevalent of EGFR kinase domain mutations, accounting for 45% of EGFR mutations in NSCLC, are in-frame deletions of exon 19, such as that found in HCC827 lung adenocarcinoma cells.***[6]

Diagnostics linked to genetic susceptibility are often referred to as 'theranostics' or companion testing.[15,16] Theranostics is used to explore targeted drug treatments, such as EL, to test a patients' likelihood to respond to the drug and then their response thereafter. Theranostics not only test for suitable therapy candidates but also reduce the use of ineffective treatments on those who are resistant to that course of cancer therapy. Regular screening of those being treated with targeted treatments is required to detect anti-cancer drug resistances early, thus avoiding the incorrect use of expensive and toxic agents. Without testing each patient, they may needlessly endure therapy that is not suitable, whilst the cancer will continue unchecked despite the use of treatments prescribed to combat the disease. The FDA released guidelines in 2014 stating that any new targeted anti-cancer drugs be accompanied by a collaborative effort to release companion diagnostics in tandem before they will consider approval.[17]

To deliver the most effective treatment to patients rapidly, a theranostic test should be carried out if a biopsy has been taken and material is available. The EGFR mutation's prevalence is highest in; Asians, females, people under the age of 65 and those who have never smoked.[16] Lindeman *et al*. concluded in 2013 of *EGFRm+* testing, that polymerase chain reaction (PCR) based activating mutation tests should be carried out on biopsy specimens.[16] This molecular testing advice by Lindeman *et al*. was given regardless of sex, race and smoking history in all advanced stage adenocarcinoma patients. Smoking is known to reduce the efficacy of EL, a small molecule inhibitor whose properties are described below.

EL is an EGFR-TKI marketed under brand name Tarceva by OSI Pharmaceuticals, owned by Genentech/Astellas. EL hydrochloride is chemically named as N-(3-ethynylphenyl)-6,7-bis(2-methoxyethoxy)quinazolin-4-amine hydrochloride and has the formula $C_{22}H_{23}N_3O_4.HCl$. The structure is given in Figure 6 and a majority of the molecule interacts with the adenosine triphosphate (ATP) binding pocket of the TKD (see green circled area that interacts with the binding pocket), however the ether groups trail behind and have no role in the interaction.[18-20] EL is an anti-neoplastic agent, which halts tumour development to prolong the patient's life and maintain a quality of life that would otherwise be detrimentally affected by untreated tumour growth. Proliferation is blocked or inhibited by EL binding reversibly to the ATP binding pocket where the phosphate group would usually attach and participate in auto-phosphorylation of the ATP-binding pocket.

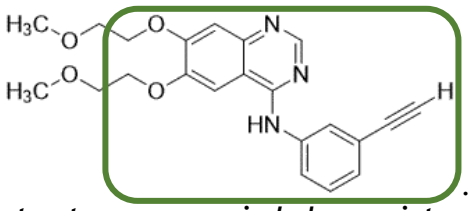

. HCl

Figure 6 EL chemical structure, green circled area interacts with the ATP binding pocket of its target the EGFR.

The remaining chemical properties of EL are condensed and summarised in Table 1 as a comparison to the drug suitability factors of Lipinski's "rule of 5".[21] The pharmacokinetic characteristics can be assessed for absorption, distribution, metabolism and excretion (ADME) following these five rules. Namely they should possess a; molecular weight <500, partition coefficient (logP) <5, number of hydrogen bond donors <5 and acceptors <10, and a low polar surface area. In addition the acid dissociation constant (*pKa*) of a drug also influences lipophilicity, solubility, protein binding and permeability.[21] EL has been clearly designed to satisfy all of these selection criteria: it is lipophilic, has the ability to permeate the membrane of the cell, and is soluble in the pH of cancerous cell environments.

Outside of the pharmacokinetic properties of the drug, EL has been selected for this study due to its Raman and SERS active signatures; the alkyne group produces a distinctive Raman and SERS peak of around 2100 cm^{-1} and 2000 cm^{-1} respectively.[22] This will be discussed in detail later. Now Raman and SERS, vibrational spectroscopic methods, are introduced.

Table 1 Summary of EL's properties. Including a comparison to Lipinski's "Rule of 5" properties and the implications for EL.[21]

	Lipinski's Rule of 5	EL	Properties
Log P	≤5	3.2	Lipophilic
MW (g)	≤500	429.9	Membrane permeability
H Bond Acceptors	≤10	6	Low H bond acceptor/donators = good bioavailability
H Bond Donors	≤5	1	
Polar Surface Area (PSA)	Low for membrane permeability	74.73 Å	Non-polar = membrane permeability
Surface Area		583.3 Å	
***pKa* (*pH*)**		5.42	Weak acid= buffers well ~pH5.42
***pI* (*pH*)**		10.32	Net +ve charge up to pH10.32
Solubility		Increases at lower *pH*	Secondary amine can be protonated

1.2 Spectroscopy

1.2.1 Raman Spectroscopy

Raman spectroscopy is a light scattering optical imaging technique that benefits from requiring minimal or no sample preparation, no external labels, and only a single monochromatic light source, yet it can be used to determine multiple vibrational energies corresponding to specific chemical bonds in a complex sample. [23,24] Nobel prize winning C.V. Raman observed the "new secondary radiation" in 1928 by focussing sunlight through a telescope onto more than 60 liquids and using a coloured glass filter to remove the elastic Rayleigh scattering. [25]

Raman scattering is a weak effect with only 1 in every 10 million photons being Raman scattered, the remaining photons being Rayleigh scattered.[26] Raman scattering, however, reveals the vibrational energy shifts of molecules within the sample, under interrogation by a monochromatic incident light source. Raman spectroscopy is an information rich and chemically specific sampling technique that generates a spectrum from which at least four parameters can be determined. These parameters are: the relative concentration of a sample, determined from the peak intensities; the composition of chemical species or atomic bonding, determined from positioning of bands; structural disorder, suggested by the width of the peaks; and changes in the environment such as temperature or pH, often reflected in a frequency shift.[27] Being an optical technique, Raman spectroscopy depends on a visible light source within the ultraviolet (UV) to near IR range of the electromagnetic spectrum.

When incident light strikes a particle it can take one of four paths; reflection, absorption, transmission or scattering. Light scattering can be elastic if the overall energy remains the same, which is known as Rayleigh scattering, or inelastic if it changes energy during the interaction. Inelastic light scattering can be subdivided further, as the light can either gain or lose energy. This depends on the energy in the system but in the majority of cases the light gains energy from the system and the scattered light emerges with higher energy. When the system is heated above room temperature (RT), this increases the proportion of anti-Stokes (scattered light with a lower energy) to Stokes scattering ratio. The incident radiation strikes a molecule, which absorbs it, promoting it to a virtual energy state, before the radiation is emitted with a higher (Stokes) or lower (Anti-Stokes) frequency from the incident radiation. These theories are explained using the Jablonski diagram in Figure 7, depicting the ground state, vibrational energy levels and virtual states.[26] Rayleigh scattered light neither gains nor loses energy (elastic scattering), Stokes

scattered light gains energy from the molecule while the molecule loses energy and rests at a higher vibrational level than it began (inelastic scattering), and anti-Stokes scattered light loses energy to the molecule while the molecule gains energy and settles at a lower vibrational state or ground state (inelastic scattering).

Fluorescence is another technique that is used in life science research and is illustrated in the Jablonski diagram in Figure 7. During fluorescence the photons are absorbed by the fluorophore elevating it to an electronic excited state, before a photon is emitted at a lower energy due to non-radiative decay followed by the fluorophore relaxing back down to a lower energy level. This process is radiative and slower than others such as absorption and vibrational relaxation (Raman). The drawbacks with fluorescence are that: it produces only one broad peak, inferring merely the absence/presence of the analyte; it suffers from photo-bleaching, which affects time course studies; it requires a fluorophore to be tagged onto the compound/molecule/protein of interest, resulting in artefactual distribution within cells; and very few drugs have an inherent fluorescent signal to track the natural spatio-temporal localisation at the intracellular level.[26,28–30] Therefore, fluorescence is not considered a viable method to directly track the drug-NP distribution within cells, and thus will not be used. Fluorescence has the advantage however, that it can be used as a complementary imaging technique to demarcate regions of the cell *e.g.* the nucleus or specific receptors such as EGFR. Fluorescence imaging has a high signal intensity and is easy to detect if a fluorescence microscope is available.

Infrared (IR) spectroscopy could be considered for this study, as it is more information rich than fluorescence and gives an intense signal due to its larger absorbance cross section in comparison with its scattering cross section. IR can be beneficial in studies as it is viewed as the complementary spectral technique to Raman, with centrosymmetric molecules typically those that are Raman active are not IR active. This is due to IR being dependent on a change in the dipole moment where as Raman is dependent on a change in the polarizability. IR can be difficult to use for analysis of aqueous samples *e.g.* cells. Water is strongly IR active, which is the reason it cannot be considered for this project. The vibrational bands of water appear in the spectral regions that this project focuses on, with vibrational bands present at 3300 cm^{-1}, 2200 cm^{-1} and 1650 cm^{-1}.[31] The selection rules for IR state that the dipole moment of the molecule changes during the vibration, whilst Raman selection rules require that the polarisability changes, therefore water produces a weak Raman signal.[32] It is possible to background subtract the water content from IR spectra and there are a vast number of high calibre IR studies on biological samples and in the clinic. However, since the 2200 cm^{-1} overlaps the region of the

spectrum that is important to the drug selected in this study, the technique has been ruled out.

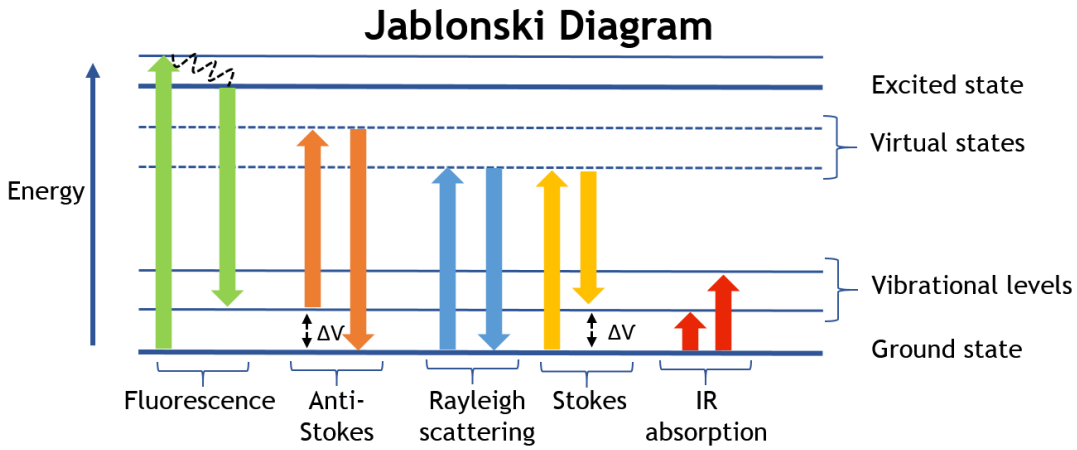

Figure 7 Jablonski Diagram. The lowest energy vibrational state is depicted as the ground state with vibrational energy levels and virtual states of increasing energy above it. Both the incident radiation (upward arrows) and the scattered radiation (downward arrows) have much larger energies than the energy of the vibration ΔV of Raman scattering.[33]

1.2.2 Surface Enhanced Raman Spectroscopy (SERS)

Raman spectroscopy was a breakthrough technique for biochemically determining components in a sample, but as mentioned earlier it yields a weak signal. Significantly, in 1974, Fleischmann and co-workers adsorbed pyridine onto a roughened silver electrode and noted a potential-dependant and strong Raman peak intensity, with a Raman cross section much higher than for conventional Raman.[23] This was the seminal experiment that first demonstrated the effect that would later be named surface-enhanced Raman spectroscopy (SERS) by Van Duyne and his team, who also explained the theory.[23,24] In 1977, Van Duyne *et al.* repeated the experiment in more depth.[24] Finally they postulated that the intense Raman intensities were due to electric field enhancement and that the pH and concentration of a solution were important to the magnitude of the peaks obtained in their results.[24] In the same year Albrecht and Creighton proposed a charge transfer effect as a mechanism for SERS signal production.[34]

This was an important discovery by Fleischmann *et al.* that was elucidated further by Van Duyne *et al., and Albrecht and Creighton.*[23,24,34] Molecules with Raman signatures that were previously too weak or masked by a low signal-to-noise ratio could now be analysed. This revelation renewed research interest in the field of Raman spectroscopy and its applications.[35] The implementation of SERS in the biomedical field for disease detection and treatment monitoring has been largely due to the specificity and sensitivity of the molecular fingerprints obtained from analytes. The enhancement factor achieved from SERS compared to Raman can be

from 10^{10} to 10^{14} at NP "hot spots" where there is less than 1 nm between particles and there is greater localised field enhacement.[36] There are two components which combined explain the SERS phenomenon, these are; the charge transfer effect (chemical enhancement) and the electromagnetic theory (electromagnetic enhancement).

The charge transfer effect depends on the chemical coupling to transfer electrons between the analyte and the roughened metal surface and therefore depends on direct contact or proximal interaction and can only explain a fraction of the enhancement observed. Since it results from direct bonding it should only increase until monolayer coverage of an analyte on the NPs surface.[26,34]

Electromagnetic theory can explain the enhancement up to 10 nm from the surface. It is dependent on the oscillations of the electrons stimulated by the incident laser at the plasmon resonance frequency, inducing the polarisation of the electrons along the surface plasmon.[24,26] This localised surface plasmon resonance (LSPR) of a coherent electron cloud oscillating on the NP surface can be observed in Figure 8.[37] The concept of a surface plasmon was first theorised by Ritchie in 1957 when modelling a thick metal foil to a thinner metal film.[38]

Selection rules can make SERS spectra different from Raman spectra of the same molecule. This was explained by Jeanmaire and Van Duyne when they discovered that on approaching monolayer coverage of pyridine on NPs, the pyridine molecules were attached perpendicular to the surface as opposed to parallel.[24] It is a requirement of scattering that the polarisability component is perpendicular to the surface, consequently the orientation of the molecule would produce a change in scattering and change in SERS intensity from surface associated elements of the compound.[26] This can reveal further information such as the orientation that the analyte is bound, due to greater enhancement of certain peaks at varying concentrations. It can also result in a change in the Raman shift and relative intensity of the bands from the bound moiety, due to an alteration in the molecules symmetry when attached to the metal surface. A specific example is an ordinary Raman assignment for the alkyne moiety in a drug called EL being 2111 cm^{-1} where as upon attachment to a gold NP, the Raman peak shifts to 2008 cm^{-1}.[22]

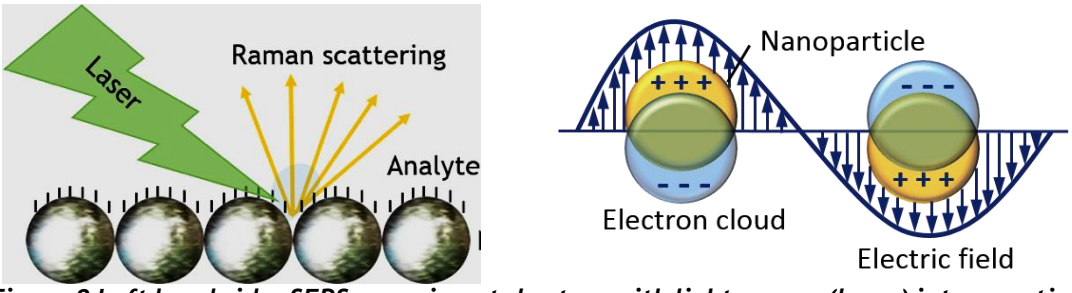

Figure 8 Left hand side- SERS experimental set up with light source (laser) interrogating a roughened metal surface with analyte deposited on top and subsequent Raman scattering. Right hand side (Adapted from Hammond et al.) LSPR with oscillations of electron clouds. Arrows represent the application of an external electric field increasing up and down the y-axis, and oscillations are occurring along the x-axis of time.[33,39]

SERS has additional advantages over other light based techniques. It is a reporter-free approach that employs a monochromatic excitation source to interrogate many samples, with particular advantages for multiplexing. SERS has narrower spectral bands by up to 100 fold in comparison to fluorescent markers, it is information rich as it can describe more than just the presence or absence of a molecule, it is non-destructive in nature and it does not suffer from photo bleaching unlike fluorescence microscopy.[26,28-30]

SERS depends on a roughened surface to obtain its enhancement, therefore NPs and their properties are contributing factors to the quality of results obtained. Next NPs and their character will be discussed.

1.2.3 Nanoparticles

NP is a broad term covering anything in the size range of 1-100 nm which can be composed of any material or composite and be created in many morphologies including stars, cubes, spheres, micelles, tubes, magnets, shells *etc.*.[28,40] Historically, NPs have been used to create unique colours in stained glass windows and are legendary in the form of the dichroic Lycurgis Cup dating from the 4th century AD.[41] This cup embodies the unique properties of the NP colloids in comparison to their bulk form: when lit from outside the cup (reflected light) appears green, and upon light being transmitted from inside it appears red. This is due to the silver and gold NPs included in the glass cups fabrication. Owing to their extinction profile, the sum of light absorption and scattering, each size, shape and material can appear as any colour of the visible section of the electromagnetic spectrum (rainbow). This is the LSPR of the NP and can be controlled and exploited in the synthesis process to meet experimental requirements. NP's small size but large surface area also make them amenable to many purposes from improved sun-cream technology to drug delivery vehicles. At this stage it should be noted that

NPs can be prepared from various materials, for the purpose of this study, the focus shall remain on gold and silver NPs.

Despite silver producing better enhancement, the excitation source used on gold for Raman studies is less damaging to cells as it is a longer wavelength, lower energy.[42] Generally 633 nm or 785 nm excitation is used for gold NPs to be in line with the LSPR typically residing in this range. Hence lower energy than the 514 nm or 532 nm lasers used to excite silver NPs. Near infrared longer than 785 nm has been ruled out for consideration due to the lack of a compatible laser source available for the Raman micro-spectrometer used, although it has excellent properties in terms of retaining the viability of the cell or tissue samples under investigation.[29] A balance must be struck between signal intensity and damage to any live cells being interrogated.

The considerations when planning a study involving a NP delivery system in pre-clinical development have been noted in many studies but are reviewed by Egusquiaguirre *et al*.[30] These are: tumour accumulation, superior dose dependent anti-cancer activity, better bioavailability, low systemic toxicity, good bio compatibility, increased drug payload, enhanced tumour regression, extended retention time at tumour site and enhanced targeting efficiency.[30] These are addressed with examples of the wide range of nanomedicines available in the next section.

1.2.4 Nanomedicine

Nanomedicine was conducted in the field of medicine for centuries before the existence of a phrase to describe the use of NPs or nanotechnology in aiding health. The first mention of 'nanomedicine' on PubMed database of medical and life science journals was in 1999 by Weber D.O., a healthcare journalist in the Health Forum Journal.[43] A full definition has since been released by the European Science Foundation (ESF) in 2004 as;

"Nanomedicine uses nano-sized tools for the diagnosis, prevention and treatment of disease and to gain increased understanding of the complex underlying patho-physiology of disease. The ultimate goal is to improve quality of life… The aim of nanomedicine may be broadly defined as the comprehensive monitoring, repair and improvement of all human biological systems, working from the molecular level using engineered devices and nanostructures to achieve medical benefit."[44]

Further to this the ESF highlighted five main disciplines of nanomedicine: analytical tools, nanoimaging, nanomaterials and nanodevices, novel therapeutics, and drug delivery systems, some of which can overlap to become combinations of the aforementioned. These elements are summarised in Figure 9.

Types of nanomedicines can be: nanoscale versions of their parent drug, composites, micelles or functionalised particles.[36,45,46] Nanomedicines are proven to be more effective at delivering a higher drug load to the relevant site. This results in a more efficacious treatment, at an overall lower dose, reducing side effects and enhancing disease alleviation for the patient. However, until now directly monitoring the drug release from NPs has proven to be elusive on a sub-cellular level.

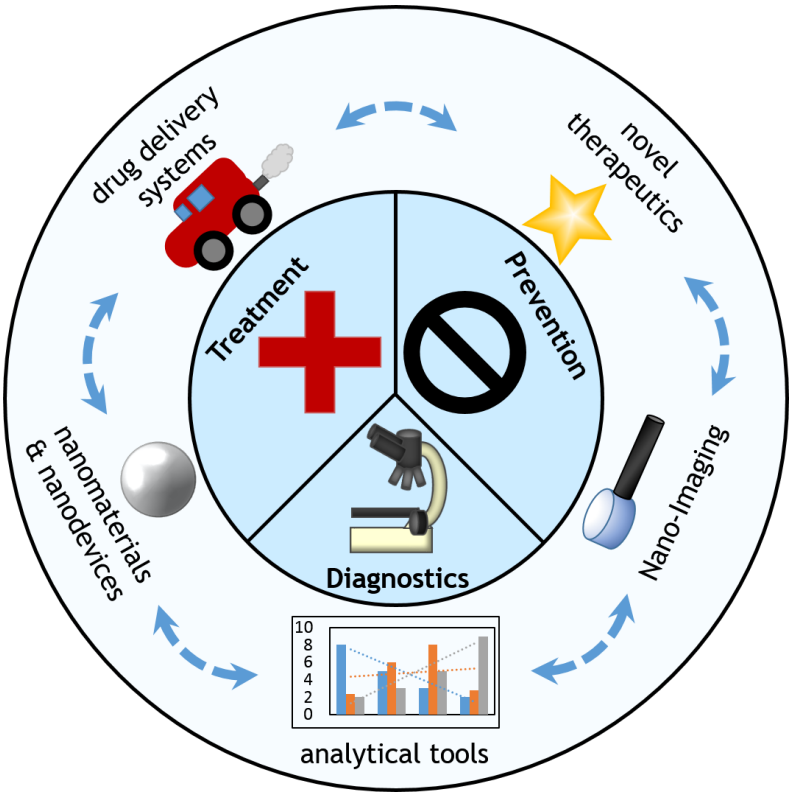

Figure 9 Nanomedicine- nano-tools for diagnosis, prevention and treatment of disease in the centre with 5 main disciplines on the periphery highlighted by the ESF: analytical tools, drug-delivery systems, nano-imaging, nanomaterials & nanodevices and novel therapeutics.

NPs can be functionalised to allow better efficacy, uptake or safety profiles in terms of biocompatibility. The following are some of the surface modification approaches used: the addition of a linker to, for example, give aptamers (short DNA sequences) space for binding the target sequence (i.e. reduce steric hindrance); DNA can be attached by thiol groups as they have a high affinity to form Au-S bonds with the gold NP's surface; pegylation can be used to stabilise the particles and prevent

aggregation; polymer wraps can change in surface charge and many more properties.[36,46,47]

An example of imaging to track the release, is of a UV filter compound (sunscreen) from a dye labelled NP by studying one vibrational mode in stimulated Raman spectroscopy (SRS) and two photon imaging.[48] SRS is a rapid signal detection method using one specified wavenumber, as opposed a full spectrum like ordinary Raman. SRS is useful for mapping areas rapidly as only one wavenumber is interrogated, however this makes it information sparse in comparison to SERS which gathers a full spectrum.

Another purpose of developing nanomedicine is for thermoablation with *e.g.* nanoshells, which seek to destroy the cancer tissue it is delivered to, whilst releasing the chemotherapy to the local area upon heating. This is achieved through heat and targeted delivery by *e.g.* functionalising with antibodies to a cell surface receptor or using magnetic NPs but it requires sensitive and specific properties of the magnet to localise them in the correct area. Thereafter there is an issue with the clearance of the particles from the targeted site. [46] NPs designed for heat release mechanisms will not be discussed further as this study does not employ thermoablation and will concentrate more on the enhanced drug delivery and imaging.

Albumin based nanocomposite spheres have been used to deliver therapeutic agents and Pijanka *et al.* suggest that greater albumin content increases cell viability as measured by cytotoxicity assays, probably due to better biocompatibility.[49] If the drug is prepared in culture media the proteins of the foetal bovine serum (FBS) should elicit a similar effect *via* the protein corona (proteins opsonised to the surface of the NP).

Micelles are size tunable drug delivery vehicles in the nanoregion that are being developed to load hydrophobic drugs such as Paclitaxel, which is usually administered in cremaphor as an oily solution. However, many patients suffer from hypersensitivity to the drug carrier. Luo *et al.* studied the size tunable element of paclitaxel micelles, self-assembled from PEG-b-dendritic oligo-cholic acid, to achieve targeted distribution.[50] They confirmed that 17-60 nm micelles enter tumours according to the enhanced permeability and retention effect (EPR) of passive entry and that larger micelles of 150 nm enter lung and liver cells. Regardless of the NP used to deliver the drug these size rules would apply and must be considered when designing a drug-NP conjugate.

A doxorubicin study on NPs with a pH-sensitive drug release mechanism was carried out by using a SERS reporter tagged silver NP, coated with a layer of pH sensitive chitosan/poly (methacrylic acid) (CS-PMAA). They were further functionalised by adding a transferrin on the surface to target transferrin receptor (TfR)-overexpressed cancer cells.[51] The pH sensitivity allowed cargo offloading in a cancer specific manner as tumours tend to be more acidic. This produced a localised drug effect that was more pronounced at the malignant site, which was favourable, as it in turn would lessen systemic toxicity to the patient by concentrating the chemotherapy.

Since 2011 further advances have been made on tailoring pH sensitive drug release by Du *et al.*.[52] They created a dual pH sensitive particle, which reverses its surface charge from negative to positive at tumour extracellular pH (~6.8) to enable cell internalisation. Thereafter a drop in pH to (~5.0) in subcellular compartments, such as the endosome, encourages doxorubicin release from the endocytosed drug carriers.[52] This is a cancer targeted approach that works without the need to investigate surface receptors, and could be beneficial if the cancer has metastasised to several sites.

Mitoxantrone is an antineoplastic drug used to treat several cancers with a limit of detection (LOD) in fresh serum samples in the region of 4.0×10^{-11} M (0.02 ng/mL) by Surface Enhanced Resonance Raman Spectroscopy (SERRS).[53] This drug is blue in solution thereby acting as a chromophore, which couples with the LSPR of the silver NPs to provide an intense resonance Raman signal. This is a clinically relevant test as levels are closely monitored to avoid cardiomyopathy having a fatal effect on the patient. However clinicians prescribing habits for this drug changed when the test was optimised in 2002 and it is no longer pertinent to cancer treatment.[53]

Mitoxantrone has also been studied as a treatment with doxorubicin, delivered together as dual chemotherapy by a liposomal pegylated NP.[54] Combination therapies to prevent drug resistance developing have become popular in many medical areas. Nanoformulations can enable delivery of a drug effectively with less systemic toxicity to a patient at a lower dose. The issue of delivering a drug in a nanoformulation is being pursued heavily in the field, such as gold nanospheres coated with oxaliplatin.

Oxaliplatin is another interesting drug, in 2010 Brown *et al.* were able to improve the IC_{50} three-fold by a new drug delivery method *in vitro*.[55] They achieved this by tethering the platinum based drug to a gold NP with a PEG linker. It was noted that

in lung cells the localisation differed and oxaliplatin tethered to gold accumulated in the nuclei. It is known that at a systemic level, tumours experience an enhanced retention permeability (EPR) effect, which is passive transport through misstructured vasculature into the cells. However the biology underpinning nano-oxaliplatin's localisation in the nuclei is open to further investigation and interpretation.

Following on from Brown *et al.*, the work presented here will investigate further the downstream effects and response associated with an anti-cancer drug-NP treatment *versus* its free-drug counterpart. This would enable an efficacy and imaging project with a global phosphoproteomic study from a more targeted treatment. Oxaliplatin is generally cytotoxic, whereas EL acts only upon the EGFR preventing the downstream signalling cascade by inhibiting phosphorylation. The imaging will be conducted on a Raman microscope to create cell maps.

1.2.5 Raman Cell Mapping

Raman cell maps are useful for locating molecules within a cell whether they are biochemical constituents, drugs or NPs functionalised with SERS active dyes. M^{c}Aughtrie *et al*. created a 3D map to multiplex the tracking of SERS active tags by producing a pseudo coloured overlay of SERS tags onto the Raman signature of a cell.[47] Some studies have been able to differentiate cell types without the addition of NPs, which is a non-destructive method to determine cell type. A Raman micro-spectrometer can accommodate various samples, including live cells with the use of environmental chambers, microfluidic devices or water immersion objectives. Figure 10 illustrates a basic schematic of the instrumentation used to SERS map during this study on fixed and live cells.

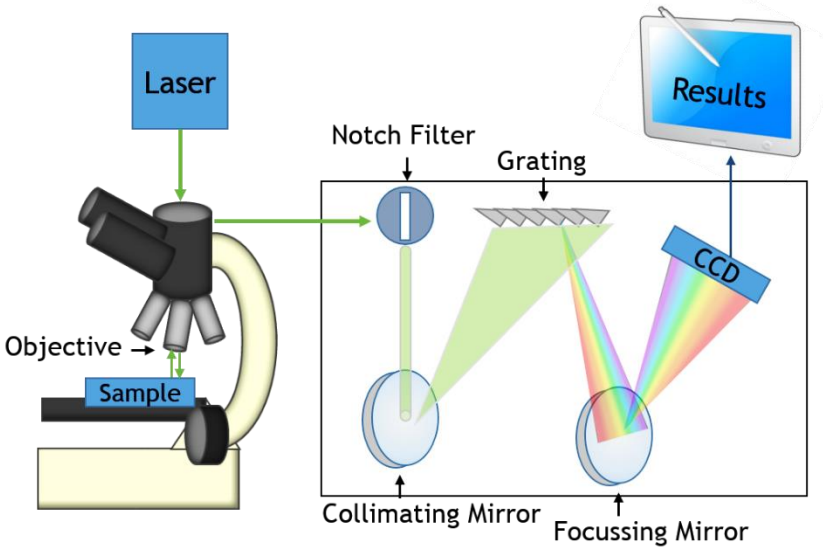

Figure 10 Raman micro-spectrometer schematic. The laser source, which can be altered when required (532 nm, 633 nm or 785 nm) entering a microscope where the objective can be air or water dipping. The scattered light travels back through the objective into the spectrometer through a notch filter, which filters out Rayleigh scattered light (laser line frequencies), then travels to a collimating mirror that is directed at a grating (this can be 1200 l/mm or 1800 l/mm). The light is diffracted onto a focussing mirror which focusses it onto an imaging sensor (charge couple device (CCD) detector), before the data is sent to the computer containing wavenumbers and intensities. Where maps are concerned, there is further dimensionality to the data in the form of X, Y and Z co-ordinates for 3D or X and Y only for 2D.

A cell study has mapped the differences between malignant, benign and varied cell types from the lung. Raman spectroscopy was able to differentiate between lung cancer cells and lung epithelial cells and also lung fibroblasts. Further to this it was identified that there was a clear difference between cells from the same lineage of fibroblast, with one rendered immortal with an increased proliferative activity. The spectral differences were found to be predominantly from the nucleus, therefore isolation of nuclei strengthened signal divergence.[56] These differences were analysed using multivariate techniques such as principle component analysis (PCA). Essentially PCA reduces the dimensionality of data allowing the variance in data to be determined. Typically it is the background that is removed as the first loading and gradually more minute discriminations are made against variances in the data. Nicholas Stone's group were able to differentiate between four prostatic adenocarcinoma cell lines using this analysis in their Raman microscopy being developed for the clinical setting to diagnose cancer types. It has also been used to delineate the boundary of malignancy during resection.[57,58] The obvious advantage of Raman mapping during surgery is to minimise tissue removal whilst ensuring complete excision of cancerous cells.

The aim of this study was to determine the anti-neoplastic agent's fate within the cell by imaging and not to diagnose malignancies. PCA was therefore not required for the Raman maps acquired to separate populations of cells, although it is a

powerful data analysis technique, the maps acquired during this study could be analysed by simple univariate investigations of the alkyne peak.

The cell mapping procedure that was followed in this study includes the peak assignments used by others including El-Mashtoly *et al.*.[59] Figure 11 is an example of a cell map including the cell fingerprint region of 1000-1800 cm^{-1} Raman shift, to delineate the lipids, proteins and other cell components. The area under the vibrational peak was used to pseudo-colour the cell and the constituent distributions. Phenylalanine from proteins in the cell is observed at ~1002 cm^{-1}, CH stretches of proteins and lipids are a broad band at ~3000 cm^{-1} although a shoulder is present at ~2850-2875 cm^{-1} primarily from the lipid content.[60] Importantly, it is obvious from the example spectrum that there is a window from 1800-2800 cm^{-1} with no Raman signature from the cell. This is described as the cellular silent region of the spectrum. EL, the drug of interest, contains an alkyne bond which produces a Raman band at ~2100 cm^{-1}.[22,27] Having this region free of complex signals lends itself to detecting the drug intracellularly with ease and interpreting the data through univariate means.

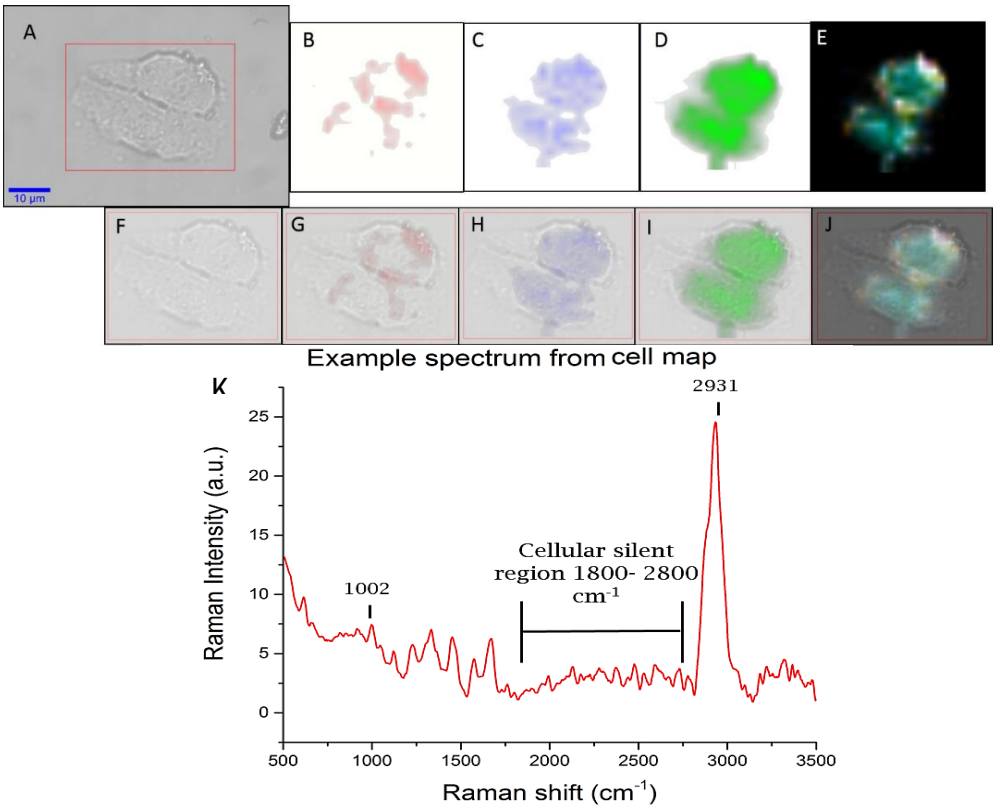

Figure 11 Label-free Raman imaging- pseudo colour maps of fixed CHO cells. A. Zoomed out white light image with 10 µm scale bar, B. red area under lipid peak 2850-2875 cm^{-1}, C. blue area under phenylalanine peak 1000-1010 cm^{-1}, D. green area under protein and lipid peak 2800-3050 cm^{-1}, E. composite (of B, C & D), F. cropped white light image, G-J merges of white light and respective pseudo colour maps from B-E above. K is an example spectrum of a Raman cell fingerprint acquired with a 532 nm laser source; 1002 cm^{-1} phenylalanine peak and 2931 cm^{-1} CH and CH_2 peak of lipids and proteins are highlighted as is the cellular silent region of the spectral fingerprint of cells.

The images in Figure 11 were acquired from a fixed cell, however there is debate surrounding how accurate a representation this is of the cells' actual state when living. This is due to the fact that the fixation process removes lipid content from the cell membranes and can potentially cause other artefactual effects.[61] Raman maps can require hours to acquire confocal 3D stacks, it is difficult to map live cells without their healthy state being compromised in an open dish due to the lower temperature and lack of correct gas composition in open air. To circumnavigate this without a costly microscope upgrade of an environmental chamber to control the temperature and a gas line to regulate the gaseous surrounds to mimic that of *in vivo*, a microfluidic device can be used.

1.2.6 Live cell imaging with microfluidic devices

Microfluidic devices are a platform that can be used to study live cells at single cell resolution but in a high throughput manner and in a cost effective way.[62] These devices can be manufactured from a mould within a day and are extremely reproducible. They have been in use since the 1970s by engineers and gained in popularity amongst the life science community in the 1990s with proof-of-concept work.[63,64] This was typically to model the *in vivo* environment without the use of animals and can also be referred to as 'lab-on-a-chip'. Figure 12 shows an example of a basic microfluidic device which is optically clear as it is fabricated from cured polydimethylsiloxane (PDMS) on a thin microscope slide.

A microscopic view is also shown in Figure 12 showing the scale of the channels and the ability to separate cells for live imaging under a Raman micro-spectrometer. Any Raman background from the PDMS is not collected, since it is used with a confocal imaging system and any background is lost through focusing simply on the cell. The basics of the device are that there is more than one inlet allowing the controlled loading of oil and aqueous sample to be added. The flow rate and channels allow the formation of liquid droplets or bubbles which hold cells for interrogation, these are surrounded by an oil suspension. The oil surrounding the sample droplets aids the retention of gases to keep the cells viable for longer.[64] The first report of Raman microscopy performed on a microfluidics platform was by Cristobal in 2006.[65] This was quickly followed by Ackermann, Henkel and Popp publishing a SERS paper quantifying drugs within a microfluidics device in 2007.[66]

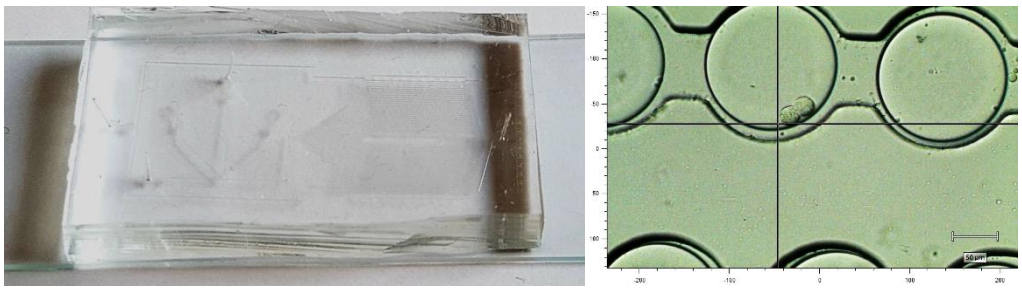

Figure 12 Left, is a PDMS microfluidics device with inlets for oil and cells to the left, followed by the channels to hold bubbles with individual cells to the right. Right, is the device under the Raman microscope, to demonstrate the liquid phase bubbles containing cells (rounded as not adhered), within the channels containing the oil phase to separate droplets.

1.2.7 Alkyne Imaging

In 2011 the first example of alkyne (C≡C) imaging within a cell was achieved by Yamakoshi *et al.*.[67] The significance of being that it is a less perturbing labelling method, as the alkyne modification conjugated to the nucleotide mimic EdU should not hinder interactions in the cell unlike bulky fluorescent tags. Although the effects of alkyne tags should still be determined empirically upon the cell. They were able to visualise cell proliferation using the alkyne tag as its Raman band resides in the cellular Raman silent region of the cell (1800-2800 cm^{-1}).[67]

Subsequently, Yamakoshi *et al.* were also the first to produce multicolour imaging within a cell without the use of fluorescent markers.[68] In this study the alkyne moiety was conjugate to an aromatic ring and a diyne amongst others. These produced bands in the Raman shift range of 2100-2250 cm^{-1} and were distinct enough to allow duplexing. The alkyne moiety is user friendly to the cell biologist using Raman spectroscopy as it is easily determined in the cell from its intensity.[68]

Palonpon *et al.* also report that high spatial and temporal resolution can be achieved with Raman mapping especially with alkyne moieties. [27,69] Recently Wei Min's group have demonstrated an impressive 20-plex carbon-rainbow of poly-alkyne variants to image organelles within cells.[70] This exceeds the multiplexing capabilities of many fluorescent images, although these were not all separated from the same cell but several were together. It would be interesting to see if all 20 probes could be barcoded together in one cell successfully. In Figure 13 it is demonstrated that by changing the alkyne content and adding *e.g.* amines and aromatic ring structures, that the Raman shift can be tuned to differentiate the organelle markers when imaging with any Raman based methods.

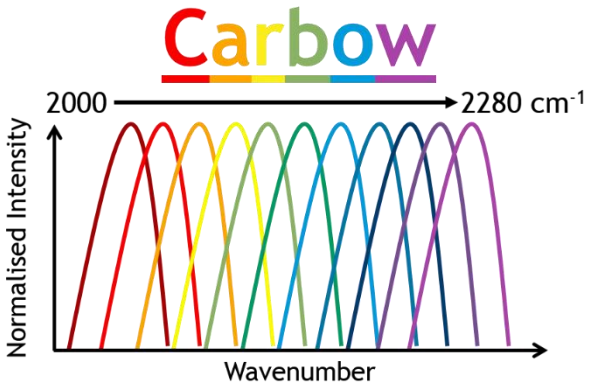

Figure 13 Carbon-rainbow of polyyne based materials for multiplexed organelle imaging, pseudo-coloured based on the difference of the alkyne based Raman shift. Adapted from Hu et al..[70]

All of the above examples of alkyne imaging are of reporter molecules with tags inserted, which could potentially affect the distribution within the cell and therefore need careful testing. The alkyne group in EL, however, which also produces a strong Raman peak allows label-free imaging of uptake, localisation and metabolism.[59] Namely, absorption, accumulation, distribution, metabolism and excretion.[59] This is possible since the alkyne is inherent to the drug's structure.

These data support the use of EL bound to NPs in this study as the intensity will only be enhanced further for imaging purposes and potentially the efficacy will be enhanced too. Careful consideration must be taken of the effect of NPs alone in the system, therefore the biocompatibility is important.

1.2.8 Biocompatibility

NPs have been scrutinised for their toxicological properties *versus* their bulk counterparts in recent years after the rise of nanomaterials in industry research and medicine.[71] In 2004 the term nanotoxicity was introduced amid concerns for their rising use and potential harmful effects exerted by their size.[72] Despite the cautious attitude of some over the use of NPs, in 2013 there were 247 nanomedicines either approved or in clinical studies.[73] On the whole, nanomedicines are reputed to have less toxicity than their parent drugs, rather than increasing efficacy.[74] Their increased uptake by cells due to their inherent size and large surface area are what make them suitable for drug development, however there are many considerations in terms of their biocompatibility as seen in Figure 14.

Biocompatibility is the ability of a material to perform with an appropriate host response in a specific application without producing an adverse effect.[75] NP biocompatibility is an area that encompasses several factors including: the cytotoxicity due to surface chemistry, the passive entry and retention in cells, the

excretion to the biliary and renal system due to size and the clearance by the reticuloendothelial system (RES).[15,73,75,76] Many drugs take the surface charge and chemistry into consideration and are coated in polyethylene glycol (PEG), a molecule approved for use in the body.[77]

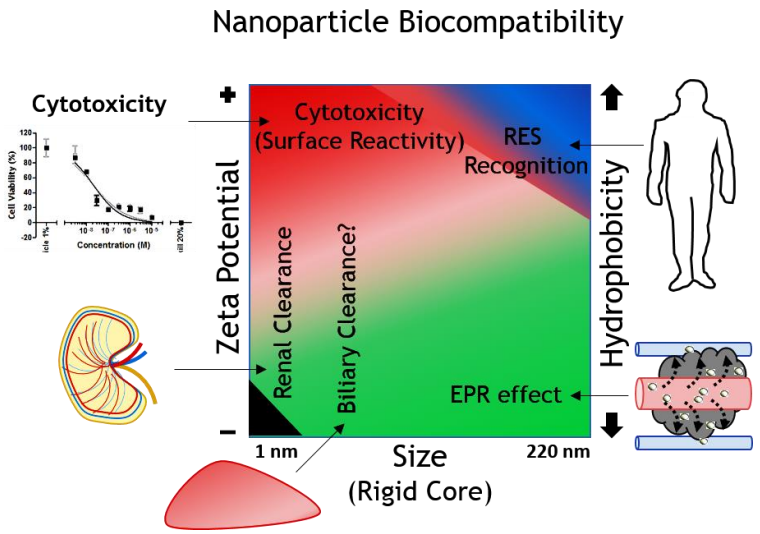

Figure 14 NP biocompatibility schematic. The physiochemical properties associated with NP biocompatibility are; size, surface charge and hydrophobicity. These impact upon cytotoxicity, renal clearance, biliary clearance, enhanced permeability retention (EPR) effect and the RES. Adapted from Grodsinski et al..[15]

The first FDA approved nanodrug in 1995 was the pegylated anti-cancer nanodrug Doxil based on parent drug doxorubicin.[78] Other agents found to be useful to aid the delivery and compatibility are proteins such as albumin.[49] In relation to cancer targeting NPs, they can be tagged with targeting molecules or ligands that recognise biomarkers such as cell surface receptors, for example, an EGFR peptide D4 has been used to target liposomes to the receptor.[79-80] Regardless of the surface presented on a NP, the size is a greater determinant of its success. To expand further, the decoration of a particle with an antibody to target a cell will not promote cellular uptake if the particle is physically too large to enter.

NPs are by their nature between 1-100 nm in size in one dimension, the importance of which is observed in Figure 14. On the whole, NPs have enhanced tumour delivery due to the enhanced permeability and retention (EPR) effect which enables passive diffusion through the leaky tumour vasculature.[79] However, despite the EPR effect macrophages may still engulf the particles for excretion through the RES. This occurs due to the proteins on the surface of the NPs and if not surface modified to have proteins such as an albumin coating, the plasma in the body can coat the particles and they would be destined for opsonisation.[15] This coating effect from the plasma and serum creates what is known as the protein corona surrounding the

surface of the NP, altering the charge. Modifying the surface with a hydrophilic polymer can counteract the RES clearance.[81]

The composition of nanomedicines can be as polymeric composites, pegylated nanodrugs or as micelles.[28,50,54,82] However, this study will use noble metals as a nanocarrier to the EGFR therefore the inherent toxicity of silver should be considered. Inert or less-toxic gold has the drawback of a lower SERS signal intensity than silver when imaging.[40,83] A careful balance needs to be struck between imaging efficiency, drug release and efficacy and the toxicology of the NPs used. For these reasons, silver for its superior SERS intensities and gold for its non-toxic properties will be explored during this nano-delivery investigation with EL.

1.2.9 Current Field of Erlotinib & Raman/SERS Imaging of Drugs

An early report of a nanomedicine study on EL was first published in 2009, where a polymer was used to encapsulate EL for delivery in rats. Marslin *et al.* found that the nanoformulation reduced cytotoxicity and resulted in controlled drug release, which could improve treatment efficacy.[84] Subsequently a cellular study on another nano-encapsulation was carried out in 2014 by Barghi *et al.*. They found EL cytotoxicity to be dose and time dependent, and drug loaded NPs were more anti-proliferative than free-EL.[85] The active site of the drug includes the acetylene group, it is important that the drug is removed from the NP intracellularly to be effective against the cancerous cells.

Nanogold spheres coated with EL are documented by Lam *et al.* who characterised them with Raman and SERS. The peak assignments for free and AuNP bound EL of the alkyne for Raman and SERS being 2111 cm^{-1} and 2008 cm^{-1} Raman peak shift respectively. Their focus was on the adsorption and desorption of EL on the NPs and the dynamic functional theory (DFT) modelling of their attachment to the surface. They concluded that attachment was most likely *via* the acetylene group, which was speculated to detach inside of cells.[22]

Free-EL was used in Raman mapping experiments down to the concentration of 100 µM, which is much greater than is clinically relevant.[59] The levels of EL detected in the serum of patients is two orders of magnitude less at 3-5 µM where the patients are treated with a typical dose of 150 mg.[59] The Raman map in El-Mashtoly's study had alkyne signal just above the noise of the background in one of 3 z-slices and could be described as extracellular, as there was no correlative study to prove it was intracellular. Additionally, the distribution in the Raman map appeared to be more crystalline, as a shard of precipitated drug, as opposed to being distributed

within an organelle. However, the localisation is described by the authors as mapped to the membrane and cellular components *via* analysis of the full Raman spectral signature using hierarchical cluster analysis (HCA). El-Mashtoly *et al*. propose that they were able to determine metabolites of EL in the cell by comparing to reference spectra of the metabolite molecules.[59] Another SERS study of metabolism focussed on 6-mercaptopurine and demonstrated that with Au@Ag NPs the metabolism could be monitored intracellularly, however due to the covalent attachment orientation, it rendered the compound biologically inactive.[86]

Overall a study of the efficacy enhancement of EL on a NP that can be tracked within the cell for its spatio-temporal distribution and metabolism has not been attempted. Downstream signalling analysis of the mechanisms of action of EL-NP on EGFR compared to free-EL, has not been published to date, and these points will be addressed herein.

1.2.10 Multi-Modal Correlative Microscopy

The SERS imaging and NP localisation should be validated using correlative techniques in order for it to be accepted by chemists, spectroscopists and biologists alike. These techniques include other light based methods such as DF microscopy for NP localisation and confocal fluorescence microscopy to interrogate biomarker expression and nuclear or other organelle staining.[87] Beyond these are techniques which do not have light based imaging artefacts, such as electron microscopy. Scanning electron microscopy (SEM) confirms the exact size of the NP and transmission electron microscopy (TEM) can be carried out on fixed and sectioned cells to confirm NP uptake within the cell and their localisation.[88]

1.2 Cellular Response to Erlotinib and Conjugates

1.2.11 Overview of Nanoparticle Toxicity

Before comparisons can be drawn between free-EL and the proposed conjugates in this study, a baseline level of toxicity must be established by the presence of NPs alone within the cell model system. There are many well established assays that could be used to assess whether NPs affect proliferation, viability, metabolic activity, migration *etc*. However, it must be stated that there are issues with NP compatibility and these high throughput colorimetric, fluorescence and luminescence based assays, predominantly yielding false positive results. This is an area hugely underestimated and ignored within the nanotechnology community. Elements that seem to be ignored are: that NPs have an intrinsic fluorescence/absorbance, that NPs can have an enzymatic effect on assay components and that NPs and analytes in the assay can affect the accurate

assessment of toxicity.[89] Most likely these physio-chemical artefacts are exploited for the intent of proving that NPs are not harmful due to the fact that most of assays return false positives- namely that cell health appears unaffected due to a greater absorbance or fluorescence read out as an artefact of the NP content.[90]

A publication by Ong *et al.* reviewed NP interference in toxicity testing and stated that 95% of papers from 2010 did not account for potential interference of NPs in these tests.[89] Ong *et al.* proved that:

"…interference could not be predicted solely by interactions between nanoparticles and assay components."

Any means selected to characterise the effect of NPs and conjugates on cells must take this into account and tests be determined empirically, to be deemed appropriate for each particle type and cell line combination.

1.2.12 Methods to Determine Drug Efficacy

EL is an anti-proliferative and cytotoxic agent the activity of which can be assessed by quantifying the inhibitory concentration on 50% of the cells (IC_{50}). As mentioned previously, this can be complicated to detect when NPs are present in the samples, therefore other techniques must be employed. These are mainly low throughput such as: Trypan blue live dead counts for cell number and viability, live/dead fluorescent stains on montages of single cells (since bulk or populations of cells are more prone to fluorescent artefacts, but on a single cell level this does not impact the results), immunofluorescence assay (IFA) staining for activated pEGFR (lack of staining indicates effective treatment of inhibiting EGFR activation), Western blot to determine the level of pEGFR/tEGFR for efficacy of the drug. However it should be examined more thoroughly downstream to map the full extent of the drug's effect on the cell. Flow cytometry which is a high throughput fluorescent cell imaging technique could be used as each cell is assessed individually. However this requires access to specialist equipment and depending on the particles used, they could infer autofluroesnce that would need knowledge on how to process the data to exclude these background fluorescent counts (known as gating for properties such as size, granularity etc).

1.2.13 Biochemical Signalling Pathways Analysis

Techniques to explore biochemical signalling pathways and the phosphoproteome are those involving protein analysis from cell lysates. On a basic level Western immunoblots are used for these analyses and an example of a higher throughput

format is the RPPA, sometimes used in drug discovery pipelines. RPPA allows multiple cell lysates to be screened for response of their biomarkers to varying concentrations of several drugs *i.e.* each array can have 36 samples of 2 µL lysate spots in triplicate, therefore 108 samples, which are blotted in a serial dilution of 4 spots, therefore one array holds 432 data points. Each slide can hold up to 7 arrays or, in other words, 7 antibodies can be used to probe the 36 samples per array, creating a possible 252 protein examinations per slide. This miniaturised format is both cost effectual for consumables and labour efficient; to obtain quantitative analysis of target protein abundance including post-translational modifications in response to drug treatments.

RPPA is a platform pioneered in 2001 by Paweletz *et al.* that produces a quantifiable output of protein expression levels by loading equal total protein quantities.[91] The normalisation is against a total protein stain, such as fast green, after having prepared cell lysates to be of equal protein content from a protein quantification assay. The format is a microarrayed fluorescent read-out that is captured from a microscope sized slide in a dot-blot fashion, as can be seen in Figure 15. This output is obtained by initially using a robot (Aushon 2470 array platform system) to spot the cell lysate onto the nitrocellulose coated slides. The slide is then treated similarly to an IFA with regards to: blocking, 1° Ab, washing, 2°, washing and signal detection. Care needs to be taken to ensure that the primary antibodies are of high quality and have been at a minimum validated by Western blot. They need to be extremely 'clean' in order to give a reliable result by RPPA, this means that there must only be one protein species present that should be sharp with no background staining.[92] In this instance a near infrared fluorophore is attached to the secondary antibody, whether it is anti-mouse or anti-rabbit.

Heatmaps are then produced from normalised protein levels and can be grouped by HCA into linked proteins and most similar samples due to their protein expression profiles. Each of these are bootstrapped (grouped) with probabilities associated with the likelihood that each cluster is linked. Therefore those samples or proteins bootstrapped with a number closest to 1 (the maximum relationship probability value) have the highest chance of being connected due to the similarity in their protein expression levels or profiles. Further to this, interactive network analyses can be performed to show links within and between pathways in a pairwise manner between 2 samples.

Overall this RPPA system is an efficient approach to assess an array of variables during a drug screen *e.g.*: concentration curves for IC_{50} values, time courses,

sensitivity in multiple cell line responses. This will allow multiple comparisons to be drawn simultaneously under the same conditions.

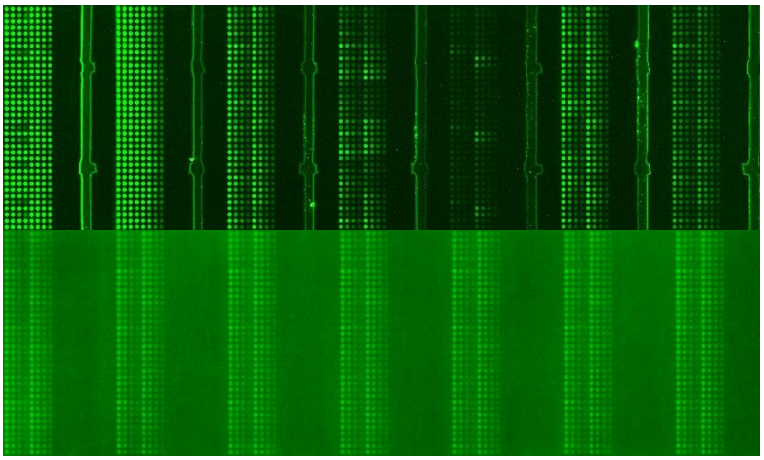

Figure 15 Typical RPPA slide stained with antibodies (top) and fast green slide of total protein loaded (bottom).

1.2.14 Potential Effects of Nanoparticles on Signalling

The effect of the metals in their nano form on the cells must be considered as controls to enable fair comparisons to be drawn, between the effects of nano-delivery and free-EL on the cells selected for this study. Silver in particular can cause cell damage by inducing a stress inflammatory response of the cell by the leaching of silver ions from the NPs surface as they oxidise within the intracellular environment.[93] The stress inflammatory response adds to the creation of reactive oxygen species (ROS) as a result of the uptake of the exogenous NPs, this then leads to oxidative stress upon exhausting supplies of antioxidants. Oxidative stress occurs when the balance of antioxidants and ROS is perturbed, resulting in overall greater ROS and depleted antioxidants within the cell.[94] Metabolic oxidative stress that is induced by normal mitochondrial activity, is believed to promote tumorigenesis by activating redox-regulated pro-growth and pro-survival signalling pathways. Redox regulation of EGFR can modulate the signalling pathways that play a role in the protection of cancer cells against oxidative stress.[95]

Waris and Ahsan described the impact that both exogenous (external factors) and endogenous (internal factors) can have on the cells as a result of oxidative stress; these have been summarised in Figure 16 adapted from their paper.[94] It is illustrated in the figure that redox sensitive kinases such as mitogen activated protein kinases (MAPK) including Erk, JNK and p38 can regulate transcription factors through phosphorylation.[94] Src, JAK, and Akt are amongst other key players responding to oxidation signalling. These proteins as well as those involved in further related signalling pathways are explored in depth in the final chapter as MAPKs are also

affected by EGFR inhibition by EL.[95] Therefore the relevant controls have been included herein to elucidate the complex and potentially opposing effects that EL, NPs and the conjugates impart upon the cells. The RPPA assay is an ideal platform to explore the multiple particle types and treatments, alongside incubations times on EL sensitive and insensitive cell lines. HCA heat maps and interactive network analyses are used to reduce the dimensionality of the data from the RPPA of >8000 thousand data points, to several figures to be concisely presented here, to conclude this EL-NP conjugate study.

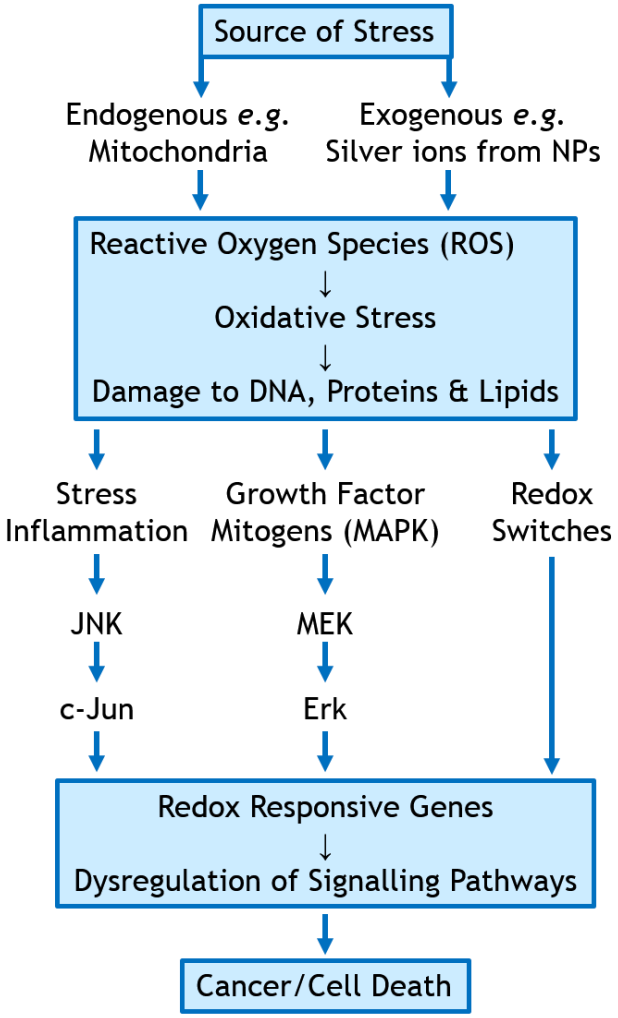

Figure 16 ROS and redox signalling on cells. Adapted from Waris and Ahsan.[94]

To bring a close the introduction, a mind map was created to summarise the experimental areas that this study employs (Figure 17). This is an analytical chemistry project at the core but since it is inter-disciplinary the map helps to contextualise the work within the biological sphere.

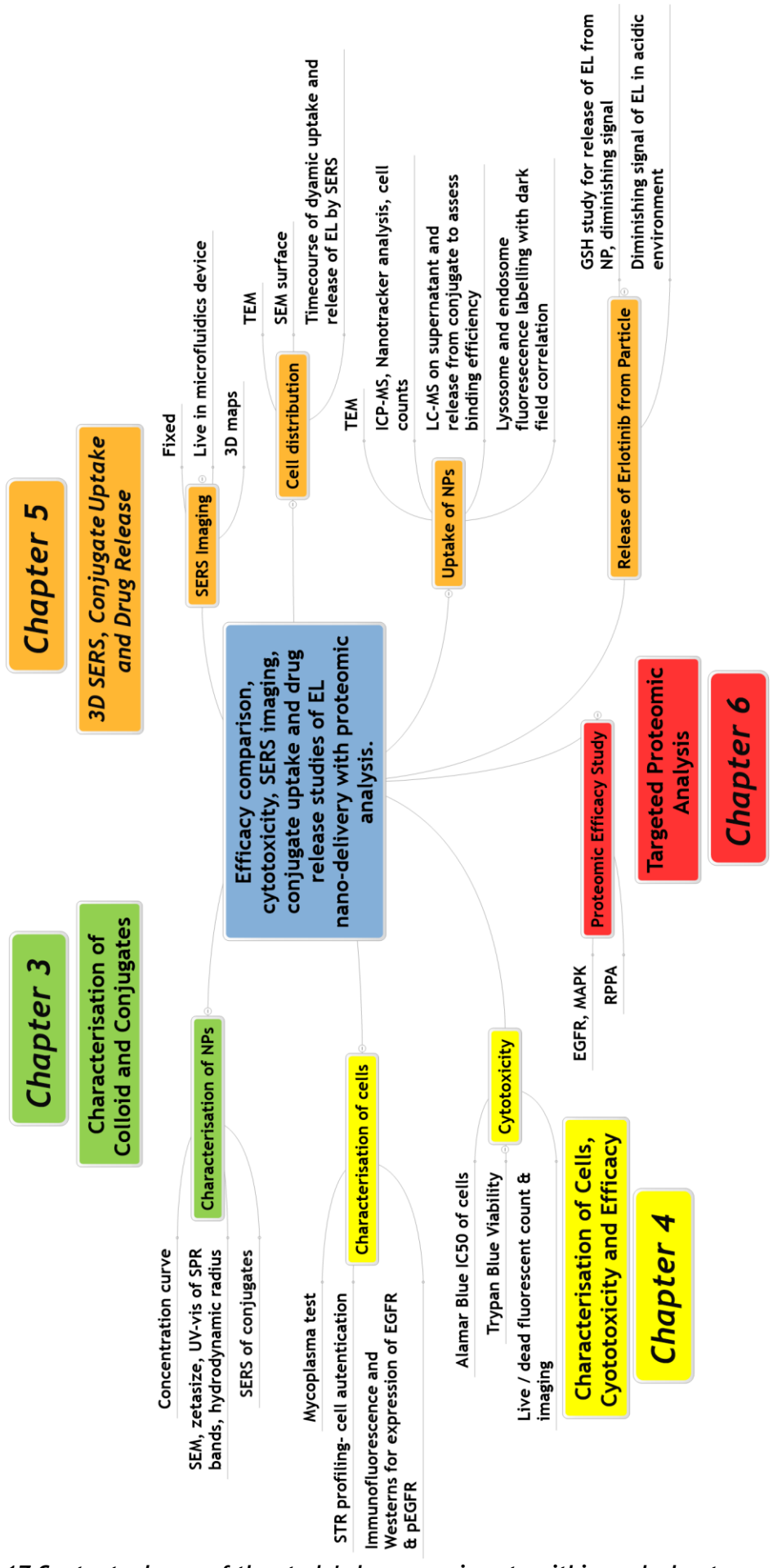

Figure 17 Contextual map of the study's key experiments within each chapter

1.3 Aims

This study aims to investigate the efficacy of nano-delivery and reporter-free imaging to track delivery and distribution of an anti-cancer drug-NP conjugate, in a drug-sensitive and drug-insensitive lung cancer cell line. Furthermore, two particle types were used to investigate any synergy that can be gained from drug loading on silver *versus* gold nanospheres.

EL is an EGFR TKI used to treat NSCLC, however like many anti-cancer drugs the underlying reason or mechanism for treatment inefficiency is largely unknown. This is detrimental to the health of patients and the associated cost burden on the health care provider of these treatments is large. This project aims to investigate the localisation, retention and uptake dyamics of EL in cells *in vitro*. Raman spectroscopic fingerprints of cancer cells will be used to create 3D maps along with SERS to track the drug-NP conjugate's effect on cancer cells. These are split into 4 main objectives in further detail below.

1. To determine the optimum concentration of EL-conjugate and characterise the SERS signal from both gold and silver conjugates along with their physiochemical properties.
    - This was carried out by extinction spectroscopy, dynamic light scattering (DLS), SEM and heandheld SERS instrumentation. This was to compare data to that already available in the literature. It is the foundation which the cell studies are based upon.
2. To determine whether EL-NP conjugates can improve the efficacy and toxicity of *in vitro* cancer cell treatment when compared with free-EL.
    - Cytotoxicity can be assessed in a number of ways using low-technology vitalality staining assays. Furthermore IFAs can be used to profile the pEGFR expression levels and distribution, as well as Western immunoblots to support these data in a quantitative manner of phospho/total EGFR expression.
3. To characterise the spatio-temporal distribution of EL *in vitro,* in fixed cells and live cells.
    - This was achieved by characterising the anti-cancer drug-NPs SERS signatures. The aim was to achieve satisfactory signal from optimal conditions at a concentration of 5 μM or less, to remain clinically relevant.[59] Cells will be SERS mapped along with correlative techniques to determine the distribution on or within the cell where the EGFR is situated.[11,59]

4. To explore the mechanisms of action of conjugated EL on NPs and whether they alter from free-EL. Furthermore, to investigate any stress, cell death or toxicity signalling associated with bare NPs.
    - Altered mechanisms of action or to prove that NP bound EL affects cancer cells analogous to that of free-EL, was investigated by exploring the downstream signalling pathways of the EGFR. Initially an immunoblot phosphorylation analysis of the EGFR was carried out before a thorough, high throughput RPPA assay was subsequently performed.

Chapter 2 Experimental

"Don't let anyone rob you of your imagination, your creativity, or your curiosity."
Dr Mae C Jemison, Astronaut, Entrepreneur, M.D.

This chapter contains details of the materials and methods used to: synthesise the NPs, prepare and characterise the conjugates, along with the imaging and quantification techniques employed to verify the SERS mapping data and the cytotoxicity and efficacy of the conjugates in lung cancer cells, and finally the RPPA functional proteomics / pathway analyses study. Some details are summarised or expanded further in the results and discussions sections that follow, particularly for the data interpretation methods associated with the RPPA as they are lengthy and are intertwined with the explanation of the results.

2.1 Conjugate Preparation

2.1.1 Nanoparticle Synthesis

All glassware was cleansed of organic residues by scrubbing with hellmanex detergent and then cleansed of metal residues using a 15% nitric acid incubation followed by aqua regia and finally rinsed thoroughly with deionised water and left to dry.

Hydroxylamine reduced silver NPs (AgHA NPs) were synthesised to obtain negatively charged silver NPs *via* the Leopold and Lendl method.[96] To obtain 40 nm silver spheres, hydroxylamine at a final concentration of 1.67×10^{-3} M was added with 3.33×10^{-3} M final concentration of sodium hydroxide in 180 mL of deionised water. 20 mL of 1×10^{-2} M silver nitrate was quickly added, whilst stirring at room temperature in a conical flask at a moderate speed with a 2 lugged glass stirring rod. Initially the solution was a dark brown colour and after stirring for 15 minutes it became a yellow amber colour.

Citrate reduced gold NPs (AuCt NPs) were also negatively charged and synthesised by the Turkevich method.[97] 40 nm AuCt NP spheres were prepared by boiling 500 mL of deionised water in a round bottomed flask mixed at a constant speed with a 2 lugged glass stirring rod over a gas flame. Sodium tetrachloroaurate (60.5 mg) was added to 1 mL deionised water before adding to the boiling water , followed by boiling for a further 10 minutes. Sodium citrate (57.5 mg) was dissolved in 7.5 mL

deionised water before adding, at once, to the boiling sodium tetrachloroaurate solution, which boiled for 15 minutes. The colour changed from black to purple-red.

2.1.2 Erlotinib-Nanoparticle Conjugation

Since EL is only slightly soluble in neutral water and it is advised that it dissolved in acidic water below pH 5 or in DMSO, stock concentrations of EL were made to 1 × 10^{-3} M and 1 × 10^{-4} M in DMSO. EL hydrochloride (N-(3-Ethynylphenyl)-6,7-bis(2-methoxyethoxy)quinazolin-4-amine hydrochloride) was added to AgHA NPs (1 mL, ~4 × 10^{-10} M) to a final concentration range of 5 × 10^{-8} M to 1 × 10^{-6} M. Samples were agitated overnight at 150 rpm to allow adsorption at ambient temperature before centrifugation (4,400 r.p.m. (2000 g) for 20 minutes) and resuspension in 1 mL dH_2O.

2.2 Stability and Characterisation Methods

2.2.1 UV-Visible Spectroscopy

Surface plasmon resonance (SPR) was measured with an Agilent Cary 60 UV-Visible (UV-vis) spectrophotometer using Win UV scan V.2.00 software. The instrument was allowed to equilibrate to RT before using poly(methyl methacrylate) (PMMA) disposable plastic micro cuvettes with 500 µL sample volumes to scan wavelengths from 300-800 nm. Where required, samples were diluted to give extinction profiles with extinction values of less than one to adhere to the Beer-Lambert law, to calculate the concentration of NPs. Measurements were plotted off-line using commercial software package Matlab 2014b.[98]

2.2.2 Concentration Estimation of NPs

Concentrations of NPs can be estimated using the Beer-Lambert Law and previously published extinction coefficients, such as those for AuCt NP reported by Haiss *et al*. and for AgHA by Yguerabide *and Yguerabide*.[99,100] To gain the concentration estimation, the NPs optical density (OD) was used as the absorbance (*A*) in Equation 1, which was divided by the extinction coefficient (ε). The path length *l* was 1 cm.

$$A = c * \varepsilon * l$$

Equation 1 Beer-Lambert Law

2.2.3 Dynamic Light Scattering

Hydrodynamic radius was measured using dynamic light scattering (DLS) on a Malvern Zetasizer Nano ZS with 800 µL of sample in a PMMA disposable micro cuvette with Zetasizer µV and APS v.6.20 software. Polystyrene latex (40 nm) was used as a standard to validate the calibration of the system before running samples. Measurements were taken in triplicate.

2.2.4 Zeta Potential

Zeta potential was similarly measured on a Malvern Zetasizer in triplicate with a standard validation being carried out, the difference being that a 1 cm dip cell electrode was used. The electrode was sonicated for 1 minute in dH_2O and rinsed before use and between samples.

2.2.5 Scanning Electron Microscopy

Silicon wafers were cleansed with methanol and allowed to air dry before adding 5 µL of NPs to again air dry. Environmental scanning electron microscope (ESEM) FEI Quanta 250 FEG-ESEM was used to image at an accelerating voltage of 30 kV and typically a spot size of 4 was selected, and an Everhart-Thornley detector collected secondary electrons. Image J (National Institute of Health (NIH)) with FiJi plug-in was used to measure the average diameter of the NPs.[101-103]

2.2.6 Nano Tracking Analysis- Quantifying Particles

Nano Tracking Analysis was performed on a Malvern NanoSight LM10 to obtain particle number / mL of suspension by means of Brownian motion passing the 642 nm laser beam. The chamber and window was cleansed with methanol and lint free wipes then dried with nitrogen gas. Observations were made from the chamber through a 20× magnification objective using video rate recording, at 30 frames per second (fps). Acquisitions of 30 second videos were captured in triplicate and the number of particles per frame were averaged per sample, and then across replicates. Particles per mL were calculated based on the fact that the chamber holds 8.416×10^{-11} L of suspension. Further to this the concentration can be calculated by factoring in Avogadro's number of $6.02214154 \times 10^{23}$ particles per mole.

2.2.7 Liquid Chromatography - Mass Spectroscopy

AuCt and AgHA conjugates were prepared in triplicate in lo-bind Eppendorf microcentrifuge tubes as in method section 2.1.2. A calibration curve of free-EL was prepared in triplicate in serial dilution from 300 nM halving the concentration with each dilution in lo-bind Eppendorf microcentrifuge tubes. Samples (triplicates) were applied to liquid chromatography–mass spectrometry (LC-MS) using an Accucore 150 C18 2.6 um 100x2.1mm (Thermo Scientific) column fitted with a guard on a Thermo Ultimate 3000 HPLC. A gradient of increasing acetonitrile (with water as the aqueous mobile phase) was used to elute analytes into a Q Exactive mass spectrometer. Samples were loaded at a flow rate of 300 µL / min in 2% B, then a gradient was run from 28-40% B. Theses parameters were optimised in pilot studies (by running 2-40% over 20 mins to define the region where EL eluted). The % B was

increased to 80% to wash the column for 4 minutes, prior to a re-equilibration at 2% for 5 mins to prepare for the next run. Eluted samples were directly sprayed into a hybrid quadrupole-Orbitrap mass spectrometer (Q Exactive, Thermo Fisher Scientific Bremen Germany). Data were acquired in wide scan positive mode. In order to generate mzML files, an R script from the work of Wills, Edwards-Hicks and Finch was used to convert from .raw to .mzML files, to then detect and extract peaks files of the extracted ion chromatograms to write to .tsv files.[104] The .tsv files were used to plot and integrate the areas of the intensity peaks. These data were used to generate the standard curve used for the quantification of the supernatant samples.

2.2.8 Kinetic Aggregation Study in Cell Culture Media

An Agilent Cary 60 UV-Vis spectrophotometer was used with Cary WinUV software to run kinetic scans with a 30 minute periodicity. PMMA micro cuvettes were used with dH_2O, and baselines were applied per cuvette. Conjugates were added to the cell media or dH_2O immediately prior to analysis. Matlab 2014b was used to analyse the resulting spectra. The cell medium spectrum was removed as background from all the test sample spectra and likewise for dH_2O and the respective spectra.

2.3 Cell Preparation, Cytotoxicity and Proteomics

2.3.1 Cell Culture Maintenance and Characterisation

Routinely NCI-H1355 human lung adenocarcinoma cells (American Tissue Cell Culture (ATCC)) and HCC827 human lung adenocarcinoma cells (ATCC) were cultured in complete high glucose Dulbecco's modified Eagles medium (DMEM) containing 4500 mg/L glucose, 584 mg/L L-glutamine (Sigma #D6429) and supplemented with 10% FBS (Gibco #10270), final 100 U/mL of Penicillin / Streptomycin (10,000 units/mL Penicillin, 10,000 U/mL Streptomycin) (Gibco #15140-122) and 2.5 µg/mL final concentration of Amphotericin B (Gibco #15290-026).

The cells were passaged twice weekly by aspirating media off before rinsing with 1X pH 7.4 phosphate buffered saline (PBS) and detaching the adherent cells with 0.25% trypsin. The PBS contains 157 mM Na^+, 142mM Cl^-, 4.45mM K^+, 10.1 mM HPO_4^{2-}, 4.6 mM $H_2PO_4^-$. Cells were then resuspended in complete DMEM before being transferred at an appropriate cell density to a new flask or dish. Cells were maintained in a humidified incubator at 37°C in a 5% CO_2 atmosphere.

Cell media supernatant was tested for the presence of mycoplasma with the MycoAlert™ Mycoplasma Detection Kit (Lonza #LT07-118) by the Technical Services

at the Medical Research Council (MRC) Human Genetics Unit (HGU) at the Institute for Genetics and Molecular Medicine (IGMM), University of Edinburgh. To prepare the cell media supernatant, the cells were grown with antibiotic and fungizone free medium that contained only FBS, for 4 days. Any cells in the media supernatant were removed by centrifuging 1 mL at 2,000 rpm for 5 minutes, the resulting supernatant was then sent for testing.

FTA® Sample Collection Kit for Human Cell Authentication Service (American Type Culture Collection (ATCC) # 135-XV) was used to authenticate both cell lines used during this study. Cells were spotted onto the FTA™ paper provided and returned for Short Tandem Repeat (STR) profiling by PCR. STRs can detect mis-identified, cross-contaminated or genetically drifted cells against a genetic database of human cells, held by LGC Standards and ATCC.

The protocol used by ATCC was described as follows:

"Seventeen short tandem repeat (STR) loci plus the gender determining locus, Amelogenin, were amplified using the commercially available PowerPlex® 18D kit from Promega. The cell line sample was processed using the ABI Prism® 3500xl Genetic Analyzer. Data were analysed using GeneMapper® ID-X v1.2 software (Applied Biosystems). Appropriate positive and negative controls were run and confirmed for each sample submitted."

2.3.2 Preparing Fixed 2D Cell Cultured Windows

In preparation for incubation with NPs and cell mapping, the cells were harvested by trypsin detachment with DMEM added at 1:10 respectively. They were then counted with Trypan blue viability stain in a haemocytometer counting chamber and seeded in 35 mm Ibidi tissue culture at a cell density of 1×10^6 cells with 2 mL of DMEM. They were incubated in the routine cell culture conditions for 24 hours before being treated with NPs.

Cell treatments were added to the dishes mentioned above with AgHA NPs, EL-AgHA, AuCt NPs and EL-AuCt conjugates or fresh media for control cells. After the incubation period of 0.5 to 24 hours the cells were washed five times with PBS before fixing with 4% v/v paraformaldehyde (PFA) in PBS for 15 minutes at RT. The cells were then washed three times with PBS and five times with water before air drying. A sample of the EL-AgHA NP conjugate was dried onto a coverslip for comparative SERS studies.

2.3.3 Immuno-Fluorescent Staining

Cells were cultured and fixed as described in section 2.3.2 onto cell culture windows. Any stimulated cells were treated with a final concentration of 50 ng/mL EGF ligand for 15 minutes. Following this the cells were fixed for 15 mins and washed with PBS before being permeabilised, and non-specific binding was blocked with 1% bovine serum albumin (BSA) in phosphate buffered saline tween (PBST) with 0.1% Tween 20 (blocking buffer) for 1 hour at RT. The α-EGFR primary antibody (Biotechne #A300-388A) was added as 1:1000 (1 µg/mL) in the blocking buffer overnight at 4°C. Any phospho-EGFR studies used α-pEGFR Y1068 (CST #3777) at 1:1000 in blocking buffer. Three PBS washes were performed before the secondary antibody α-rabbit Ab was added at 1:500 in blocking buffer for 1 hour at RT. Subsequently DAPI staining was added at 300 nM final concentration for 20 minutes before washing with PBS, then a final 3 washes in dH_2O.

2.3.4 Trypan Blue Cell Viability Counts

Cells were seeded as described in section 2.3.2 but instead of individual 35 mm dishes, 6 well plates were used. Cell number was 0.5×10^{-6} and media volume 2 mL. Cells were treated with AgHA NPs, AuCt NPs, the EL conjugated forms at final concentration of 0.17 nM NPs and 300 nM EL to match the free-EL treatment concentration and an untreated control, in triplicate and left to incubate for 72 hours before counting. After 72 hours the media was removed, cells were rinsed with PBS and 0.5 mL of trypsin was added to detach cells before 0.5 mL of complete medium was added to recover the cells for counting. If required cells were diluted before counting on the haemocytometer, both live (non-blue cells) and dead (blue stained cells) cells were recorded.

Statistical analysis was carried out on MiniTab v.18.1 using $p<0.05$ significance level to test the null hypothesis of no difference in the sample means by one-way ANOVA, where equal variance was assumed and a two sided confidence interval was selected. After a significance was established within the group as a whole from the one-way ANOVA, a Tukey's post-hoc analysis was conducted. This assessed significant differences in a pairwise approach, to then group statistically significant samples together.

2.3.5 Alamar Blue Assay

Alamar Blue (Invitrogen, #DAL1100) was used as a less toxic option to screen a variety of cell lines for response and the resulting IC_{50} of a panel of cell lines to EL. Alamar blue measures the metabolic activity of the cell and can be read colorimetrically or by fluorescence, the latter being more sensitive.

The cells were plated at a density of 10,000 cells per well in the inner 60 wells of a 96 well plate. Outer wells were filled with 200 µL PBS to prevent evaporation of media from treated wells. The treatments were added in triplicate for 1 – 4 day incubation periods to assess the anti-proliferative effect of the conjugate and parent drug.

EL hydrochloride sourced from LKT and EL from Selleck were both dissolved in DMSO from Sigma Aldrich. Both treatments were added to the cell wells at 10 µM, 3 µM, 1 µM, 0.3 µM, 0.1 µM, 30 nM, 10 nM and 3 nM in a volume of 100 µL of complete DMEM. Controls of untreated with media only and in media were included as 100 % and cell death viability measures respectively, as well as, media only and media with alamar blue, to serve as background measures. After 3 days had passed, Alamar Blue was added at 10 % of the media volume and left to incubate for 2-8 hours in the cell incubator. Duration was dependant on the proliferation rate of the cells as the enzymatic turnover rate and hence colour change was determined by cell number.

A TECAN Spark 20M plate reader was used to analyse the results using Spark Control V2.1 software. The plates were read colorimetrically from the bottom at 570 nm and 600 nm absorbance. The fluorescence was also collected with excitation filter wavelength of 540 nm, bandwidth 25 nm and emission filter wavelength of 590 nm, bandwidth 10 nm. The results were stored as an excel spreadsheet and processed on GraphPad Prism v.5.01.

2.3.6 Live/Dead Staining Assay

Cells were plated as per the experimental section Chapter 2 with cell density seeded at 0.5×10^6 cells per 35mm Ibidi chamber and left to adhere overnight. 1 mL of NPs were added to cells at a final concentration of ~ 0.17 nM. First the conjugate treatments were prepared with 300 nM final EL concentration and left to incubate at RT overnight rotating at 150 rpm. NPs and conjugates were centrifuged at 2,000 g, supernatant removed and resuspended in 100 µL dH_2O. Finally the washed NPs and conjugates were mixed in 2 mL of the cell media to incubate with the cells for 4 – 72 hours.

Fluorescent images were taken at 4, 24, 48 and 72 hour intervals to assess cell viability and proliferation. To do so the treated media was removed and retained aseptically before the fluorescent stain was added. Invitrogen's LIVE/DEAD™ Viability/Cytotoxicity Kit, for mammalian cells kit was used (#L3224, ThermoFisher Scientific). The final concentration solution of these was prepared in PBS at 2 µM

calcein AM (live cell staining) and 4 µM EthD-1 solution (dead cell staining). 750 µL of the prepared staining solution was incubated with the cells for 15 minutes in the cell incubator before removing for imaging. On completing the imaging at the first time point, the respective treated cell media were returned to the cells and incubated until the next time point when the process was repeated for live/dead staining.

All images were collected at the same acquisition settings and then processed using Image J (National Institute of Health (NIH)) with FiJi plug-in to measure the area of fluorescent stain. Details of the instrument and software can be found in the experimental section 2.6.2. A sample size of 3 images were analysed per sample with 9 montaged image squares per replicate image. Thus 27 fields of view were assessed per treatment.

MiniTab v.18.1 was used for statistical analysis following the methods used in section 2.3.4.

2.3.7 Inductively Coupled Plasma - Mass Spectrometry (ICP-MS)

Inductively Coupled Plasma – Mass Spectrometry (ICP – MS) was carried out by staff at the Laboratory of the Government Chemist (LGC group), after the samples had been prepared as below.

The cells were plated at 1×10^6 cells per well in a 6 well dish before being treated with AgHA NPs and 300 nM EL AgHA conjugates (see 2.1.2) or vehicle alone. Subsequently dishes were rinsed with 1 mL PBS which was removed and an aliquot retained for particle estimation by NanoSight Nano Tracking Analysis (NTA) (see 2.2.6) and UV-Vis spectrometry. Trypsin (0.5 mL) was added to detach cells from the dish and 1 mL of complete media was used to neutralise the trypsin. Cells were then centrifuged at 1,000 rpm for 5 min to separate the cells from the media and any particles that were contained therein. An aliquot of the supernatant was retained to estimate particle concentration. The cells were then lysed using Radio-Immune Precipitation Assay (RIPA) lysis buffer (Thermo Fisher #10017003) to release the particles from the cells for quantification by ICP-MS.

ICP-MS was carried out by LGC and a detailed report is found within Appendix A starting at page i. Experimental details were described as follows:

"Sample Preparation

Sample tubes were gently shaken to mix the solution thoroughly prior to opening. Approximately 0.05 g of sample was accurately weighed into PTFE microwave

digestion vessels, followed by the addition of 0.1 g of 2 mg kg-1 of Indium (In), which will be used as an internal standard to correct for any instrumental drift or ionisation effects. 1.4 g of HNO_3 (UpA grade, Romil Ltd., Cambride, UK) and 0.45 g of ultrapure water (>18.2 MΩcm-1, Elga Maxima, UK) were added to each vessel which was subjected to the following conditions:

1) 10 minutes ramp to 180°C at 800 W
2) 10 minutes hold at 180°C at 800 W
3) 15 minutes at 0 W

After digestion, the digest solutions were made up to 20 g with ultrapure water (>18.2 MΩcm-1, Elga Maxima, UK) (to achieve a final acid concentration of 7%) and analysed without further dilution.

Calibration standards

Quantification of the samples was performed via external calibration using a silver standard from an accredited supplier (VHG, Manchester, USA). The working standards were prepared daily by gravimetric dilution in 7% HNO_3 to match the acid concentration in the samples. The working range was 0 to 60 µg kg^{-1}. Calibration curves achieved correlation coefficients of at least 0.995. Indium was added to all the calibration points, as an internal standard, with a final concentration of 10 µg kg^{-1}, matching the concentration in the samples.

Instrumentation

The analysis was carried out using an Agilent 8900 ICP-QQQ-MS. The samples were introduced into the plasma via a micromist nebuliser, operating at a pumping mode of 0.1 rpm, and using a Scott type double pass spray chamber cooled to 2°C.

The 107,109Ag and 113,115In isotopes were measured in no gas mode. The instrument was tuned daily for optimum signal intensity and stability with typical operating parameters.

Quality Control

To ensure the quality of results a reference material was submitted to the same sample treatment as the samples. During analysis, up to 8 samples were bracketed by a 'check' standard, typically the middle calibration standard, to ensure there was no drift in the signal. Additionally, spike experiments were performed by adding RM8017 to the cell lysates followed by the same microwave digestion as the samples (see sample preparation section), to check for possible matrix effects."

2.3.8 Single Particle ICP-MS (spICP-MS)

spICP-MS was conducted by LGC and full details are found from page i of Appendix A. Experimental details are described as follows:

"Sample receipt and storage

Cell lysates samples were received from University of Strathclyde in 1.5 mL Eppendorf tubes containing approximately 300 µL of sample which were stored at 4°C until analysis.

Calibration standards

NanoXactTM PEG coated Ag NPs from Nanocomposix, Inc with the mean diameter of 40 nm (lot: PTM0006) were in-house characterised using a reference method and consequently used for spiking experiments and for the determination of the transport efficiency, a key parameter that influences the accuracy of number concentration data. Ionic Ag standard from VHG Labs, Inc. (lot: 127001-5) was used in spiking experiments and also to determine the detector's response.

Sample Preparation

NanoComposix was diluted to the required concentration in 0 2.5% TMAH (Tetramethylammonium hydroxide), 0.1% Triton-X solution in order to calculate the transportation efficiency. Ionic Ag standard was diluted in 2.5% TMAH, 0.1% Triton-X prior to detector's response determination. All dilutions were prepared gravimetrically. Sample preparation was undertaken using a method previously developed in-house, in which samples were digested using basic hydrolysis to keep the integrity of nanoparticles. Briefly, upon arrival, cell samples were digested by mixing with 50 µL of 15% TMAH per 25 µL of cell lysate followed by 1 h sonication in an ultrasonic bath and 24 h incubation at room temperature in the dark. Once the incubation time was finalized, digested samples were diluted approximately 20-fold with 0.1% Triton-X100. Further dilutions were prepared in 2.5% TMAH + 0.1% Triton X-100.

Instrumentation

spICP-MS measurements were performed using an Agilent 8900 ICP-QQQ-MS. The samples were introduced into the plasma via a micromist nebuliser, operating at a pumping mode of 0.1 rpm, and using a Scott type double pass spray chamber cooled to 2°C. The instrument was equipped with the MassHunter4.3 (version: G72dC

C.01.03) software and microsecond detection capability, allowing the analysis in single particle mode. The instrument performance was verified daily with 1 µg L-1 tuning solution (1 µg L-1 of Ce, Co, Li, Tl and Y in 2% HNO3). After the daily performance check, the ICP-MS conditions were optimized to obtain maximum 107Ag sensitivity with a minimum background contribution using 1 µg L-1 ionic silver solution. Analyses in fast transient analysis (TRA) mode were performed with 'No Gas' using a dwell time of 0.1 ms per point, with no settling time between the measurements and using the newly developed Single Particle Application Module of ICP-MS MassHunter software. The general settings of the ICP-MS are given in Table 1. After each sample run the instrument was cleaned with 1% HNO3 0.1% Triton X-100 solution followed by ultrapure water after each sample. Each sample was measured 2-3 times under repeatability conditions."

Table 2 Typical operating parameters for spICP-MS measurements

Parameter	Agilent 7700
RF Power (W)	1550
Sampling depth (mm)	7
Carrier gas (L min^{-1})	1.09
Make up gas (L min^{-1})	0
Sample/skimmer cones	Ni/Ni
Sample uptake rate (mL min^{-1})	0.35
Spray Chamber (°C)	2
Dwell time (ms)	0.1
Acquisition time (s)	60
Isotopes measured	^{107}Ag

2.3.9 Western Blot Phosphoproteome Analysis

Cell culture was conducted as per Chapter 2 (except cells were cultured in 9 cm dishes at a density of 6 × 10^6 cells and treatments were appropriately scaled up in volume, the final volume being 8 mL)

Reagents

Cell Lysis

- RIPA buffer (Thermo Fisher #10017003)
- Protease and phosphatase inhibitor tablets (Pierce # A32959 Lot #SA2286913)

Protein Estimation- Bicinchoninic Acid Assay (BCA assay)

- BSA (Sigma-Aldrich #A3733-100G) (concentration curve for BCA)
- Solution A- Pierce #23228
- Solution B- Pierce #1859078

Western Blotting

- 10 x TBS
- TBST (1.5% tween 20 in 1xTBS)

- 4-15% gel Mini Protean TGX stain free Pre-cast gels (BioRad #456-8085)
- 10X TGS (BioRad #161-0772 (1X 25 mM Tris, 192 mM Glycine, 0.1% (w/v) SDS, pH8.3))
- Trans-Blot Turbo Transfer Pack- 0.2 µm nitrocellulose (Bio-Rad #170-4159)
- BSA (Sigma-Aldrich #A3733-100G) (5% in TBST as blocking buffer)
- 1° Phospho-p44/42 MAPK (Erk1/2) (Thr202/Tyr204) (D13.14.4E) XP® Rabbit mAb (CST #4370)
- 1° Anti-EGFR mAb [EGFR1] Rabbit α-EGFR (Bethnyl Ab #A300-388A) 1 mg/mL use at 1 ug/mL (1:1000) overnight
- Pierce ECL Western Blotting Substrates- thermo fisher # 32106
- Re-Blot Plus Strong 10x Solution (stripping) (EMD Millipore #2504)

Instrumentation

- Vacusafe Comfort Aspirator, IBS Integra Bioscience to remove PBS from cell washes.
- Eppendorf Centrifuge 5424R (Refrigerated) to collect cell lysates.
- TECAN Spark 20M plate reader with Spark Control V2.1 software for protein determination with BCA assay.
- Stuart Orbital Shaker (SSL1) to wash membranes.
- Biorad PowerPac HC 330W to run the gel electrophoresis.
- Biorad TransBlot Turbo Transfer System to transfer from the gel to the membrane.
- Biorad ChemiDoc MP Imaging System- Universal Hood III with Image Lab V.4.1 software to image the protein levels on the membrane.
- Microsoft Excel 2013 was used to create protein calibration curves from the BCA assay.

Cells were plated at a density of 6×10^6 cells in 8 cm dishes with 8 mL of medium and left for 24 hours before NP, conjugate, and EL treatments were added for 4 or 24 hours. The NPs and conjugates were added to a final concentration of 0.15 nM in 8 mL of media. The conjugates had a range of final concentrations from 1 nM to 1 µM of EL. The free-EL treatment also ranged from 1 nM to 1 µM. Treatments were aspirated on ice and ice cold PBS was used to wash the cells twice before angling the dishes and allowing all excess PBS to gather for aspiration (this results in an undiluted sample). Pre-chilled lysis buffer consisting of RIPA buffer and protease and phosphatase inhibitor tablets was added at a volume dictated by the estimated cell number which was 0.25 - 1.0 mL per 5×10^6 cells, as advised in the manufacturer's guidance. Cells were then scraped and transferred to a 1.5 mL centrifuge tube and incubated on ice for 30 minutes, agitating every 5 minutes.

Finally the lysate was pelleted by centrifugation at 13,000 g for 15 minutes at 4 °C, then the cell lysate supernatant was decanted to another centrifuge tube and stored at -80 °C.

Protein content was estimated per sample with a BCA assay. A calibration curve prepared by adding to a 96 well plate in duplicate 0, 1, 2, 3, 5, 7, 10 µg/uL protein from a stock BSA solution of 1 mg/mL. Each of these was made to a total volume of 10 µL, similarly the test samples were added as 1 µL to 9 µL dH_2O. The BCA reagent was made freshly each time and added at the last moment as a 1:50 dilution of Solution B:Solution A. The BCA reagent (100 µL) was added to each well and incubated for up to 1 hour at 37 °C before reading on the TECAN Spark Plate reader. The results were plotted on Microsoft Excel 2013 to achieve a linear response of over 0.997 R^2 value. The absorbance of the test samples were plotted against this and a concentration gained from the equation of the line.

The cell lysate samples were then prepared for SDS-PAGE electrophoresis gel loading, typically at 20 µg in 20 µL final volume with 10x SDS loading dye and denatured at 90 °C for 5 mins. Gels were loaded with 20 µL of the denatured cell lysate and 4 µL of molecular weight ladder before running at 180 V for 45 minutes.

Gels were transferred onto nitrocellulose membranes using the BioRad TransBlot Turbo Transfer System using the Midi gel 10 minute transfer setting. The membranes were trimmed and incubated in blocking solution for a minimum of 1 hour at RT or overnight at 4 °C whilst rocking. Primary antibodies were prepared in the blocking solution at 1:1000 and were left to incubate at 4 °C overnight whilst rocking. Three washes were performed with TSBST whilst rocking at 10 minute intervals, before adding the secondary antibodies for 1 hour at RT rocking, then washes were conducted once more as before.

The membranes were then handled gently with tweezers to avoid damaging them, the excess TBST was blotted off. ECL reagents were prepared at 1:1 immediately before use and added to the membrane to incubate for 3 mins before shaking off an excess. Bands were imaged on a Biorad ChemiDoc MP Imaging System- Universal Hood III with Image Lab V.4.1 software to quantify the protein levels on the membrane from the protein species observed as bands.

Phospho-proteins were always probed for first and then the membrane was stripped with Re-Blot Plus Strong 10x solution made to 1X in dH_2O for a maximum of 15 minutes. The membrane was then rinsed thoroughly with water and the process of blocking, primary antibody, washes and secondary antibody incubation *etc*. was

repeated. The second probing for protein was always for the total protein relating to the phospho-protein counterpart.

2.3.10 Reverse Phase Protein Array

1 x 10^6 cells were plated in 6 well cultre dishes for one day before treatment with 10 nM EL, 10 nM EL-0.34 nM AgHA NPs, 10 nM EL-0.34 nM AuCt NPs, 0.34 nM AgHA NPs, 0.34 nM AuCt NPs and 0.1 % DMSO vehicle control for 4 or 24 hours. PBS andlysis buffer were pre-chilled before use and cells were scraped from the dish over ice.

Cells, in biological triplicate, were washed with PBS and lysed in 1% Triton X-100, 50 mM HEPES (pH 7.4), 150 mM sodium chloride, 1.5 mM magnesium chloride, 1 mM EGTA, 100 mM sodium fluoride, 10 mM sodium pyrophosphate, 1 mM sodium vanadate, 10% glycerol, supplemented with complete ULTRA protease inhibitor and PhosSTOP phosphatase inhibitor cocktails. Cleared lysates were serially diluted to produce a dilution series comprising four serial two-fold dilutions of each sample, which were spotted onto nitrocellulose-coated slides (Grace Bio-Labs) under conditions of constant 70% humidity using the Aushon 2470 array platform (Aushon Biosystems). Slides were hydrated in blocking buffer (Thermo Fisher Scientific) and then incubated with validated primary antibodies (all 1:250; listed within the appendix). Bound antibodies were detected by incubation with anti-rabbit DyLight 800-conjugated secondary antibody (New England BioLabs). An InnoScan 710-IR scanner (Innopsys) was used to read the slides, and images were acquired at the highest gain without saturation of the fluorescence signal. The relative fluorescence intensity of each sample spot was quantified using Mapix software (Innopsys).

The linear fit of the dilution series of each sample was determined for each primary antibody, from which median relative fluorescence intensities were calculated. Signal intensities were normalized to total protein printed (determined from a fast-green stained array slide). Only primary antibodies with normalized signal intensities at least 1.5 times the value of the secondary antibody alone in at least one sample were included in the analysis to exclude data derived from weak or non-specific signals.

Results were pre-processed in Microsoft Excel 2013 to normalised against the Fast Green protein loading values, before performing heairarchical cluster analysis to create heatmaps in Gene Cluster 3.0 v.1.56 and Java TreeView v.1.1.6r4.[105,106] Student's T-test significance testing was done with GraphPad Prism version 5.01 for Windows, GraphPad Software, San Diego California USA, www.graphpad.com,

before interactive network analyses were carried out with Cytoscape v.3.6.1 supplemented by GeneMANIA plug-in application v.3.5.0.[107,108]

2.4 Transmission Electron Microscopy

2.4.1 Sample Preparation

Cells were cultured in 35 mm culture dishes at a density of 1 x 10^6 cells in 2 mL of medium. 300 nM EL-NP conjugates were prepared as described in 2.1.2 and incubated with the cells at a final concentration of 0.2 nM for 4 hours in standard cell culture conditions.

Fixative was prepared fresh with 2.5% glutaraldehyde in 0.2 M Pipes pH 7.2 and pre-warmed to 37°C. Medium was removed and cells washed thoroughly 5 times to remove excess particles. Cells were fixed for 15 minutes in 750 µL of fixative in the fume cupboard before scraping to dislodge the cells. Cells were pelleted at 10,000 g before being processed and sectioned for analyses.

Specimens were then post-fixed in 1% osmium tetroxide in 0.1 M sodium cacodylate for 45 minutes, then washed in three 10 minute changes of 0.1 M sodium cacodylate buffer. These samples were then dehydrated in 50%, 70%, 90% and 100% ethanol (x3) for 15 minutes each, then in two 10-minute changes in propylene oxide. Samples were then embedded in TAAB 812 resin. Sections, 1 µm thick were cut on a Leica Ultracut ultra-microtome, stained with toluidine blue, and viewed in a light microscope to select suitable areas for investigation. Ultrathin sections, 60 nm thick were cut from selected areas, stained in uranyl acetate and lead citrate then viewed in a JEOL JEM-1400 Plus TEM operated at 80 kV spot size 2. The TEM facility at the University of Edinburgh is supported by the Wellcome Trust Multi User Equipment Grant (WT104915MA).

2.4.2 Measurements

Representative images were collected on a GATAN OneView camera before processing dimensions of NPs with Image J, as performed previously with SEM results (2.2.5).[101–103]

2.5 Raman Spectroscopy

2.5.1 Colloidal Based Measurements with CBEx and Snowy Range Instruments

A concentration curve was carried out for EL conjugated to AgHA and AuCt NPs that were assessed by SERS analysis. SERS analysis was carried out on Snowy Range CBEx 2.0 handheld Raman spectrometer (Snowy Range Instruments, Laramie WY USA)

equipped with a 638 nm laser with a maximum laser power of 40 mW (23 mW at sample), and also Snowy Range Sierra 2.0 (Snowy Range Instruments, Laramie WY USA) equipped with a 532 nm laser with maximum power of 50 mW. Samples were deposited in glass vials for interrogation. Unless stated otherwise, all sample volumes were 600 µL and spectra were collected using 100% laser power at the sample with a 0.05 s accumulation time. The software used to acquire spectra was Peak 1.1.112. Resulting spectra were baseline corrected in Matlab 2014b typically using polynomial smoothing of 1×10^7 and asymmetry of 1×10^{-3}.[98]

2.5.2 Raman Mapping with Renishaw In Via

A Renishaw InVia Raman confocal microscope was used to create initial depth profiles, to establish the focal plane of the fixed cells in correlation with the white light images. Subsequently 3D SERS maps were collected in edge Streamline HR high confocality mode at 1 µm resolution in X and Y directions and 3 µm between Z-stacks. A 60× magnification NIR APO Nikon water immersion objective with a 1.0 NA was used on the samples at a laser power of 1.2 mW (10% power) at the sample, from a HeNe 633 nm excitation source with a 300 ms acquisition time per point, and a 1200 l/m grating in high confocality mode. Wire 4.2 software was used to pre-process the data by using their proprietary nearest neighbour then width of feature cosmic ray removal and baseline subtraction features. Thereafter signal to baseline analysis was used to create pseudo colour maps for the area of the alkyne peak at 1982 cm^{-1} Raman shift by selecting the peak area of 1940-2040 cm^{-1} and also the lipids and proteins from the peak area of 2800 – 3000 cm^{-1}.

2.5.3 Raman Mapping with Microfluidics device

The device was prepared by Dr Marjorie Willner following the protocol described in detail in their microfluidics paper published in the analyst chemistry journal, which references the technique previously outlined by McMillan *et al.*.[109,110] Cells were plated at 1 x 10^6 cells per 35 mm dish as in SERS imaging studies, the difference in preparation from 2.5.2 was during the harvesting and washing of cells to load the device and that they were not fixed (neither on a surface matrix nor in cell suspension). The cells were detached as per routine cell culture by trypsinisation (2.3.1), an extra 4 mL of cell culture media was added to wash the cells by centrifugation at 1000 rpm for 3 minutes. The supernatant was removed and 1 mL pre-warmed PBS was added to redisperse the cells, immediately before delivery, cells were gently passed through a syringe and 25 G needle to remove any cell aggregates. The microfluidic device was connected to 2x 1 mL syringes with poly(tetrafluoroethylene) tubing. The continuous oil phase was filled with FC-40 (3M Company) fluorinated oil with 2 wt % block copolymer fluorosurfactant (designed by

the Weitz Group at Harvard and supplied by RAN Biotechnologies, catalog no. 008-FluoroSurfactant, Beverly, MA, U.S.A.). The aqueous dispersed phase of PBS used to carry the droplets of cells was connected to another syringe. Appropriate sized droplets were formed to view individual cells by employing a flow rate of ~ 0.2 mL/hour, controlled by the automated syringe delivery pump. Thereafter, the cells were focussed on within the device and imaged as in the SERS mapping experimental section 2.5.2.

2.6 Multi-Modal Imaging

2.6.1 Dark-Field Microscopy

A Nikon Eclipse LV100 microscope with Halogen 50 W light source LV-LH50PC, CoolSnap HC Photometrics camera and the following filters- Semrock Brightline FITC-3540B-NTE and TXRED-4040B-NTE and DAPI filter cube with 365-414 Ex and 438/26- 483/32 Em – was used. The objective used was cover glass correcting 20 ×/0.45 S Plan Fluor Nikon WD 8.2-6.9 and MetaMorph V.6.3r0 software by Molecular Devices for NP localisation and uptake studies.

2.6.2 Confocal Fluorescence Microscopy

A Leica Microsystems TCS SP8 with continuous wave visible lasers and Leica DMi8 inverted microscope and DFC 7000T and TL LED cameras was used. The software was Leica Application Suite X V.3.1.5.16308 to carry out biomarker and live/dead studies using a Leica 63× magnification HC PL APO water objective with a 1.2 NA. Intensity and area of fluorescence was measured using Image J (National Institute of Health (NIH)) software with FiJi plug-in for live/dead studies.[102]

Chapter 3 Characterisation of Erlotinib - Nanoparticle Conjugates

"All sorts of things can happen when you're open to new ideas and playing around."
Stephanie Kwolek, Kevlar inventor, Lavoisier Medal for technical achievements.

3.1 Introduction

In the main introduction of this thesis, the issue of elucidating intracellular drug localisation was discussed. This is pertinent to understanding the reasons for ineffective cancer treatments and being able to prescribe the best second or third line treatments. The main concerns impeding progress in this *in vitro* research area, are the requirements for dye tags or reporter molecules, as a means to visualise small molecule inhibitors or inferring localisation through downstream effects on the cell. It cannot be assumed that these dyes do not affect the drugs' efficacy and that no anti-proliferative effect means that there is no drug within the cell.

Once basic physio-chemical characterisation of the NPs and EL conjugates have been analysed, the conjugates will be added to cells. The results presented here will explore the Raman and SERS signatures of the parent drug EL and the electrostatically attached EL conjugate. To address obtaining together a good SERS signal and low-toxicity of the bare NPs; both AuCt and AgHA colloids were explored as conjugates.

3.2 Rationale of Colloid Choice, Synthesis & Characterisation of Nanoparticles

AgHA NPs were used initially as proof of principle in this project to detect a SERS signal intracellularly from EL. It was selected for its known ability to produce the most intense SERS signal of all the metallic NPs; silver has superior extinction properties explained by the LSPR associated with the enhancement in its optical cross-section.[111-113] No Raman reporter was used in this system, therefore initially the inherent SERS signal of the conjugate was the priority, hence selecting AgHA NPs. However, to address any cytotoxicity concerns linked with AgHA, AuCt NPs were also included at various stages in the study. Unless stated otherwise, preliminary studies were conducted in AgHA, and AuCt was included in selected experiments.

The Leopold and Lendl method was used to synthesise the AgHA NPs at a size of ~40 nm of monodispersed, negatively charged, roughened, spherical silver colloid reduced with hydroxylamine hydrochloride.[96] This was selected over the Lee and Meisel citrate reduction method to synthesise silver NPs, as it is quicker and safer, since it does not require reflux and is able to create more reproducible monodispersed particles, with uniform shapes between batches. Mott and Maenosono note that Ag citrate NPs can be synthesised in larger spheres of ~ 40 nm but this is at the expense of both the shape and size uniformity.[113] The Turkevich method was used to prepare spherical colloidal gold of ~40 nm, which was also negatively capped with the exception that it was citrate reduced.[97] In general, negatively charged NPs were selected, as it allowed the overall positively charged EL molecules (Table 1) to be electrostatically attached to the surface.

3.3 Characterisation of Colloid

3.3.1 Scanning Electron Microscopy (SEM) of Colloids

Several batches of AgHA NPs were used throughout the project, Figure 18 (A) presents a typical SEM image, which was used to measure the diameter. Here, a mean size of 44 ± 7 nm was recorded from measuring 20 AgHA NPs with ImageJ (National Institute of Health (NIH)) with FiJi plug-in.[101,114] The same method was employed to assess the size of the AuCt NPs resulting in monodispersed spheres with a diameter of 38 ± 4 nm (Figure 18 B). Again several batches were required and they were all ~40 nm on average.

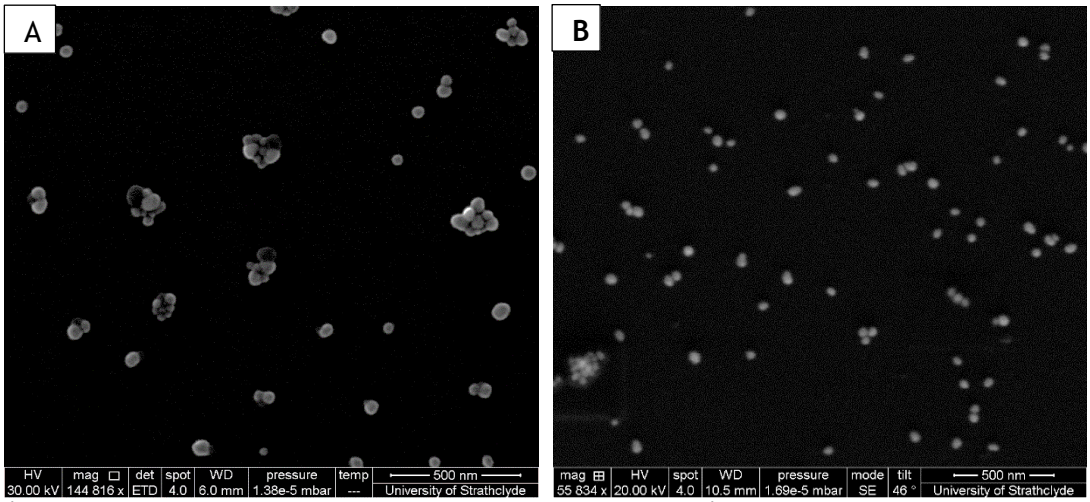

Figure 18 SEM on carbon wafer of (A) AgHA NPs, mean diameter 44 ± 7 nm (n=20) and (B) AuCt NPs, mean diameter 38 ± 4 nm (n=20), both scale bars 500 nm.

3.3.2 Localised Surface Plasmon Resonance of NPs

A UV-Vis spectrometer was used to collect information regarding the general size and monodispersity of the particles. The extinction profile, that is a combination of absorption and scattering, was found to have a lambda max of ~400 nm for 40 nm

AgHA NPs (Figure 19). It is generally accepted in the nanometrology field that FWHM <100 nm is considered to be a colloid constituted of monodispersed sized AgHA NPs. The AuCt NP colloid had a surface plasmon band at ~525 nm indicating that the NPs are ~ 40 nm (Figure 19), according to Haiss *et al.* published extinction profiles to estimate size and calculate colloid concentrations.[99]

Each batch of particles were characterised when synthesised and as a control with each experiment to monitor concentration and stability. In Figure 19 the extinction profile of the batch of NPs from the SEM (in Figure 18) can be seen. They had a λ maximum of 406 nm with a full width half maximum (FWHM) of 71 nm, satisfying the monodispersity approximation and that they were roughly 40 nm. The extinction coefficient calculated by Yguerabide *et al.* of 2.87 x 10^{10} M^{-1} cm^{-1}, was used to estimate a concentration of typically ~0.34 nM NPs.[100]

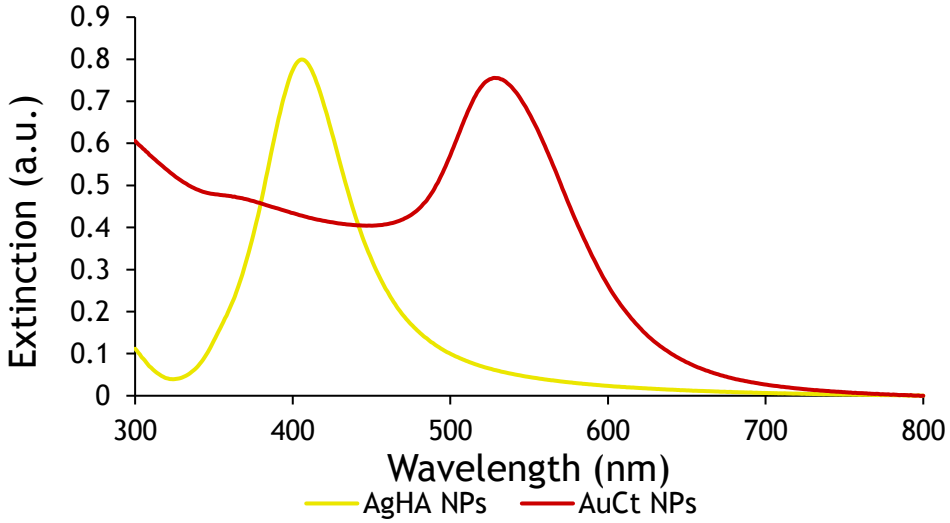

Figure 19 Extinction profile of AgHA NPs- λ max = 406 nm, FWHM = 71 nm, concentration = 0.34 nM and AuCt NPs- λ max = 528 nm, FWHM = 105 nm, concentration = 0.34 nM.

3.3.3 Hydrodynamic Diameter and Zeta Potential of NPs for Stability

DLS can be used as an approximation of the hydrodynamic diameter and the stability or zeta potential can be judged using a Malvern Zetasizer instrument. The hydrodynamic diameter of the AgHA NPs was 48.3 ± 0.5 nm with a polydispersity index (PDI) of 0.272 which confers that the particles, as with the UV- Vis spectrum, are monodispersed. The zeta potential was -57.9 ± 7.7 mV confirming that the particles are negatively charged and that they are stable, again this can be seen by the one clear narrow peak on the UV-Vis spectrum (Figure 19). The hydrodynamic diameter of AuCt NPs was 38.4 ± 0.1 nm with a PDI of 0.049 ± 0.011 and the zeta potential was -55.6 ± 6.6 mV from an average of 3 readings. These measurements

indicate that the AuCt NPs are stably, negatively capped with a size of around 38 nm and that they are extremely monodispersed from the low PDI number.

The Zetasizer was only used initially as an indication of the physiochemical characteristics. The preferred option was to observe the stability using the extinction profile for peak dampening and secondary peak appearance in the UV-Vis spectrum, along with the SEM for size and monodispersity. Overall they were found to be more reliable and informative than the Zetasizer. Furthermore during drug loading studies, the hydrodynamic diameter did not seem to alter probably due to the small molecular size of EL. Therefore, SERS intensity was used to confirm the surface attachment of EL. This was justified because there was no Raman signal detected from the EL only in solution at the concentration and acquisition settings used.

3.4 Functionalisation of NPs and Physio-Chemical Characterisation of Erlotinib Concentration Curve

The first step of the study was to establish the optimum EL- AgHA NP conjugate preparation to image within cells. This entailed producing a stable conjugate to add to cells, with a strong SERS signal, at a clinically relevant concentration. A preliminary detailed concentration curve was conducted at 50 or 100 nM increments from 0 to 1000 nM EL on AgHA NPs. Later comparisons were made between equal concentrations of similar sized AgHA and AuCt particles with the EL. The conjugation protocol to adsorb the EL onto the NPs is described in section 2.1.2.

3.4.1 Colorimetric Assessment of Conjugate Stability

The rising concentration effect of EL on the stability of the particles was shown in Figure 20. The photo clearly showed that 800 – 1000 nM EL on AgHA NPs caused complete precipitation of the colloidal suspension due to aggregation. It is thought that this could be due to approaching monolayer coverage inducing self-aggregation, since no aggregating agent was added. To investigate the concentrations where no change can be seen by eye, UV-vis spectroscopy was used for SPR assessment of the samples.

The footprint of EL in the geometry it attaches to the NP surface was 0.7 nm, approximating 1 angstrom bond size across the 7 bond widths of the molecule as it attached from the acetylene group to the particle.[22] Assuming the use of 39 nm spheres, the area of the sphere was calculated ($A=\pi r^2$) to be 5188.1 nm^2 and EL molecules attached to the surface was 7412 according to the EL footprint. Using 8.68 x 10^{10} particles /mL to obtain a total surface area and hence estimate the

number of molecules of EL that can attach it was calculated as 6.43 x 10^{14} molecules of EL. Subsequently, taking into account Avogadro's number and the 1 mL volume, the monolayer coverage of EL on 39 nm spherical NPs was 1.07 x 10^{-6} M. In Figure 20, the stability of the particles were observed to deteriorate due to aggregation when approaching the monolayer coverage concentration, which was 1.07 x 10^{-6} M.

Figure 20 EL on AgHA NP conjugate concentration curve left to right of the image, EL from 0, 50, 100, 150, 200, 25, 300, 350, 400, 500, 600, 700, 800, 900 and 1000 nM EL.

3.4.2 Localised Surface Plasmon Resonance of Conjugates

The LSPR was examined to establish the functionalisation efficiency and the stability of the conjugates. Figure 21 shows that with increased concentrations of EL the peak dampens at the lambda maximum and a new peak appeared at around 600 nm. These two features combined indicate that the colloid was no longer stable at the higher EL concentrations. It demonstrated that aggregation was causing particles to cluster together and precipitate out of solution, thus creating large aggregates that reduced the extinction at 405 nm and increased it in the red shifted area of the UV-Visible spectrum. Hence, anything above 500 nM EL was not considered for this study as the level of aggregation cannot be controlled and the particles must be less than 100 nm to enter cells and deliver the EL for monitoring by SERS imaging.[93,115]

To examine the LSPR more thoroughly, the lambda maxima were plotted in Figure 22, where it was clearly seen that beyond 600 nM there was an increase in λ max recorded. This change in the physiochemical properties of the particles would not be favourable to continue with, in cellular experiments. To complete the physiochemical characterisation the hydrodynamic diameter and zeta potential were measured as an indication of functionalisation of EL onto the NP's surface and its stability once it was self-assembled.

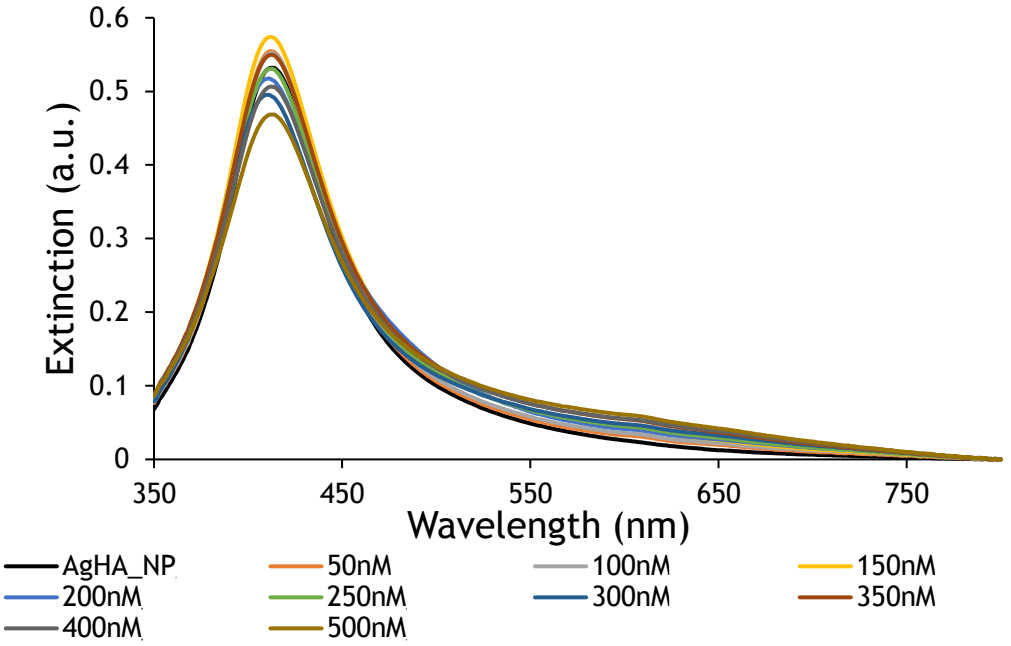

Figure 21 UV-Vis spectra displaying the extinction profiles of EL on AgHA NP conjugate concentration curve from 0 to 500 nM, 600- 1000 nM were omitted for clarity.

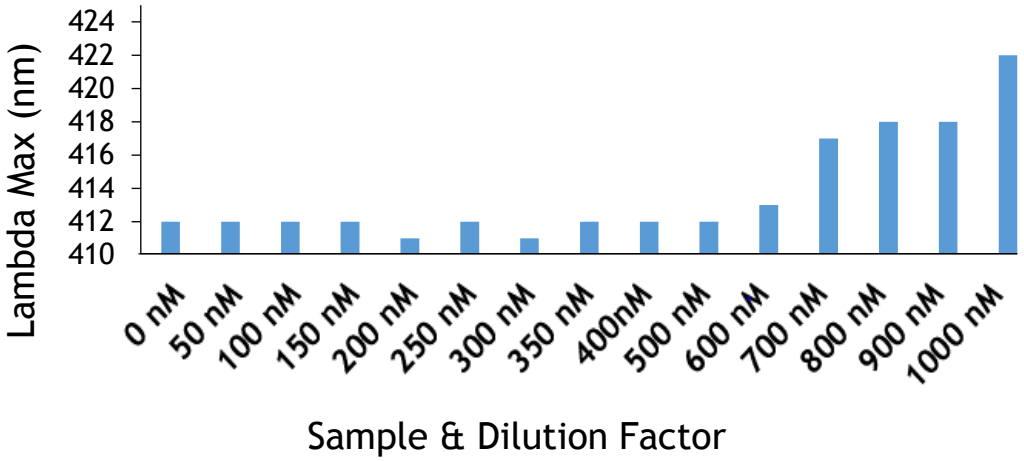

Figure 22 Lambda max from the extinction profiles of the UV-Vis spectra of EL on AgHA NP conjugate concentration series (0 - 1000 nM EL on AgHA).

3.4.3 Hydrodynamic Diameter & Zeta Potential of Conjugates for Stability

The Zetasizer was used to examine the properties of the AgHA conjugates in the concentration curve, including the hydrodynamic diameter and the zeta potential, which were measured in triplicate to obtain an average and standard deviations (SDs) following the method in 2.2.3 and 2.2.4. It was observed in Figure 23 both A & B that there was no real fluctuation in zeta potential values or hydrodynamic diameter as the concentration of the EL was increased. This was probably due to the small molecule size of the EL that does not appear to be extending beyond the scattering of light from the water loosely associated with the surface of the particles. EL was only slightly positive and no difference in charge was detected in the zeta potential; this means that the particles are still relatively stable but the

surface attachment cannot be determined by this method. To ascertain whether or not EL had electrostatically bound to the surface a SERS spectrum was required.

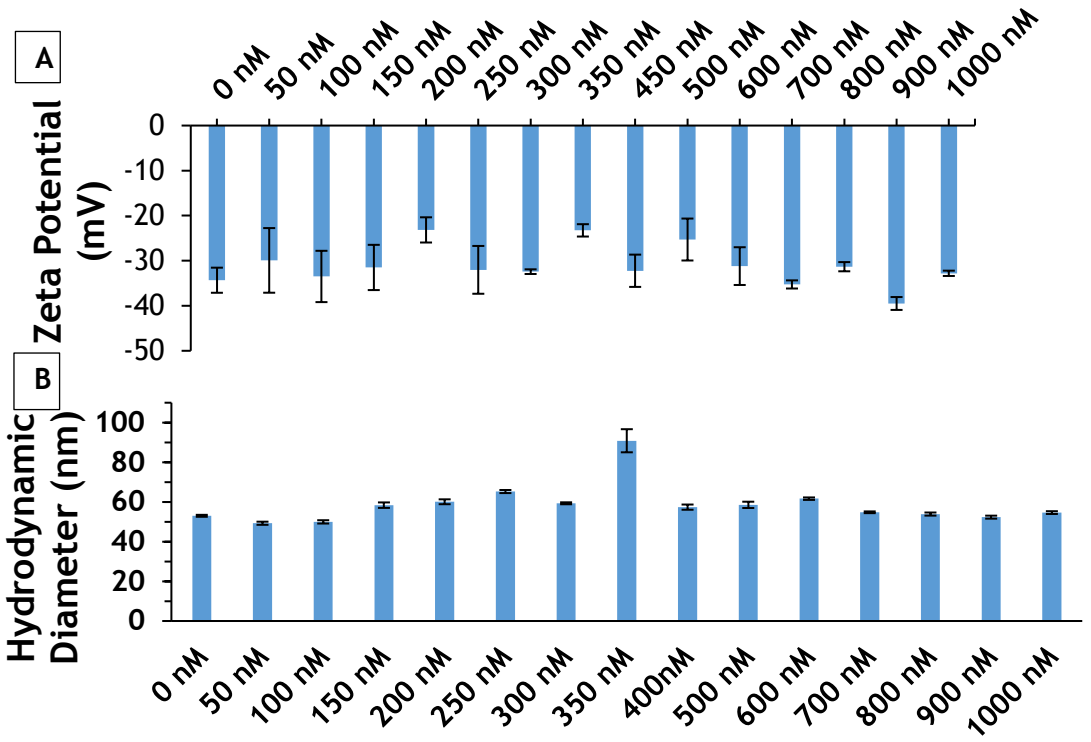

Figure 23 Physiochemical characterisation of EL on AgHA NP conjugate concentration curve from 0 to 1000 nM, with error bars displaying the SD. A) Zeta potential, B) hydrodynamic diameter.

3.4.4 Solid & Colloidal SERS

Following on from the physiochemical characterisation of the EL-AgHA NP conjugates, it was pertinent to establish the SERS signal of the conjugates as confirmation of attachment. Figure 24 compared the Raman and SERS spectra respectively of the solid and colloidal conjugate signal of EL hydrochloride, on both AgHA and AuCt NPs. EL's chemical structure was also included in the figure. Closer inspection of the spectra showed that certain peaks were lost in the SERS spectrum compared to the Raman spectrum. This was due to the selection rules of SERS, whereby bonds in a geometry perpendicular to the metal's surface are further enhanced, which can sometimes mask weaker vibrations. Most importantly, Figure 24 provided evidence that the alkyne moiety band assignment had a spectral shift from the solid EL powder to the conjugated form for both AgHA and AuCt NPs. More specifically, the alkyne peak shifts from 2111 cm^{-1} to 1985 cm^{-1} and 2010 cm^{-1} respectively for AgHA and AuCt conjugates. Referring back to the aim of imaging the localisation and secondly assessing the release of the EL from the nanodelivery system, it was vital to this study that free-EL could be distinguished from its NP-bound EL counterpart. Figure 24 proves that this discrimination was an achievable goal.

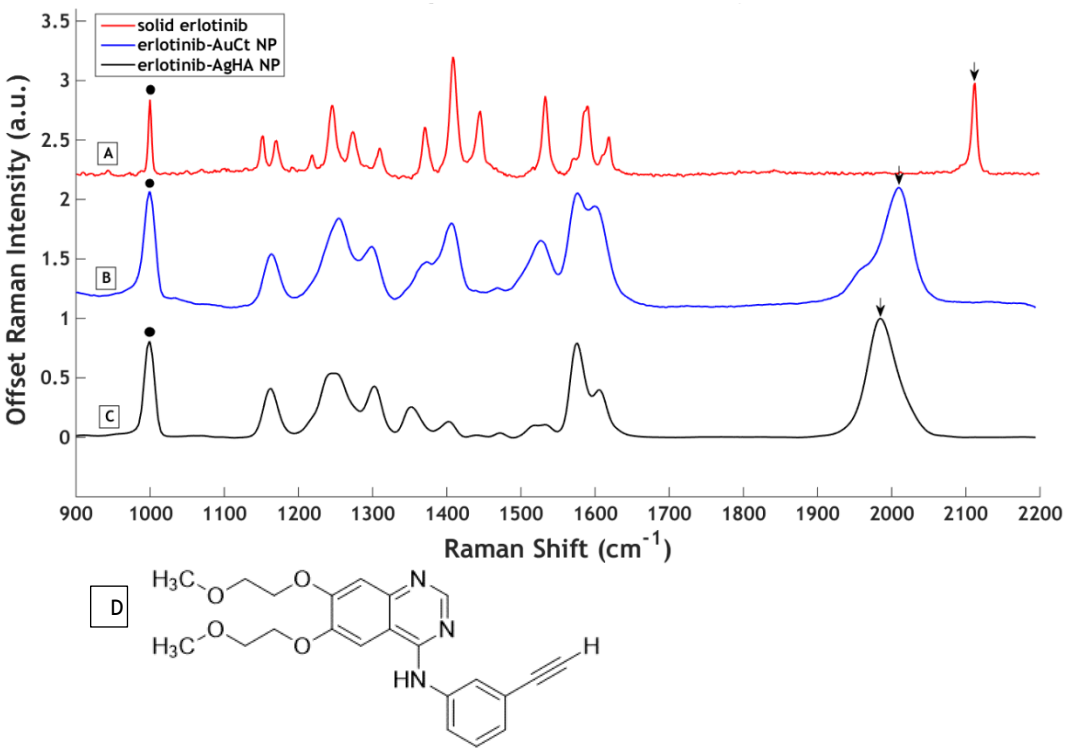

Figure 24 Normalised Raman and SERS spectra of EL hydrochloride. (A) solid EL acquired with 3 accumulations of a 10 s scan by 633 nm laser (3.4 mW power), (B) 300 nM EL-AuCt NPs, (C) 300 nM EL-AgHA NPs. Both B and C acquired by 638 nm laser (23 mW power at sample) 0.5 secs 5 acquisitions from 3 samples averaged. All spectra were normalised to 1 against the maximum peak intensity for each sample. Black dots highlight phenylacetylene ring in-plane bending peak and black arrows demonstrating the spectral shift of the acetylene stretching peak, depending on the surface attachment to NPs. (D) Structure of EL.

The band assignments of EL mentioned above were in alignment with those peak assignments already published in the literature.[22,59] Figure 24 clearly shows the phenylacetylene ring in-plane bending at around 1000 cm^{-1} and then the acetylene stretching peak, which was different for Raman and on the 2 SERS substrates. Table 3 summarised the remaining peak assignments of the EL spectrum from ordinary Raman (OR) of the powder and the solution based SERS samples seen in Figure 24 using information from the DFT computational energy modelling of Lam *et al's* 2014 EL paper.[22] The Raman shifts presented from this study in Table 3 were in agreement with the shifts previously published.[22] The Raman shift of the alkyne moiety observed here supported their theory that the molecule binds *via* its acetylene group to the NP's surface.

It was discernible from Figure 24 that there was a shoulder to the lower Raman shift region on the alkyne peak of the EL-AuCt NP SERS spectrum. Joo and Kim studied the effects of various anions on peaks which appear in this region (~1960-1985 cm^{-1}) of phenylacetylene and concluded that the binding to the surface of the Au NP was altered depending on the concentration and type of anions present.[116] Hence, the presence of the anions can result in multiple peaks in the γ C≡C stretching region

and due to the weaker Raman intensity than the main C≡C vibration they can appear as a 'shoulder' instead of clear peaks. Furthermore, Joo and Kim discuss that the Raman shift of the acteylene vibration will vary dependent on the metallic surface it binds to as a result of the adsorption geometries. The data presented here were in agreement with this postulation made by Joo and Kim.[116] It must also be stated that the surface chemistry, although overall negatively charged in both cases, was not exactly comparable due to the different reducing methods of synthesis for the Ag and Au NPs used here. However they had similar zeta potentials of -57.9 mV and -55.6 mV respectively.

Once the SERS signal was achieved and peaks were assigned, a more detailed study was required to ascertain the optimum concentration of EL to be used for cell mapping. Initially, AgHA NPs were investigated as a pilot study before expanding into AuCt NPs when a better understanding of the concentrations required was obtained.

Table 3 Raman and SERS peak assignments, first 2 columns are data based on Density Functional Theory (DFT) calculations from Lam et al.[22] The remainder of the results are from this study, spectra are presented in Figure 25. Key: Ordinary Raman (OR), ν: stretching; β: in-plane bending; ϒ: out-of-plane bending.

OR (cm^{-1})	SERS (cm^{-1})	OR (cm^{-1})	Au SERS (cm^{-1})	Ag SERS (cm^{-1})	Peak Assignment
999	996	1000	999	100	β (phenylacetylene ring)
1150	1160	1151			νas (O-CH_3)
1170		1169	1164	1163	β (C-H)
1244	1251	1246	1254	1244	β (C-H), β (N-H), ν (C-N)
1273	1297	1273			ν(quinazoline ring)
1408	1402	1408	1406	1403	ν (quinazoline ring), β (N-H), β (C-H)
1444		1444	1468	1471	β (N-H), ν (phenylacetylene ring)
1533	1527	1533	1526	1532	ν (quinazoline ring), β (NAH)
	1571	1571	1576	1576	ν (quinazoline ring), β (N-H)
1589	1599	1589			ν (phenylacetylene ring), β (N-H)
1617		1619	1600	1605	ν (phenylacetylene ring), β (N-H)
2111	2008	2111	2010	1985	ν (C≡C)

3.4.5 SERS Concentration Curve of Conjugate

A SERS concentration curve of the conjugates based on the data from the physiochemical characterisations was carried out to explore the optimum EL concentration to image.

Presented in Figure 25 was a correlative study of the same samples interrogated in the physiochemical characterisation section of this chapter. Indicated previously, the only method that was successful in determining the NP functionalisation was SERS analysis. To recap this was because the hydrodynamic diameter, zeta potential and SPR band of the EL loaded NPs did not markedly alter from those of the bare NPs. That was to say that peak dampening was observed only when particles were unstable at higher EL concentrations but there was no indication at lower concentrations if the EL was attached to the surface by these modes of investigation.

More specifically, Figure 25 was a detailed study of the effect of the concentration of EL on the SERS signal from the conjugates, it focussed predominantly on the most stable range of 0-500 nM in 50 or 100 nM increments. For clarity only concentrations of 0-500 nM EL were included in the full spectral graphs of (A) and the alkyne peak had been enlarged for ease of viewing in (B). It was seen from the spectra in (A & B) that with increasing concentration up to 500 nM EL that the SERS intensity increases. The γC≡C peak isolated in (B) was used to determine the peak area values across the full concentration range studied. In Matlab 2014b, these peaks were baseline corrected and the area under the peak was calculated and plotted as a bar chart in (C).[98] Analysis of the area under the peak of the alkyne across the concentration gradient concludes that beyond 400 nM EL the SERS signal drops. The SERS data were concurrent with the stability test results of the SPR band position from the UV-Vis experiment (Figure 21 & Figure 22) and the colour of the samples in the micro centrifuge tubes in Figure 20. Overall a good compromise on signal detection and control of the level of aggregation (which affects the size of particles or clusters entering the cell) meant that 300 nM was established as a sensible concentration of EL to continue with throughout the study.

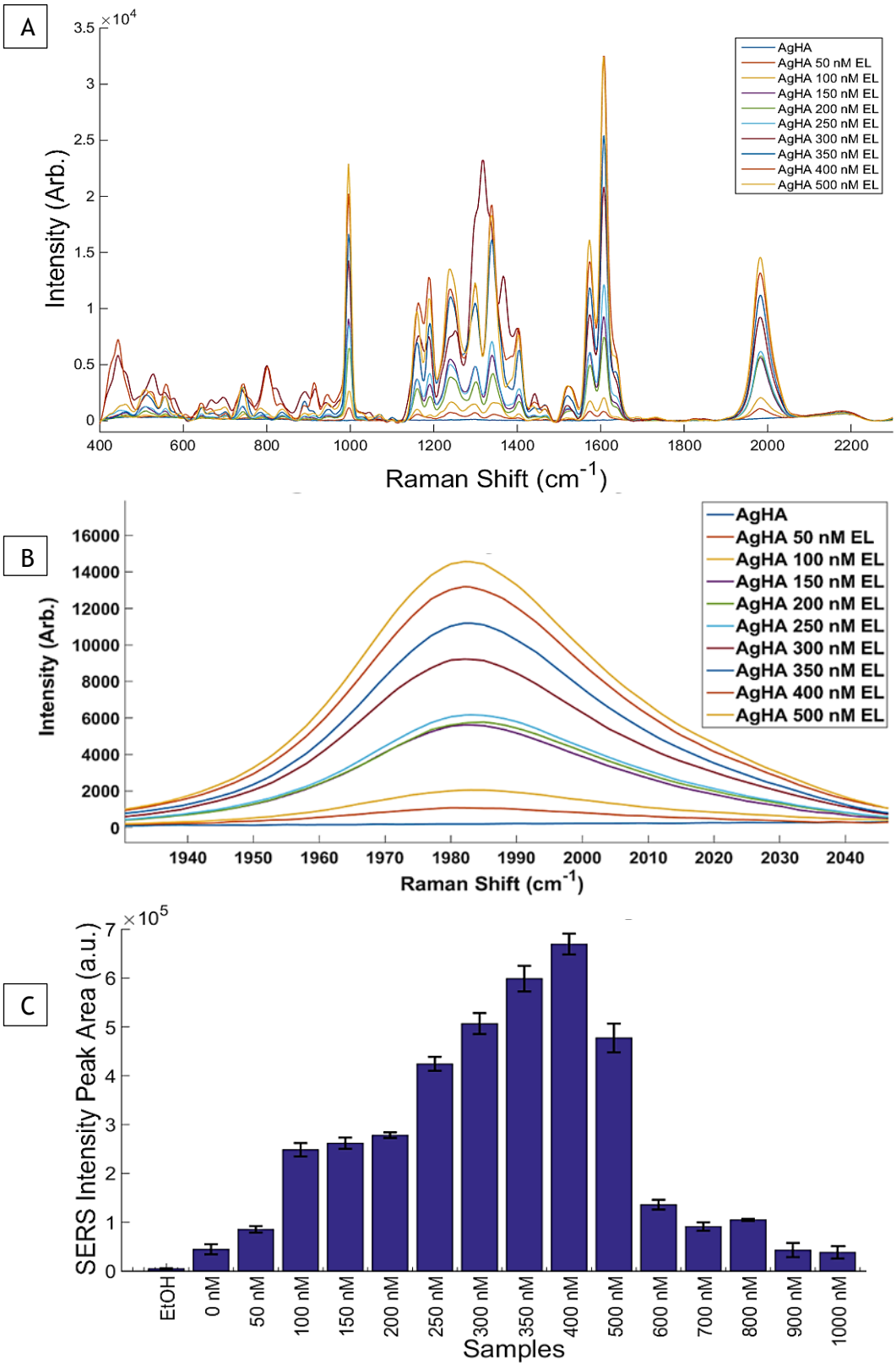

Figure 25 SERS of EL on AgHA NPs- (A) SERS spectra of 0 - 500 nM EL, (B) zoomed into the alkyne peak, (C) bar chart of peak areas of alkyne peak over the extended range up to 1000 nM EL. Acquisition time was 0.5 s, 5 acquisitons averaged, CBEx 638 nm laser power source at maximum of 40 mW, at sample was 23 mW.

Progressing the experiment further, it was pertinent to ascertain whether the AuCt NPs would display a similar response to the concentrations of EL used to functionalise the AgHA NPs. Since the physiochemical properties were not as

informative as the SERS data when assessing the EL-AgHA NPs, the next experiment was designed to compare only the alkyne SERS peak area of AuCt NPs to that of AgHA NPs and assess the colour of the particles by eye. The concentration of both metallic NPs were controlled to be the same of ~0.34 nM from UV-Vis concentration estimation, both particles were ~ 40 nm spheres (Figure 18). This was also an opportunity to determine the optimal means to process the data and decide how to measure the alkyne signal, by peak area or peak intensity.

The conjugate samples of 0-1000 nM EL on AuCt and AgHA NPs were prepared in triplicate following the 2.1.2 method. A CBEx handheld spectrometer was used at an excitation wavelength 638 nm to obtain 5 acquisitions of spectra per replicate of the samples (n=3). Presented in Figure 26 are the resulting spectra that were baseline corrected and plotted in Matlab 2014b.[98] Spectrum (A) was EL-AuCt NPs plotted with the same intensity scale as spectrum (B) EL-AgHA NPs, spectrum (C) showed that EL-AuCt NPs had a scale that was 10x less than that for the AgHA NP conjugates. It can be seen from (D) that both sets of the conjugates appeared to be just as stable in AuCt and AgHA up to 300 nM EL. The main exception between the two was the 1000 nM EL-AuCt conjugate which looked more stable, however after the wash step the sample precipitated out of solution completely and turned clear.

To discuss the different intensity response of Ag *versus* Au NPs when detecting the adsorbed EL analyte it should be remembered that the NPs were of a comparable: size, shape and concentration. The only obvious differences being the metal material and the surface chemistry, as the reducing agent was hydroxylamine hydrochloride for Ag NPs and sodium citrate for Au NPs. However, as stated in section 3.3.3 the zeta potential, or surface charge, was similar at -57.9 mV for AgHA and -55.6 mV for AuCt NPs.

The surface charge can correlate with the amount of adsorption and average SERS signal.[117] As mentioned previously, the binding geometries can affect the SERS signal intensity of certain peaks on different materials, which was observed here.[116] Overall the full Raman spectrum appears to be less intense for AuCt NPs than for AgHA NPs, this may be due to the reducing agents not being the same.

It could be that the gold produces 8x less intense SERS signal than silver, this was shown by Kustner *et al.* in 2009 when comparing SERS intensities from red laser interrogation of gold spheres to that of gold shells over spherical silver cores.[118] The AgHA conjugate may form a small number of aggregates that are not observed in the UV-vis at the ~600 nm region but nonetheless this minority population could

give a great enhancement, where as any AuCt aggregates would create a second SPR peak beyond the laser line wavelength and would not be enhanced as much by a 633 nm laser.

Pilot experiments were carried out by synthesising AuHA NPs to test the theory that surface chemistry could be responsible (data not included). However the NPs were found to be unstable and yielded too low a concentration to make it a viable option to pursue further.[119] It was also found that it was difficult to make reproducible batches of AgCt NP, so they were ruled out as not being a fair comparison to AuCt NPs.[120]

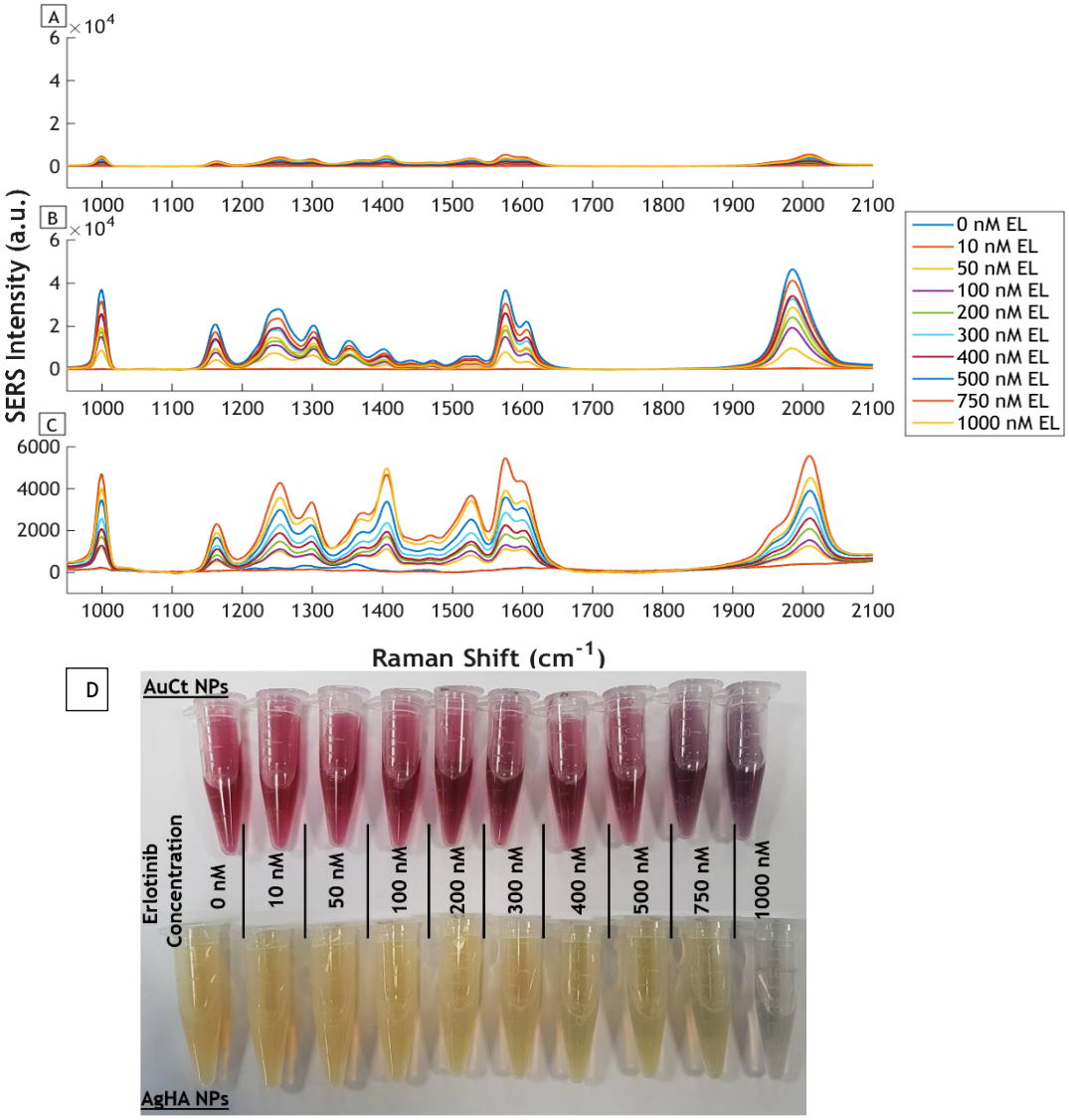

Figure 26 SERS signal from (A) AuCt NPs (0.34 nM), (B) AgHA NPs (0.34 nM) and (C) AuCt NPs (0.34 nM) same samples again but at a smaller scale on Y-axis to resolve peaks. Conjugates were ranging from 0-1000 nM EL. Interrogated with CBEx 638 nm handheld spectrometer at full power (40 mW at laser source or 23 mW at the sample) for 0.05 s with 5 acquisitions averaged per replicate, n=3. Alkyne Raman shift of AgHA NPs = 1985 cm^{-1} and for AuCt NPs = 2010 cm^{-1}. (D) Photograph of the conjugates after incubation with EL but before washing excess EL off.

To scrutinise the AuCt *versus* AgHA NPs comparison further, the peak areas were calculated as detailed earlier in this chapter for Figure 25 (C). The peak intensity was calculated by determining the maximum SERS intensity of the alkyne peak for all samples and then plotted as a bar chart with the SDs. Presented in Figure 27 (A) and (B) are the alkyne peak areas and peak intensities respectively. The intensity values were obviously different between these sets of data but the overall trend across the concentration gradient and SD values are equivalent. It was concluded that both methods would be acceptable for any future signal intensity investigations for cell maps. Additionally it was visible by eye from Figure 25 (D) that once the colour of the colloid becomes darkened slightly (750 nM) that the stability begins to deteriorate and this was mirrored in the SERS signal, as the peak intensity and peak area both deceased above 500 nM EL.

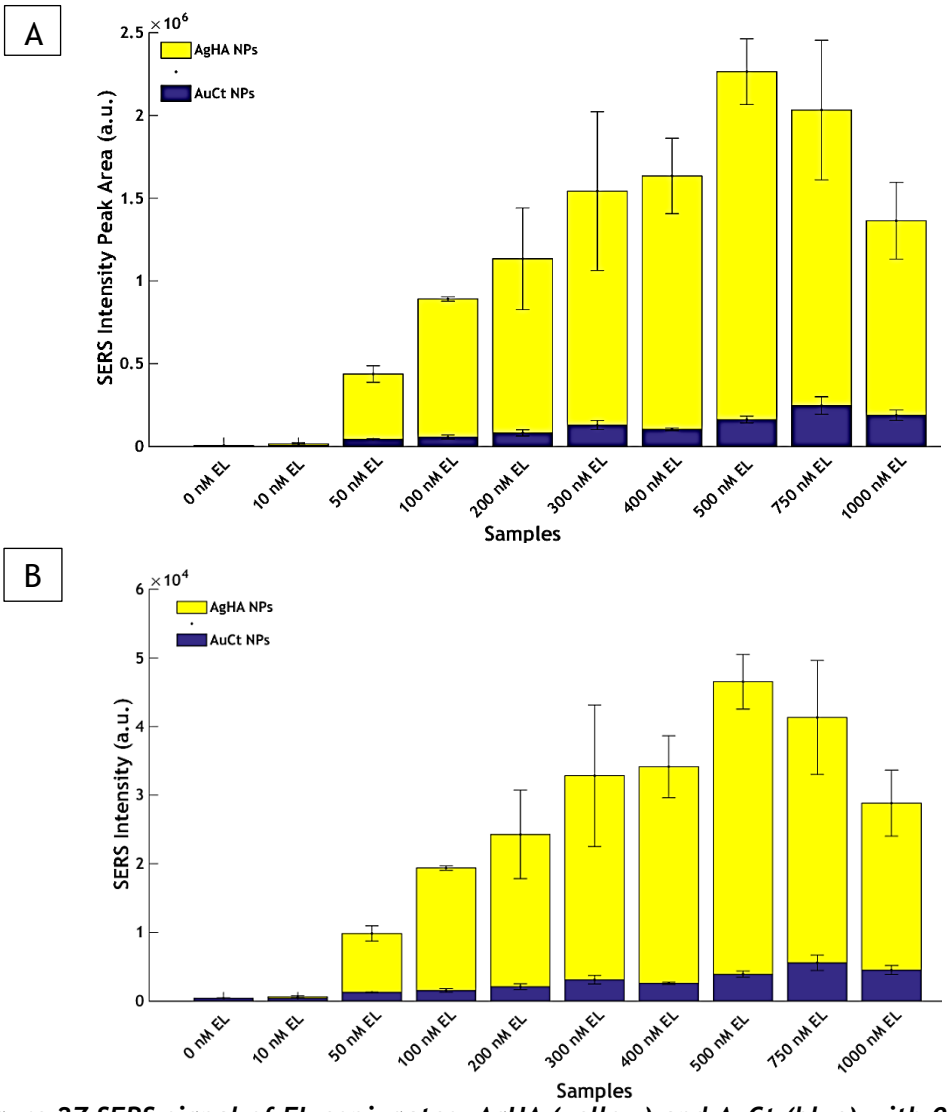

Figure 27 SERS signal of EL conjugates: AgHA (yellow) and AuCt (blue) with 0-1000 nM EL. Interrogated with CBEx 638 nm handheld spectrometer at full power (40 mW) for 0.5 s with 5 acquisitions averaged per replicate, n=3. (A) Alkyne vibration (area under the peak) ± SD, (B) signal intensity of the alkyne vibration from AgHA 1985 cm^{-1} Raman shift (yellow) and AuCt 2010 cm^{-1} Raman shift (blue) ± SD.

3.5 Summary

The key results from chapter 3 are summarised to conclude this section. AgHA and AuCt NPs were synthesised as monodispersed ~40 nm spheres, were negatively charged and stable. Conjugates were prepared by functionalising the colloid with EL in a self-assembly electrostatic approach. The alkyne Raman peak was found to shift from 2111 cm^{-1} to 2010 cm^{-1} and 1985 cm^{-1} from the powder EL to AuCt and AgHA conjugates respectively. This Raman shift indicates that the molecular binding is *via* the acetylene to the particles' surface. Concentration series indicate that 300 nM EL was a sensible sub-monolayer level of functionalisation for 40 nm NPs to remain stable, it was found that with monolayer coverage causes self-aggregation occurring at ~1 μM EL.

Taking into account the functionalisation characterisation data from this chapter on SERS signal and stability of conjugates, it was decided to progress onto the cell studies with 300 nM EL conjugates. This was for use in 3D SERS mapping to address the aim of conjugates distribution. Another factor to be addressed was the toxicity of the NPs, conjugates and free-EL to the cells. To be able to carry out the efficacy and toxicity studies the cells needed characterised for biomarker expression levels and EL sensitivity. These topics are addressed within the next chapter.

Chapter 4 Cytotoxicity and Efficacy of Conjugate *versus* Free-Erlotinib

---

"Solely the dose determines that a thing is not a poison."
Prof. P.T. Paracelsus, Alchemist & physician, 'Father of Toxicology' (1493-1541)

4.1 Introduction

During the introduction of this thesis, the concept of toxicity and efficacy of nanomedicines depending on the delivery mode, size and particle type was outlined. Currently discussion within the cancer community surrounds the repurposing of existing drugs, amongst other avenues, to advance treatment for patients. One such route would be the re-formulation of treatments as nanomedicines, there are various examples of this in recent years, which have been approved for use by the FDA.[73,79,121]

In order to utilise re-formulations in the treatment of patients, they must be rigorously tested *in vitro* before following the *in vivo* pre-clinical and clinical trial regulated work flow. In order to be approved, the intervention must first of all be proven to be safe, secondly that it was effective and finally, better than the current standard treatment. Non-inferiority studies must prove that they are safer or more cost effective for the patient if they are not improving efficacy.

In NP research to date, there has been lack of agreement in the field over the correct means to assess toxicity of NPs themselves. In short, each cell type and particle type need tested empirically, due to auto fluorescence of metallic particles causing interference with more advanced, automated plate based fluorescent assays.[89] Hoskins *et al.* also reported the issue of over estimation of viability with many cell assays, it is endemic within the field and needs careful consideration.[90]

This chapter aims to address the *in vitro* stage of the aforementioned cytotoxicity and efficacy of the nano-delivery of EL, in comparison to the standard free-EL delivery. As mentioned in the previous paragraph, this can be difficult to perform owing to the unique properties of metallic particles in their nanoscale size. Here, various techniques have been used including basic live or dead cell staining and more complex protein analyses of EGFR expression and downstream signalling pathway studies by immunofluorescence and Western blots.

4.2 Rationale of Cell Line Choice

Tarceva (EL) was originally prescribed for patients in the USA for the following indications as stated in the prescribing information leaflet:

"The first-line treatment of patients with metastatic NSCLC whose tumors have EGFR exon 19 deletions or exon 21 (L858R) substitution mutations as detected by an FDA-approved test. The maintenance treatment of patients with locally advanced or metastatic non-small cell lung cancer whose disease has not progressed after four cycles of platinum-based first-line chemotherapy. The treatment of patients with locally advanced or metastatic non-small cell lung cancer after failure of at least one prior chemotherapy regimen… TARCEVA in combination with gemcitabine is indicated for the first-line treatment of patients with locally advanced, unresectable or metastatic pancreatic cancer…"[122]

Therefore, as NSCLC was the major indication that EL was used to treat, it was decided to use lung adenocarcinoma cells as a model during this study.

In order to not only image the EL-NP conjugate inside the cell but also to assess its effectiveness, care was taken to select a cell line that harbours the mutation rendering it sensitive to EL, *EGFRm+*. To determine whether the conjugate delivery could enhance the effect of EL on a wild-type, or insensitive cell line, a control cancer line was selected without the mutation, *EGFRwt*. HCC827 (ATCC® CRL-2868™) is a human lung adenocarcinoma EL sensitive cell line with the EGFR activating mutation. H1355 (ATCC® CRL-5865™) is a human lung adenocarcinoma EL insensitive cell line without the sensitizing mutation; both cell lines originated from the ATCC.[123] Previous imaging studies in the field have selected cell lines which do not respond to EL and were therefore not clinically relevant. In this case it was important to the second aim of the study to investigate drug efficacy.[59]

4.3 Characterising Cell Lines

4.3.1 Mycoplasma Testing to Verify as Infection Free

Mycoplasma is a cell infection caused by simple and small (100 nm) bacteria that are problematic in cultured cells, and which cannot be detected by a light microscope. Mycoplasma are resilient against many antibiotics as they do not possess a cell wall, which is the target of most antibiotics. Contamination rates can vary from 10-87% and this is an issue as its presence can affect the properties of the cells.[124-127] Miller *et al*. found by microarray data that mycoplasma infection can affect the signalling and expression of growth factors, oncogenes, cell adhesion,

stress responses and metabolism.[128] It was deemed prudent to ensure that both the cell lines were infection free, as well as to authenticate their genetic origin.

The H1355 and HCC827 cell lines were tested for mycoplasma with the biochemical MycoAlert™ Mycoplasma Detection Kit used by Technical Services, MRC HGU, IGMM, University of Edinburgh. The kit by Lonza lyses any viable mycoplasma to release enzymes which catalyse the conversion of ADP to ATP. The luciferase enzyme in the kit substrate produces a light signal from the energy produced by ATP. A ratio of ATP levels was obtained by taking measurements both before and after addition of the substrate, anything >1.4 was positive, <1 was negative and in between the cells need incubated for a further 48 hours before re-testing collected media.

In this case the mycoplasma results were negative, as seen in Table 4. The test line H1355 passage 13 resulted in a ratio of 0.75, which was <1 and categorized as a negative result. HCC827 passage 12 results are seen in Table 4, the ratio was 0.64, which was <1 and also a negative result.

Table 4 Mycoplasma test results for H1355 and HCC827 cell lines

Sample	2nd Reading	1st Reading	Score	Result
H1355 Positive Control	522	95	5.49	Positive
H1355 Negative control	62	129	0.48	Negative
H1355 p13	**41**	**55**	**0.75**	**Negative**
HCC827 Positive Control	970	233	4.16	Positive
HCC827 Negative Control	86	281	0.31	Negative
HCC827 p12	**70**	**109**	**0.64**	**Negative**

4.3.2 Cell Line Authentication- Short Tandem Repeat Profiling

Cross contamination or misidentification of cell lines can lead to studies with ill-informed conclusions formed as a result of the mistake. Further to this is the inaccurate reporting of the true nature of a cell line, whereby cells are described as *e.g.* ovarian when they are in fact pancreatic. The true extent of the problem will never be known but a recent publication has highlighted the issue and certain journals now have a pre-requisite that any cell lines used are authenticated before a manuscript is considered. Vaughan *et al.* wrote a perspective piece on the issue, stating that as many as 18-48% of cell lines are believed to be misidentified, effectively invalidating any research or pre-clinical data collected.[129] This has many

implications but at a basic research level, it was a waste of consumable budgets and public funding to carry out experiments on incorrect cell lines. It is an endemic issue in life science research that needs quashed through cell line authentication each time a new cell line is received by a laboratory as a gift from another research group.

Cell lines can be verified by genetic profile testing. Here, authentication of the genetic STR profile of NCI-H1355 and HCC-827 was performed utilising the cell line authentication service run by ATCC. The description of the protocol entailed is quoted below.

"Cell lines were authenticated using Short Tandem Repeat (STR) analysis as described in 2012 in ANSI Standard (ASN-0002) Authentication of Human Cell Lines: Standardization of STR Profiling by the ATCC Standards Development Organization (SDO) and in Capes-Davis et al., Match criteria for human cell line authentication: Where do we draw the line? Int. J. Cancer. 2012 Nov 8. doi: 10.1002/ijc.27931."[130]

The results of the STR profiling can be found in Figure 28, identifying the cells as A) NCI-H1355 or ATCC catalogue number CRL-5865 human lung adenocarcinoma cells. This was determined by a 100% match for the 8 core loci by an allele matching algorithm. Figure 28 B) presents the STR results of the HCC827 line used in this study as a 100% match for HCC827, which is catalogued as CRL-2868 by ATCC and is also a human lung adenocarcinoma cell line.[123]

Originally H1355 was gifted for use in this study under the cell name H3255, which should have been hypersensitive to EL.[6] During the cell authentication by ATCC's STR profiling it was identified as H1355, which was also a lung adenocarcinoma but was *EGFRwt* and not *EGFRm+* as it should have been. It was genetically a monoculture and presumed that a simple mislabelling of cryovials occurred before it was received for this study. Therefore, any initial studies conducted in this line still stand as legitimate controls, despite at the time thinking it should have been responsive to EL. The cells were tested when suspicion arose over the provenance of the cells, since they were not responding to EL treatments as anticipated. Subsequently several cell lines were acquired from the IGMM, ECRC, Edinburgh (Prof. Margaret Frame and co-worker's laboratories) to run a screen for respondents to EL. The HCC827 cells that had previously been identified as a sensitive line was available, once EL sensitivity was confirmed experimentally over a 72 hour metabolic activity assay, the cells were also authenticated by ATCC.

A)

ATCC®
Cell Line Authentication Service
STR Profile Report

FTA Barcode: STRA7361
ATCC Sales Order: SO0152500

Addendum: Comparative Output from the ATCC STR Profile Database

% Match	ATCC® Cat. No.	Designation	D5S818	D13S317	D7S820	D16S539	vWA	THO1	AMEL	TPOX	CSF1PO
100	STRA7361	H3255_NCI	11,13	12	12	8,13	14,17	9	X	9,12	12,13
100	CRL-5865	NCI-H1355; Lung Carcinoma; Human (Homo sapiens)	11,13	12	12	8,13	14,17	9	X	9,12	12,13

B)

ATCC®
Cell Line Authentication Service
STR Profile Report

FTA Barcode: STRA8811
ATCC Sales Order: SO0226325

Addendum: Comparative Output from the ATCC STR Profile Database

% Match	ATCC® Cat. No.	Designation	D5S818	D13S317	D7S820	D16S539	vWA	THO1	AMEL	TPOX	CSF1PO
100	STRA8811	HCC827	12	9	11,12	12	18	6	X	8	11
100	CRL-2868	HCC827 ; Lung Carcinoma; Human (Homo sapiens)	12	9	11,12	12	18	6	X	8	11

Figure 28 Cell line authentication by STR profiling conducted by ATCC identifying A) NCI-H3255 as NCI-H1355 human lung cancer cells and B) HCC827 as HCC827 lung cancer cells.

Further characterisation was conducted once the relevant cell lines were authenticated, such as profiling the EGFR biomarker expression levels.

4.3.3 Epidermal Growth Factor Receptor Expression Levels and Distribution

Constitutively active EGFR is observed even in the absence of the EGF ligand to activate the receptor. To assess the EGFR expression pattern, a series of conditions were set up for both cell lines. The cells were incubated without FBS (starving conditions *i.e.* lacking ligands) and the standard culture conditions of 10% FBS (which naturally contains hormones and stimulating ligands) for 24 hours in duplicate. Afterwards one set of each cell line was then exposed to 50 ng/mL of human EGF (hEGF) ligand for 20 minutes before the fixation and permeabilisation protocol from section 2.3.3 wer followed. The antibody incubations were followed as per 2.3.3 using α-EGFR 1° antibody and α-mouse 2° antibody. The cells were then imaged on the confocal microscope system described in 2.6.2. The images were acquired at consistent settings across all samples to highlight any changes in expression levels and patterns of EGFR in an unbiased manner. The excitation sources used for the blue DAPI and red fluorescence were 405 nm and 561 nm wavelength respectively. The objective was Leica 63x water immersion 1.20 NA HC PL APOCS2.

Representative images were montaged into Figure 29 for both HCC827 (A-D) and H1355 (E-H) cell lines. The first column is a merge of all other columns, second

column is bright field, third column is DAPI nuclear staining (blue) and the last column is EGFR staining (red).

First to describe the HCC827 cell samples: Figure 29 A) was 0% FBS and no hEGF which had diffuse staining and some punctae; B) was 0% FBS with 50 ng/mL hEGF that shows similar staining as (A) but slightly more intense and a greater number of punctae; C) was 10% FBS and no hEGF which had far more EGFR staining in both a diffuse and punctate distribution than (A) and (B); D) was 10% FBS and 50 ng/mL hEGF that had similar distribution to (C) except it was very intense and saturated in the perinuclear area demonstrating a large amount of EGFR activation.

Next to describe the H1355 sample: Figure 29 E) was 0% FBS and no EGF which had faint diffuse and punctate distribution but less intense than similar conditions (A) for HCC827 cells; F) was 0% FBS with 50 ng/mL hEGF that showed similar staining as (E) but slightly more intense punctae; G) was 10% FBS and no hEGF, which had more intense EGFR staining than (E) and (F) in a diffuse distribution and the punctae were less obvious; H) was 10% FBS and 50 ng/mL hEGF, the EGFR staining was slightly diffuse with the most intense punctae out of all the H1355 cell conditions but far less than HCC827 cells which became saturated.

In summary, the images for H1355 *EGFRwt* cells had faint EGFR expression in the absence of ligand, which indicated low levels of constitutively active EGFR. HCC827 *EGFRm+* cells have strong EGFR signals present even without hEGF or FBS, demonstrating that the mutation confers a high level of constitutively active EGFR. Both cell lines possess constitutively active EGFR but HCC827 expressed the biomarker at a far greater level. Ultimately this means that any cell cycle synchronisation experiments whereby researchers would traditionally starve cells to synchronise the population of cells would not be successful. This was because the removal of FBS does not prevent EGFR activation and expression as auto-phosphorylation occurs. These data gave an indication that a greater expression level of EGFR was expected in Western blots for HCC827 EL sensitive cells when compared to the EL insensitive H1355 cells.

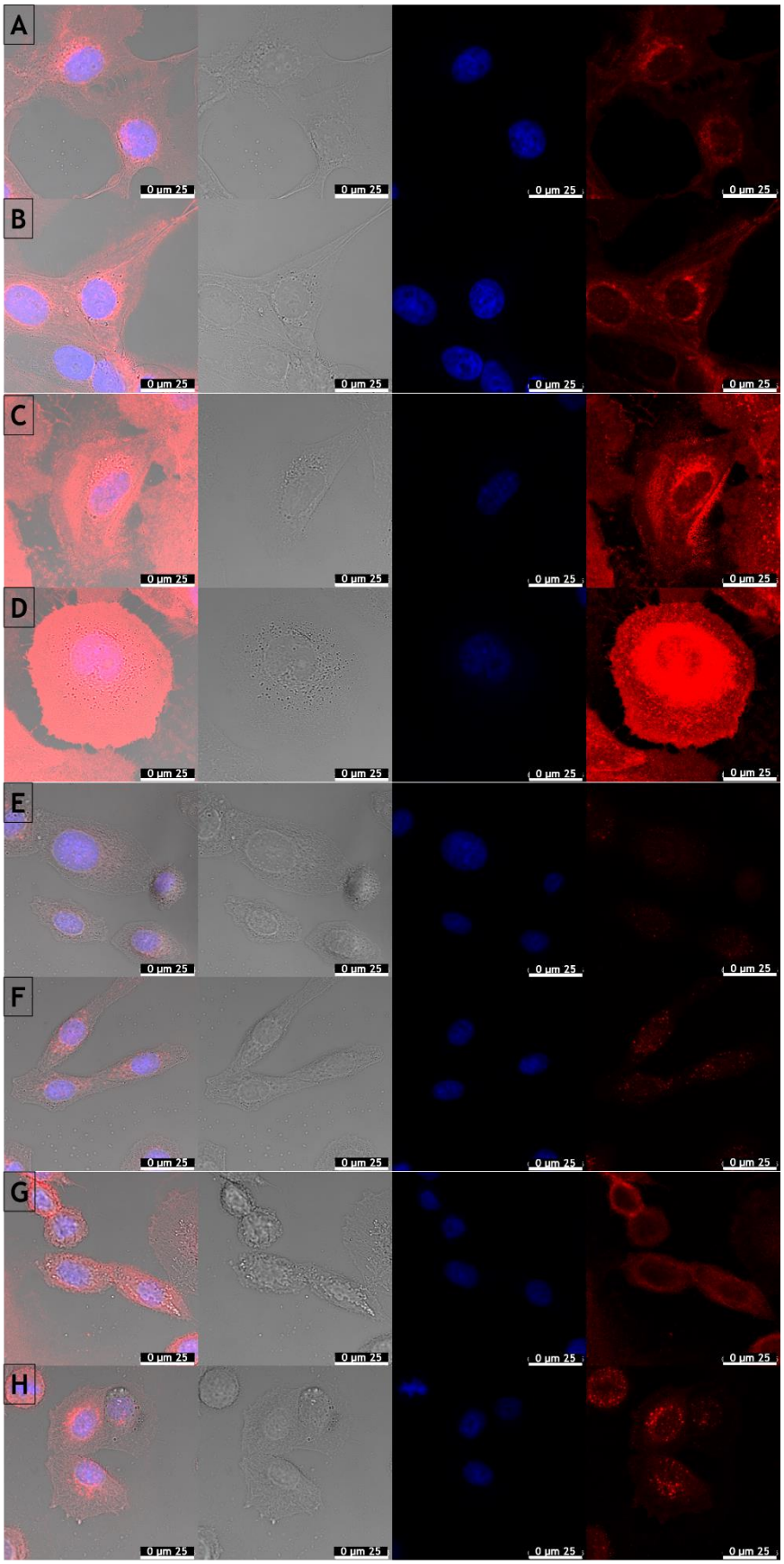

Figure 29 FBS starvation study of EGFR expression on HCC827 (A-D) and H1355 (E-H) cell lines starved for 24 hours before adding media: 0% FBS (A,B,E&F), 10% FBS (C,D,G&H), no EGF (A,C,E&G), with 50 ng/mL EGF for 20 minutes (B,D,F&H). Scale bars 25 µm. From left to right- merged, bright field, DAPI nuclear stain in blue, EGFR in red. Acquired by 63x water objective, 1.33 NA, laser power and acquisition settings kept constant to emphasise any staining differences.

Next the finer details of the specific effect that the free-EL and conjugated EL had on its target biomarker the EGFR was studied. This gave an idea of the treatments' effect on phosphorylation at an intracellular level.

4.4 Efficacy of Erlotinib and its Conjugates

4.4.1 Immuno-fluorescence Assay of pEGFR Biomarker Inhibition

To establish base levels of EGFR and therefore control phosphorylation intensities, an IFA study was carried out on the HCC827 and H1355 cells to determine the expression level and distribution. HCC827 and H1355 are known to possess constitutively active EGFR and this was verified by the FBS titration study carried out in Figure 29. It can be seen that without stimulation by EGF, there was a diffuse staining indicating presence of the receptor. Once stimulated the punctate distribution appears which demonstrates the activation of the receptor and its internalisation. This would suggest that it would be difficult to remove all traces of phosphorylation of EGFR since it was constitutively present, however after treatment with EL it should be reduced compared to untreated controls. Expression levels can be examined more thoroughly and quantified by Western Blot.

Cells were plated as detailed in 2.3.3, the cells were exposed to the treatments listed below in Figure 30 for 4 hours after which 50 ng/mL hEGF was added for 20 minutes before fixation and permeabilisation as in 2.3.3 with the following antibodies: α-pEGFR 1° was used at 1:1000 (CST #3777) 4°C overnight and α-rabbit 2° (CST #7074) for 1 hour at RT. All images were acquired at the same settings in order to not skew expression level intensity of pEGFR.

In Figure 30, HCC827 was assessed for pEGFR levels after 4 hours incubations with treatment of: A) 100 μM EL (death control), B) DMSO (vehicle control), C) 300 nM EL, D) AgHA conjugate, E) AuCt conjugate, F) AgHA NPs 0.3 nM, G) AuCt NPs 0.3 nM. The first column was a merged image of bright field, DAPI and pEGFR, the second was DAPI nuclear staining (blue) and the last column was pEGFR staining (red). Qualitatively, it was seen that (F) and (G) had a lower expression level of pEGFR than the DMSO control (B) and this may be due to fluorescent quenching by the NPs within the cells. The 100 μM EL positive control (A) for maximum EL effect against EGFR had supressed almost all expression of pEGFR. The 300 nM EL sample (C) had markedly less pEGFR expression than the DMSO control (B). AgHA conjugate (D) had a similar level to the 300 nM EL (C) and less than its respective AgHA control (F). AuCt conjugate (E) had a similar intensity of pEGFR compared to AuCt NPs (G).

There appears to be a delayed uptake of conjugates into the cell to deliver their drug payload. Therefore, with a greater incubation time of 24, 48 or 72 hours the AgHA conjugates may have had more of an effect. The SERS and uptake studies in chapter 5 shed further light on this hypothesis. It was anticipated that the 300 nM EL would reduce the pEGFR expression to appear much like the 100 µM sample, given time to act fully. Unfortunately, due to time constraints the H1355 cells were not tested for pEGFR expression as more antibody could not be sourced before the project ended.

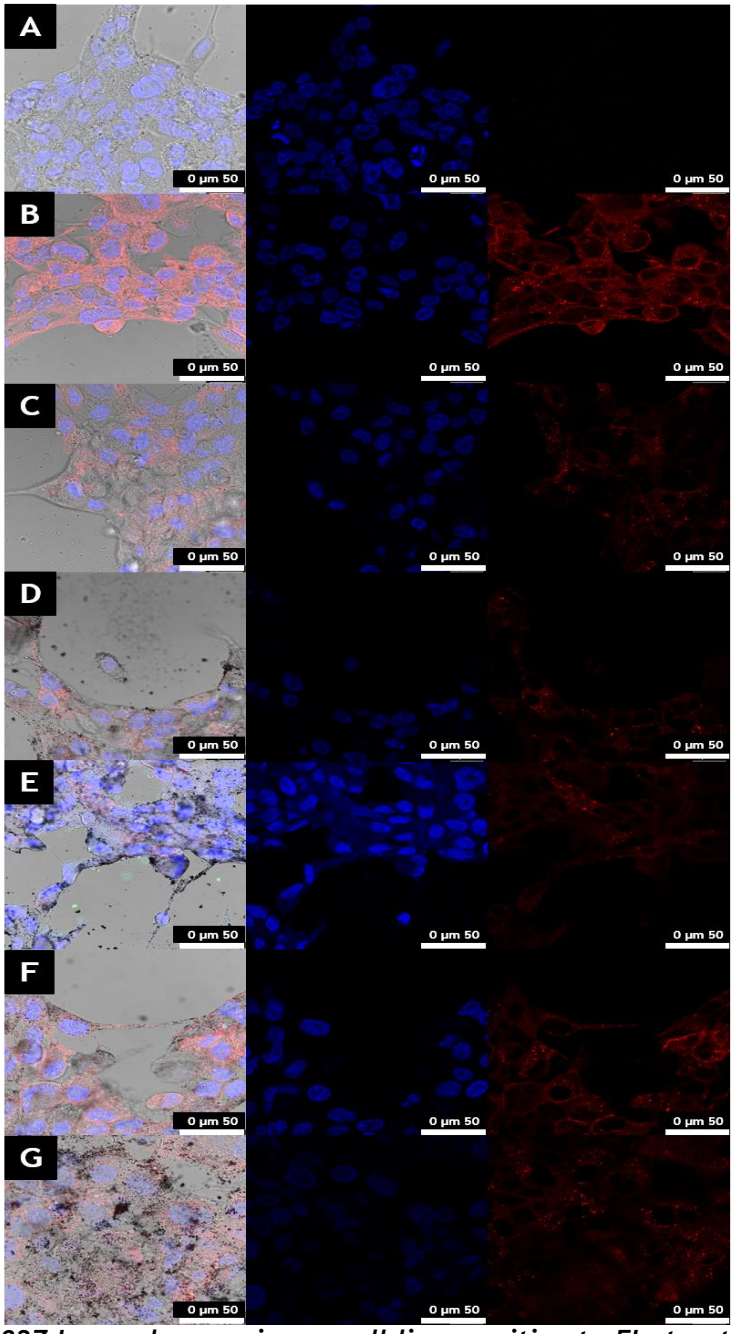

Figure 30 HCC827 Lung adeoncarcinoma cell line sensitive to EL, treated for 4 hours with A) 100 µM EL +ve control for blocking activation of EGFR, B) DMSO control, C) 300 nM EL, D) AgHA conjugate, E) AuCt conjugate, F) AgHA NPs 0.3 nM, G) AuCt NPs 0.3 nM. Scale bar 50 µm. Left merge of α-pEGFR and DAPI with bright field, midddle nuclear DAPI stain (blue), right α-pEGFR (red). All acquisitions at the same laser power and intensity gain.

After the distribution of pEGFR was qualitatively, the EL sensitive line HCC827 was prioritised for immunoblotting. Western blots were used to quantitatively probe the expression levels of pEGFR for a concentration range of treatments. This was to further characterise the response of the cells to the various treatments and try to understand the differences between the AuCt and AgHA conjugates on the sensitive cells.

4.4.2 Phospho-proteomic Study by Western Blot

The phospho-proteomic studies were used to indicate activation levels of protein pathways and hence effectiveness of TKIs. Western blots were used to quantify what was observed in the immunofluorescence section 4.4.1.

HCC827 cells were plated, treated, harvested, *etc*. as described in experimental section 2.3.9. The Western blot was probed for pEGFR then stripped and re-probed for both tEGFR and GAPDH, as seen in Figure 31 (A). Qualitatively, the GAPDH shows equal loading across all the samples, this was used as a housekeeper protein to confirm equivalent loading. A range of concentrations were incubated with the cells for 4 hours: 0, 10 nM 100 nM and 1 μM EL, either free, as AgHA conjugates or AuCt conjugates. The controls were: DMSO vehicle control, AgHA bare NP control and AuCt bare NP control.

The EGFR species in the free-EL samples of Figure 31 (A) have slightly less intensity than the AgHA and AuCt conjugate samples. Each of the respective controls for pEGFR expression: DMSO vehicle control, AgHA NPs and AuCt NPs have similar expression levels, although the vehicle control had a broader protein species, hence more expression. It is seen that with increasing EL concentrations both free-EL and AgHA conjugates see a dose dependent response until the protein species almost disappears at 1 μM. In the AuCt conjugates, the pEGFR species only start to reduce in intensity at 1 μM EL. When comparing the IC_{50} of EL on HCC827 cells (10 nM EL) marked by the asterisk in black, yellow and red, it appears that the AgHA conjugate had the greatest difference from its respective control (AgHA NP). From the Western blot, it appeared that there was equal protein loading from the GAPDH species present, the AuCt conjugate had little to no effect on pEGFR levels, and the silver conjugate was as effective as free-EL, if not slightly better at the lower concentration of 10 nM EL on pEGFR with less species visible.

To investigate more thoroughly, the protein species were quantified for area and intensity on ImageLab software for GAPDH as the loading control, EGFR and pEGFR, and the resulting ratios are plotted in Figure 31 (B). It was clear that the vehicle

DMSO control had the greatest ratio of p/tEGFR, by around 3 fold of the other 2 bare NP controls. A dose dependant response was seen with both free-EL and EL AgHA conjugate, whereas the AuCt conjugate only had an effect at 1 μM. The absolute ratios for the AgHA conjugates were as low as the free-EL, making them biologically relevant and as effective as free-EL. However, to take into account any effects that the presence of the bare NPs had on tEGFR, the conjugates were compared against their respective controls.

Figure 31 (C) shows the p/tEGFR ratio for treatments, normalised to each of the respective controls for the: DMSO vehicle, AgHA NPs and AuCt NPs. Here, it gave a clearer view that the AuCt conjugate was unsuccessful in preventing phosphorylation of the EGFR of the cancerous cells. Conversely, the free-EL and the AgHA conjugate were effective in preventing phosphorylation and was ultimately why the cells died after longer incubations, as they could no longer proliferate. Although it would be interesting to investigate longer incubations with EL it becomes problematic as the cell numbers decrease in successfully treated samples. Therefore, it was practically difficult to harvest adequate cell numbers, to provide enough protein quantities, to carry out the full Western protocol.

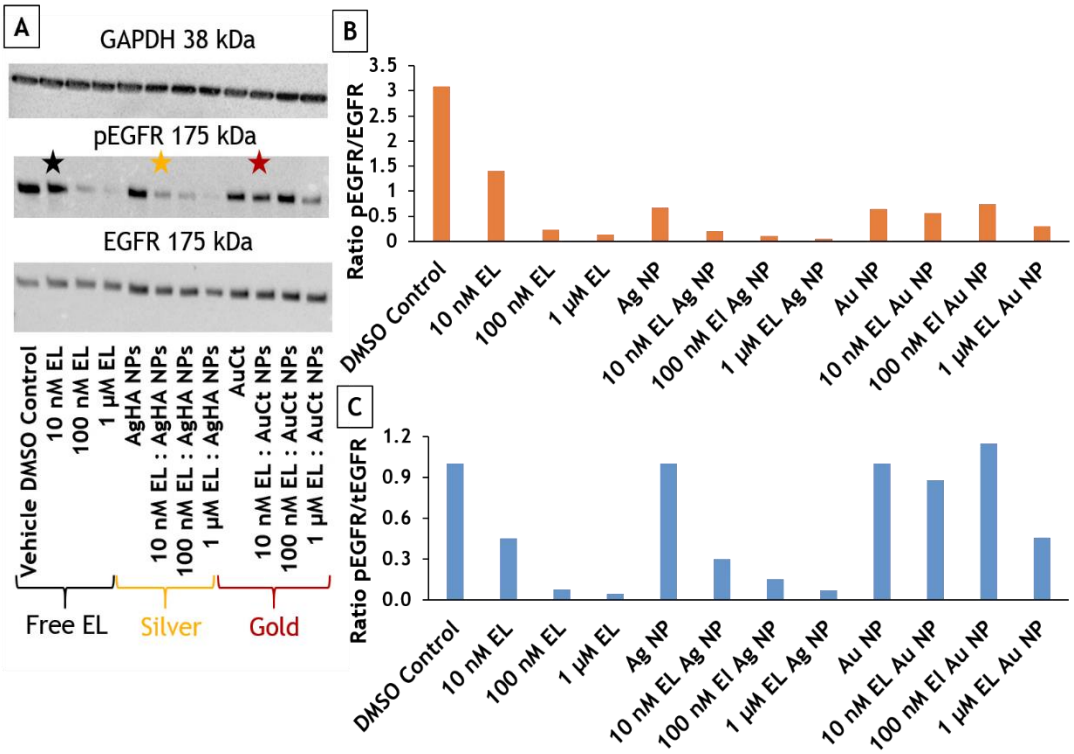

Figure 31 Western Blot of HCC827 lung adenocarcinoma cells with free-EL, EL-AgHA conjugates, and EL-AuCt conjugates, α-GAPDH housekeeper loading control, α-pEGFR and α-tEGFR. B) pEGFR/tEGFR/GAPDH protein expression normalised to the DMSO vehicle control, C) p/tEGFR/GAPDH normalised to respective controls of vehicle control, AgHA NPs and AuCt NPs.

Studying the phosphorylation status of EGFR drug target and other proteins was impractical at later timepoints. A more relevant measure of efficacy was toxicity studies on viability levels. It was an opportunity to assess whether there was a delay in the effect exerted by the conjugates in comparison to the free-EL, since the drug needs to be released from the particle before the active site was exposed and available to block the ATP-binding site target. Cytotoxicity studies are addressed herein.

4.5 Cytotoxicity Tests

There are many 96-well format assays available for high-throughput analysis of cell viability, metabolic activity, proliferation *etc.* in biological laboratories. The processes followed, the pros and cons are described in detail in many manuscripts and book chapters.[89,131-135] Within the nanometrology field, a consensus is yet to be reached on the optimum test. The inclusion of NPs into a cytotoxicity test system requires empirical testing per cell line and particle type combination. This is to ensure these trusted and long established biological assays are unaffected by the nanoscale optical, surface chemistries and other properties of the metals *e.g.* catalysis.

During this study, various 96-well plate based toxicity tests were conducted with unsuccessful results and for brevity have been excluded from the thesis. However, they are mentioned in the interest of progressing science in a collegiate, informed and productive manner. The reason that these tests did not work was primarily due to unrealistic false positive read-outs that made the cells appear to be *e.g.* 200% more viable than the control cells. After conducting full spectral scans for colorimetric based assays it was found that the SPR of the particles tend to overlap with the collection wavelength, and it increased the absorbance in a false positive manner as a result. The assays tested were Alamar blue, MTS (3-(4,5-dimethylthiazol-2-yl)-5-(3-carboxymethoxyphenyl)-2-(4-sulfophenyl)-2H-tetrazolium)), MTT 3-(4,5-Dim- ethylthiazol-2-yl)-2,5-diphenyltetrazolium bromide), CellTiter (all metabolic activity assays using colorimetric or fluorescent outputs) and ATP lite (ATP monitoring system using luciferase to detect ATP in viable cells through luminescence). In the interest of transparency and fairness, these were not fully tested on the AuCt NPs, predominantly on AgHA NPs, and AuCt may experience less issues than AgHA NPs particles due to a more red shifted SPR. To meet the requirements of this study, however, a reliable and accurate test needed to be sourced that was suitable for all treatments to be compared concurrently and equally.

Draq5 fluorescent DNA stain and Draq7 dead cell stains were used on the Incucyte dynamic cell monitoring system based within the cell incubator for microscopically imaging longitudinal studies instead of relying upon end point analysis. This was also unsuccessful as the NPs affected the image processing software. It seemed that the presence of the NPs in the media caused auto-fluorescence and the thresholding tool could not differentiate the background noise from genuine cell signal. Additionally, at higher concentrations of EL or more concentrated samples of NPs the aggregates that formed were classified as cells due their size and shape.

Further to this, Draq5 and Draq7 were also tested briefly for a Raman read out, instead of fluorescence, in the hope that fluorescent artefacts would be circumnavigated. However, there was high background from both the dead cell Draq5 and viable cell Draq7 controls. It was hypothesised that this was due to surface enhanced fluorescence, when the stain was in close proximity with the particles, rather than a true interaction with the live cells or DNA intercalation for Draq5 and Draq7 respectively.

Mentioned in the introduction of this thesis was the spotlight on the issues of light based artefacts in the presence of NPs by Ong *et al.*. They discussed that NPs cannot be tested individually with assay components, as there was a complex interplay between these and the cells and media.[89] Therefore, despite including NPs and assay components alone as a control, this cannot be trusted to fully demonstrate the artefactual background results created by these particles. To expand upon this further, another study is highlighted in the following paragraph on the catalytic properties of AgHA NPs.

One such study that exploits the pseudo-enzymatic or catalytic activity was that by Keating *et al.*, which uses the peroxidase-like activity of silver NPs on peroxidase substrate 3,3',5,5'-Tetramethylbenzidine (TMB).[136] This study does not discuss the caveats of fluorescent based cell toxicity assays and its purpose was to describe the benefits of NPs exerting an effect on substrate turnover by producing a colorimetric change. This exemplifies why fluorescent assays are not suitable for use in this study with silver NPs. The pseudo-enzymatic effect of AgHA NPs would make cells appear more viable than they are, by producing a higher read out in samples, even where they have killed the cells.

Another means of testing viability could be flow cytometry, although this is not always readily accessible to every research group and as a result can be expensive. Flow cytometry can measure a number of cell qualities using nuclear stains and

antibodies for certain death or viability markers.[137-139] Low-tech approaches can also be utilised but these are usually low-throughput and time consuming, although they are reliable even in the presence of NPs. The following are examples of low-throughput approaches that could be utilised for NP toxicity assays to circumvent the light based artefactual effects. Wound scratch healing assays, which measure the rate of growth to recover from the area of a well or plate cleared of confluent cells. Simple Trypan blue viability counts of detached cells. Clonogenic assays, whereby the number and size of colonies formed from a small number of single cells can be quantified. These can take up to several weeks to grow colonies of cells that are pre-exposed to treatments before staining to count and plate. After 2-4 weeks, these are then fixed and stained with crystal violet to be counted and have their area measured.

Clonogenic assays were tested during this study however there was a lot of optimisation to ascertain the initial cell number to be plated. The time spent renewing the media with treatments over the course of several weeks was labour intensive and costly in reagents. Ultimately the correct cell number was not established for each line, but given more time this could have been a viable alternative to flow cytometry or plate based assays.

Live/Dead fluorescent cell stain was available for imaging on a smaller scale than 96-well plates. Here, the bulk effect of colloid on autofluorescence was not observed, as cells were analysed on an individual basis. A trusted method was developed to acquire images and use software to count the number of cells and the area of fluorescence for both live and dead cells. This was still relatively low throughput but the data was reliable.

Finally, cells were counted by a very low-throughput and labour intensive but efficient reagent and instrument-wise using a cost effective option of Trypan blue cell viability counting. These data are discussed later in the chapter along with live/dead viability counts. First, the H1355 and HCC827 cells were assessed for response to free-EL alone. Therefore, a standard plate based assay approach was sufficient for this baseline stage.

4.5.1 Alamar Blue Metabolic Assay

Alamar blue is a mitochondrial metabolic assay that measures the cell's metabolic activity levels to establish the concentration of drug that inhibits 50% of cells from growing (IC_{50}). This can be used to measure the anti-proliferative activity and toxic effects to cells, as a result of less enzymatic turnover of the assay substrate because

there are less cells or more unhealthy cells present that have a damaged metabolic capacity. Fluorescent and colorimetric based assays have been unsuccessful during these studies with the inclusion of NP or conjugate treated cells. The failure of these assays was due to the interference of the optical density (OD) or artefacts in fluorescence. However, alamar blue was still useful to characterise the cell lines response to free-EL only. This enabled an IC_{50} to be calculated for each cell line as validation that they responded as they should do, based on their *EGFRm+* status. HCC827 with *EGFRm+* should be sensitive with a low IC_{50} (nanomolar range) and H1355 which is *EGFRwt* should be insensitive with a high IC_{50} (micromolar range).

Whilst conducting the IC_{50} experiments the results were yet to be received for the cell authentication. Initial experiments were indicating that H1355 was not responding to EL as anticipated (*i.e.* when it was thought to be hypersensitive H3255). Therefore, a fresh batch of EL was tested alongside the original vial used to rule out any questions over the potency of the batch being tested. This new batch was EL from Selleck, which dissolves more readily than the original EL hydrochloride formulation from LKT. The alamar blue screening protocol followed is described in 2.3.5. The results were quantified and plotted in GraphPad Prism version 5.01 for Windows, GraphPad Software, San Diego California USA, www.graphpad.com.

Figure 32 presents the dose-response curves for the 2 EL sources in both cells lines, (A) HCC827 sensitive line and (B) H1355 insensitive cell line. DMSO was the vehicle control for 100% viability and 20 µM staurosporine was the cell death control, and the EL treatments were ranging from 3 nM to 10 µM. It was immediately obvious that (A) responded to the EL, whereas (B) did not, due to the sigmoidal *versus* gentle gradient curve respectively. Within the HCC827 cells (A), the IC_{50} of both sources of EL and EL hydrochloride have comparable results with 8.7 nM and 15.4 nM of EL respectively. These data concur with previously published IC_{50}'s in the field of between 2-10 nM.[140-142]

In Figure 32 (B) the H1355 cells have IC_{50} values several orders of magnitude greater than that of the sensitive cell line. The Selleck EL IC_{50} was 0.4 µM and the LKT EL hydrochloride IC_{50} was 0.3 µM EL concentration. This was one order of magnitude less than reported in the literature of 3 µM but was close enough to demonstrate that they are EL insensitive.[6,143] Although the line gifted as the EL hypersensitive H3255 was not responding as it should have been according to the literature of an IC_{50} of 12-89 nM EL, once identified as H1355 it was then in line with acceptable and published findings.[140,144]

The cells have been authenticated as contaminant free and genetic profiles were identified. These data were all evidence that the HCC827 and H1355 cell lines were responding as expected to EL and was verification that they could be used to examine the efficacy of EL conjugates against the free-EL with all the correct controls in place. Therefore, the study progressed to viability counts including the conjugate treatments.

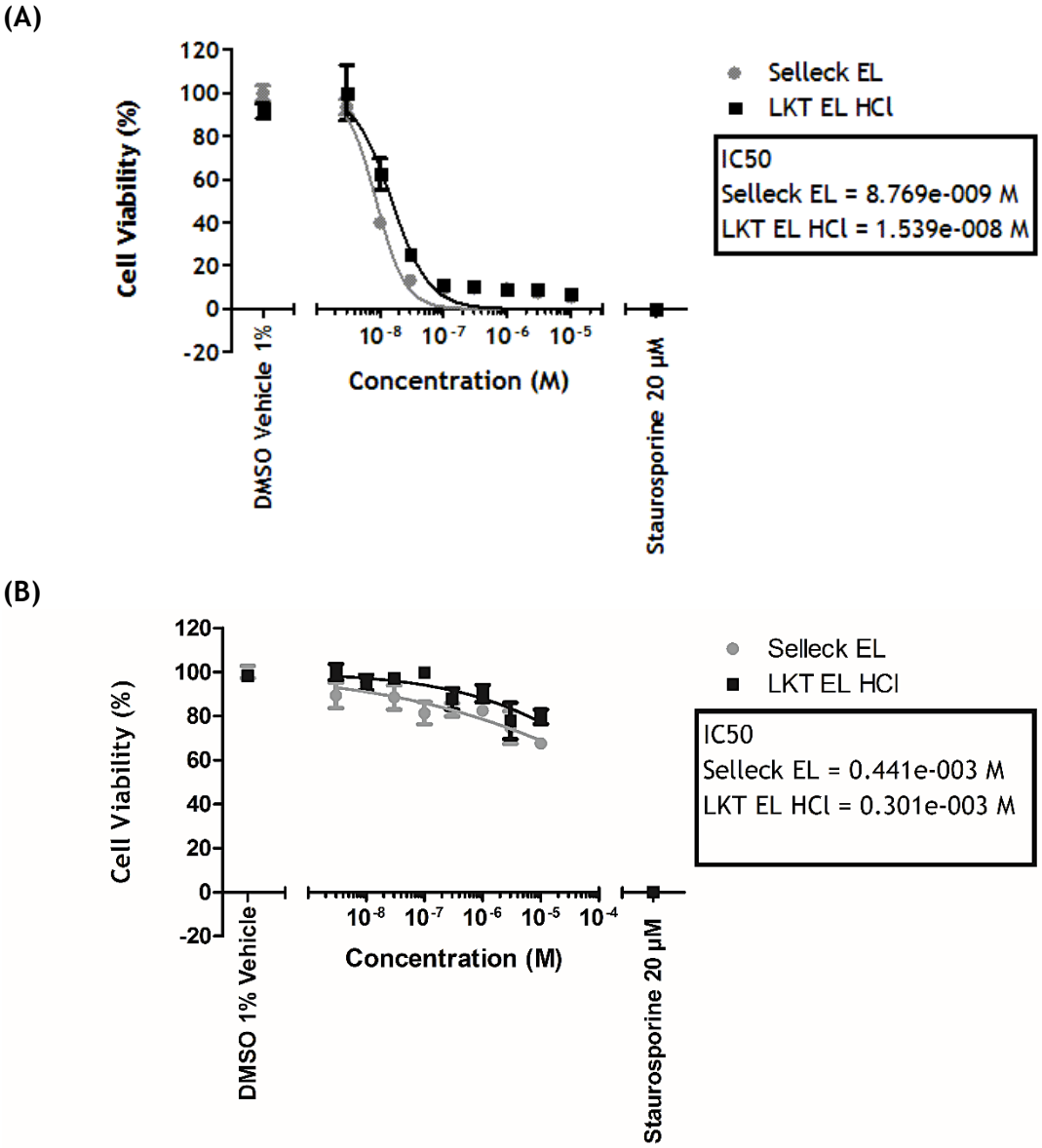

Figure 32 Cytotoxicity screen by Alamar Blue assay at 72 hours incubation with two sources of EL; Selleck for EL and LKT for EL hydrochloride from 3 nM to 10 µM. A) HCC827 lunge adenocarcinoma EL sensitive cells and B) H1355 lung adenocarcinoma EL insensitive cells.

4.5.2 Trypan Blue Viability Cell Counts

Trypan blue is a vital cell dye that is traditionally used to perform basic cell counts when maintaining and plating cells by counting with a haemocytometer chamber slide. The dark blue dye can penetrate the cell membrane of any non-viable cells that have not fully undergone cell death to the point of degradation. Therefore, the cells can be counted and blue dyed cells can be excluded from the total cell counts to provide a live cell number. This pilot study on the viability of the HCC827 cells was to test the suitability of the method to assess the viability of all treatments across both cell lines. Here the cells were plated as described in 2.3.4 and the statistics were carried as explained in the same methods section.

The cells were all counted in the 4 corner squares of the haemocytometer and this was repeated in triplicate wells per treatment. From this the blue stained dead cells were subtracted from the total cell number and then normalised to the DMSO vehicle control as 100% viable. These data were plotted in Figure 33 as a bar chart with averages and error bars that are ± the SD. All the controls (1% DMSO vehicle, AgHA NPs and AuCt NPs) have comparable viabilities within the range of 100% inclusive of SDs. The response to treatments with EL varies, with the free-EL being most effective but having the largest error bar as 1 replicate had 0 cells (22% ± 18%). 300 nM EL-AgHA NP conjugate killed the cells at a similar rate to the free-EL of 29% ± 12% viability. Finally, the 300 nM EL-AuCt NP conjugate had a viability that was equivalent to the controls of 95% ± 5%. This bar chart indicates that the cells were sensitive to treatment from free and AgHA-bound EL but not AuCt-bound EL. Furthermore, the cell line was unaffected at these concentrations of AgHA and AuCt bare control NPs. To delve deeper into the differences the statistical analyses are reviewed.

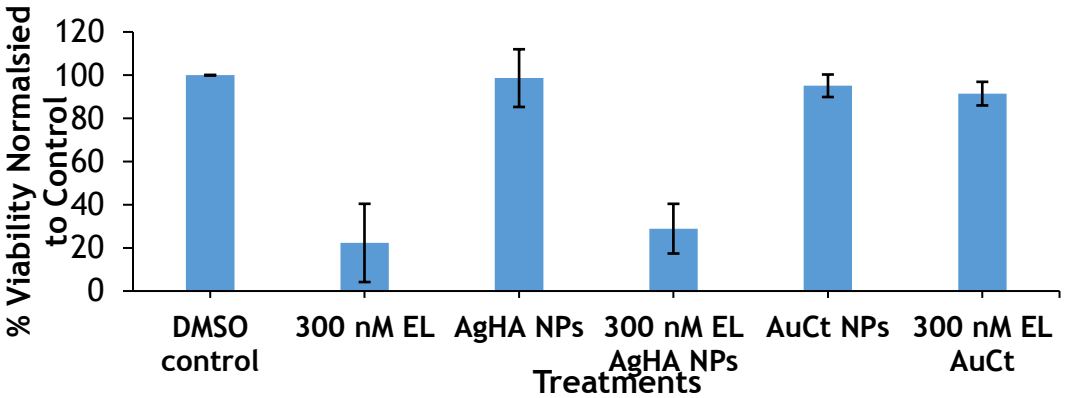

Figure 33 Trypan blue viability count of HCC827 lung adenocarcinoma cells treated by DMSO vehicle control, EL, conjugates (AgHA & AuCt) and NPs (AgHA & AuCt).

Statistical analyses were carried out in MiniTab v.18.1 to extract any significant differences between the samples. To analyse the variance between the samples, a one-way ANOVA was carried out at significance level of $p<0.05$, with the null hypothesis that all the sample means were equal. The resulting significance value was $p<0.001$, meaning that the null hypothesis was rejected and that there was a significant difference between the sample means.

In order to determine where the variance occurred between the samples a post-hoc Tukey's test was conducted. This allows multiple pair-wise comparisons to be made reducing the type I error in comparison to completing multiple paired t-tests that would have compounded the false positive error rates.

Tukey's simultaneous comparison of 95% confidence intervals (CIs) was used to compare the difference of the means between all the samples tested. In Figure 34 any CIs that span over zero are not significant. The further the interval was positioned from the zero line, the greater the significance. Therefore, the top 2 most significant differences of means were the control against 300 nM EL and 300nM EL-AgHA conjugate samples. These data reflect the difference observed in Figure 33 and are expanded upon in Table 5 and Table 6.

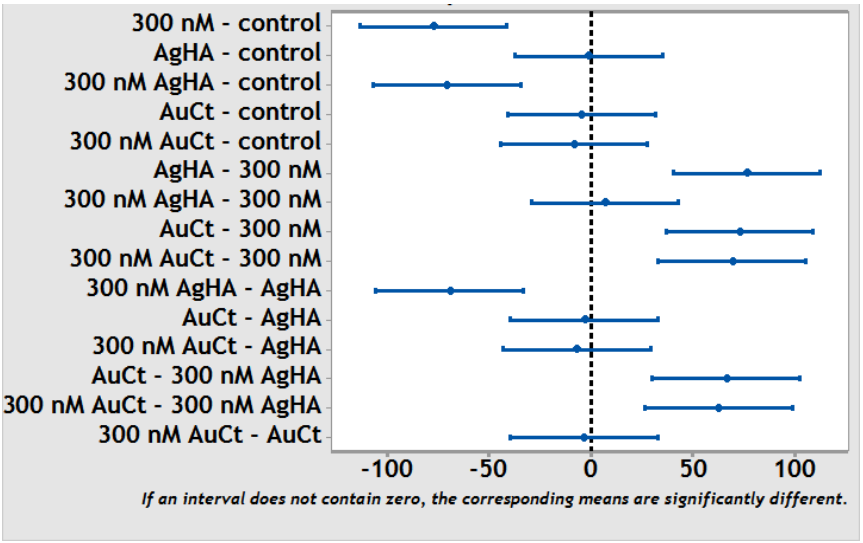

Figure 34 Tukey's 95% confidence intervals, difference of means of viability. Control (DMSO vehicle), AgHA NP, AuCt NP, AgHA conjugate, AuCt conjugate, 300 nM EL, 100 µM EL (death control) on HCC827 cells.

Table 5 demonstrates the results from Figure 34 more concisely by grouping the samples to highlight the most similar viability means. Here all of the controls (DMSO, AgHA and AuCt NPs) are grouped with AuCt conjugate as group A. This indicates that AuCt conjugate has little to no effect on the cells, much like the controls. Then AgHA conjugate and 300 nM EL were together as group B, the treatments which affected cell viability. The groupings made a distinction between those treatments

that had an observable difference on the cells *i.e.* the top 2 most significantly different samples and the rest which did not affect the cells. The mean values are listed in the grouping information Table 5 and the pooled SD was ± 13.2. The groupings data can be analysed further by assessing the P-values at the individual confidence level tabulated in Table 6.

Table 5 Grouping Information for Viability Using the Tukey Method and 95% Confidence Interval. Control (DMSO vehicle), AgHA NP, AuCt NP, AgHA conjugate, AuCt conjugate, 300 nM EL, 100 µM EL (death control). Group A differ significantly from group B.

Factor	N	Mean	Grouping*	
DMSO Control	3	100.00	A	
AgHA	3	98.61	A	
AuCt	3	95.08	A	
300 nM AuCt	3	91.42	A	
300 nM AgHA	3	28.89		B
300 nM	3	22.30		B
**Means that do not share a letter are significantly different.*				

Table 6 details the P-values for each pairwise comparison that was assessed during the Tukey's post-hoc analysis, the individual confidence level of each pairwise comparison was 99.43%. The table has been colour coded to show the significance levels of each comparison, where any significance was found: $p<0.001$ in red (0.1% false positive rate), $p<0.010$ in orange (1% false positive rate), and $p<0.050$ in green (5% false positive rate). The trend observed was that any comparisons involving 300 nM EL or the EL-AgHA conjugate produced a significant result, all being $p<0.001$. In fact, a majority were $p<0.0005$ which was a 0.05% false positive error rate and shows that the results were highly statistically significant.

Table 6 Tukey's simultaneous tests for difference of viability means, adjusted P-values. Control (DMSO vehicle), AgHA NP, AuCt NP, AgHA conjugate, AuCt conjugate, 300 nM EL.

	Control	300 nM EL	AgHA	AgHA Conj	AuCt	AuCt conj
Control						
300 nM EL	0.0001					
AgHA	1.0000	0.0002				
AgHA Conj	0.0003	0.9879	0.0003			
AuCt	0.9968	0.0002	0.9994	0.0006		
AuCt conj	0.9628	0.0004	0.9824	0.0009	0.9992	
P-value key			Individual Confidence Level = 99.43%			
p<0.001	p<0.010	p<0.050				

To conclude on the Trypan blue viability counts of HCC827 cells and the statistical analyses carried out, the only test treatment that did not have a significant effect on the cells was the AuCt conjugate. None of the controls had a significant effect on the cells which all measured around 100% viable (DMSO, AgHA NP and Auct NP). Both 300 nM EL-AgHA conjugate and free 300 nM EL were effective in killing and

preventing proliferation in the HCC827 cell line that was sensitive to EL. This means that 300 nM EL-AgHA conjugate and 300 nM EL were not only statistically significant, in their difference, but they were more importantly biologically significant in their anti-proliferative and killing effect on the cancer cells compared with the negative control. AuCt conjugate was neither statistically nor biologically significantly different to the control. This would suggest that the EL was either not bound to the AuCt at as high a concentration initially and therefore a lower dose was delivered to the cells, or that the EL had too high an affinity for the AuCt NP surface and was not released within the cell. If EL was not released from the NPs, to allow the active site to bind to the TKD of the EGFR, it would have no anti-proliferative action or effect on killing the cells.

Moving forward however, these data have no images to uphold the validity of the numbers, as they were manually counted with no further evidence to validated accuracy. Therefore, it was decided not to continue with this labour intensive method and to instead use the live/dead fluorescent cell imaging that could be quantified using ImageJ and images included as proof of where the numbers originate from.

4.5.3 Live/Dead Toxicity Assay

Invitrogen's LIVE/DEAD™ Viability/Cytotoxicity Kit was used to assess the viability of the cells. On an individual cell basis, there are no artefactual fluorescent effects seen upon imaging, unlike the whole population based cell viability micro well-plate fluorescent assays. Hence, the justification for using the LIVE/DEAD method on the cells containing NP and conjugate samples. Cells were plated as described in 2.3.6 where cells were incubated for 72 hours with a DMSO vehicle control, AgHA NPs, AuCt NPs, 300 nM EL-AgHA, 300 nM EL-AuCt, 300 nM EL or death control 100 μM EL. Cells were observed at timepoints of 4 hours, 24 hours, 48 hours and finally 72 hours. This image based assay was in the absence of an unbiased micro well-plate based assay, the 72 hour time point was selected as an end point for quantification, as EL is an anti-proliferative drug and it allowed several cell cycles to occur. Essentially, this lower throughput method was used as an alternative to Alamar blue that was used for the cell characterisations with the free-EL.

Figure 35 is a representative merged fluorescent image montage of all the treatments at 72 hours for HCC827, the EL sensitive cell line, green was calcein stained live cells and red are ethidium bromide stained dead cells, both merged with bright field for cell delineation. The images presented clearly show that all the AgHA NP (D) and AuCt NP (B) metal controls have a similar cell number to the DMSO

control (F), which had perhaps suffered slightly from the DMSO vehicle control incubation as there was more red (dead) staining. In other words, DMSO used to suspend the EL was more harmful than the presence of NPs. This was hard to judge by eye and would become clearer from quantification and perhaps the set of samples should be split further and have the metals as respective controls, as opposed to having the DMSO control as the 100% viability level for all samples. In future, a lower v/v percentage of DMSO could be used as the vehicle to deliver EL, however this needs investigated carefully for solubility reasons.

Comparisons drawn between the AgHA NP and AuCt NP metal controls and their respective EL treatments indicated that the AuCt conjugate (A) was less effectual than the AgHA conjugate (C). There was greater live staining and hence more cells present for the AuCt NP conjugate (A) than in the AgHA conjugate, which had few live cells and signs of many dying red stained cells (C). Both AgHA NPs and AuCt NPs have almost zero evidence of dying cells or impact on proliferation.

Finally, and most importantly, were the comparisons between the conjugate based delivery and free-EL's effect on the cells viability. It was clear that the free-EL had the greatest impact on cell number and health than either of the conjugates. Mentioned earlier in this discussion, it could be partly due to a greater level of DMSO than in the conjugate samples. This was because the conjugates were washed to remove any unbound EL and there was only trace amounts of DMSO in their samples. The EL was definitely responsible for the greatest portion of cell death as there was only one cell observed in all the 100 μM EL (G) samples amongst much cell debris in all the 27 fields of view imaged, which far exceeds the kill effect of the DMSO control.

To summarise: neither Au or Ag NPs affect cell health at the concentrations present in HCC827 cells, the AgHA conjugate exerted an anti-cancer cell effect that was greater than its control, the AuCt conjugate does not appear to be effective at all, the DMSO control had impaired cell health slightly but the 300 nM EL free-drug was the most effective treatment at destroying the cells and preventing new cell growth. 100 μM EL was an effective death control for the HCC827 EL sensitive cell line.

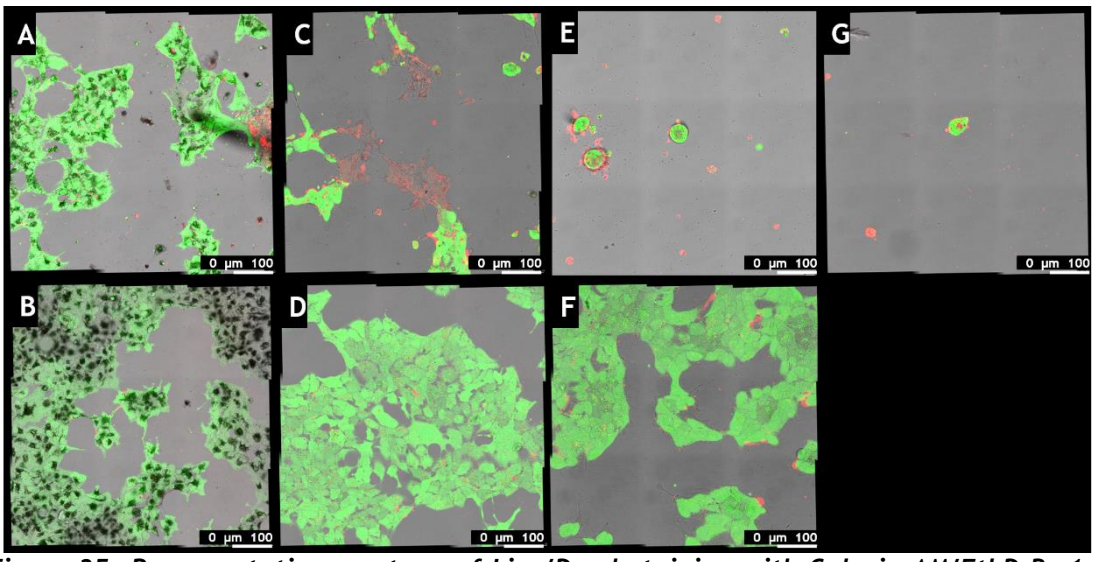

Figure 35 Representative montage of Live/Dead staining with Calcein AM/EthD Br-1 (Green/Red) of HCC827 cells treated for 72 hours with (A) 300 nM EL AuCt conjugates, (B) AuCt NPs, (C) 300 nM EL AgHA NPs, (D) AgHA NPs, (E) 300 nM EL, (F) DMSO control and (G) 100 µM EL death control. Scale bars 100 µm.

The live/dead fluorescent images were quantified by setting the scale in Fiji (Image J) and using the freehand tool to outline the stained areas and count the total surface area of live and dead cells per sample in 3 fields of view that were composed of 9 stitched image acquisitions. Ultimately a total of 27 fields of view were measured per sample.[101,114] Each set of counts were normalised to the respective DMSO control as 100% and plotted as a bar chart using Excel.

The results of quantification in Figure 36 reflect the conclusions made qualitiatively from the images. That the DMSO control was indeed lower than the counts for the AuCt NP and AgHA NP samples when the SD was taken into account. Despite claims that silver is toxic to cells in the literature, it was not the case in these cells at the concentration of AgHA NPs used.[135,145] The most obvious trend was that 300 nM EL, 100 µM EL and EL-AgHA conjugates all had an effect on the cells compared to the respective controls and the only EL related treatment which did not display this result was the EL-AuCt conjugate. The AuCt NPs and AuCt conjugate had comparable levels of cell viability, however, the error bars were large and this was due to one sample in each being different to the remaining 2 which were similar. Repeating the test with more biological replicates would avoid the problem of large error bars.

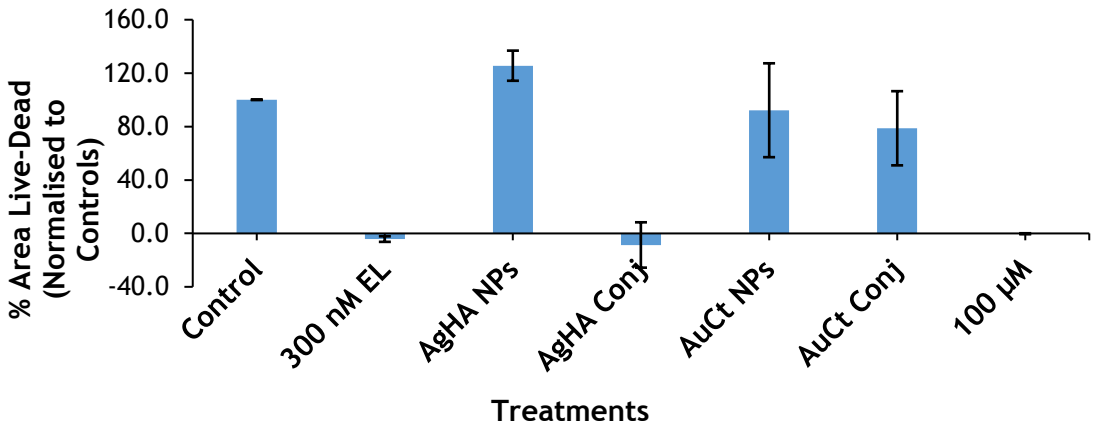

Figure 36 Quantification of the area of live-dead cells of HCC827 lung adenocarcinoma cells treated by DMSO vehicle control, EL, conjugates (AgHA & AuCt) and NPs (AgHA & AuCt).

Statistical analyses were performed as outlined in 2.3.4 and further explained in the last section of the Trypan blue counts.

The one-way ANOVA set a null hypothesis of no difference of the means of viability. This was rejected as $p<0.05$ indicating a significance was found and a Tukey's post-hoc analysis was conducted as per 2.3.4.

Tukey's simultaneous comparison of 95% confidence intervals (CIs) was used to compare the difference of the means between all the samples tested. Any CIs that span over zero are not significant. The significance of a sample was greater the further the interval was positioned from the zero line. Therefore, the top 3 most significant differences of means were AgHA NPs with 300 nM EL, 300 nM EL-AgHA conjugate and 100 µM EL. These data reflect the difference observed in the images in Figure 35 and the quantifications in Figure 36. These differences are expanded upon in Table 7 and Table 8.

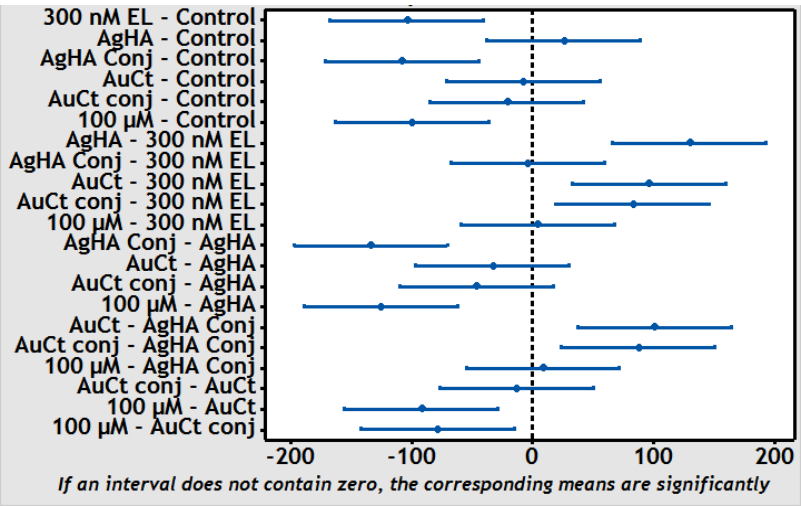

Figure 37 Tukey's 95% confidence intervals, difference of means. Control (DMSO vehicle), AgHA, AuCt NP, AgHA NP conjugate, AuCt conjugate, 300 nM EL, 100 µM EL (death control) on HCC827 cells.

Table 7 demonstrates the results from Figure 37 more concisely by grouping the samples to highlight the most similar samples. Here, all of the controls were grouped with 300 nM EL-AuCt conjugate as group A. Then 300 nM EL-AgHA conjugate, 300 nM EL and 100 µM EL were grouped together as group B. This made a distinction between those treatments that had an observable difference on the cells *i.e.* the top 3 most significantly different samples and the rest which did not affect the cells. The mean values were listed in the grouping information table and the pooled SD was ± 22.8. The groupings data was analysed further by assessing the P-values at the individual confidence levels tabulated in Table 8.

Table 7 Grouping Information Using the Tukey Method and 95% Confidence Interval on HCC827 cells. Control (DMSO vehicle), AgHA NP, AuCt NP, AgHA conjugate, AuCt conjugate, 300 nM EL, 100 µM EL (death control). Group A differ significantly from group B.

Factor	N	Mean	Grouping *	
AgHA	3	125.57	A	
Control	3	100.00	A	
AuCt	3	92.20	A	
AuCt conj	3	78.70	A	
100 µM	3	-0.25		B
300 nM EL	3	-4.25		B
AgHA Conj	3	-8.70		B

Means that do not share a letter are significantly different.

Table 8 details the P-values for each pairwise comparison that was assessed during the Tukey's post-hoc analysis, the individual confidence level of each pairwise comparison was 99.58%. The table was colour coded to show the significance levels of each comparison, where any significance was found: $p<0.001$ in red (0.1% false positive rate), $p<0.010$ in orange (1% false positive rate), and $p<0.050$ in green (5% false positive rate). The trend observed was that any comparisons involving 300 nM EL, AgHA conjugates or 100 µM EL produced a significant result, with a majority of these being $p<0.001$, several being $p<0.010$ and one being $p<0.050$.

Table 8 Tukey's simultaneous tests for difference of means, adjusted P-values for HCC827 cells. Control (DMSO vehicle), AgHA NP, AuCt NP, AgHA conjugate, AuCt conjugate, 300 nM EL, 100 µM EL (death control).

	Control	300 nM EL	AgHA	AgHA Conj	AuCt	AuCt conj
Control						
300 nM EL	0.0010					
AgHA	0.8060	0.0001				
AgHA Conj	0.0007	1.0000	0.0001			
AuCt	0.9990	0.0020	0.5730	0.0010		
AuCt conj	0.9040	0.0080	0.2250	0.0050	0.9890	
100 µM	0.0010	1.0000	0.0002	0.9990	0.0030	0.0110
P-value key			Individual Confidence Level = 99.58%			
p<0.001	p<0.010	p<0.050				

To conclude on the live dead staining of HCC827 cells and the statistical analyses carried out, the only test treatment that did not have a significant effect on the cells was the AuCt conjugate. Both AgHA conjugate and free 300 nM EL were effective in killing and preventing proliferation in the HCC827 cell line that was sensitive to EL. This means that AgHA conjugate and 300 nM EL are not only statistically significant but they are biologically significant in their anti-proliferative and killing effect on the cancer cells compared with the negative control. AuCt conjugate is neither statistically nor biologically significant to the control. This would suggest that the EL was either not bound to the AuCt NPs at as high a concentration initially and therefore a lower dose was delivered to the cells, or that the EL had too high an affinity for the AuCt NP surface and is not released within the cell. If EL was not released from the NPs to allow the active site to bind to the TKD of the EGFR, it had no anti-proliferative action or effect on killing the cells. The live/dead cell data concurs with the basic Trypan blue viability counts. Therefore, the live/dead assay was deemed reliable and was also used to investigate the treatments on the EL insensitive cell line H1355.

The method used for the HCC827 cells to carry out the live/dead assay in this section was replicated for the H1355 EL insensitive cells.

Figure 38 is a representative merged fluorescent image montage of all the treatments at 72 hours for H1355, green was calcein stained live cells and red were ethidium bromide stained dead cells, both merged with bright field for cell delineation.

The images presented in Figure 38 had less cells overall than the HCC827 experiment and this was likely due to the fact that the cell doubling time is slightly longer and over 72 hours this had resulted in less cells in all the samples. Given the lower levels of constitutively active EGFR (which promotes proliferation) in H1355 compared to HCC827, as seen in Figure 29 this is not an unexpected result. From the images, there were 4 samples that looked similar and viable from the green staining, these were: A) 300 nM EL-AuCt conjugate, B) AuCt NPs, E) 300 nM EL, and F) DMSO vehicle control. The samples which had suffered from cell death illustrated by few cells and red dead cell staining were: C) 300 nM EL-AgHA conjugate, D) AgHA NPs, and G) 100 µM EL death control. The silver samples had few cells remaining whether it be the EL-conjugate or bare NPs, this indicated a sensitivity to the NPs themselves at this concentration, as opposed to the drug. The H1355 cells were clearly less tolerant of the NPs than the HCC827 cells were, however since a majority of the study had already been conducted with the NPs at this concentration, these were used for the

remainder of the study. This was because one of the most important aims was to investigate the effects of nanodelivery on the sensitive cell line *EGFRm+* and that H1355 cells were simply acting as an *EGFRwt* control. Sample G) the 100 µM EL death control, had not responded as completely to the treatment as in the HCC827 cell line. However, there were 2 reasons for this: firstly the cells were less sensitive to EL and secondly that the drug appeared to form some small crystals in this sample. In hindsight, a standardised death control should have been used on both cell lines, such as, a large concentration of staurosporine, had it been available at that point.

Comparisons cannot be made between the 300 nM EL-AgHA conjugate and the 300 nM EL-AuCt conjugate as the silver killed the cells on its own as bare NPs, therefore, any effect from the EL-AgHA conjugate was not due to the effects of EL. The cells responded to extremely high levels of EL but this would appear to be equal to the effect of silver. The 300 nM EL does not seem to affect the cells much more than the DMSO control. The EL-AuCt conjugate was maybe slightly better at killing the cells than the bare AuCt NPs but this would require further analysis. Therefore, the areas of live-dead cells were normalised to the control and charted for a more quantitative representation of the data.

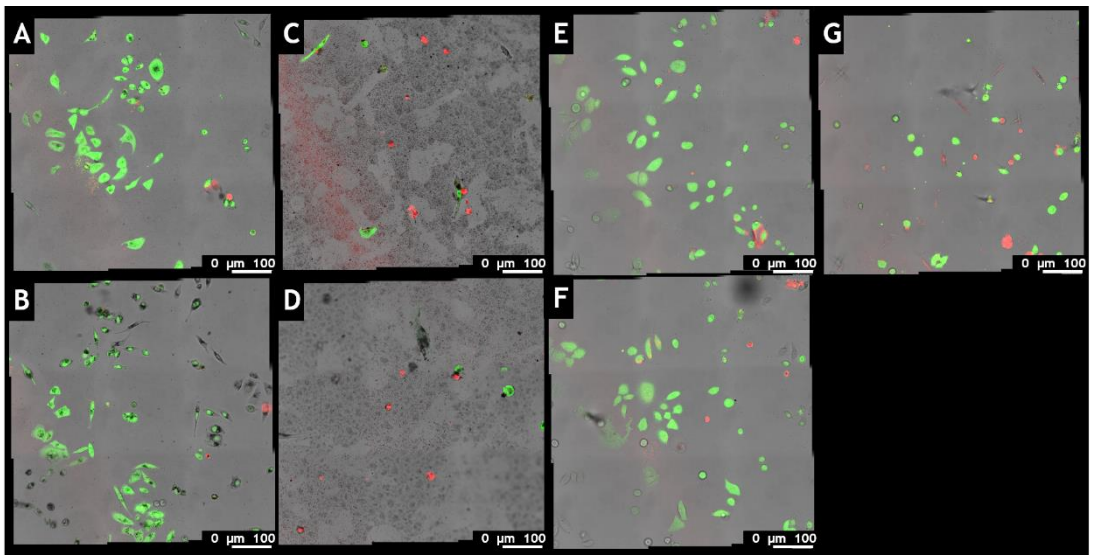

Figure 38 Representative montage of Live/Dead staining with Calcein AM/EthD Br-1 (Green/Red) of H1355 cells treated for 72 hours with (A) 300 nM EL AuCt conjugates, (B) AuCt NPs, (C) 300 nM EL AgHA NPs, (D) AgHA NPs, (E) 300 nM EL, (F) DMSO control and (G) 100 µM EL death control. Scale bars 100 µm.

The results of the areas measured for live-dead cells is charted in Figure 39. Here, more quantitative details were revealed than in the qualitative images of Figure 38. The bar chart shows that: 300 nM EL sample had a slightly lower viability than the DMSO control, both the silver samples were clearly affecting viability, 300 nM EL-

AuCt conjugate had a similar effect on the cells as the 300 nM EL free-drug treatment, and the death control showed similar levels of cell death as the silver treatments.

To treat the data the same as the HCC827 cells, statistical analysis was carried out.

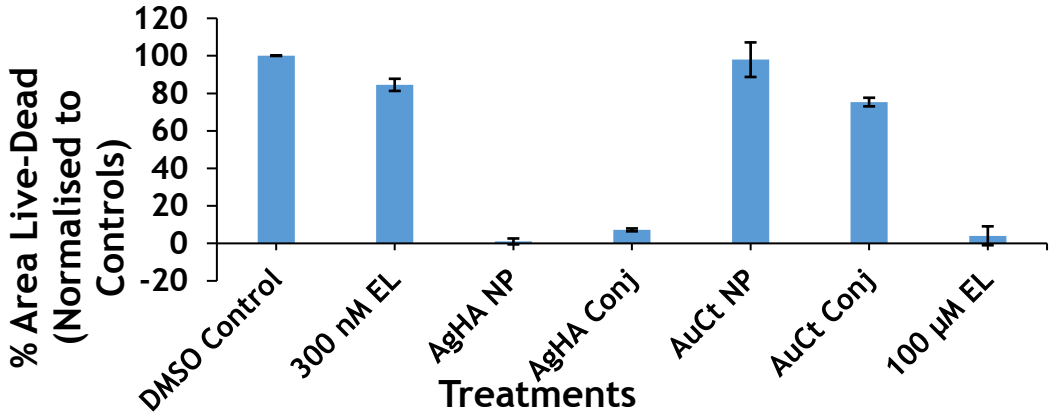

Figure 39 Quantification of the area of live-dead cells of H1355 lung adenocarcinoma cells treated by DMSO vehicle control, EL, conjugates (AgHA & AuCt) and NPs (AgHA & AuCt).

Statistical analyses were performed as outlined in 2.3.4 and further explained in the last section of Trypan blue counts.

The one-way ANOVA was set with a null hypothesis of no difference of the means of viability. This was rejected as $p<0.05$ therefore significance was found and a Tukey's post-hoc analysis was conducted as per 2.3.4.

Tukey's simultaneous comparison of 95% confidence intervals (CIs) was used to compare the difference of the means between all the samples tested. Any CIs that span over zero are not significant. The significance of a sample was greater the further the interval was positioned from the zero line. There was a definite trend from Figure 40, whereby any sample pairwise comparisons including AgHA NP, EL-AgHA conjugate or 100 µM EL were observed around the 100th percentile of the 95% CIs. The samples comparing any of DMSO control, AuCt NP, 300 nM EL or EL-AuCt conjugate were either spanning the zero line as not significant or adjacent to the zero percentile line. Consequently, DMSO, AuCt NP, 3000 nM EL or EL-AuCt conjugate were not as highly significant as AgHA NP, AgHA conjugate or 100 µM EL against the other treatments. To resolve this further, the significant differences were compared in a groupings information Table 9.

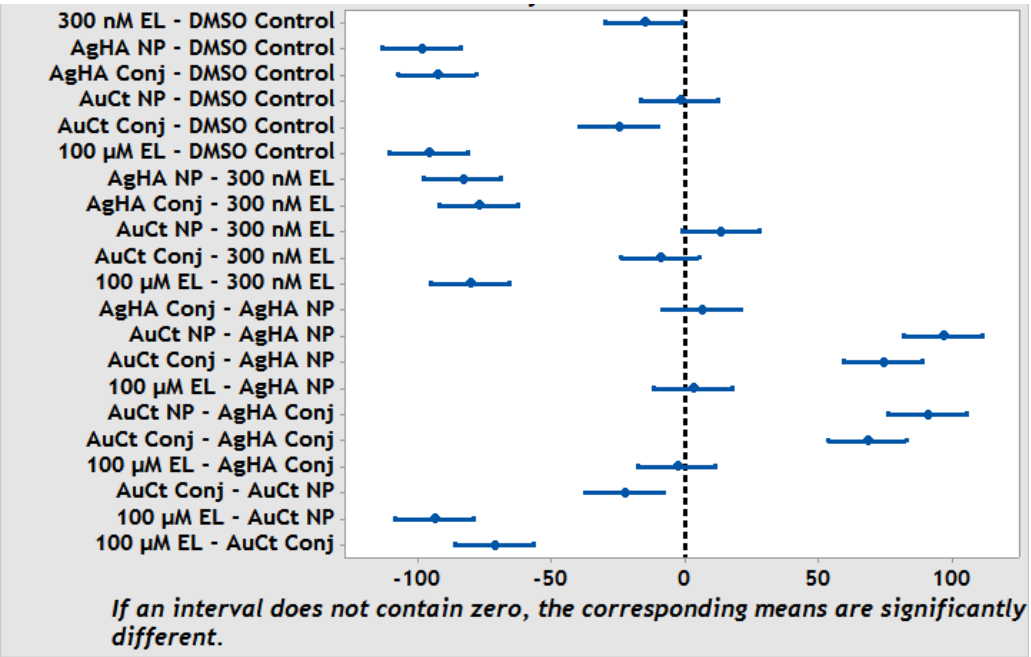

Figure 40 Tukey's 95% confidence intervals, difference of means. Control (DMSO vehicle), AgHA NP, AuCt NP, AgHA conjugate, AuCt conjugate, 300 nM EL, 100 µM EL (death control) on H1355 cells.

Table 9 showed the means and the groupings information from the Tukey's pairwise comparisons, the pooled SD was ± 5.27. The groupings data was more complex than for the HCC827 cell line, presumably due to the EL insensitivity and silver sensitivity. Group A contained DMSO control and AuCt NP control, which left the cells viable. Group B matched AuCt NPs and 300 nM EL, the reason for this grouping was not so clear and perhaps would not exist if more replicates were assessed. Group C contained 300 nM EL and the EL-AuCt conjugate, which both affected the cells viability slightly, 84.52% and 75.35% respectively. Group D contained all the treatments which effectively killed the cells, these were AgHA NPs, EL-AgHA conjugate and 100 µM EL. To further explore the statistical analysis, the individual P-values were tabulated and are seen in Table 10.

Table 9 Grouping Information Using the Tukey Method and 95% Confidence Interval on H1355 cells. Control (DMSO vehicle), AgHA NP, AuCt NP, AgHA conjugate, AuCt conjugate, 300 nM EL, 100 µM EL (death control).

Factor	N	Mean	Grouping*			
DMSO Control	3	100	A			
AuCt NP	3	97.94	A	B		
300 nM EL	3	84.52		B	C	
AuCt Conj	3	75.35			C	
AgHA Conj	3	7.199				D
100 µM EL	3	4.05				D
AgHA NP	3	1.04				D

* Means that do not share a letter are significantly different.

Table 10 lists the P-values for each pairwise comparisons from the Tukey's post-hoc analysis, the individual confidence level was 99.58%. The table was colour coded to show the significance levels of each comparison, where any significance was found: $p<0.001$ in red (0.1% false positive rate), $p<0.010$ in orange (1% false positive rate), and $p<0.050$ in green (5% false positive rate). The trend observed was that any comparisons involving AgHA NPs, EL-AgHA conjugate or 100 µM EL produced a significant result with a $p<0.001$. Moreover, the significance level of most were extremely significant at $p<0.00002$. The statistics indicated that the only non-significant comparison to DMSO control was AuCt NPs. Additionally, 300 nM EL and EL-AuCt conjugate had some effect of partial killing on the cells, granted there was a significant difference within the 300 nM EL and EL-AuCt conjugate pairing too. This significant difference suggested that one had a better efficacy, from Figure 38 it appeared to be the EL-AuCt conjugate that was more effective. Care was taken to draw the correct comparisons and the relevant controls were considered. For DMSO control *versus* 300 nM EL there was a $p<0.03592$ and for AuCt NP *versus* AuCt conjugate there was a $p<0.00183$, this suggested that EL-AuCt conjugate was more effective than free-EL in H1355 cells. However, caution should be exercised, as this experiment was only 1 biological replicate and it has already been stated that it would benefit from being seeded at a greater density of cells on day 0.

In future, a greater cell number should be used for the H1355 cells to give a more accurate representation of the effects on the cells from the treatments. In summary, the H1355 cells were sensitive to the concentration of silver NPs used in this experiment, the 300 nM EL. The 300 nM EL-AuCt conjugate had a statistically significant effect on the viability of cells compared to the other treatments, although a majority of cells were still viable. TheThe greatest cell death was observed in 100 µM EL, AgHA NPs and AgHA conjugate.

Table 10 Tukey's simultaneous tests for difference of means, adjusted P-values for H1355 cells. Control (DMSO vehicle), AgHA NP, AuCt NP, AgHA conjugate, AuCt conjugate, 300 nM EL, 100 µM EL (death control).

	Control	300 nM EL	AgHA	AgHA Conj	AuCt	AuCt conj
Control						
300 nM EL	0.03592					
AgHA	0.00002	0.00002				
AgHA Conj	0.00002	0.00002	0.77674			
AuCt	0.99875	0.08398	0.00002	0.00002		
AuCt conj	0.00080	0.38605	0.00002	0.00002	0.00183	
100 µM EL	0.00002	0.00002	0.99045	0.98782	0.00002	0.00002
P-value key			Individual Confidence Level = 99.58%			
p<0.001	p<0.010	p<0.050				

4.6 Summary

In conclusion to chapter 4: the cell viability tests, pEGFR distribution in IFAs and p/tEGFR quantities from Western blot, all correlated to reflect the same result in terms of efficacies of the cell treatments. The cells were shown to be infection free and their identity was authenticated, both cell lines possess constitutively active EGFR. Afterwards, this chapter gave an insight into the cytotoxicity and efficacy of the conjugates, EL and bare NPs on the two cell lines. The AuCt conjugates were ineffectual, whereas the AgHA conjugates had an impact on phosphorylation status and cell viability that was similar to free-EL. Statistical analysis robustly supported that AgHA conjugates and free-EL were significantly better at killing cells and preventing proliferation than the AuCt conjugates in the HCC827 cell line but not in the H1355 cell line.

Additionally, it was discovered that at the concentrations of NPs used that the cell lines responded differentially. HCC827 was unaffected by NPs alone but H1355 viability was severely affected by AgHA NPs. The 300 nM EL-AuCt conjugate and 300 nM EL were shown to affect the viability of the H1355 cells, however insufficient seeding density of the cells mean that caution should be used before reporting this further.

It was established that the sensitive model cells responded to free-EL and EL-AgHA conjugate treatments (addressing the efficacy aim), the scene was set to carry out uptake and imaging studies to address the SERS imaging aim. To characterise spatio-temporal distribution of EL intracellularly and to determine whether EL-NP conjugates can improve the efficacy compared to free-EL.

Chapter 5 3D SERS Characterisation & Correlative Uptake Studies

---

"Ask the right questions, and nature will the open the doors to her secrets."
Sir C.V. Raman, Nobel Prize in Physics 1930, 1888-1970

5.1.1 Introduction

Nanomedicine is a burgeoning field aiming to increase drug efficacy, by perturbing diseased cells in a more targeted manner with existing drugs. This is achieved by delivering a greater drug load on the NPs large surface area to the less structured 'leaky' cancer cells for example. Subsequently the systemic drug levels are lower, leading to less side-effects for the patient. However, it is difficult to determine release of drug molecules *in situ*, or visualise this in real time, non-destructively.

Pre-clinical drug development studies could benefit from combining the visualisation of the drug intracellularly, with observing the release of the treatment from the NP delivery vehicle. Therefore, a live cell, higher throughput system would be advantageous.

Overall this chapter aimed to understand the distribution of unlabelled EL conjugates, within the cell by Raman interrogation, to be confirmed by multiple correlative techniques. The drug release was investigated spectroscopically over time, *in vitro,* in both fixed and live cells.

To address the aim of characterising the spatio-temporal distribution of EL in cells, 3D confocal SERS microscopy was used to achieve this goal of mapping the conjugate's intracellular localisation. The uptake was also confirmed by SEM, TEM and ICP-MS. The EL loading was investigated by LC-MS and release was explored by pH studies, IFAs for lysosomes and DF microscopy for NPs.

5.2 Imaging SERS Uptake Study *In Vitro* Fixed Cells

The aim of this section was to image cells in 3D to ascertain the intracellular distribution of EL conjugates. In order to do so, the limit of diffraction and spatial resolution needed to be calculated, to understand the capabilities of the Raman microspectrometer instrumentation. The lateral (x,y) dimensions and axial (z) dimension have different spatial limits due to the diffraction barrier. This determines the ability to delineate an object side by side (lateral) and within a depth profile (axial). These were calculated from the Abbe's diffraction limit Equation 2 and Equation 3, where δlat is lateral resolution, δlat is axial resolution, numerical aperture is (NA), λ is the wavelength of excitation source and *n* is the refractive index of the media used for immersion, in this case water at 1.33.[146] These were calculated for the Nikon 60x/1.0W DIC N2 NIR Apo water immersion objective used during these confocal studies with 633 nm laser excitation to be 393 nm and 1684 nm for lateral and axial resolutions respectively. These are of course theoretical values and in practice the limits are actually larger. There was no benefit to going lower than step sizes of 0.5 µm laterally or 2 µm axially, as it would then have been oversampling and inefficient use of the instrument time-wise.

$$Abbe'sresolution\ (x,y)\ \delta lat = \lambda/2NA$$

Equation 2 Lateral resolution

$$Abbe'sresoltuion\ (z)\ \delta axial = 2\lambda n/(NA)2$$

Equation 3 Axial resolution

Test studies were carried out initially, to assess these boundaries and compare regular mode with confocal mode whilst using the pinhole in to be truly confocal. There was a weaker signal with confocal mode and the pin hole in, and it also created a map of signal that was contained within a sensible cell size limit *i.e.* < 20 µm. Whilst using the regular mode, the depth of signal would carry over to be many tens of microns deep, which was artefactual, as cells are generally no more than 20 µm. When adhered to a substrate, such as a coverslip they were in fact more compact in the axial dimension, usually around 10-15 µm of depth. Finally, in the confocal mode with the pinhole in using water to immerse the fixed cells and objective, the step sizes selected were 1 µm laterally and 3 µm axially as optimal parameters.

The conjugates were functionalised for the cell incubations as described in 2.1.2, and the SERS signal of the conjugates were always assessed before introducing to the cells as mentioned in 2.5.1. The cells were prepared for the SERS mapping experiments as per method section 2.3.2 and Raman maps were acquired as detailed

in 2.5.2. The cells were incubated with the AgHA and AuCt conjugates and control NPs for 0.5, 2, 4 and 24 hours to assess the uptake and EL release.

Briefly, the maps were acquired at 0.3 s at 10% power with a 633 nm excitation source. This was to balance signal intensity, against both the timely acquisition of images and ablation of cells containing particles resulting from the photothermal effects. Each map was created around an individual cell with a 1 µm lateral resolution and the depth profile was 15 µm composed of 5 Z-slices. The bright field image was in the centre with 2 Z-slices Raman mapped above and below that focal plane in 3 µm increments. The water helped to dissipate the laser power and prevent burning that was experienced through an air objective. The water immersion objective had a higher NA and hence a better resolved imaging potential too. Despite focussing initially on AgHA and traditionally 532 nm interrogation source being used to match the SPR band for the optimum SERS signal, the laser line selected here was the 633 nm wavelength. This was because the lower energy, longer wavelength prevented the issue of cell burning, plus it was better for the AuCt sample comparisons.

The Raman vibrations of interest were: the alkyne stretch of bound EL on the conjugate at ~ 1985 cm^{-1}, when EL was released but close enough to the NPs surface 2100 cm^{-1} was detected indicating free-EL, and finally, the context of the cell from the multiple CH, CH_2 and CH_3 stretches of lipids ~2850 cm^{-1}, DNA and proteins ~2950 cm^{-1} ranging from 2800 – 3000 cm^{-1}.[22,60,146]

5.2.1 Exploratory SERS Maps in H1355 Canecerous Lung Cells EL-Insensitive

SERS maps were initially collected in the H1355 cell line with 300 nM EL-AgHA conjugates that were incubated for 4 hours and fixed. The spectra were basline corrected, cosmic rays were removed and then exported to Matlab for processing. Matlab was used to extract each Z-slice of data and create 2D images of pseudo coloured maps. The maps display the SERS signal intensity of the peak area of bound-EL, or more specifically, the bound-alkyne moiety's vibration of 1940-2040 cm^{-1} Raman shift.

Figure 41 A) indicates one of the Z-slices processed in Matlab for bound-EL signal with yellow being most intense signal. To put this into context B) shows the bright field image of the cell under interrogation and in red is the area that was Raman mapped. Figure 41 C) is an overlay of the SERS pseudo coloured map onto the area of the cell mapped. The red circles demarcate the the point spectra selected to demonstrate that no singal comes from outside the cell (blue) and the bound EL

signal inside the cell (orange). Figure 41 D) shows the spectra selected in the map of C), it is clearly seen that the signal of the bound-EL of ~1985 cm^{-1} is from within the cell. Furthermore, other example cell spectra demonstrate a Raman shift that matches the vibrations of free-EL. In some cases both bound and free-EL can be seen simultaneously and is presumably due to capturing the dynamic process of release from a cluster of conjugates. Results of other cells are shown in Figure 41 E) displays the SERS signal from the colloidal conjugate (blue) against an example cell spectrum (orange) displaying both the bound and free-EL alkyne vibrations. A further, clearer example is shown in F). Observing free-EL could be explained by either a high concentration of free-EL in a small membrane bound organelle, or the EL being released from the NP but still residing within 10 nm of the surface to allow electromagnetic enhancement. This would be difficult to determine, since free-EL in the cell cannot be seen until concentrations reach 100 μM as published by El-Mashtoly *et al.*.[59] The signal in that publication is difficult to see above the noise. Therefore, the highly localised concentration of EL in the cells of this study, could be induced by the delivery mode on NP and that is why it would be difficult to determine the origin of this signal, as a free-EL control would not be useful.

To address the aim of imaging by SERS in 3D, a visual was created within the Renishaw InVia Raman microspectrometer's Wire 4.2 software. This was again using the 1940-2040 cm^{-1} peak area above the baseline for the signal intensity. Figure 41 G) is the 3D pseudo-coloured map produced within Wire 4.2. The 3D volume is shown overlaid above the bright field image and the cube delineates the boundaries of the area mapped. It is observed from the figure that there is signal from within the cell and that this signal does not enter the nucleus, it displays a perinuclear or cytoplasmic distribution.

To confirm that the signal was from within the cell another SERS map was used to create a waterfall plot of the average signal per Z-slice, through the axial depth of the cell in Figure 42. The waterfall plot details that there is more signal within the cell than on the top and bottom layers.

In summary, this experiment demonstrates that a SERS signal was detected from the AgHA conjugate, within the H1355 cells after a 4 hour incubation. The signal exists within the cytoplasm of the cell. The EL signal was observed not only when it was attached to the NP but there was also evidence of free-EL from the alkyne vibration at ~2111 cm^{-1}. The origin of the free-EL signal is difficult to establish given that it may be due to a highly localised concentration from the conjugated EL

delivery method.These data provided enough evidence that a time series would be useful to monitor the conjugate uptake and distribution within the cell.

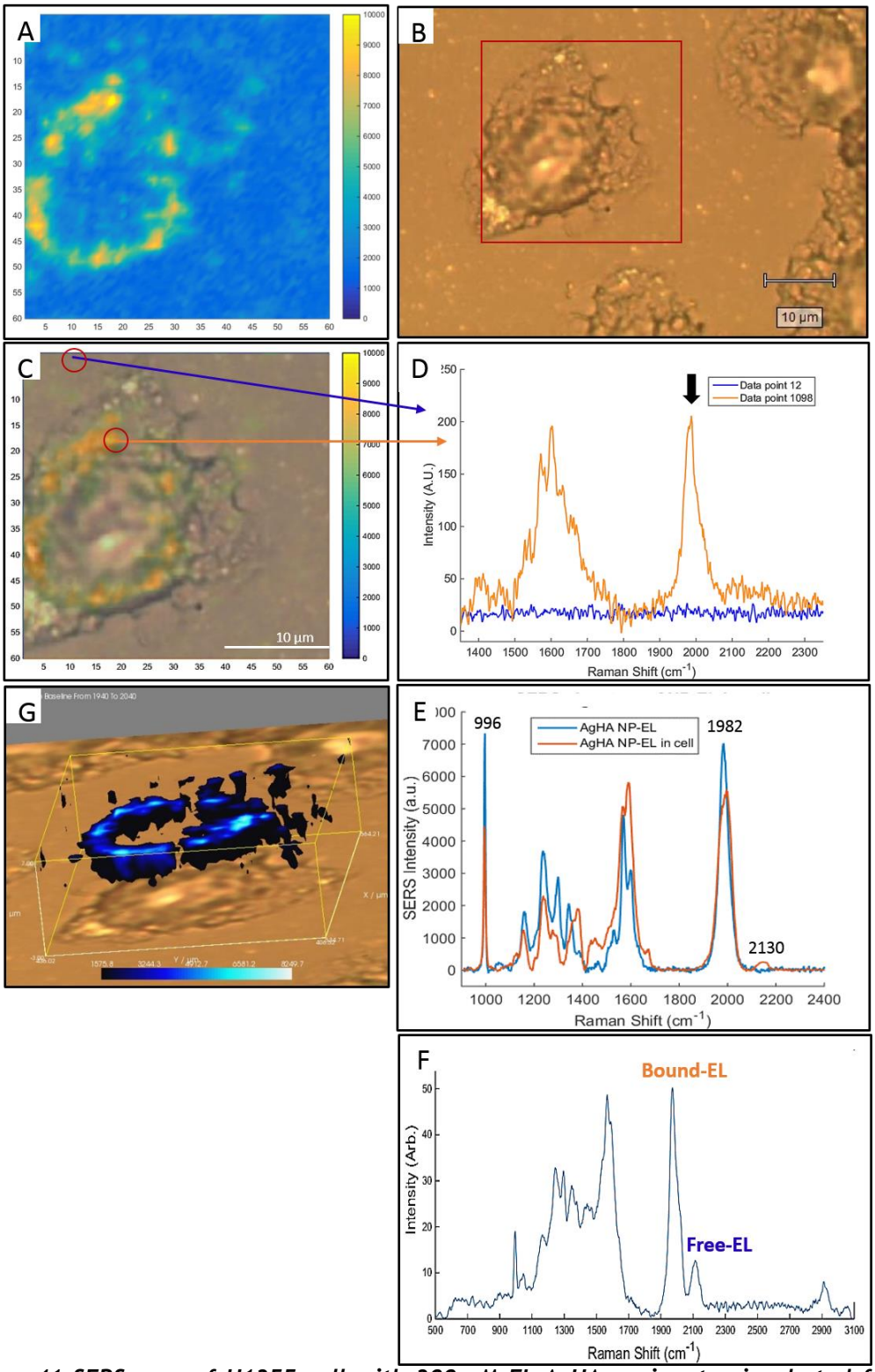

Figure 41 SERS map of H1355 cell with 300 nM EL-AgHA conjugates incubated for 4 hours. A) 2D pseudo coloured map (X,Y scales are µm) created in Matlab over peak area 1940-2040 cm^{-1}, B) bright field image of the cell (Scale bar 10 µm.), C) overlaid pseudo-coloured map and bright field image, D) SERS spectra of signal on conjugates in the cell in orange and outside the cell in blue, E) colloidal SERS signal of conjugate blue and cell SERS signal of conjugate orange, F) cell spectrum with both bound and free alkyne vibrations, G) 3D pseudo-coloured SERS map from Wire 4.2 software of Renishaw InVia microspectrometer.

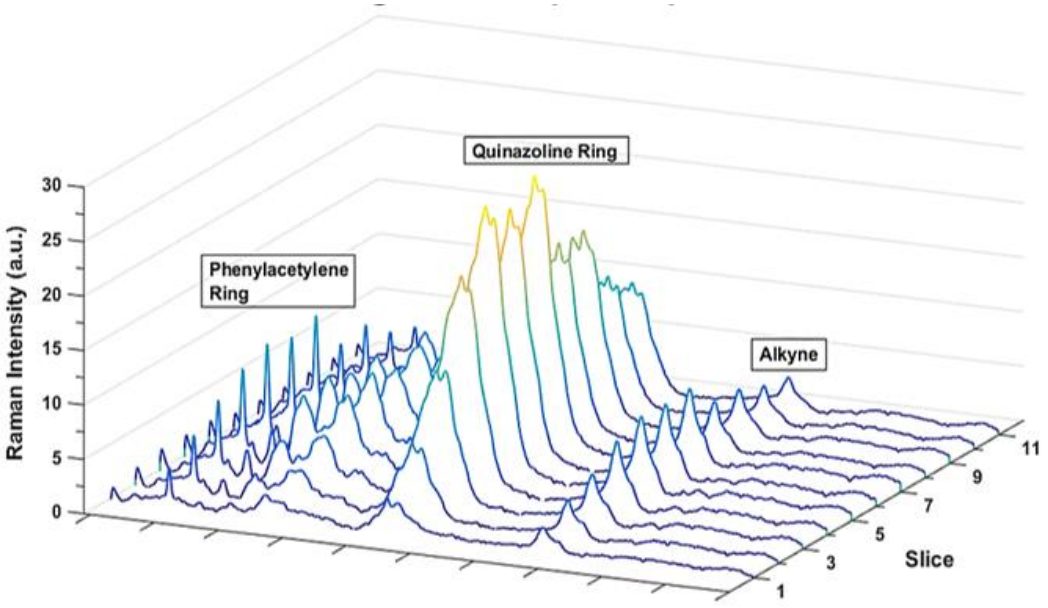

Figure 42 Waterfall plot of averaged SERS signal per Z-slice of map at 2 µm intervals in the axial dimension, overall 22 µm depth.

5.2.2 SERS Mapping of Conjugate Spatio-Temporal Uptake Study

The spatio-temporal uptake of the conjugates were assessed in both H1355 and HCC827 cell lines, with both bare NP and conjugates for AgHA and AuCt particles, the incubation periods selected were 0.5, 2.0, 4.0 and 24.0 hours. Under scrutiny, was the volume of the cell occupied by the signal from the bound-EL, free-EL, and to provide cell context, the CH_2 signal that is present in DNA, lipids and proteins. The process of the EL release from the conjugates was examined by observing the area of the cell occupied by bound and free-EL signals. An overview of the SERS data handling pipeline is detailed within the flow chart of Figure 43. The workflow is described here in sequence, with figures cross-referenced that illustrate the output from Matlab or Wire to provide visuals at each stage.

The need to ascertain the quality of the SERS signal in the 3D maps and review the vibrational species present was dealt with in the flow 1 in red (Figure 43). The Raman peaks were analysed within Matlab after exporting image files and the spectra were acquired from the Wire 4.2 software of the Renishaw InVia Raman microscopectrometer. Before exporting, the spectra had cosmic rays removed and baseline correction was applied. The spectra were averaged per Z-slice within Matlab, to demonstrate the cofocality achieved per cell and that the signal was within the cell body and not on the surface, Figure 44.

Flow 2 in orange (Figure 43) was then followed to understand the qualitative signal and determine the localisation and uptake over time in 2D and 3D visualisations. To gain the signal to baseline per peak area, the Wire software was used to provide a graphical overview image in Figure 45, which aided in signal thresholding in flow 3.

Flow 3 in green (Figure 43) demonstrates the quantitative calculation made on the EL-conjugate uptake over time. A Matlab coding script was created by Dr. Lauren Jamieson to meet the requirements of the author. To determine the proportion of the cell that the bound-EL, free-EL and CH_2 cell context Raman vibrations occupied. The first basic output of this script is displayed in Figure 46 as the sum total of SERS signal (*i.e.* instensity from across the full spectrum) per slice and the bright field image was added for context. Images were saved at each step to show the original image size, the scaled image to the pixel size of the map acquired, and the intensity of each peak of interest per Z-slice as in Figure 47. Before this however, the correct threshold of signal above noise had to be ascertained to use against all Raman maps. An example of the thresholding conducted within Wire, before applying it within the Matlab processing, was montaged in Figure 45. Areas of the masked cell shape with signals that exceeded the threshold requiremets for signal above noise, were used to calculate the percentage of each slice area with each SERS signal (bound-EL, free-EL, CH_2 cell components). The percentage of the total cell volume with each SERS signal were calculated as a measure of cell uptake of conjugates over time for AgHA and AuCt conjugates and the bare control NP uptake from the cell context vibrations (Figure 50, Table 11). Finally, comparisons were drawn of percentage normalised signal of each molecular vibration to track the uptake of conjugates and then release of EL over time for both conjugate types (Figure 51, Table 12).

Now that the workflow from Figure 43 has been explained, the results from the figures produced are discussed in turn, starting with the first step of averaging all spectra per slice and considering the overall quality of spectra from the cell.

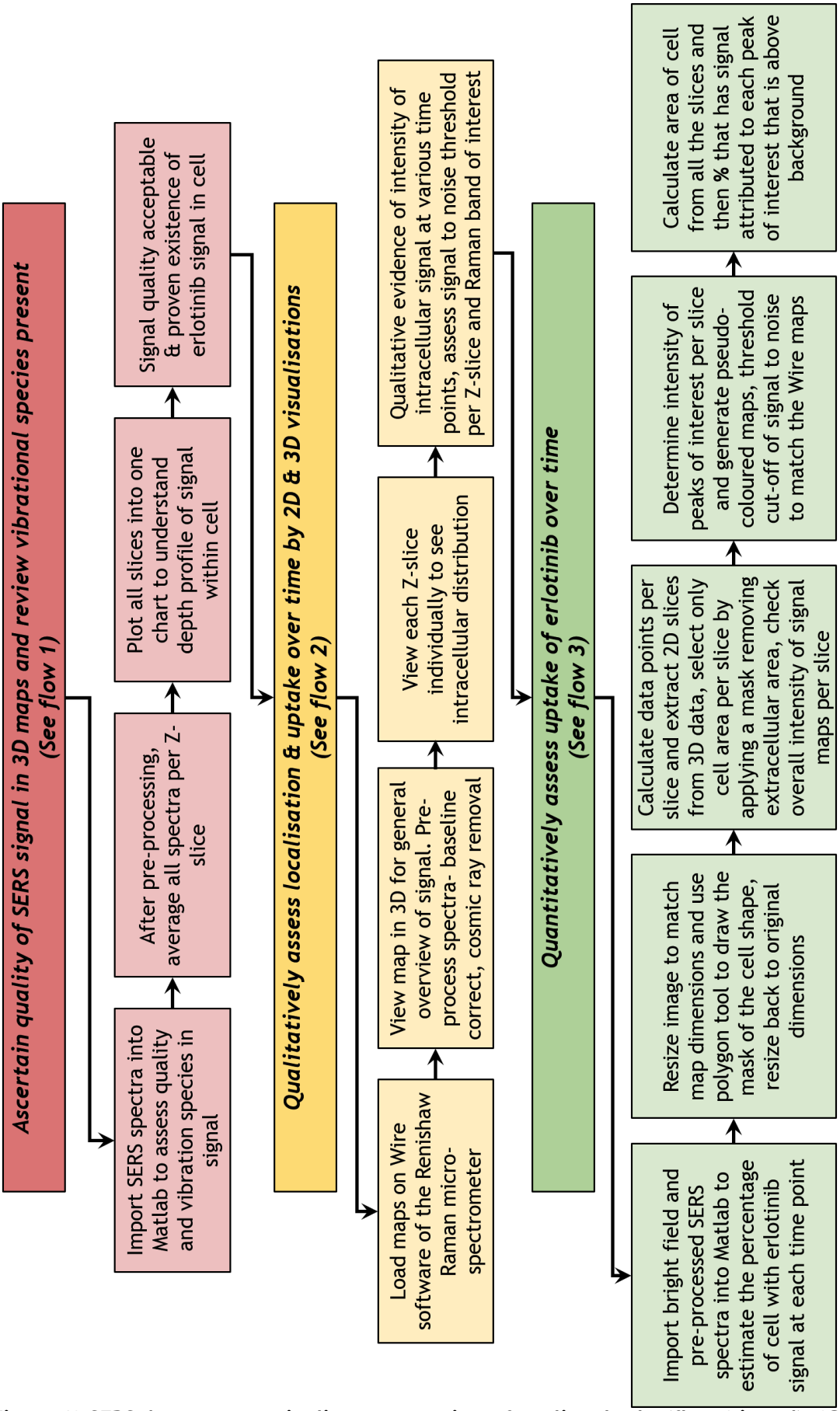

Figure 43 SERS data process pipeline: an overview of quality checks (flow 1 in red), 2D & 3D visualisations (flow 2 in orange) and quantification of NP uptake (flow 3 in green).

Figure 44 displays the average spectra for the 5 Z-slices per cell for each time point of the AgHA conjugates samples from 0.5 to 24 hours. The insensity scale on the Y-axes are all set to 200 arbritrary units for normalisation purposes and each slice is offset. The peaks that represent the CH, CH_2 and CH_3 stretches from the cellular components composed of DNA, lipids and proteins at ~2850-2950 cm^{-1} Raman shift are clearly seen from 0.5 hours in (A) but the alkyne stretches of bound or free-EL are not yet visible at ~1985 or 2111 cm^{-1}. At 2 hours (B) the bound-EL starts to become visible at ~1985 cm^{-1} Raman shift, especially in slices 2-4 (depths 3-9 µm from the 12 µm deep volume map) indicating that the conjugates have entered the cell's cytoplasm. At 4 hours (C) the alkyne vibration for bound-EL is more intense than at 2 hour and is clearly visible, there is a small peak at the free-EL vibration and the intensity of the CH vibrations varies theough the depth of the cell. This is all evidence that the conjugates are within the cell, especially slice 4. The greatest signal from the time series is detected at 24 hours (D) where both alkyne Raman shifts were visible for bound and free-EL and the cell components are also the most intense out of all of the incubation times.

From Figure 44 (D) it is clear that the Raman shift of the alkyne was influenced by the cellular envinironment, as there was a shoulder present or 2 molecular vibrations. This structural disorder can be explained by various contributions. The sensitivity of alkynes to their solvent has been investigated and although not fully characterised in the field, it is known that solvatochromism occurs.[147] Solvatochromism is the change in colour of a solute dependent on the solvent that the molecule or compound is dissolved in, this also extends to the spectral characterisitics within analytical chemistry. Blasiak *et al.* showed in 2017 that the alkyne Raman band shifts from ~2100 cm^{-1} in DMSO, to 2120 cm^{-1} in water and finally to ~2130 cm^{-1} in hexane.[148] They conclude that the polarity and proticity are the major influences on frequency shift of the molecular vibrations. In this instance, depending on where the conjugates have agglomerated, the direct environment and interactions with the conjugates may change *e.g.* within the cell this could have been in a lipid rich membrane bound organelle that would be different from being free in the cytoplasm. Additionally, the binding geometries have been discussed by various groups in the field as affecting the Raman shift of alkynes by up to 200 cm^{-1}.[149,150]

Figure 44 demonstrates the temporal uptake pattern of the conjugates. The cell engulfs the particles from 0.5 hours, due to the cellular components signal at ~2850-2950 cm^{-1} Raman bands. The EL signal appears from 2 hours and becomes prominent at 4 hours within the cell and the strongest signal was observed at 24 hours

indicating a greater number of particles present. To investigate the distribution of conjugates, Figure 45 explored the SERS signal per slice as pseudo-coloured images using Wire 4.2 software as per flow 2 of Figure 43.

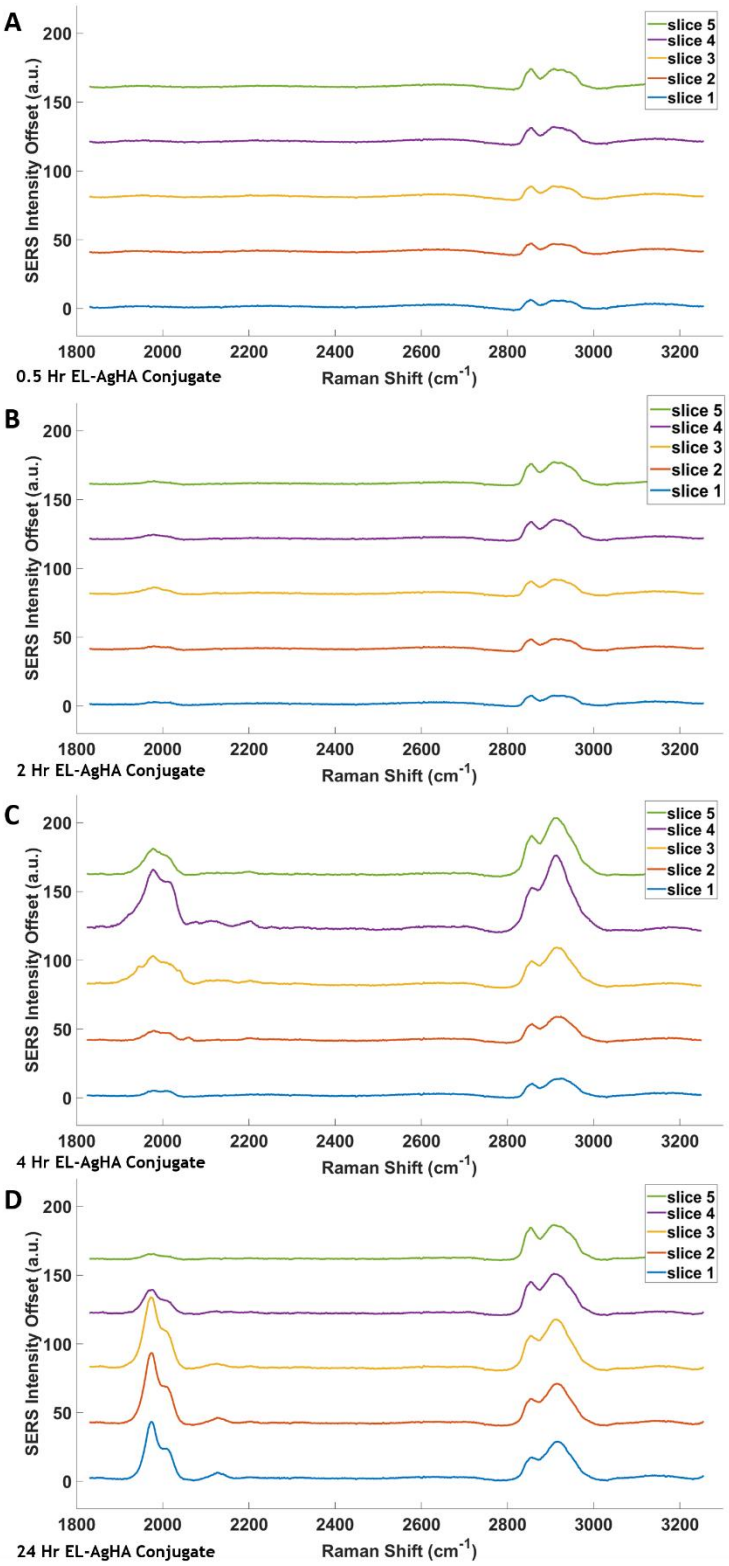

Figure 44 SERS spectra of average signal per Z-slice (5 slices) in HCC827 cells with EL-AgHA conjugates at: A) 0.5, B) 2, C) 4 and D) 24 hours incubations. Total depth per cell was 12 µm at 3 µm step size. Peak of interests are conjugated EL (bound acetylene) ~1985 cm^{-1}, free-EL (unbound acetylene) ~2100 cm^{-1} and CH_2 cell protein, lipid and DNA ~2850-2950 cm^{-1} Raman shift. Fixed cells interrogated with 633 nm laser.

The spatial distribution of the conjugates are observed in Figure 45. For brevity, only the 24 hour and 0.5 hour time points were selected for this report. However, as detailed in the process to handle all the SERS maps, this was conducted for all samples (Figure 43, flow 2). The peak areas of interest were entered into the maps analysis tool in Wire 4.2 to generate a pseudo-coloured map from the peak signal above baseline. These peak areas were determined from the Raman bands observed for the bound-EL (1940-2040 cm^{-1}), free-EL (2040-2140 cm^{-1}) and cellular components of DNA, lipids and proteins (2850-2950 cm^{-1}). The bound-EL in hot orange coloured maps and cell components in cool blue coloured maps of Figure 45 were easily observed, the free-EL maps in pink were harder to differentiate above the background noise of black pixels. Both the bound-EL and CH bands were observed within the cell volume boundary and varied in intensity across the axial focal planes, evidently the conjugates were producing signal intracellularly. Further to this, there is a circle that is clear of SERS signal that is where the nucleus resides. It is common that NPs do not permeate the nucleus and must be tagged with nuclear localisation sequences to gain entry.[47] The distribution seen here can be described as, perinuclear or cytoplasmic, the exact ultrastructural features containing the particles are later explored by TEM.

The final task to be resolved by the 3D SERS mapping was to attempt quantification over time of the bound-EL and free-EL. It would be difficult to determine total particle uptake over time by this method and there are other established techniques such as spICP-MS that are more adept at that type of quantification. Instead flow 3 of Figure 43 can provide a comparative number of the percentage of a cell occupied by a SERS signal to investigate the dynamic release of EL from the conjugate within the cell. The first step of that process was to use Matlab to plot figures of the overall signal from the full X-axis or Raman spectrum for the cumulative SERS signal per layer mapped.

The full spectrum per point acquired was used for the SERS signal intensity plotted in Figure 46. The SERS intensity in the Y-Axes were normalised to the most intense signal which was 7×10^4 arbritary units. This gave a true indication of the conjugate signal across the depths of the cell volume, as well as within a layer. The bright field image was imported into Matlab and resized to the pixel dimensions of the SERS map, thereafter a cell mask was applied to delineate the cell margin. Later this was used for the volume calculations.

Slice 2 and 3 had the most intense signals indicated by the yellow/white pseudo-colour and slice 5 had the least intense signal with dark red colouration for the 24

hour conjugate cell in Figure 46. This Matlab processed map matches the distribution observed within the Wire produced graphics and gave confidence in the scripts created in collaboration with Dr. Lauren Jamieson.

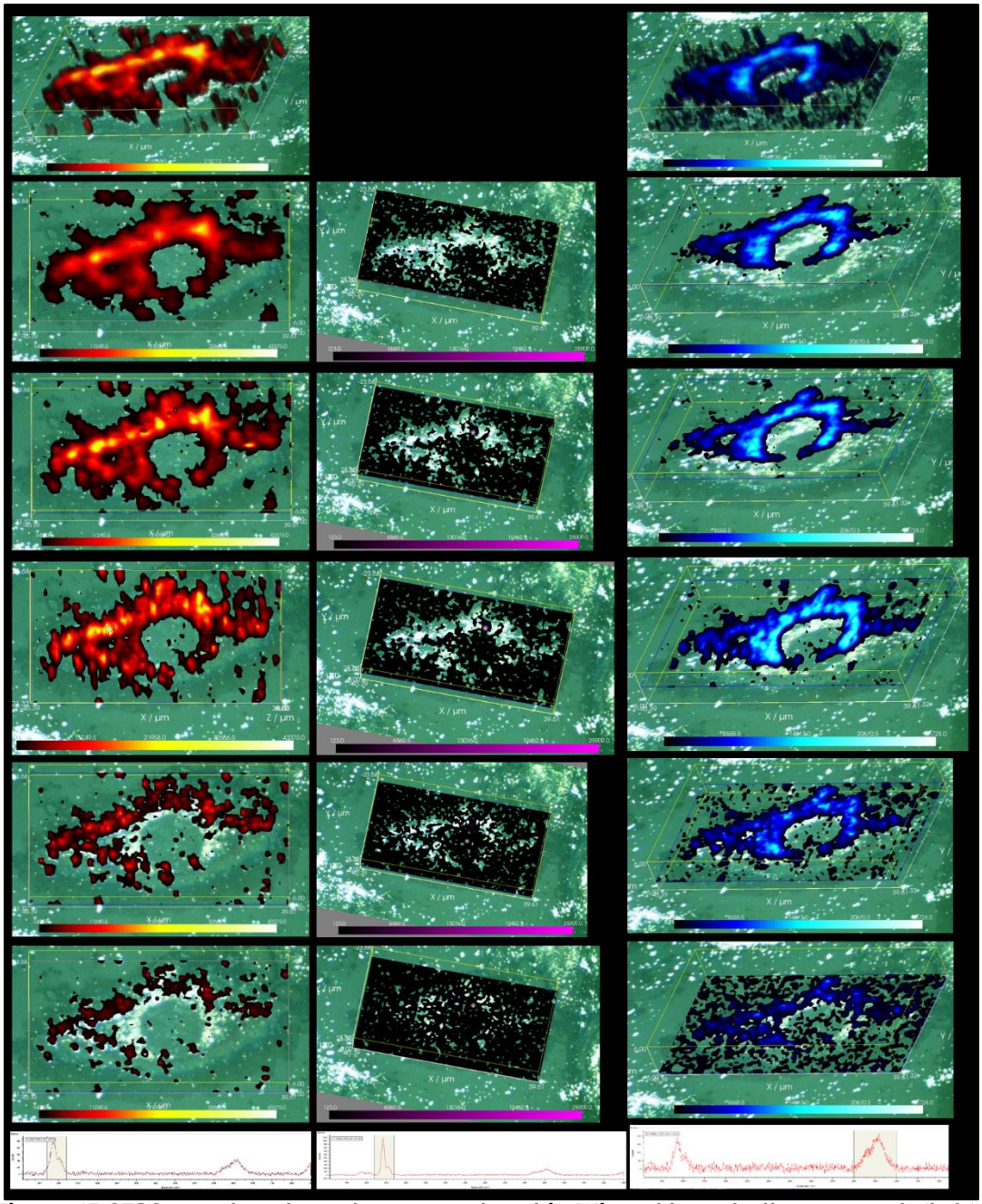

Figure 45 SERS pseudo-coloured maps produced in Wire of bound-alkyne stretch (left), free-alkyne stretch (middle) and CH_2 stretch (right). Example spectra at the bottom, bound-alkyne (1940-2040 cm^{-1}), free-alkyne (2040-2140 cm^{-1}) and CH_2 (2800-3000 cm^{-1}).

The script then enabled thresholding of peak intensities to create the pseudo-coloured maps per Raman peak of interest. At this stage, the Wire produced maps were referred to as guidance for the threshold levels, to establish signal above noise. These maps were created again for the bound-EL, free-EL and CH_2 molecular vibrations. Figure 47 is based on the same cell assessed in Figure 46.

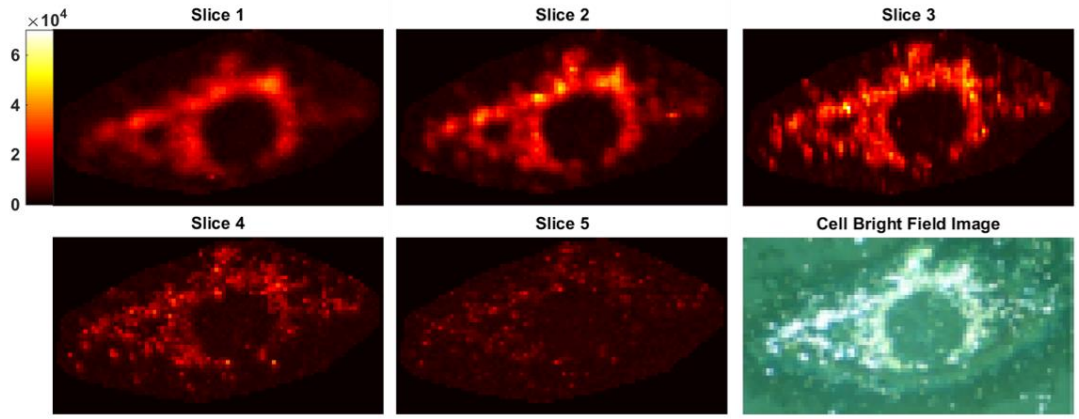

Figure 46 Cumulative SERS signal per slice and cell bright field image for 24 hour incubation of AgHA conjugate in HCC827 cells, intensity bar applies to all slices.

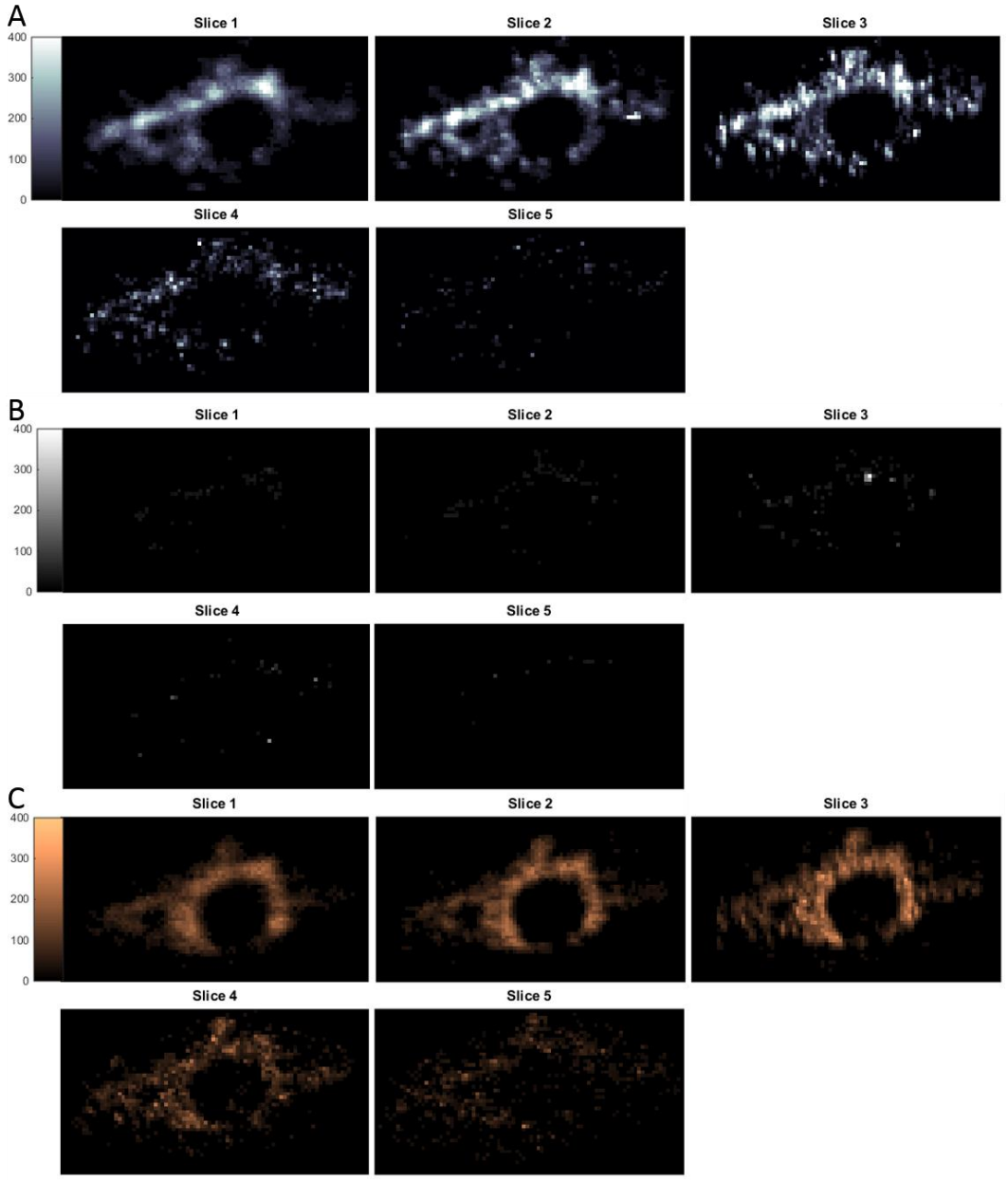

Figure 47 SERS map of HCC827 cells with AgHA conjugates at 24 hour incubation, 2D pseudo-coloured maps from 5 Z-slices at 3 µm intervals. A) Bound-EL alkyne peak ~1985 cm^{-1}, B) free-EL alkyne peak ~2111 cm^{-1} and C) cell context of DNA, Lipid and protein signal from CH_2 peak ~2850-2950 cm^{-1}.

The pseudo-coloured maps within Figure 47 for the Raman bands of interest, were all normalised to an arbritrary 400 units intensity, again to normalise both inter and intra sample comparisons across Z-slices and timepoints. This particular figure was created from the 24 hour timepoint. Maps in A) were all depth slices for the bound-EL or ~1985 cm^{-1} Raman shift, which showed presence of signal across all layers with slice 3 being most instense. Likewise in B) for free-EL band of ~2111 cm^{-1} Raman shift the most instense signal was seen in slice 3 in the middle depth of the cell. In C), there was signal from all layers with slice 3 again being most intense for the cell componenets *i.e.* CH vibrations. These areas that display signal above the threshold were used in the calculations for the area of each slice occupied by each Raman signal.

For comparison, the 0.5 hour AgHA conjugate cell is seen in Figure 48 and Figure 49. There is a faint signal detected in 4 of the 5 layers of the cumulative SERS signal check in Figure 48. It can be seen in the bright field image that there is an aggregate of conjugates in the top left hand corner of the cell. There was SERS signal co-localisation with this aggregate that is observed as the brighter pixels in the cell bright field image. Figure 49 does not display many pixels with SERS signal from either of the expected EL peaks (A & B (bound and free respectively)), however some signal is observed in C) for the CH_2 signal (cell components). These spatial maps reflect the results from the averaged spectral plots from the time series Figure 44, in that the EL was not visible but there was minimal signal from the CH_2 vibrations. To remain brief, the remainder of the maps were not included within this thesis but were produced and saved as part of the quantification process.

To quantify the volume of the cell containing each SERS signal that was visualised in spectral plots and maps, the cell mask was applied. From the cell mask, an area was calculated per slice and multiplied by the number of slices, in this case 5. This was considered as the total cell volume. Thereafter, the number of pixels containing a signal above threshold that appeared as a coloured pixel in the pseudo-coloured maps (*e.g.* Figure 47 or Figure 49). The SERS signal coverage was calculated as area per slice and then the volume from the slices combined per peak of interest. These percentage volumes of the cell were presented graphically and tabulated (Figure 50 and Table 11).

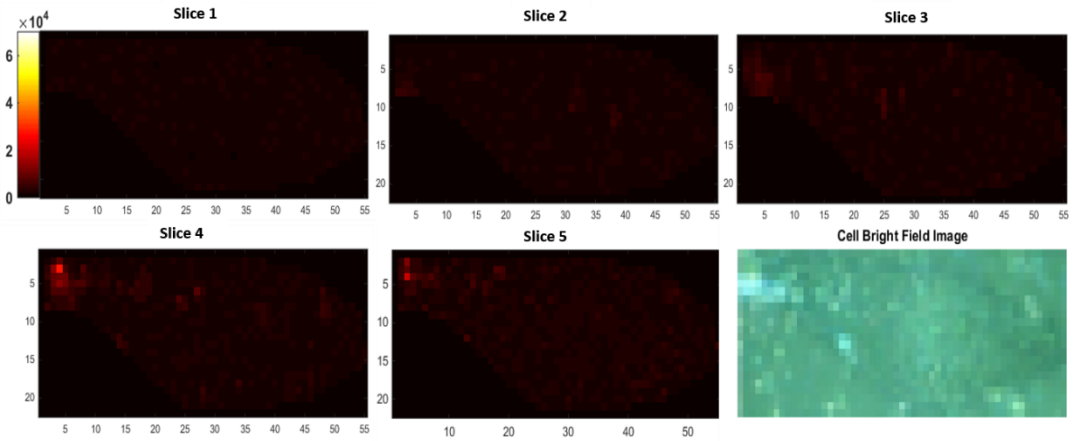

Figure 48 Sum total of SERS signal per slice and cell bright field image for 0.5 hour incubation of AgHA conjugate in HCC827 cells, intensity bar applies to all slices.

Figure 49 SERS map of HCC827 cells with AgHA conjugates at 0.5 hour incubation, 2D pseudo-coloured maps from 5 Z-slices at 3 µm intervals. A) Bound-EL alkyne peak ~1985 cm^{-1}, B) free-EL alkyne peak ~2111 cm^{-1} and C) cell context of DNA, Lipid and protein signal from CH_2 peak ~2850-2950 cm^{-1}.

The numbers from the HCC827 EL-sensitive cells' 3D SERS timecourse study were encouraging that the method was reliable to track NP uptake and EL delivery without the need for a Raman reporter. The inherent signal of the EL was enough to track the progress of the nanodelivery drug treatment. The bar chart in Figure 50 demonstrated that the cells took up more conjugates over time as the percentage of the cell containing the alkyne vibration increased from 0.5 to 24 hours. The AgHA conjugate cell showed a steady increase in alkyne signal and hence EL treatment on the conjugate within the cell, the amount of free-EL also increases over time. The AuCt conjugate was seen within the cell through the increased SERS signal was the CH_2 stretching, as opposed to through the EL signal. There appeared to be more free-EL than bound alkyne but on closer inspection this was noisy spectra in that region of the AuCt conjugate. Through rounds of smoothing the background noise reduced but excessive data processing reduces the quality of the data where genuine peaks reside and skews the results therefore wasn't used. When the SERS signal components were combined and a percentage of the total signal from the selected signals was calculated, AgHA again outperformed AuCt. This was because the signal of alkyne on AgHA conjugates increased proportionally over time from 7.7 % of the total signal at 0.5 hours to 46.4% at 24 hours. Whereas, the AuCt conjugates went from 0 % up to 3.4 % and back down to 0.4 % at 24 hours and were likely background noise (Table 11). The released EL proportion varied in both the AgHA and AuCt conjugates with no trend.

The percentage signal for all 3 bands of interest were normalised creating a ratio of on-particle-EL to off-particle-EL signal. This insight was expected to reveal more about the dynamics of the release of the drug from the NP in the cell and direct investigations towards the mechanisms that were inducing the detachment. Figure 51 and Table 12 were the results of the normalised percentage cell volume of each signal. Figure 51 displays that the AgHA NPs only produce the CH_2 signal in green, where as the AgHA conjugate produces a greater percentage of bound-EL signal over time. Released EL can be seen in the AgHA conjugate at 4 and 24 hours. The AuCt NPs display some signal of the free-EL at 24 hours but as discussed earlier this was due to several noisey pixels that had bands at 2100, 2200 cm, 2300^{-1} and in other cellular silent areas fo the spectrum. This was discussed in personal communications with others in the field as vibrations in the cell that occurs rarely and is never discussed or documented. The $2329cm^{-1}$ Raman stretch has been ascribed as N_2 in several studies.[67,68]

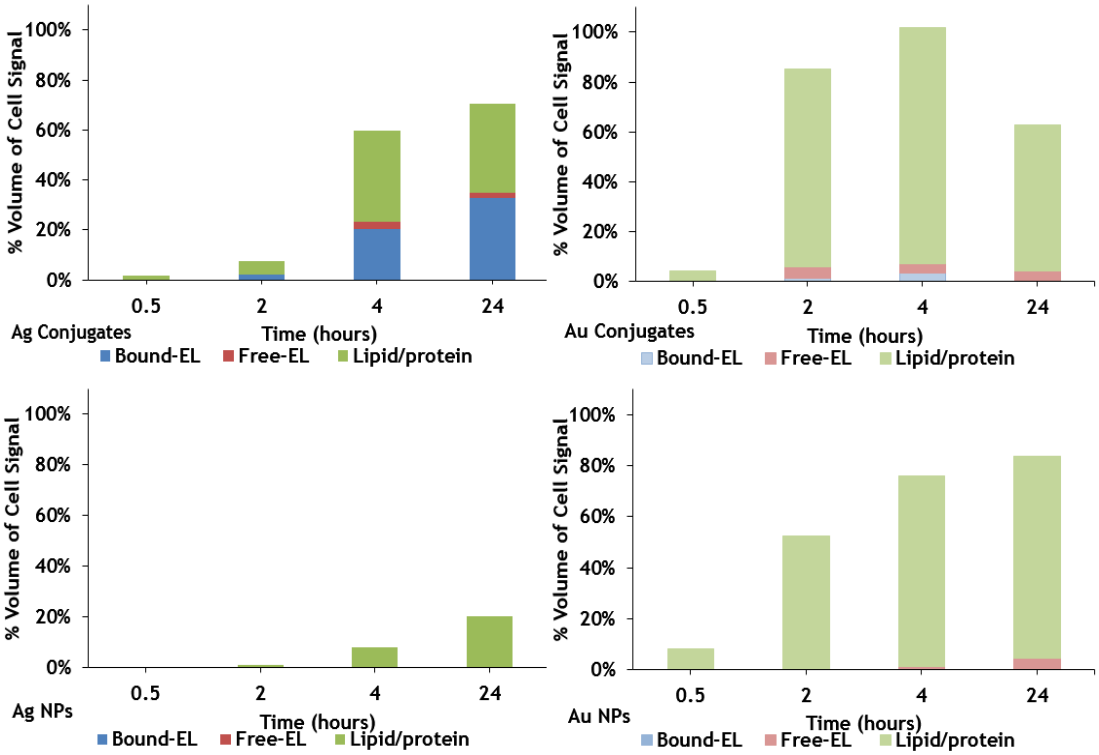

Figure 50 Percentage volume of HCC827 cell occupied by SERS signals from AgHA and AuCt conjugates top (left to right respectively) and AgHA and AuCt NPs bottom (left to right respectively), at time points: 0.5, 2.0, 4.0 and 24.0 hours. The % of signal from bound-EL (~1985 cm^{-1}), free-EL (~2111 cm^{-1}) and lipid/protein (~2900 cm^{-1}) Raman vibrations in the cell.

Table 11 Percentage volume of HCC827 cell occupied by SERS signals from AgHA and AuCt conjugates, and AgHA and AuCt NPs, at time points: 0.5, 2.0, 4.0 and 24.0 hours. The % of signal from bound-EL (~1985 cm-1), free-EL (~2111 cm^{-1}) and lipid/protein (~2900 cm^{-1}) Raman vibrations in the cell.

Sample Name	SERS Signal (% of the Volume of the Cell)	0.5 Hours	2.0 Hours	4.0 Hours	24.0 Hours
300 nM EL-AgHA Conjugate	Bound-EL	0.1%	2.2%	20.4%	32.6%
	Free-EL	0.1%	0.1%	2.7%	2.1%
	Lipid/protein	1.4%	5.2%	36.8%	35.6%
AgHA NPs	Bound-EL	0.0%	0.0%	0.1%	0.2%
	Free-EL	0.0%	0.0%	0.1%	0.3%
	Lipid/protein	0.1%	1.3%	7.8%	19.9%
300 nM EL-AuCt Conjugate	Bound-EL	0.0%	1.5%	3.4%	0.2%
	Free-EL	0.0%	4.4%	3.9%	4.2%
	Lipid/protein	4.5%	79.2%	94.5%	58.4%
AuCt NPs	Bound-EL	0.0%	0.0%	0.0%	0.2%
	Free-EL	0.0%	0.2%	1.1%	4.2%
	Lipid/protein	8.3%	52.4%	74.7%	79.3%

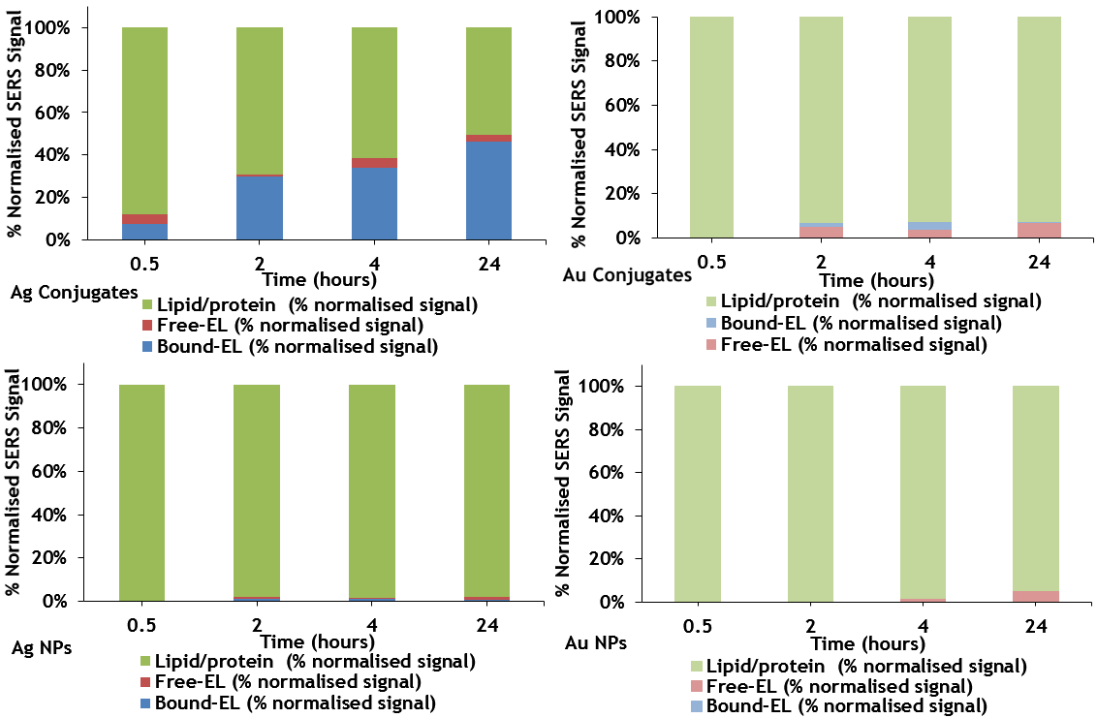

Figure 51 Percentage normalised SERS signal in HCC827 cells from AgHA and AuCt conjugates top (left to right respectively) and AgHA and AuCt NPs bottom (left to right respectively), at time points: 0.5, 2.0, 4.0 and 24.0 hours. The % normalised signal from bound-EL (~1985 cm^{-1}), free-EL (~2111 cm^{-1}) and lipid/protein (~2900 cm^{-1}) Raman vibrations in the cell.

Table 12 Percentage normalised SERS signal in HCC827 cells from AgHA and AuCt conjugates, and AgHA and AuCt NPs, at time points: 0.5, 2.0, 4.0 and 24.0 hours. The % normalised signal from bound-EL (~1985 cm^{-1}), free-EL (~2111 cm^{-1}) and lipid/protein (~2900 cm^{-1}) Raman vibrations in the cell.

Sample Name	SERS Signal (% Normalised Signal)	0.5 Hours	2.0 Hours	4.0 Hours	24.0 Hours
300 nM EL-AgHA Conjugate	Bound-EL (% normalised signal)	7.7%	29.8%	34.0%	46.4%
	Free-EL (% normalised signal)	4.6%	1.0%	4.6%	3.0%
	Lipid/protein (% normalised signal)	87.7%	69.3%	61.4%	50.6%
AgHA NPs	Bound-EL (% normalised signal)	0.0%	1.0%	1.1%	1.0%
	Free-EL (% normalised signal)	0.0%	1.0%	0.7%	1.3%
	Lipid/protein (% normalised signal)	100.0%	97.9%	98.3%	97.8%
300 nM EL-AuCt Conjugate	Bound-EL (% normalised signal)	0.0%	1.8%	3.4%	0.4%
	Free-EL (% normalised signal)	0.4%	5.2%	3.8%	6.6%
	Lipid/protein (% normalised signal)	99.6%	93.0%	92.8%	93.0%
AuCt NPs	Bound-EL (% normalised signal)	0.0%	0.0%	0.1%	0.2%
	Free-EL (% normalised signal)	0.2%	0.3%	1.5%	5.0%
	Lipid/protein (% normalised signal)	99.8%	99.7%	98.5%	94.8%

Overall, the AgHA conjugate was best to track the EL delivery and release from the particles, whereas the AuCt conjugate performed better at delineating the margins of the cell.

Progressing the study, cells were tested for the ability to form spheroids in order to assess the uptake by 3D SERS, in 3D cell cultures, to take the model one step closer to *in vivo* conditions. However, there was not enough time remaining to carry out the experiments. The HCC827 cells readily created spherical and tightly bound spheroids that were ideal for culturing in U-bottom 96 well plates. Instead, to

progress the study, the cells were interrogated as singular live cells, inside of a microfluidics device in collaboration with Dr Marjorie Willner.

5.3 Live Cell *In Vitro* SERS Imaging in Microfluidics Platform

There are arguments that fixed cells can cause artefactual results in many imaging techniques and that live cells should be used where possible. To explore whether the SERS maps have any differences from fixed to live cells, microfluidics devices were used in collaboration with visiting scientist Dr Marjorie Willner, Virginia Tech, Virginia, USA.[109] These devices are capable of maintaining cell viability by enclosing the cells in a preformed platform containing medium such as PBS or media that will buffer the environment and prevent drying.

An example live cell map is summarised in Figure 52 to demonstrate that the signal was comparable to that of the fixed cells. This was reassuring as some literature states that the signal in cell studies was not reliable when fixed and produced different results from live cells.[61,133] Here, it confirms that the fixed cell experiments yielded relevant and reliable results.

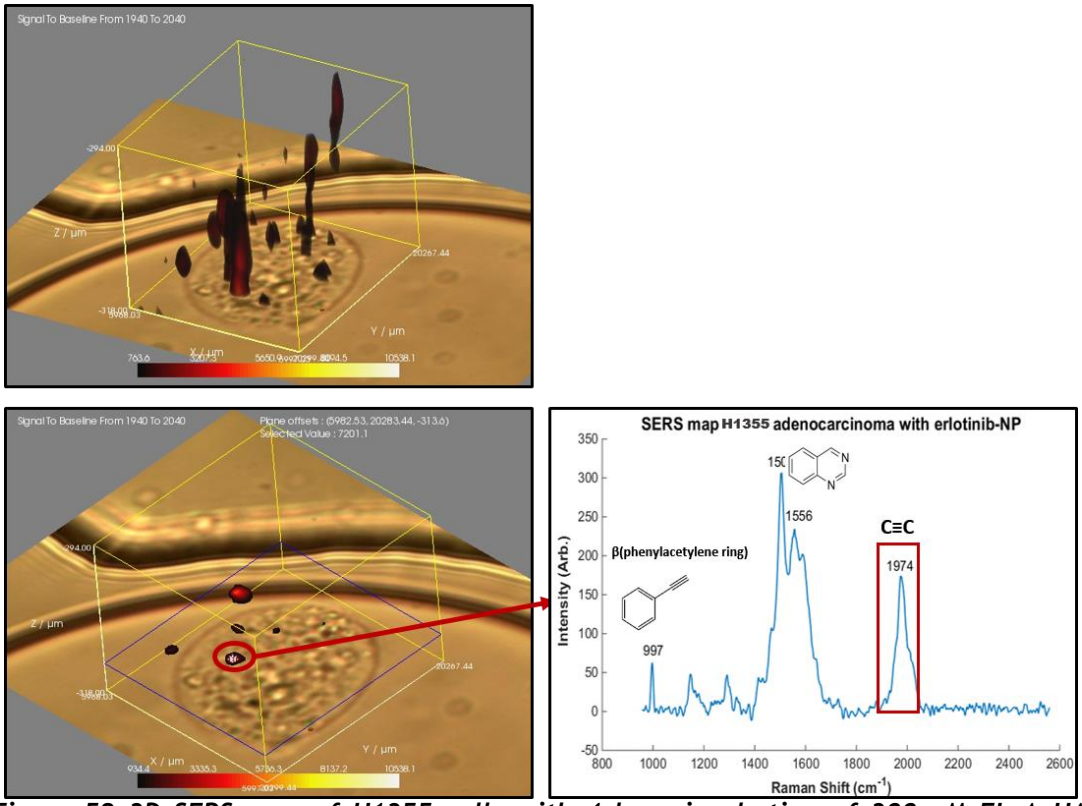

Figure 52 3D SERS map of H1355 cells with 4 hour incubation of 300 nM EL AgHA conjugates in microfluidics device. Laser source is 532 nm at 10% power, acquisition time 0.3 s, X and Y at 1µm resolution, Z at 4 µm intervals with 1800 l/mm grating and 50x objective. Bottom right is an example spectrum with alkyne peak.

Overall the signal was harder to detect within the platform but this could be due to the cell preparation differing to that from the fixed cells. The cells were incubated with treatment for 4 hours and then they were scraped and washed for 5 minutes 1k rpm centrifugation step. Potentially those cells with many conjugates were not in the cell pellet recovered, or it affected the integrity of the cells. Another and more likely potential loss of signal, was due to the requirement to use a different objective and the quality being poorer and affecting the signal return to the detector. Additionally the bright field set up was not optimal for focussing onto the cells within the device and the focal plane may have differed. The medium used was PBS and not water, as water would have lysed the cells by osmotic pressure unlike the fixed cells where this was not a concern. However, a signal was still achieved, although a 532 nm laser source performed better with the AgHA conjugates in this set up. This conflicts with earlier arguments made here, to use the less damaging to cells 633 nm laser. However the greater volume of sealed PBS contained within the microfluidics device, dissipated the heat from the intense laser spot and the burning was no longer an issue when using this live cell method. This was evidenced by the fact that the burning that would usually be observed spectrally as amorphous carbon, was not detected under the same acquisition settings that would have caused burning in fixed cells.

This is the first report known to the author at time of writing, of inherent drug signal deteceted within live cells of a microfluidic device, *i.e.* not requiring a dye or label to image its presence.

3D SERS mapping is a relatively recent advancement in the Raman imaging field, first being reported by McAughtrie *et al.* in 2013 unlike 3D fluorescence imaging, which is now an accepted means of stating a sub-cellular localisation of a fluorescence signal.[47] 3D SERS mapping, since it is still in its infancy, appears to require correlative studies to add credibility to the data. Correlative uptake studies are described next that explore the intracellular localisation of the conjugates.

5.4 Correlative Uptake Studies SEM, TEM and Dark-Field Microscopy

The 3D SERS maps indicated a definite subcellular localisation of the conjugates yet it is difficult to discern the exact localisation with SERS alone, as it swamped the Raman signal of the cell's components. This is not an issue restricted to this study as others have noted this effect in their works and only NPs with targeted probes and dyes can be used to delineate organelles and unlabelled cell components cannot be detected concurrently by conventional Raman without damaging the cell.[47,151]

Here, SEM and TEM explored the distribution within organelles by looking at the ultrastructural features of the cell.

5.4.1 Scanning Electron Microscopy for Surface Bound

SEM was used to observe the distribution of NPs on the cell. It was difficult to observe within the cell due to the nature of the technique, therefore TEM was later carried out for ultrastructural analysis.

The distribution did not appear to differ between cell line or NP metal material from the SERS data. Consequently silver was selected in the control line H1355 to be representative of all samples when looking at the SEM of surface attachment of conjugates on the cells. The conjugates were prepared as in method 2.1.2 and incubated for 4 hours as per the procedure for SERS mapping samples 2.3.2. The cells were grown and conjugates were added as per method 2.3.2, with the exception that instead of a glass window, a gold chip was used as a surface for the cells to adhere to and to aid the conduction of electrons during the SEM procedure.

The SEM was conducted in secondary electron mode and it can be seen in Figure 53 that NPs were attached to the cell surface, despite 5 washes, indicating that the internalisation process had begun. Evidence of this endocytosis was seen later in the TEM images to support that the particles were engulfed by the cell after settling onto the cell surface. Figure 53 (A) displays the cell in dark grey with the conjugate clusters on the surface in a whiter shade, (B) is a magnified view of an aggregate of AgHA conjugates associated with the cell surface. The next area of interest was the intracellular distribution as shown by TEM.

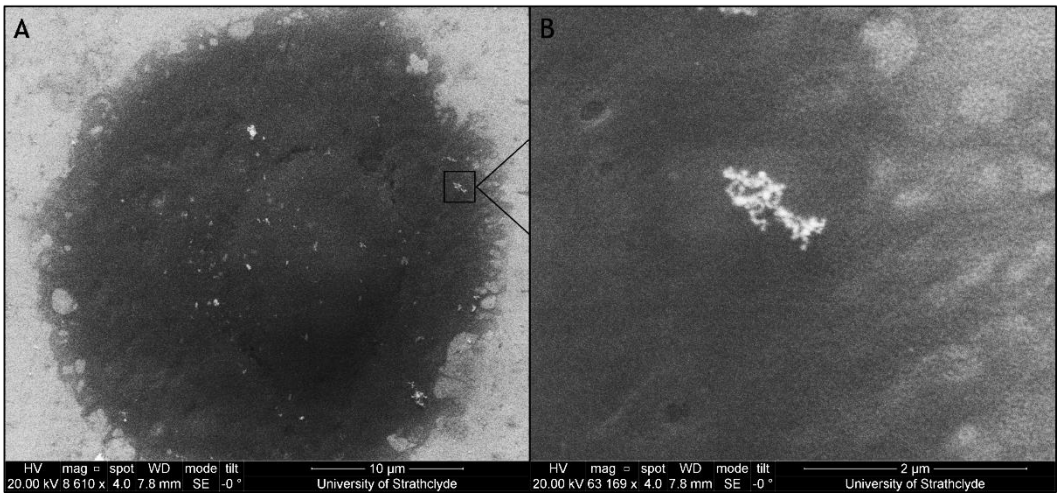

Figure 53 Representative SEM of H1355 lung adenocarcinoma cell with 300 nM EL-0.2nM AgHA NPs incubated for 4 hours on a gold chip in SE mode. A is the whole cell with evidence of surface attachment of NPs (lighter spots) and inset B is a cluster of particles at a greater magnification.

5.4.2 Transmission Electron Microscopy for Intracellular Localisation

TEM was carried out to determine the general distribution of the NPs within the cell to correlate with the results of the optical imaging carried out by 3D SERS mapping. The detailed aim of the TEM study was: to ascertain whether the NPs were within, or on the cells, to study the general subcellular localisation of NPs, and finally to establish whether internalised NPs were engulfed in endosomes or within other organelles.

Cells and conjugates were prepared as they were for SERS mapping (2.3.2), except the procedure stopped at the PBS washes. The cells were then scraped from the culture dish's surface and centrifuged at 1000 rpm for 5 minutes to wash and pellet the cells for TEM fixation as described in section 2.4.1.

NPs were spotted onto a silica wafer to determine the morphology, size and monodispersity of the batch of AgHA NP colloid used in the cells. Image J (National Institute of Health (NIH)) with FiJi plug-in was used to measure the average diameter of the NPs.[101-103] The average size of AgHA NP in the H1355 lung adenocarcinoma EL insensitive cell experiment was 39 nm ± 10 nm from sample size of 38 NPs, which were all seen to be approximately spherical in Figure 54. The process to characterise the NPs was repeated for the HCC827 lung adenocarcinoma EL sensitive cell TEMs. EL-AgHA NPs and EL-AuCt NPs were air dried onto a silica wafer and images were acquired by TEM for measurement, their sizes were 40.8 ± 4.8 nm and 41.0 ± 3.4 nm respectively. From Figure 54 it is clear that the AuCt and AgHA conjugates were equivalent in both size and shape, therefore were fair comparisons in terms of morphology plus they were both negatively charged. The optimum size of a NP to enter a cell is 40 nm, therefore all the conjugates were within that region and were fit for purpose.[15]

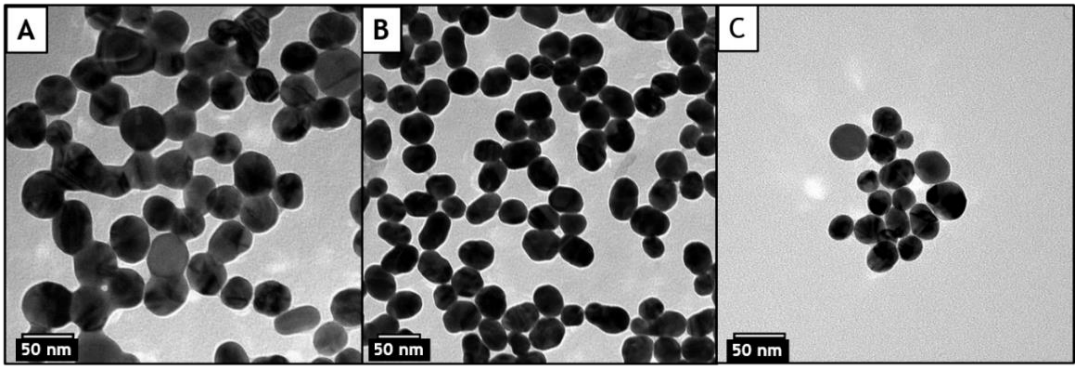

Figure 54 TEM of NPs: A) AgHA NPs for HCC827 cells, B) AuCt NPs for HCC827 cells, C) AgHA NPs for H1355 cells. Scale bars 50 nm.

The resulting TEM images in Figure 55, Figure 56 and Figure 57 show evidence of the NPs localisation as: on the cell surface, being engulfed (macropinocytosis),

inside the cytoplasm but not within a membrane bound organelle, intracellular within vesicles or endosomes or other unknown structure, inside of mitochondria and mitophagosome, inside membrane of an autophagosome vacuole and causing cell death or next to and in a ruptured cell.

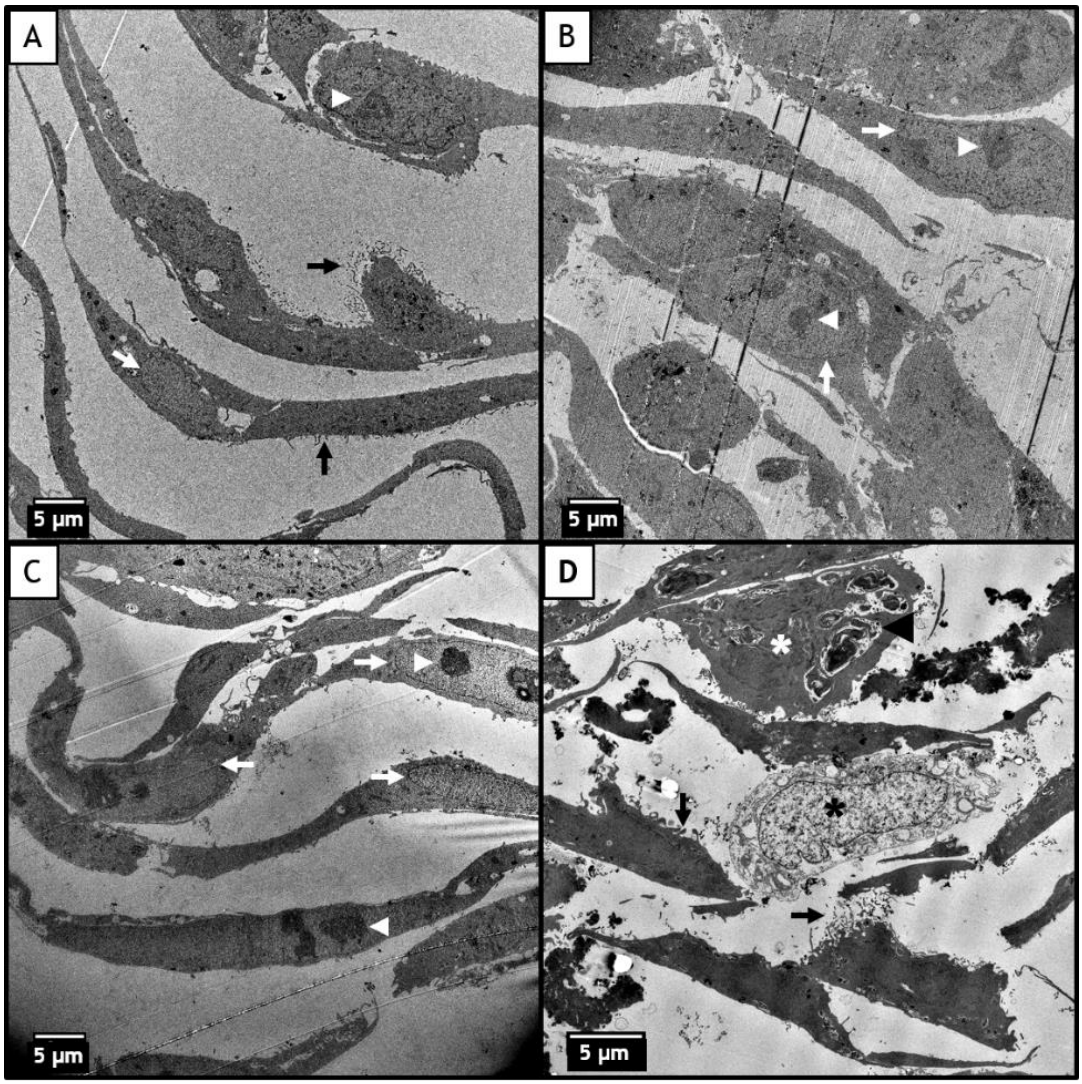

Figure 55 TEM representative images of cells. A-C are HCC827 lung adenocarcinoma EL sensitive cells, D is H1355 lung adenocarcinoma EL insensitive. A) HCC827 cells with EL-AgHA NPs, B) HCC827 cells with EL-AuCt NPs, C) HCC827 control cells with no NPs, D) H1355 cells with EL-AgHA NPs. Conjugates 300 nM - 0.2 nM NPs incubated for 4 hours. Scale bars are all 5 µm. Key: Black arrows are microvilli, white arrows are nuclei, white arrowheads are nucleosomes, black arrowhead autophagosomes, white asterisk apoptotic cell, black asterisk necrotic cell.

HCC827 and H1355 cell comparison overview in Figure 55 shows that the cell morphology, nuclei size and overall structure are similar. However, the AgHA conjugate treated cells had slightly more protrusions, microvilli or filopodia in both cell lines. Apoptosis, programmed cell death, was observed in both cell types with signs of vacuolation and autophagosomes and nuclear chromatin condensation in the silver samples. The main difference between the HCC827 and H1355 silver treated cells were that the latter had more evidence of necrosis, which was an unregulated and highly destructive manner of cell death in response to an external

stimuli or toxins. In the centre of Figure 55 (D) is a cell that showed necrotic signs from an increased size or a swollen cell appearance, a translucent cytoplasm and a disrupted cell membrane.[152] Furthermore, surrounding cells and extensive debris was seen in an 'exploded' lytic state of disarray in both Figure 55 (D) and Figure 56 (A & C). It appeared from the TEM that H1355 cells were either sensitive to silver exposure or were affected by the EL from the conjugates. However, extensive papers in the literature discussed sensitivities of different cells to varying concentrations of silver.[135,145,153,154] However, the H1355 cells have an inhibitory concentration of 50% of the cells growth (IC_{50}) in the micromolar region, reported in 2009 as 27 μM and 3.31 μM by Gandhi *et al.* and Sos *et al.*.[143,155] Therefore, the EL was not responsible for the cell death. From earlier comparisons drawn between efficacies and toxicities of the conjugate and NP treatments and between the metals, on both cell types through biological studies, it was seen that AgHA NPs were toxic to H1355 cells. Therefore, the intracellular evidence here after 4 hours incubation supported the overall cell health of the population seen in Figure 39. Next the focus was directed to the EL sensitive cell line HCC827.

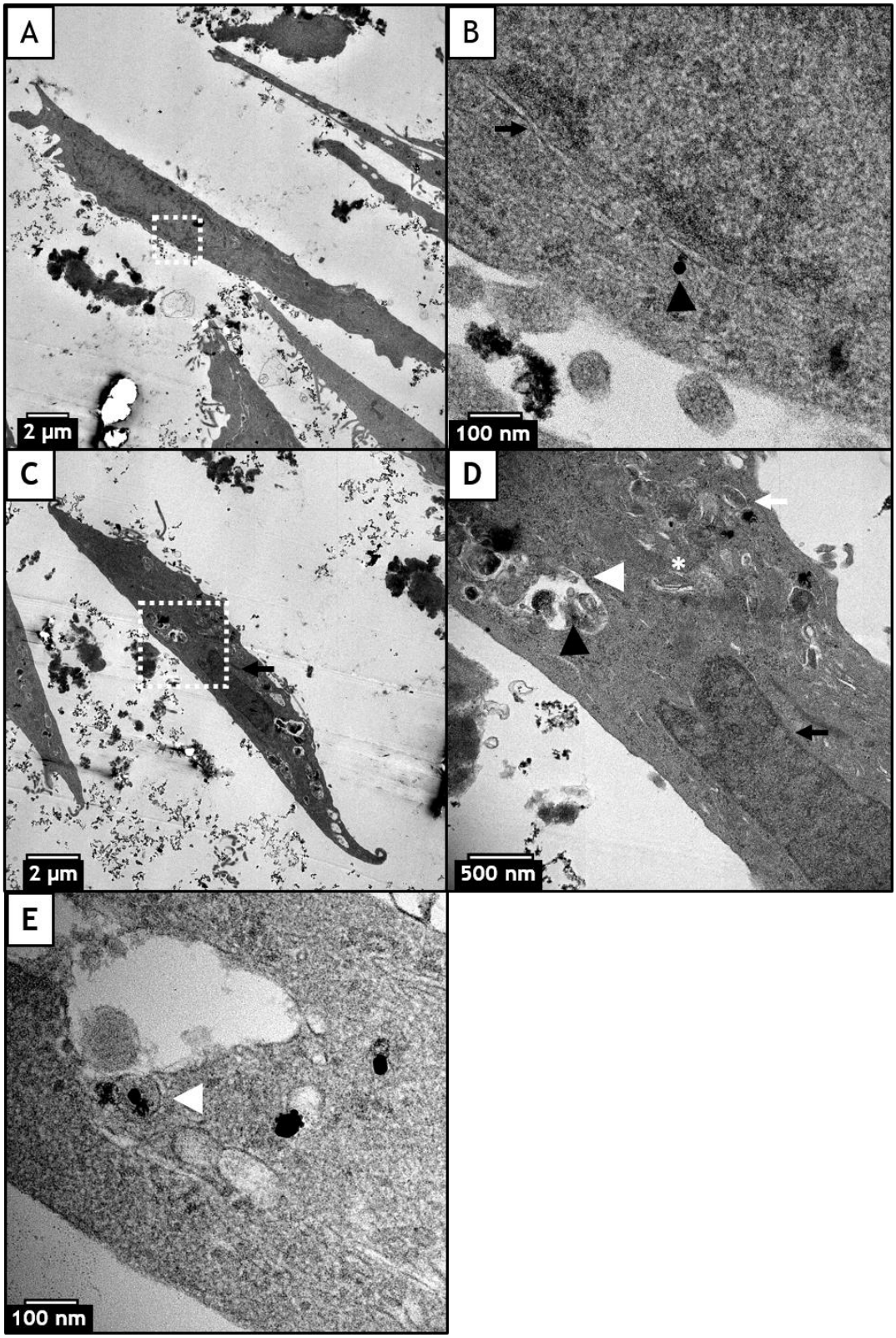

Figure 56 TEM images of H1355 lung adenocarcinoma EL insensitive cells with 4 hour incubation of 300 nM EL – 0.2 nM AgHA NP: A) cell with AgHA conjugates (white dashed box indicating magnified area in B), B) magnified view of A with black arrowhead pointing to 26 nm AgHA conjugate in cytosol, black arrow indicates the nuclear membrane, C) black arrow indicates the nuclear membrane and white dashed box shows area magnified in D, D) black arrow indicates the nuclear membrane, black arrowhead points to a conjugate NP, white arrow indicates early autophagosome, white arrow head indicates late autophagosome and white asterisk above mitochondrion, E) contains conjugate NPs with white arrowhead highlighting a membrane bound particle.

HCC827 cells displayed distinction in response to AuCt and AgHA conjugates as observed in Figure 57. The AuCt conjugates tended to be aggregated in large clusters (>15 NPs per aggregate), which were either membrane bound or simply agglomerated together within the cytoplasm (*i.e.* not membrane bound). There was less evidence of vacuolation or indicators of apoptosis or necrosis in the AuCt conjugate samples, it appeared to be more akin to the control cells with no conjugates (Figure 55 C). The AgHA conjugates were more inclined to remain as individual particles or fewer particles (<5 NPs per aggregate) within aggregates and were either free in the cytoplasm or membrane bound, these packages could have been endosomes or lysosomes. Endosomes are the bodies used to traffic from the cell membrane to the cytoplasm or nucleus and lysosomes are low pH organelles that can fuse with the endosomes and destroy the contents of any marked for destruction. Discrimination between lysosomes and endosomes was challenging purely from TEM images, consequently a correlative study would aid in elucidation of the type of organelle that engulfs the conjugates. Such correlative studies were: an IFA with antibodies to proteins specific to each organelle, a fluorescent pH marker that differentiated the lower pH lysosomes or a pH study of the release of the EL from the conjugate monitored by Raman mapping.[70,156–158]

Strikingly, the AgHA conjugates were present in greater numbers within the mitochondria compared to the AuCt conjugates. Mitochondria can signal both anti- and pro-apoptotic messages to the cell *via* protein cascades dependent on the extent of toxic insult they receive, they are key redox regulators.[94,159,160] The higher distribution of AgHA conjugates within the mitochondria was also accompanied by many more mitochondria being present, or greater signs of mitochondriogenesis (biogenesis of new mitochondria), along with more prolific mitophagy (mitochondrial autophagy within an autophagosome) (Figure 57 A). Turnover of mitochondria is a normal cell process to retain healthy homeostasis and remove or repair any damaged mitochondria, this can occur through fission and fusion respectively.[161] However increased mitophagy can result in too large a burden of autophagy and thus promote cell death.[133,162,163] This could be one contributing factor to any lethal effects seen on HCC827 cells by the AgHA conjugate treatment and must be carefully compared against its bare AgHA NP control. Mitochondria maintain a negative membrane potential, therefore was anticipated that the negatively capped bare NPs would be retarded from entering the respiratory organelle. Conversely it was theorised that the electrostatically bound positively charged EL would enable ingress of conjugates to the mitochondria, enabling a greater extent of cell death from the inherent toxicity of silver ions *i.e.* in an

additive or synergistic effect.[154] These theories were tested in the toxicity section of this study in section 2.3.6. Where HCC827 cells responded significantly more to the AgHA conjugate treatments but did not suffer loss of viability from the bare AgHA NPs.

Thus far, the distribution was proven to be intracellular for all cell types and NP materials with varying effects on the cells health status, although unanswered questions remained. Whether the membrane bound organelles that the large clusters of AuCt NPs resided in were the same type of organelle that the smaller clusters of AgHA NPs were within for the HCC827 cells Figure 57. The next section explored whether these organelles included lysosomes or not by using an IFA followed by DF microscopy and pH sensitive fluorescent dyes.

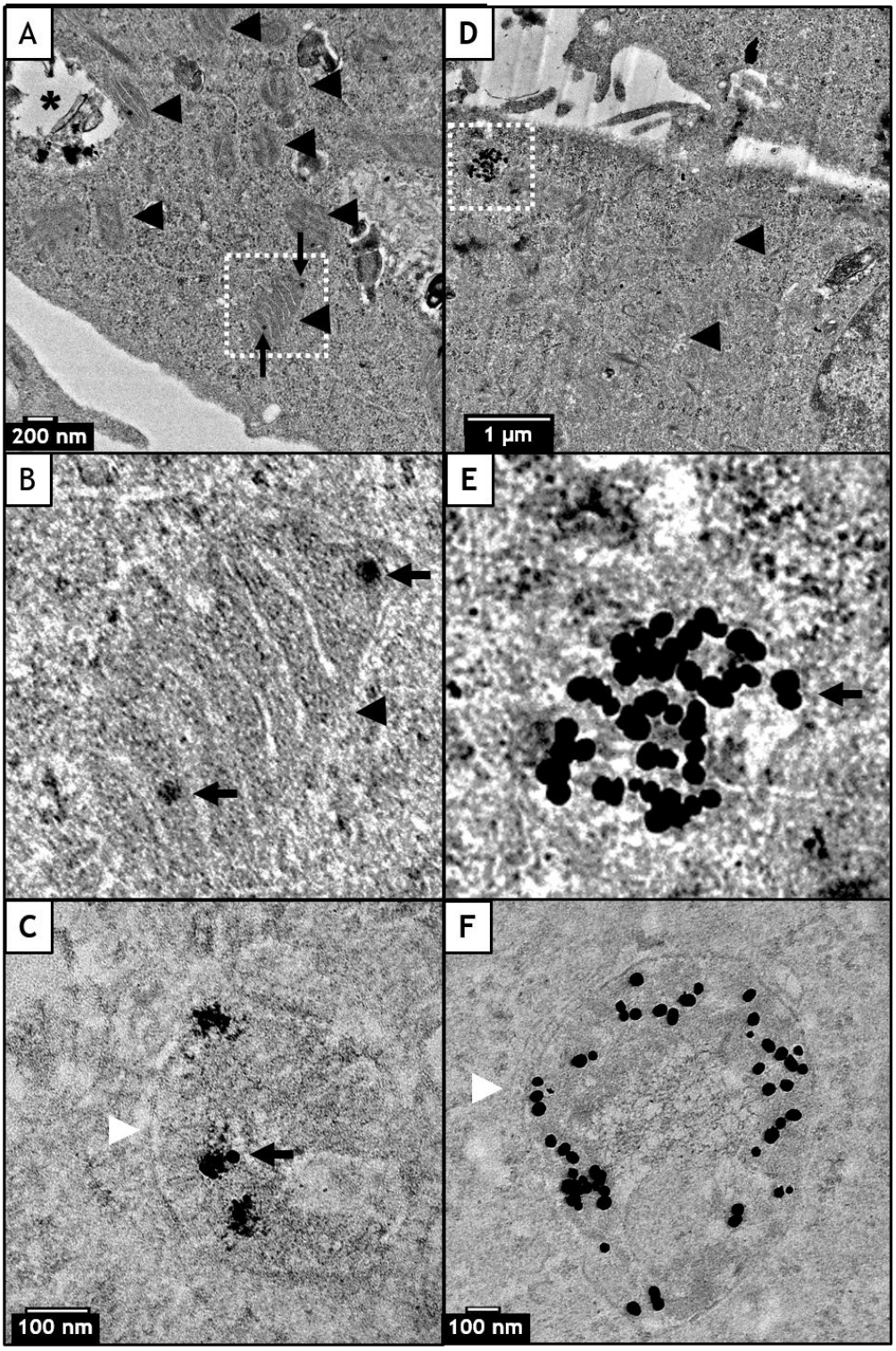

Figure 57 TEM images of HCC827 lung adenocarcinoma EL sensitive cells with 4 hour incubation of 300 nM - 0.2 nM NPs. A-C are AgHA conjugate samples and D-F are AuCt conjugate samples. A) is a cell with many mitochondria- asterisk indicates mitophagy occurring in an autophagosome, many mitochondria are indicated by black arrowheads, AgHA conjugate are demarked by black arrows and one, B) is enlarged view of white box in A with the mitochondrion marked by black arrowhead and conjugate NPs are indicated by black arrows, C) are AgHA conjugates marked by black arrow within a membrane bound vesicle, endosome or lysosome indicated by white arrowhead, D) is a cell containing AuCt conjugates which are highlighted in the white box, mitochondria are marked by black arrowheads, E) is an enlarged view of whitebox in D showing an aggregate of AuCt conjugates within the cytoplasm but not within an organelle, F) white arrowhead indicates many conjugates within a membrane bound vesicle or endosome or lysosome sized as 0.95 µm x 1.2 µm.[133,164]

5.4.3 Lysosome Immunofluorescence Assay

An IFA was carried out with a lysosome specific antibody. This was to determine whether the conjugates were entering lysosomes and if the lowered pH environment was a contributing factor to the EL release from the NPs and the better efficacy seen by the AgHA conjugates from the TEM study. The active site of EL, containing the alkyne moiety was exploited to load the EL onto the NPs. The pilot test was conducted on the EL sensitive cell line HCC827 with the AgHA conjugate initially. The EL therefore needed to be released to enable efficacy. It was indicated by other studies, that a lowered pH environment could induce release within lysosomes.[162,165] It was then logical, if this was the mode of action, that there would either be more lysosomes in the silver conjugate cells or that the lysosomes would co-localise with the particles present. If there was a different staining pattern for the AgHA conjugates than for the AuCt conjugate, then it would have helped to elucidate whether a unique subcellular localisation was partly responsible. Surface chemistry of the two metallic NPs was another factor that could have been responsible for a different cellular response to the treatments, if they had localised in the same subcellular compartment then this should have been investigated further.

Conjugates were prepared as outlined in 2.1.2 and HCC827 cells were plated as in method section 2.3.2 before treatments were incubated with the cells for 4 hours and fixed as in 2.3.2. The immunostaining was performed as in 2.3.3. and the antibodies used were the primary mouse α-LAMP1 mAb (#ab25630 Abcam) overnight and the rabbit α-mouse Alexa488 secondary antibody was incubated for 1 hour before washing and following the remainder of methods section 2.3.3. The images from these samples were acquired on the multiphoton system described in 2.6.2. at identical acquisition settings for: laser power, collection time, accumulations and averaging.

Figure 58 presented bright field images of the cells and green fluorescent images of the α-LAMP1 staining for lysosomes in the following samples: (A) DMSO control, (B) 300 nM EL, (C) 0.15 nM AgHA NPs, (D) 300 nM EL - 0.15 nM AgHA NPs, (E) 0.15 nM AuCt NPs, (F) 300 nM EL - 0.15 nM AuCt NPs. Mentioned in the previous paragraph was the identical acquisition settings used for image collection of all samples, this was to ensure that any alteration in signal intensity or distribution was due to real sample differences and not an artefact of poor control over image attainment. All samples including the non-NP controls had similar green intensity levels of LAMP1 protein and likewise an equivalent distribution. There was one exception to this when examining the images scrupulously, which was sample (f) 300 nM EL - 0.15 nM AuCt NPs which appeared to have a slightly stronger fluorescent staining. If this was

a true reflection of the result and not just auto-fluorescence of conjugates or a different focal plane, it would suggest that this sample had a far greater number of lysosomes with more LAMP1 expression. This was contradictory to the hypothesis underpinning this experiment that a greater number of lysosomes would free-EL from the silver NPs to allow EGFR inhibition. This result instead suggested one of two conclusions. One: that AuCt was uptaken by the lysosomes and as a result prevented the conjugate from exerting any effect upon the mutant cancer cells. Two: that the focal plane on sample (f) was different from all the other samples, which a Z-stack in future would be able to elucidate, or a wide field microscope that does not have the confocality of the microscope that was used here, as confocal images exclude the fluorescence from z-positions other than the focal point.

To aid in clarifying the lysosome antibody staining result, further correlative studies were required. To begin with, a technique which would more definitively answer the localisation question of which organelles the NPs or conjugates were being enveloped in was DF microscopy. DF is a light scattering imaging technique that illuminates the unstained NPs or conjugates position and can be used in tandem with fluorescent studies to give context to the subcellular landscape. Hence, co-localisation studies of NPs and lysosomes are feasible by exploiting DF and fluorescence microscopy with organelle stains or immunofluorescent labelling of proteins.

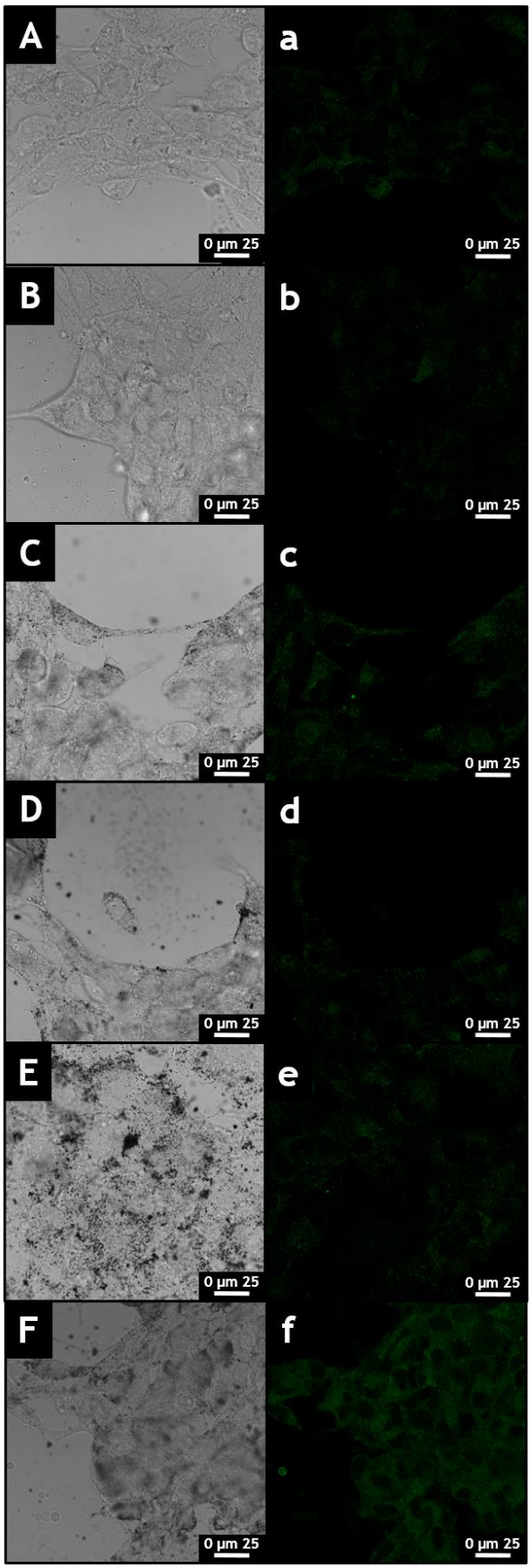

Figure 58 HCC827 lung adenocarcinoma cells treated for 4 hours with: (A) DMSO control, (B) 300 nM EL, (C) 0.15 nM AgHA NPs, (D) 300 nM EL - 0.15 nM AgHA NPs, (E) 0.15 nM AuCt NPs, (F) 300 nM EL - 0.15 nM AuCt NPs. Upper case are white light, lower case are a-LAMP1 antibody for lysosomes. Scale bars 25 µm. All images acquired at same settings.

5.4.4 Dark-Field Microscopy for Lysosome Uptake

The aim of the DF microscopy experiment was to determine whether the conjugates were co-localised with the red lysosome staining. Conjugates were prepared as detailed in 2.1.2, the cells were grown as per 2.3.2, the conjugates were incubated for 4 hours and CytoPainter was applied for 30 mins before fixing the cells as per 2.3.2 and DF imaging was carried out using the instrumental set up described in 2.6.1. The CytoPainter (#ab139488 Abcam) fluorescent dye kit was for: ER (green), lysosome (red) and nuclear staining (blue). The experiment was carried out initially with HCC827 cells and the AgHA conjugate.

Full sized original images can be found in Figure 59, they were enlarged and cropped to better visualise the details within the cell for co-localisation purposes. Figure 60 contained enlarged images displaying (A) DF, (B) lysosome stain (red), (C) merged A & B, (D) DAPI nuclear stain (blue), (E) endoplasmic reticulum (ER) stain (green), (F) merged A,B, D & E, (G) bright field image, (H) merged fluorescent images B, D & E, (I) merged A, B, D, E & G

Figure 60 A) AgHA conjugates were distributed on the cell surface and intracellularly but were excluded from the nucleus which reinforces the SERS data. B) the red punctate staining was seen on the cell surface (artefactual staining of conjugates) but predominantly they were perinuclear. C) co-localisation of conjugates and lysosomes were seen but also some lysosomes (red) with no conjugates are occurring around the nucleus. D) the nucleus was stained blue but there were also conjugates illuminated as a by-product of the stain on the outer region of the cell and was not due to DNA content, this was not observed as much perinuclearly (where the ER and lysosomes reside). E) ER staining was mainly diffuse situated around the nucleus, but there was also evidence of artefactual stains of conjugates observed in a punctate distribution near the cell boundary. F) showed the distribution of the 'white' conjugates in the context of the sub-cellular staining of the nucleus (blue), lysosomes (red) and ER (green), from this it was obvious to see the co-localisation of the NPs and lysosomes. It was difficult to discern which lysosome staining was genuine from those that are artefacts of the conjugates, since the DF scattering was so bright. H) was a merge of fluorescent staining only of the sub-cellular organelles and was useful for gauging the level of false punctate staining as a result of the conjugates in the organelle channels (D- blue, E- green and B- red) since the overlay forms a purple colour, from this co-localisation it was observed that only the perinuclear fluorescence was as a result of the lysosomes as the DAPI staining should only be nuclear, therefore, any purple punctae near the cell surface were deemed as background or noise from the conjugates. By means of deduction the true

lysosome signal was generally perinuclear in locale. From C & F it was concluded that some of the conjugates were within lysosomes once enveloped inside of the cell.

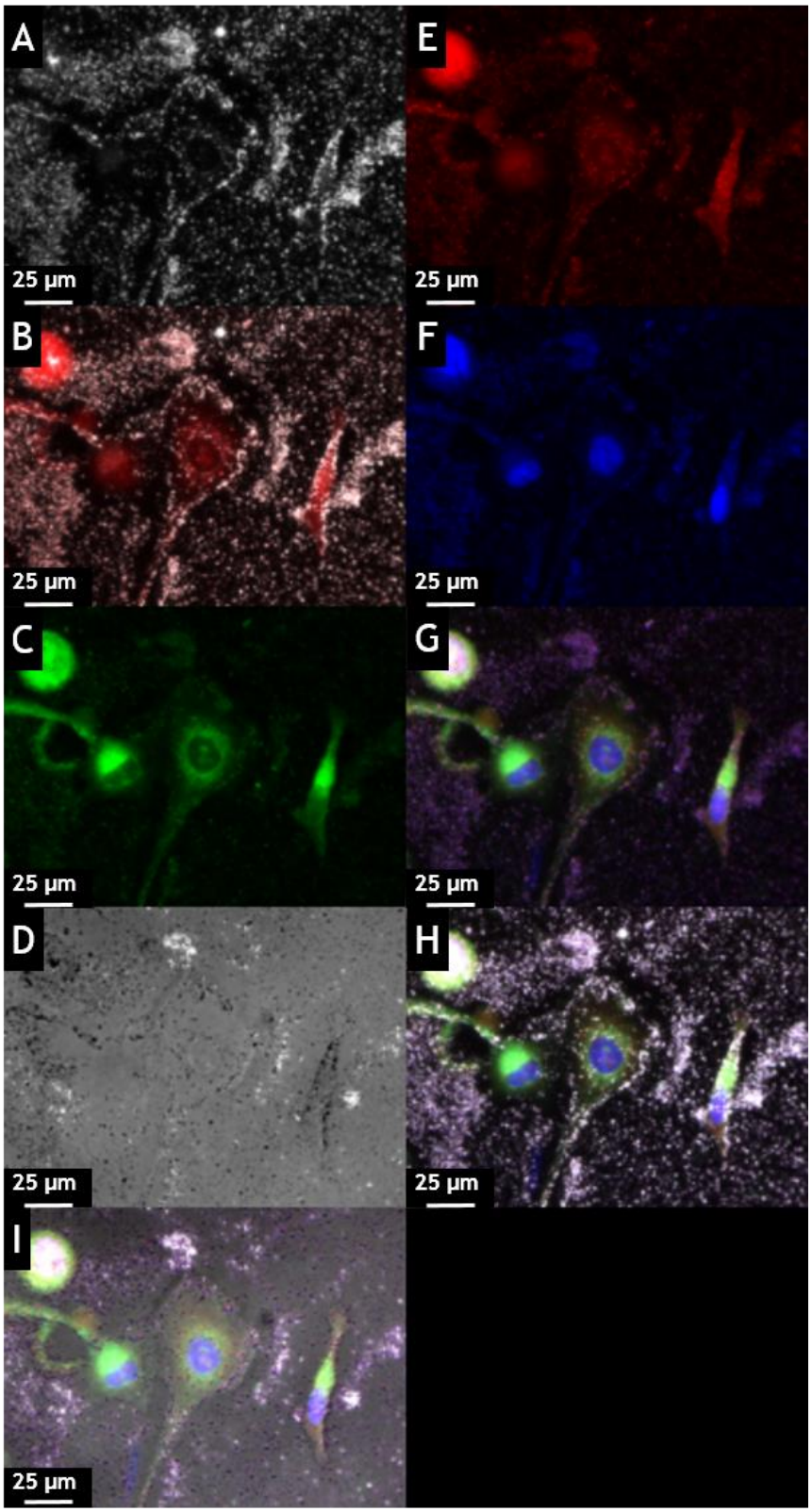

Figure 59 DF microscopy images of HCC827 cells with EL-AgHA NP conjugates stained with CytoPainter (Abcam). A) DF, B) merge f A & E, C) endoplasmic reticulum (green), D) bright field, E) lysosomes (red), F) nuclear DNA stain DAPI (blue), G) merge of C, E & F, H) merge of G and A, I) merge of H and D. All scale bars 25 µm.

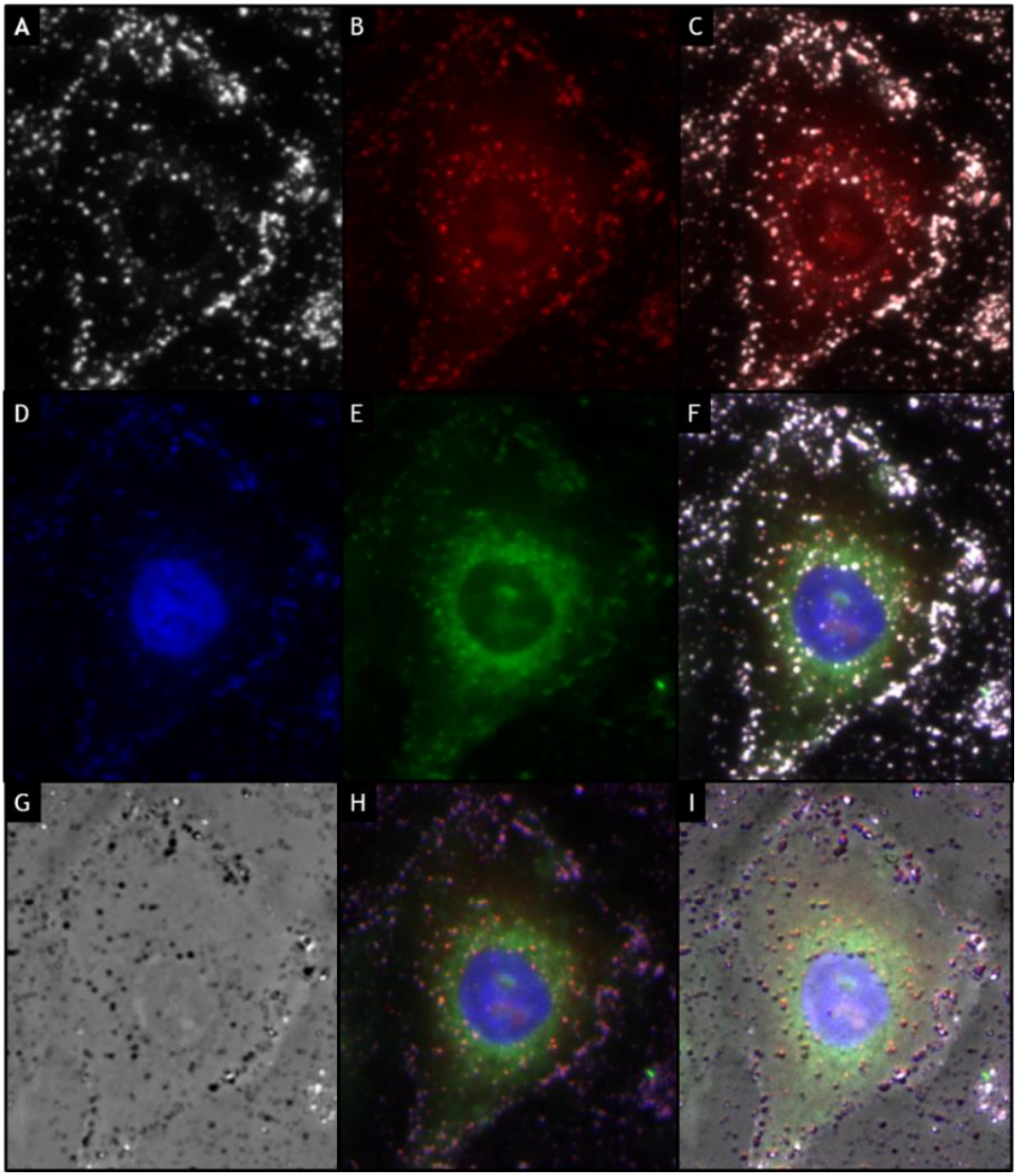

Figure 60 DF microscopy and fluorescent imaging of HCC827 cells treated with 300 nM EL- 0.15 nM AgHA conjugate for 4 hours, fixed and stained using CytoPainter (#ab139488 Abcam). Magnified view of Figure 59 (A) DF image, (B) lysosome stain, (C) merged A & B, (D) DAPI nuclear stain, (E) endoplasmic reticulum (ER) stain, (F) merged A,B, D & E, (G) white light image, (H) merged fluorescent images B, D & E, (I) merged A, B, D, E & G.

To scrutinise the artefactual staining discussed in the previous paragraph, a validation experiment was carried out to examine the level and distribution of staining observed as a consequence of the conjugates being present in this set-up. This was with and without the fluorescent dyes from the CytoPainter kit. The experiment was an incubation of the conjugates in media without cells, replicating that conducted on the cells with conjugate, plus with and without stain. The images from this are included in Figure 61. The conjugates on their own where no dye is present, were clearly observed under fluorescent interrogation. For brevity only the

red channel (lysosome stain) was included here, since it was most pertinent to the artefact query.

When the cells were incubated with conjugates but without CytoPainter the staining pattern was strictly to the boundaries of the cells and did not appear to be perinuclear, where the lysosome staining was evident in the CytoPainter stained cells. From this it was apparent that although artefactual staining occurs of the NPs that these tend to be mainly on the cell surface and there is genuine lysosome staining surrounding the nuclei. However, since this DF and fluorescence microscopy study had its flaws, the remainder of the conjugate and cell samples were not included here for conciseness. The small aggregates of silver formed an SPR band equivalent to the red wavelength region, causing the autofluorescence issue. Recent advancements in the Raman world have lead to polyyne organelle markers that could now be used to determine the contect of the cell and align with the conjugates for Raman and SERS co-localisation studies.

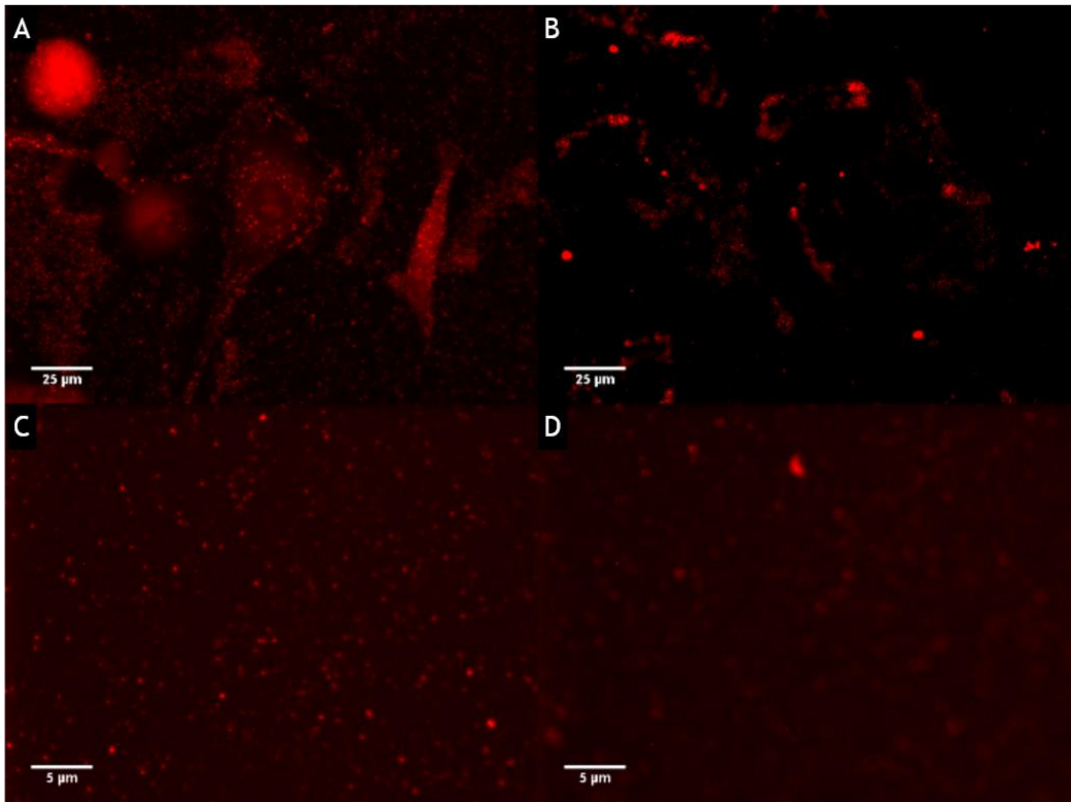

Figure 61 CytoPainter staining validation experiment. A & B are HCC827 cells with 4 hour incubation of EL-AgHA NP conjugates, C & D are incubation of EL-AgHA NP conjugates in media only. A & C have CytoPainter staining, B & D do not have CytoPainter staining. A & B 25 µm and C & D 5 µm scale bars.

Concluding remarks on Figure 60 and the DF experiment were that despite the further correlative tests indicating that conjugates caused artefactual staining in the fluorescent dye channels, there were also punctae where no conjugates resided and were therefore genuine lysosomes. This was further qualified by ensuring the

punctae were not present in the other fluorescent channels and therefore unique to the lysosome stain. Despite this study still not producing definitive results, it indicated that there was some co-localisation of conjugates with the lysosomes which had a lower pH than other membrane bound vesicles such as endosomes. Both experiments employed thus far to investigate the sub-cellular localisation of the conjugates within the cell were optical imaging techniques, IFA and DF with fluorescent microscopy. These methods introduced light based artefacts and therefore utilising a technique which does not suffer from this experimentally introduced artificial effect was deemed beneficial for this research question. SERS exploits the properties of the conjugates to assess analyte attachment, the lysosomal environment is more acidic, which promotes detachment of the EL from the NPs surface by deprotonation. Combined these properties made a pH time course release study an ideal SERS experiment to resolve the question over the conjugates localisation.

5.5 Erlotinib Release from Conjugate Study

5.5.1 Conjugate Stability in Medium & pH Dependent Release of Erlotinib

To establish whether a pH change was the underlying mechanism of the release of EL from the conjugate, and to make a connection with the pH of any relevant vesicle bound organelles in which they were engulfed within (endosomes and lysosome) a pH stability time course was carried out on the conjugates in DMEM cell culture media.

AgHA conjugates were prepared as in 2.1.2 and DMEM media was pH adjusted from pH 7.6 to pH 7.4, pH 6.8, pH 6.0, pH 5.0, pH 4.0 and pH 3.0 using hydrochloric acid. These pHs were selected according the pH of different compartments of the cell during the endocytosis process and of normal and cancerous cell environments. These were summarised in Figure 62.

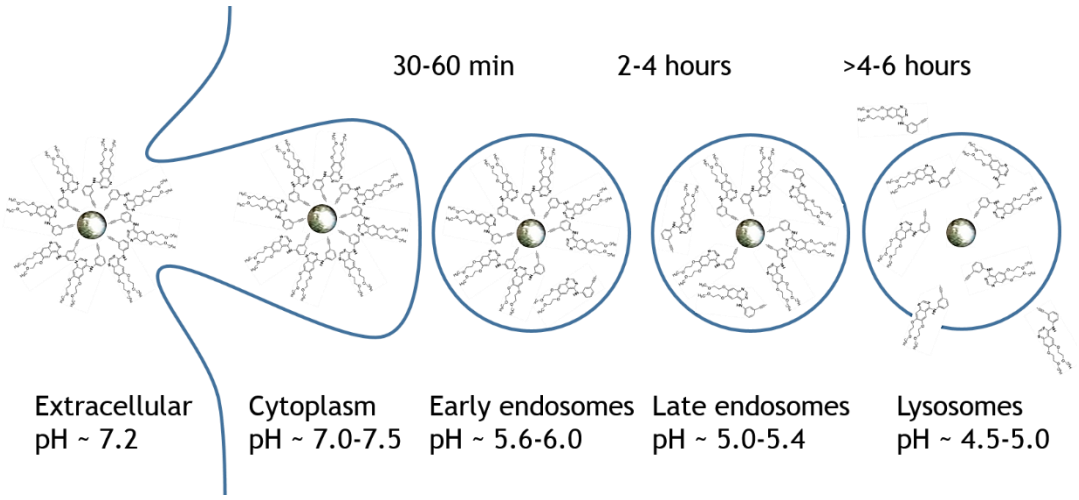

Figure 62 Endocytic uptake of NPs and the pH of the organelles involved in the process: early endosomes, late endosomes and lysosomes over several hours.[93,156]

The conjugates were then incubated in the media and readings were taken on a UV-vis spectrometer immediately, then at 1, 4 and 24 hours. These were plotted in Figure 63 with samples grouped per time point. It was seen immediately that pH 4.0 (green line) was affected compared to the others at 0 hours, seen by the peak dampening and the shoulder of the peak in the red shifted area increased which both indicate instability and sample aggregation. At 1 hour the pH 4.0 (green line) sample remained the same and now pH 3.0 (purple line) had lost its SPR band completely as the conjugates had completely precipitated out of solution. All the samples then remained the same as at 1 hour when analysed at 4 and 24 hours. Traditionally aggregation is used as a method to enhance SERS detection. This would suggest that the lower pH released the EL, in addition to causing aggregation.

The finer details of pH samples 7.6 – 5.0 were examined by compiling Table 13 of all the SPR bands to assess if there were any spectral shifts indicating a change in stability. The λ max. for the stable conjugates was 417 nm as can be seen through all time points for pH 7.6, 7.4, 6.8 and 6.0, although from the UV-vis spectra it was not obvious that there were any alterations to the extinction spectra of pH 5.0. When Table 13 was consulted the λ max. red shifted marginally to 420 nm by 24 hours, indicating a small change in stability, although there were no obvious signs of peak dampening for the pH 5.0 sample. The SPR band of pH 4.0 fluctuated slightly, although it began and ended at 424 and 423 nm respectively. The pH 3.0 sample started to aggregate by 1 hour reaching a λ max. of 426 nm and had clearly precipitated by 4 hours to reach a λ max. of 792 nm at 4 hours and then 800 nm at 24 hours.

In conclusion, all particles were stable up to the 24 hours incubations, except for pH 4.0 and 3.0, which showed signs of aggregation or complete precipitation out of

solution respectively from 1 hour onwards. The implications of this to the surface chemistry of the NPs and the attachment status of EL remained to be assessed by SERS.

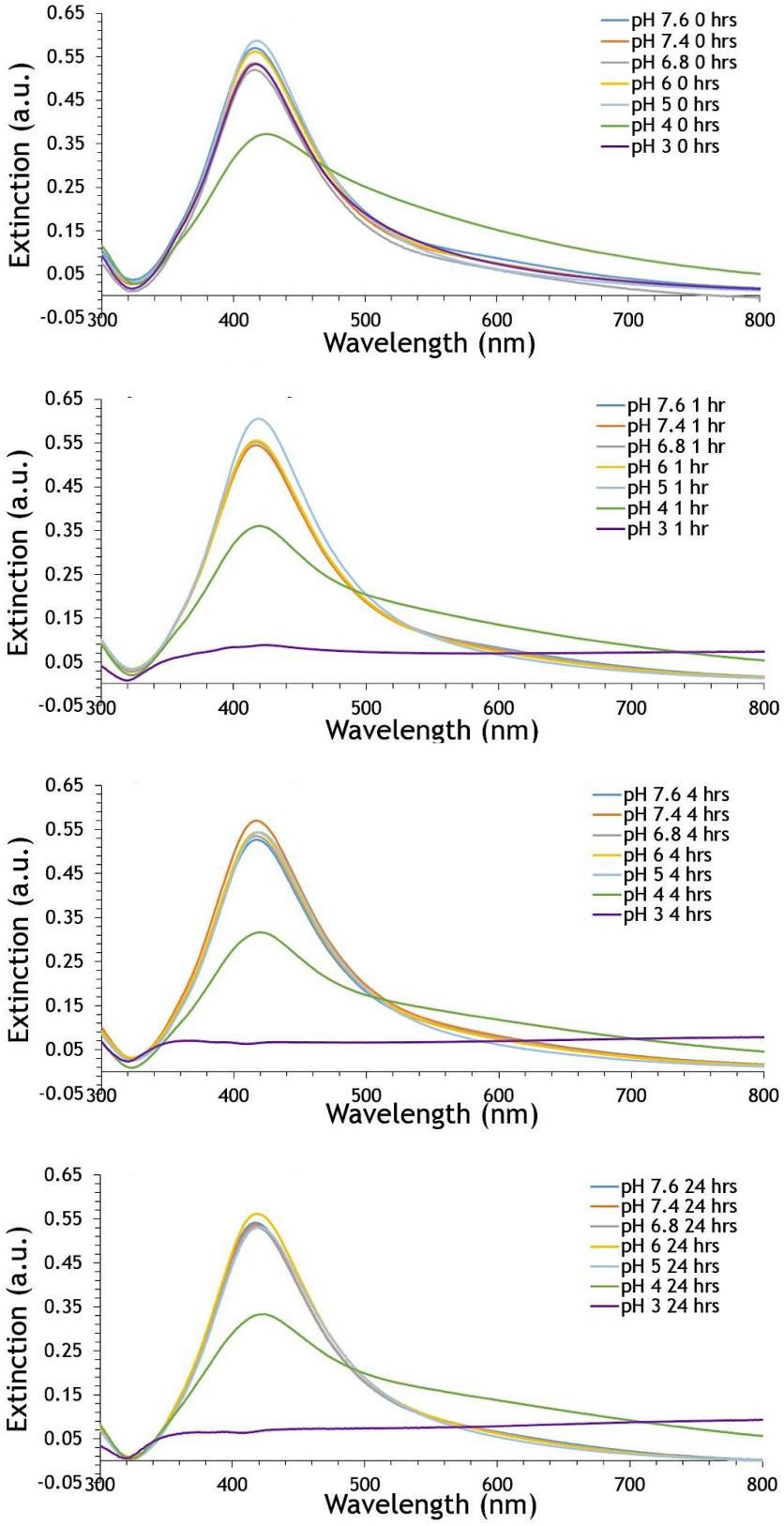

Figure 63 pH stability study of extinction spectra of 300 nM EL- 0.15 nM AgHA NP conjugates in media that is pH adjusted from the standard pH 7.6 to pH 7.4, pH 7.0, pH 6.8, pH 6.0, pH 5.0, pH 4.0 and pH 3.0; all at 0, 1, 4 and 24 hours.

Table 13 Surface plasmon resonance bands of 300 nM EL- 0.15 nM AgHA NP conjugates in media that is pH adjusted from the standard pH 7.6 to pH 7.4, pH 7.0, pH 6.8, pH 6.0, pH 5.0, pH 4.0 and pH 3.0; all at 0, 1, 4 and 24 hours.

	Surface Plasmon Resonance Band (nm)						
Time (Hours)	**pH 7.6**	**pH 7.4**	**pH 6.8**	**pH 6.0**	**pH 5.0**	**pH 4.0**	**pH3.0**
0	417	416	416	416	418	424	417
1	**417**	417	417	417	419	420	426
4	**417**	416	416	418	420	419	792
24	**417**	417	417	418	420	423	800

The samples assessed by UV-vis spectroscopy were also interrogated by SERS over time. Figure 64 presented the SERS intensity of the alkyne peak at time points 0, 1, 4 and 24 hours. It was immediately clear that samples pH 4.0 and 3.0 experienced decrease in signal at 1 hour, although pH 4.0 performed slightly better than pH 3.0 initially, it dropped to the same signal intensity at the 24 hour time point of nearly zero. The remainder of the samples all dropped slightly over time to 24 hours, except pH 6.8 which raised marginally but attention was paid to the SD which increased, so an outlier was thought to be an underlying cause of the seeming upturn in intensity. The fact that samples pH 7.6 – pH 5.0 retained signal at 24 hours was in alignment with the SPR data, especially since within these, pH 5.0 signal reduced the most reflecting its greater change in SPR band over time (Table 13).

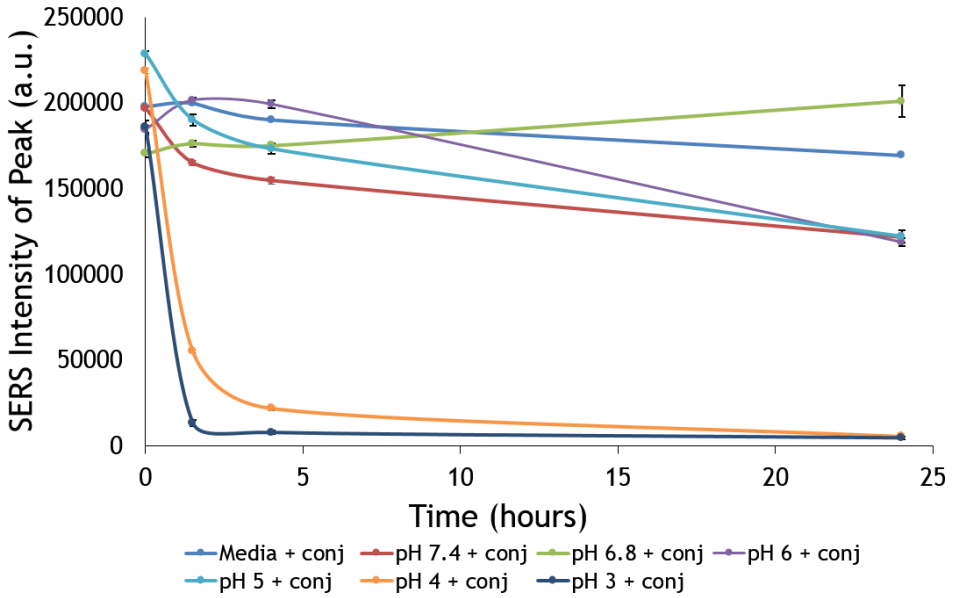

Figure 64 SERS stability of 300 nM EL-AgHA conjugates in pH adjusted media over time. DMEM media (pH 7.6), pH 7.4, pH 7, pH 6.8, pH 6, pH 5, pH 4, pH 3. Interrogated with CBEx 638 nm spectrometer at full laser power (40 mW at source, 23 mW at sample) for 0.2 s, 5 acquisitions averaged, intensity of alkyne peak area (~1985 cm^{-1}) plotted ± SD.

In summary, pH 3.0 and 4.0 lost SERS signal by 4-24 hours, whereas the rest retained most of the signal at 24 hours. What remained unresolved was whether the lower pHs caused destabilisation of the particles, which in turn encouraged release of the EL drug molecules during aggregation. Conversely, was the EL still bound but the precipitation caused the loss of SERS signal, rather than the analyte desorbing to result in the signal decrease. Since salts are frequently used to induce aggregation to enhance SERS signals it could be former, as opposed to the latter.

The literature indicated that pH alone cannot explain or replicate the cancer cell environment when investigating drug release mechanisms. Glutathione (GSH) is a reducing agent known to be elevated in cancerous cells and was also investigated as contributing to the effect of EL release from the NPs within the cells.

5.5.2 Glutathione Dependent Release of Erlotinib from Conjugate

GSH is noteworthy as it is present in cancer cells at higher concentrations. Despite normal levels producing an antioxidant, detoxifying effect, higher levels can be mutation inducing and responsible for chemotherapy resistances.[166] GSH is associated with cell proliferation and reduced level of GSH can result in tumours being sensitised to radiotherapy. Through conjecture it can be said that silver ions, which are known to cause toxicity, could enhance treatment in the same way that trials have been conducted with GSH depleting molecules to enhance platinum based therapies.[72,167] Wang *et al*. created a smart pH and reductive responsive nanoformulation to release the drug load after encountering a lower pH in the extracellular environment and then a greater reductive GSH concentration inside of the cancerous cell.[168]

Lam *et al*. carried out desorption time course studies of EL from 10 nm gold particles with 2 mM glutathione.[22] This released the EL which was observed by a loss of SERS signal over time. However, the stability of the particles was not monitored in this study, the loss of SERS signal alone cannot singularly prove beyond doubt that GSH triggers desorption. Here in this thesis, it was shown that a lower pH of 3.0 - 4.0 reduced the SERS signal but this was accompanied by destabilisation of the conjugates, which in itself detrimentally can affect SERS intensity. Therefore, it cannot be stated categorically that a lower pH triggered the release of the EL from the particle. Taking into account the complex environment inside of the cell, a GSH induced release study was conducted on the conjugates in DMEM cell media. GSH concentrations from various sources in the literature were used as a guide.[139,167,169]

AgHA conjugates were prepared as in 2.1.2 and the GSH concentration range was buffered in DMEM media at 0, 2, 5, 10 and 50 mM. The conjugates were added to the GSH spiked media and incubated at 37°C for 0, 1, 4 and 24 hours, at which time they were analysed in solution by UV-Vis and SERS at 638 nm.

Instantly at timepoint 0 hours in Figure 65 it was clear that all concentrations except 0 mM GSH had impacted the stability of the conjugates, as there was peak dampening at the silver SPR band of 415 nm and a second aggregate peak appeared at > 600 nm. The deterioration of the conjugate stability was both concentration and time dependent. The extinction of the unaffected 0 mM GSH sample remained at 0.58 a.u. The extinction of the 2 mM GSH sample reduced from ~0.35 a.u. at 0 hours to 0.16 a.u. at 24 hours. All other samples finally settled to a similar extinction of 0.16 a.u, if not immediately, then over time. All of the samples except the 0 mM GSH precipitated completely out of solution turning from yellow stable colloid to clear with large aggregates clustered at the bottom of the sample tube. Since 2 mM was more resilient the SPR was examined in Table 14 as was carried out for the pH release study.

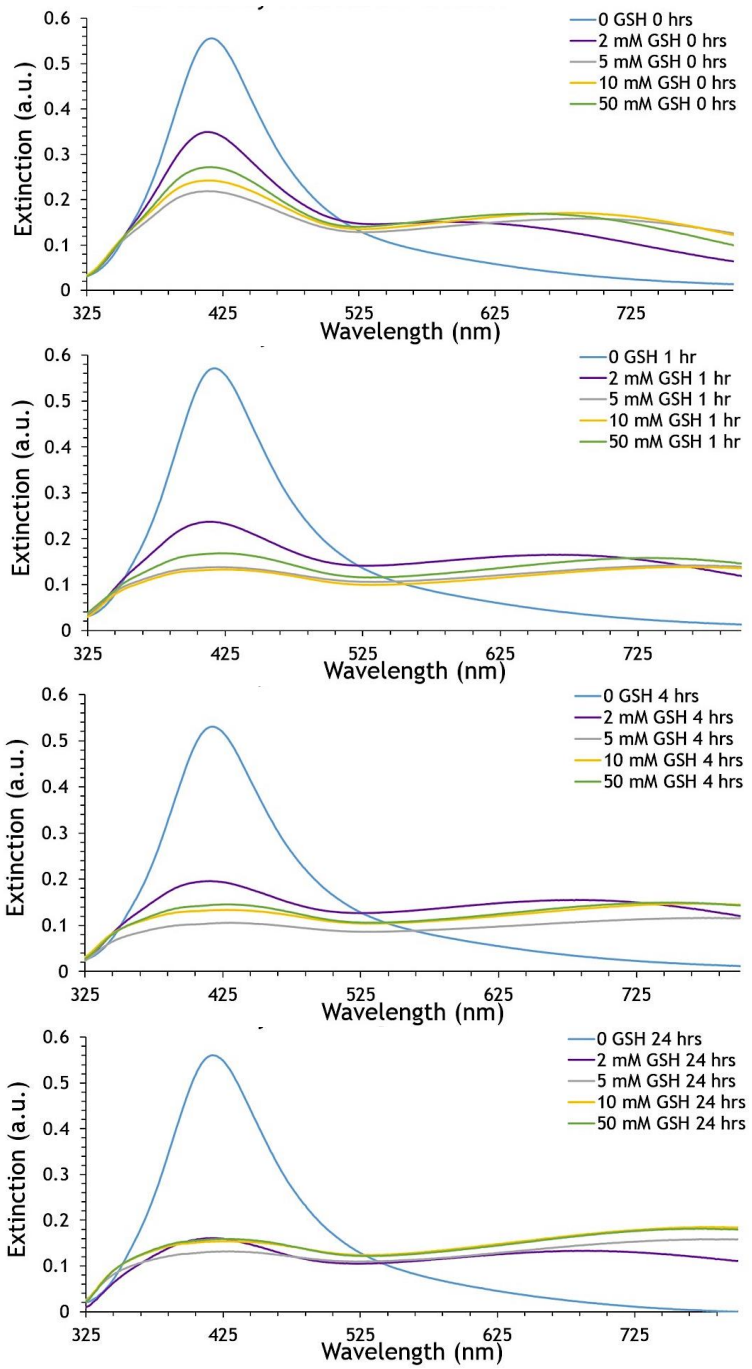

Figure 65 Glutathione (GSH) SERS stability study. Time points of 0, 1, 4 and 24 hours with 300 nM EL-AgHA conjugates in DMEM media with GSH ranging from 0, 2, 5, 10 and 50 mM.

Table 14 shows the SPR bands for all the GSH samples (0, 2, 5, 10, 50 mM). The only unaffected sample was the control of 0 mM GSH at 417 nm, 2 mM was least perturbed out of the rest of the samples with 413 nm at 0 hours and 417 nm at 24 hours. Whilst the SPR did not seem to vary much for 2 mM GSH and the extinction spectrum in Figure 65 displayed the reduction of the 413 nm peak and an increase in the > 600 nm SPR band. All of the remaining samples 5, 10 and 50 mM sample's SPRs increased from ~414 nm to > 700 nm by 4 hours. Where the extinction spectra indicated qualitatively the affect the GSH had on the conjugates, the tabulated

SPRs quantified the data in a more detailed manner and confirmed what was visualised in Figure 65. Next the SERS spectra were scrutinised.

Table 14 Surface plasmon resonance bands of 300 nM EL- 0.15 nM AgHA NP conjugates in media with glutathione gradient 0, 2, 5, 10 and 50 mM GSH; all at 0, 1, 4 and 24 hours.

	Surface Plasmon Resonance Band (nm)				
Time (Hours)	**0 mM GSH**	**2 mM GSH**	**5 mM GSH**	**10 mM GSH**	**50 mM GSH**
0	417	413	414	414	417
1	417	415	766	764	421
4	418	416	783	773	744
24	417	417	773	773	770

The SERS spectra were acquired on a CBEx handheld 638 nm spectrometer as detailed in 2.5.1. These were collected as 5 acquisitions per sample which were baseline corrected in Matlab 2014b and the area of the alkyne peak was integrated using the 'trapz' or trapezoidal integration function. These areas were averaged and the SD calculated, these were plotted as a timecourse in Figure 66. The 0 mM GSH control sample saw a small decrease in signal, however all other samples were already half the signal intensity at 0 hours to reduce further by an order of magnitude at 1 hour. There was just above background signal from 1 hour to 24 hours for samples 2, 5, 20, and 50 mM GSH. Considering the SERS intensity data alone it suggested that the GSH displaced the EL from the surface. However, it is clear from the extinction spectra and SPR bands that it could have been destabilised particles that were responsible for SERS signal loss.

Glutathione has sulfur atoms which are known to displace more weakly associated analytes and form strong covalent thiol bonds with the surface of the NPs. It cannot be ruled out that this did not take place to a certain extent but due to time restrictions the experiment could not be repeated with a lower GSH concentration to test this theory further by using lower concentrations in a titration approach. However, the literature would suggest it has a role to play in releasing EL from the particles once inside the cells, along with the lower pH.[165,168]

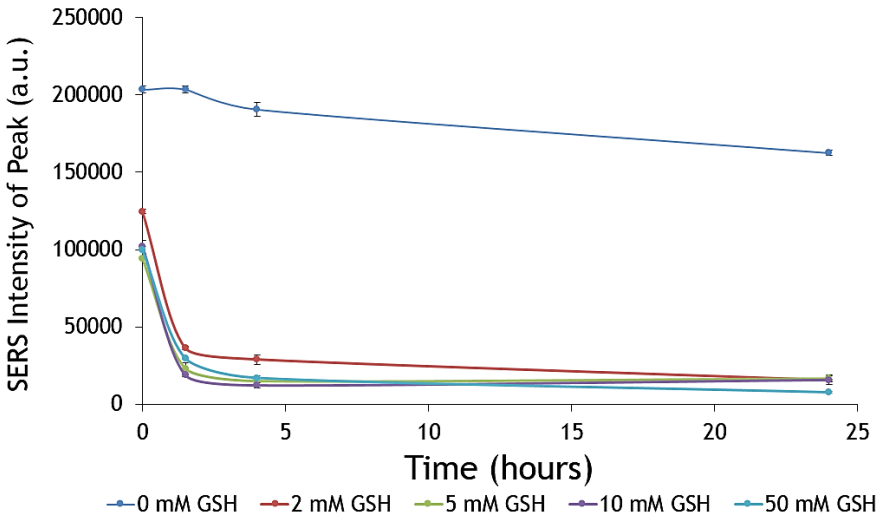

Figure 66 SERS stability of 300 nM EL-AgHA conjugates in media and glutathione (GSH) curve over time. DMEM media with 0, 2, 5, 10 and 50 mM GSH. Interrogated with CBEx 638 nm spectrometer at full laser power (40 mW at source, 23 mW at sample) for 0.2 s, 5 acquisitions averaged, intensity of the alkyne peak area (~1985 cm^{-1}) plotted ± SD.

5.6 Drug Loading onto NP and Uptake Quantification

5.6.1 UV-Visible Spectrometry Determination of Drug Loading onto NPs

The quantity of EL added to NPs to prepare the conjugate must not be assumed as being 100% bound to the surface. Therefore, efforts were made to quantify the EL washed off into the supernatant to ascertain the remaining quantity of attached EL. UV visible spectroscopy was tested during this study as a simple method to quantify EL from the absorbance of the drug. A similar method was used by Mathrusri Annapurna, Venkatesh and Krishna Chaitanya in 2014 to determine the quantity of EL in tablets to meet pharmaceutical standards.[170] However, the lowest concentration detected was 0.5 µg/mL (1.16 µM), which was above the 300 nM EL loaded onto the NPs in this case.[170] In order to establish empirically the lowest detection levels of the instrument, a concentration curve of EL in DMSO standards was prepared at 1 nM, 10 nM, 100 nM, 1 µM, 10 µM, 100 µM EL. The peak absorbance at 347 nm was used to plot a straight line graph. It was found that 1 – 100 nM was undetectable above the baseline of the DMSO blank (data not included). Subsequently, a concentration curve was performed from 100 nM up to 100 uM EL to calculate the LOD and limit of quantitation (LOQ).

To calculate the LOD and LOQ it is imperative to have a linear relationship between absorbance and concentration with an R^2 value close to 1. Thereafter, the gradient of the line (m) can be used along with the SD of the blank to calculate LOD ad LOQ. The equation of a straight line is seen in Equation 4 and the LOD and LOQ are in Equation 5 and Equation 6 respectively.

$$y = mx + c$$

Equation 4 Equation of a straight line.

$$LOD = (3\ x\ SD\ of\ blank)/gradient\ of\ the\ slope$$

Equation 5 Limit of Detection.

LOQ = (10 x SD of blank) / gradient of the slope

Equation 6 Limit of Quantification

The LOD and LOQ were calculated following Equation 5 Equation 6 to obtain 41.5 nM and 138.3 nM of EL respectively, as calculated from the concentration curve in Figure 67. This standard curve was used to ascertain the quantity of EL from the supernatant, unfortunately this LOQ was not deemed to be low enough to allow absolute quantification. When considering that there was 1 set of samples used in this standard curve measured thrice, the real LOQ would be even higher as the SD between replicates would have more variation. Subsequently LC-MS was employed as a means to determine EL loading to the surface of the NPs, as a more sensitive mode of analysis. The drug loading was crucial for comparison to free-EL efficiencies in the biological studies which followed in this study.

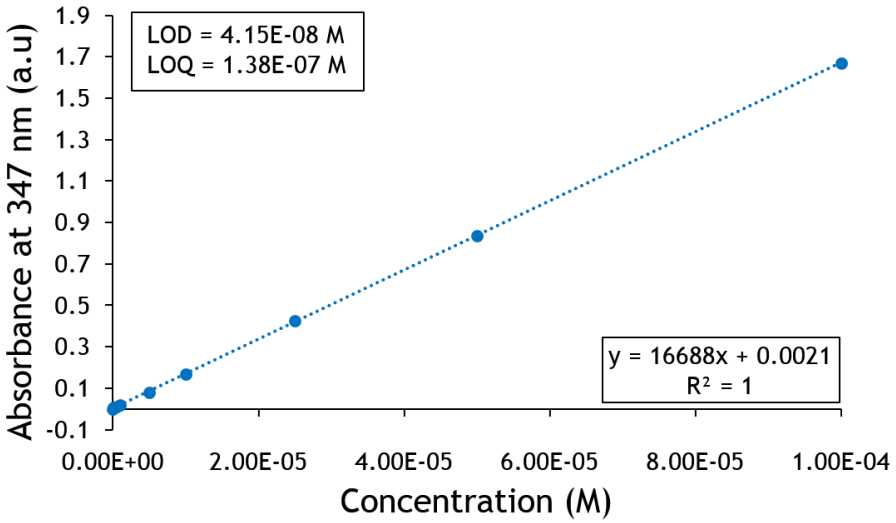

Figure 67 EL Concentration Curve by UV-Visible spectroscopy from 1 nM to 100 µM. N = 1.

5.6.2 LC-MS Determination of Drug Loading onto NPs

The LC-MS was carried out as outlined in section 2.2.7 for the AgHA and AuCt conjugates once a standard curve was obtained. The samples were prepared in triplicate for the standard curve of EL from 0- 300 nM EL and for 0 nM EL conjugates, 10 nM EL conjugates and 300 nM EL conjugates. Several blanks were ran between each sample and the standard curve to prevent carry over contaminating samples.

Figure 68 summarises all of the results: A) was the area integrated under the mass peak of 394 at retention time of between 4-5 mins for all samples, B) was the standard curve in log scale of the peak areas used to calculate the LOD and LOQ, C) was the intensity of EL from the supernatant of EL-AgHA conjugates, D) was similar to C except it was the peak area of the AuCt conjugates.

From the standard curve it was calculated that the LOD was 15 pM and the LOQ was 100 pM EL. The obvious conclusion from the peak areas in Figure 68 (C) and (D) that there was a difference in the adsorption of EL onto each metal type. In AgHA conjugate there was a steady increase in the quantification of the control (0 nM EL), 10 nM and 300 nM EL and indicated that not all of the EL was binding to the AgHA NP surface as it was present in the wash step supernatant. The concentration quantified from the 10 nM and 300 nM EL sample supernatants were 64 pM and 95 pM respectively. In the AuCt conjugates, all samples had a signal that was 2 orders of magnitude less than the AgHA conjugates. Furthermore, the 2 test samples of 10 nM and 300 nM were displaying data values similar to the zero EL control and therefore, it was concluded that no EL was released from the NPs during the wash step of the conjugates into the supernatant. The EL quantified in the AuCt conjugate supernatant of 10 nM and 300 nM samples were 6 pM and 4 pM respectively, these were well below the LOD and LOQ and were considered background.

The conjugates were also tested by LC-MS to assess what was actually bound, to do this the EL needed displaced from the NPs. The obvious reagent to do this was one with sulfur that binds strongly to the NP surface, such as 1,4-dithiothreitol (DTT). DTT was used in other studies where the displaced fluorescently labelled DNA, which was the functional element that was then assessed by fluorescence.[171] The DTT would be detrimental to any future samples on the MS column and consequently, an alternative approach was tested. The conjugates were centrifuged at the highest speed (14k rpm) in the centrifuge to try and force the EL off the surface. This test did not yield any signal above background and only the supernatant data was useful in this discussion, and it was inferred that the remainder was still bound to the NPs.

To summarise the LOQ value was 100 pM, which is just above the AgHA conjugate supernatant values. Technically, the EL quantity in the conjugate supernatants cannot be used as an absolute quantification. A trend that is undisputed, was that AgHA conjugates released more EL into the supernatant than the AuCt conjugates. Additionally, both NP types were monodispersed spheres of 40 nm with matching concentrations before preparing the conjugates. It was presumed that the

difference was due to the binding strength of the EL to the metal surfaces. The stronger binding affinity of EL to AuCt NPs corroborates the earlier data of the EL efficacy studies. It was statistically significant that the AgHA conjugates were better in their ability to kill the EL sensitive cells than the AuCt conjugates in the live/dead cytotoxicity study Figure 36.

After the EL loading was established as being almost absolute onto the particles at the IC_{50} of 10 nM and also at 300 nM EL, it was of interest to gauge the conjugate uptake by the cells. This was to estimate the final concentration of EL delivered. To do this, ICP-MS quantified the total metal content within a cell lysate sample and the conjugate uptake was estimated.

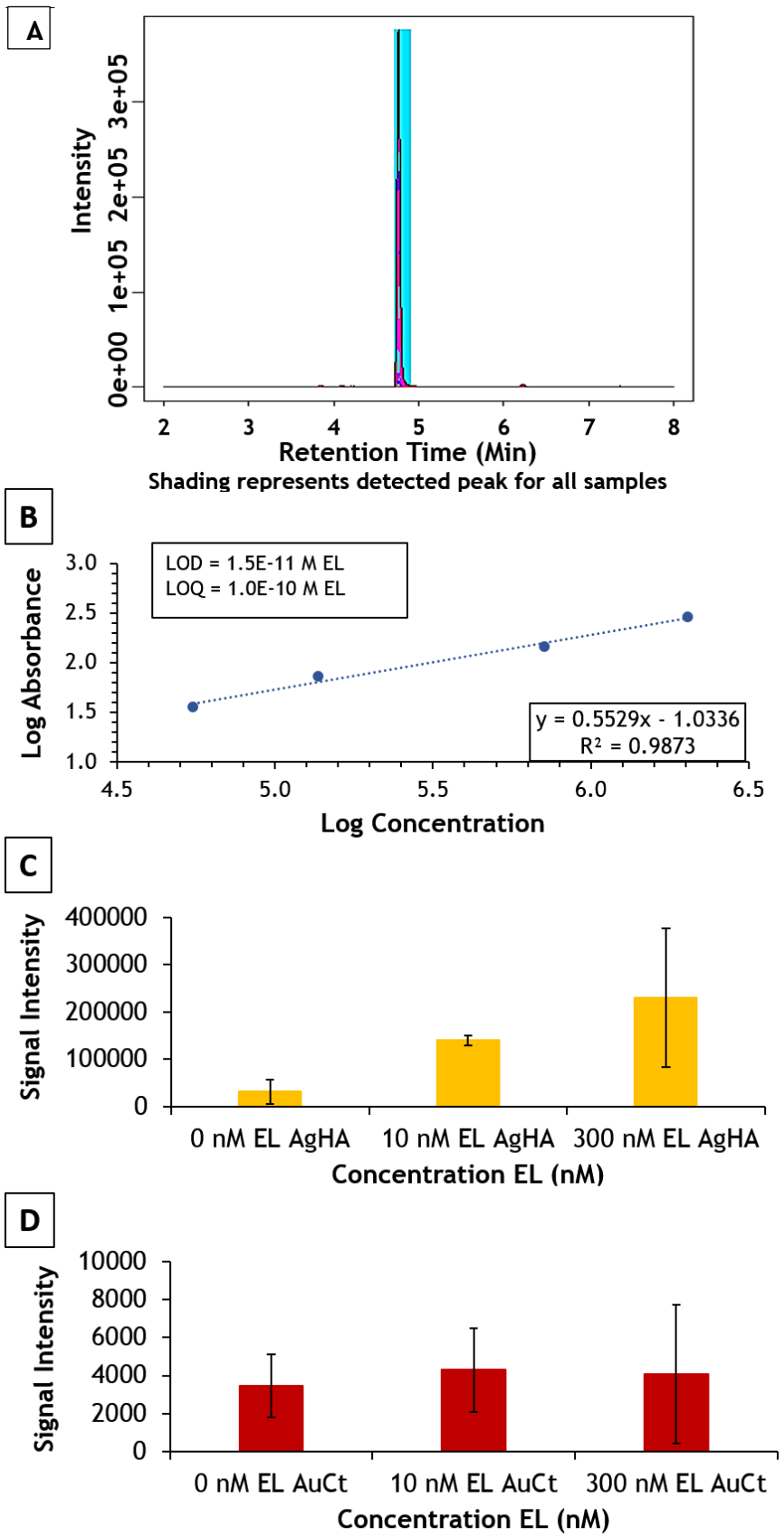

Figure 68 LC-MS of EL on AuCt or AgHA conjugates. A) Integration of peak for all samples highlighted in blue, B) standard curve of EL 36, 73, 146 and 292 pM, (C & D) Supernatant of 10 nM and 300 nM EL conjugates in for (C) AgHA conjugates and (D) AuCt conjugates.

5.6.3 ICP-MS Determination of Cellular NP & Conjugate Uptake

ICP-MS is routinely used to quantify metal content in samples following a standard calibration. LGC conducted the analysis on the mass spectrometer after samples were prepared by the author. The aim of the experiment was to quantify the conjugate uptake in the cells, at this stage H1355 cells were used with AgHA conjugate and AgHA NPs as a control. Two approaches were taken to calculate the total silver content per cell, one was to trypsinise the cells for detachment from the plates, and the other was to scrape the cells and a slow speed wash to separate the cells from the excess particle treatments. Figure 69 is a schematic overview for the trypsinisation cell dissociation method.

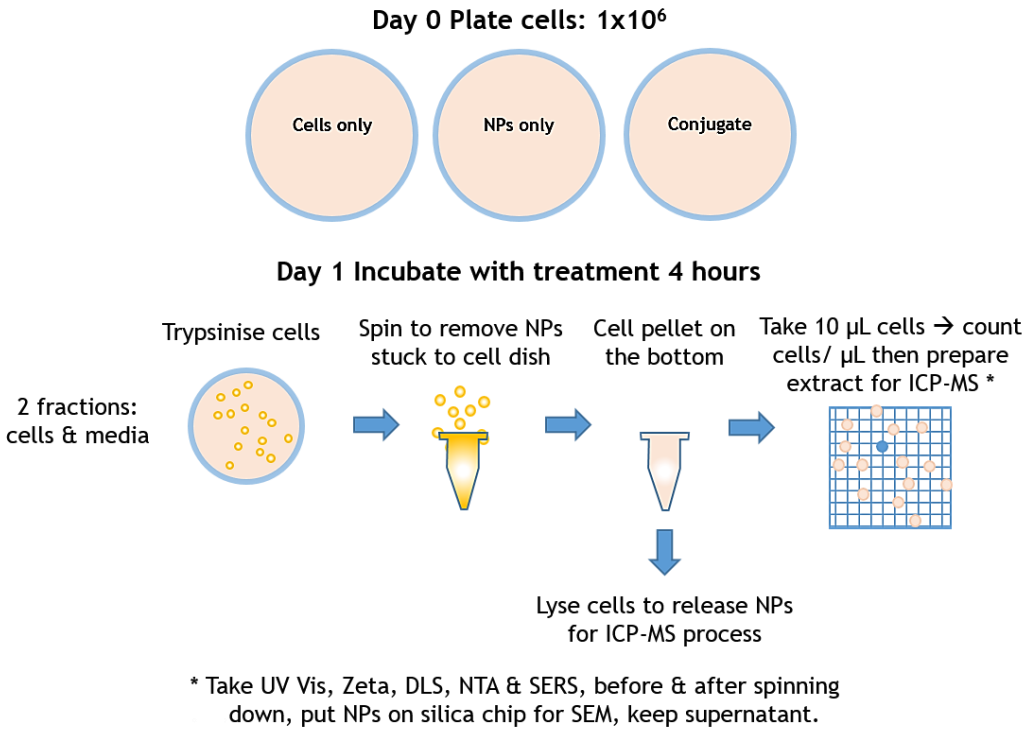

Figure 69 Experimental set-up for sample preparation of ICP-MS samples.

Aliquots were taken from each fraction in the cell preparation and lysis steps to estimate the NPs and conjugates present per cell before quantifying the silver content by ICP-MS. Several fractions were previously retained as described in 2.3.7; from the media, from the PBS wash step, from the supernatant where cells were centrifuged to separate them from the detachment buffer or PBS. Each of these fractions had the particles estimated per mL by NTA (see 2.2.6). The cells were also counted once removed from the dish. The NTA estimation was later compared to the ICP-MS quantification. The purpose of Equation 7 was to determine if it was a reliable method for routine experiments with NPs in cells, without the need to rely upon collaborators with specialist instrumentation and expertise to perform the

expensive quantification technique ICP-MS. To estimate the NP content per cell using the NTA estimations, the following calculation was carried out:

NP content per cell = stock NP or conjugate - media - PBS wash - supernatant from wash / number of cells

Equation 7 Particle uptake estimation per cell by NTA estimation.

All fractions were corrected for the total volume and dilution factors of each fraction *i.e.* 1 mL AgHA NP, 2 mL media, 1 mL PBS wash, 500 µL cells. The results were as seen in Table 15 with ~6000 and ~10000 particles per cell for AgHA NP and conjugates respectively.

Table 15 NTA of particles per H1355 cell

Sample	Particles Total in Cells	Number of Cells Total	Particles per Cell
AgHA NP	1.66×10^{10}	2.40×10^{6}	6197
300 nM El on AgHA NP	2.6589×10^{10}	2.70×10^{6}	9845

Three replicates were tested per sample to gain average ICP-MS data. The experimental quality controls and initial ICP-MS data handling is detailed within the report prepared by LGC in the appendix starting on page i.

Cells without particles acted as a negative control for metal content, this was reported in Table 16 for both scraped and trypsinised cells. The mass fraction in mg kg^{-1} was listed for each sample replicate, there were 3 for each treatment and 2 replicates for the controls. Trypsinised cells with AgHA NPs had on average 12.3 mg kg^{-1} with AgHA conjugate containing 13.2 mg kg^{-1}. Scraped cells with AgHA NPs measured 5.0 mg kg^{-1} with AgHA conjugate indicating 8.6 mg kg^{-1}. These values were in turn used to estimate particles/mL to give the starting [Ag] by considering the content of metal in other factors, such as washes and supernatants, as mentioned in Equation 7 and the results were listed in Table 15.

Subsequently the results from the ICP-MS experiment detailed in Table 16 were used to follow Equation 8 to calculate the particles/mL numbers and factor in the cell numbers to quantify the absolute number of particles / cell. They were: 9794 ± 54 particles / cell and 6667 ± 250 particles / cell respectively for conjugates and NPs (Table 17).

Table 16 Silver Mass Fraction in H1355 Cell Lysates

Type of sample	Customer name	Analyte	Unit	Mass fraction	Standard uncertainty	Expanded uncertainty (k=2)	Relative expanded uncertainty (%)	k
Control cells (trypsinised)	1A tryps (replicate 1)	Ag (total)	mg kg^{-1}	<LOQ*	N/A	N/A	N/A	N/A
	1A tryps (replicate 2)	Ag (total)	mg kg^{-1}	<LOQ*	N/A	N/A	N/A	N/A
Cells incubated with AgHA NPs (trypsinised)	1B tryps (replicate 1)	Ag (total)	mg kg^{-1}	12.5	0.3	0.6	5	2
	1B tryps (replicate 2)	Ag (total)	mg kg^{-1}	12.4	0.3	0.6	5	2
	1B tryps (replicate 3)	Ag (total)	mg kg^{-1}	12.1	0.3	0.6	5	2
Cells incubated with conjugate (trypsinised)	1C tryps (replicate 1)	Ag (total)	mg kg^{-1}	13.4	0.3	0.7	5	2
	1C tryps (replicate 2)	Ag (total)	mg kg^{-1}	13.1	0.3	0.7	5	2
	1C tryps (replicate 3)	Ag (total)	mg kg^{-1}	13.2	0.3	0.7	5	2
Control cells (scraped)	3A scrape (replicate 1)	Ag (total)	mg kg^{-1}	<LOQ*	N/A	N/A	N/A	N/A
	3A scrape (replicate 2)	Ag (total)	mg kg^{-1}	<LOQ*	N/A	N/A	N/A	N/A
Cells incubated with AgHA NPs (scraped)	3B scrape (replicate 1)	Ag (total)	mg kg^{-1}	4.8	0.1	0.2	5	2
	3B scrape (replicate 2)	Ag (total)	mg kg^{-1}	5.2	0.1	0.3	5	2
	3B scrape (replicate 3)	Ag (total)	mg kg^{-1}	5.1	0.1	0.3	5	2
Cells incubated with conjugate (scraped)	3C scrape (replicate 1)	Ag (total)	mg kg^{-1}	8.2	0.2	0.4	5	2
	3C scrape (replicate 2)	Ag (total)	mg kg^{-1}	9.3	0.2	0.5	5	2
	3C scrape (replicate 2)	Ag (total)	mg kg^{-1}	8.2	0.2	0.4	5	2

*LOQ: 0.014 mg kg^{-1}

Correlating the NTA data to the ICP-MS quantification was found to be an acceptable estimation for future studies. The averages by ICP-MS and NTA estimation were both in the order of 10^3 and the error from NTA to ICP-MS results were within ±0.5 % for conjugates and ±4 % for NPs. Therefore, NTA can be used in any future studies to estimate the particles uptaken by a cell. There was a slightly greater uptake of conjugates *versus* NPs but it was not at a statistically significant level and was still within the same order of magnitude. The cell scraping method yielded a lower recovery of metal content *versus* the trypsinisation, it was likely that this method was less efficient at harvesting the cells with NPs present.

Table 17 ICP-MS quantification of silver content per H1355 cell

Type of Sample	[Ag] (mg/kg)	Particles/mL	Expected* (particles/mL)	Cell No. (cells/mL)	Particles / cell
Control cells (3A)	<LOQ (0.014)				
Cells & AgHA NP (3B)	5.03	1.54×10^{10}	1.66×10^{10}	2.40×10^{6}	6667
Cells & conjugate (3C)	8.56	2.63×10^{10}	2.70×10^{10}	2.70×10^{6}	9794

*Expected was estimated by NTA, calculated particles per mL from ρ_{Ag}=10.49 g/cm^3

These ICP-MS data obtained and presented in Table 17 reflects what would be expected from observations within the TEM images of this thesis. The data here is also in agreement with observations in the wider literature, from ICP-MS and alternative techniques. Hsiao *et al.* used ICP-MS to measure Ag NP uptake per cell from incubating with 10 µg/mL and found that each cell contained on average 2000 NPs.[172] Alternatively, Rosman *et al.* microtomed consecutive slices of fixed cells to image and quantify by TEM. Thereafter, pseudo-3D TEM was conducted by measuring the number of particles in aggregates and counting aggregates per 1 µm slice of a cell, they were able to estimate 2700 ± 1100 silver spheres per cell.[173]

To calculate the total EL loaded onto conjugates, LC-MS of the supernatant (Figure 68) was considered along with the NTA particle number estimation (Table 15), cell counts and the ICP-MS quantification (Table 17). LC-MS showed almost absolute attachment and therefore, 894973 molecules of EL were delivered per NP functionalised with 300 nM EL. The number of particles in 1 mL of 0.34 nM colloid was 8.68×10^{10}. ICP-MS measured 9794 conjugates per cell and the cell counts were 2.7×10^{6} cells in total. These values are summarised in Table 18 and used to calculate the final EL delivery. This equated to a final delivery of 39 nM EL that the cells were receiving. To remove doubt, that does not include those conjugates attached to *e.g.* the plastic-ware of the cell culture dish. It would be interesting know the absolute concentration of free-EL uptaken by cells, this could be done in future by LC-MS of the lysed cells, it will not necessarily be the full amount that is incubated and delivered into the cell. The delivery could then be controlled to treat cells with equivalent molecules of drug and directly compare the efficacies in this manner, as a normalised comparison of molecules of EL per cell.

Table 18 Summary of variables considered for final delivery of EL by AgHA conjugates. Letters in first column are used as a key for the description of how the numbers were derived, descriptions are in the middle column and the values are in last column.

A	**Particles / mL**	**8.68×10^{10}**
B	**MW EL (g)**	**429.9**
C	**Molecules of EL / mL in 1M** *[=B*Avogadro's constant*0.001]*	**2.59×10^{23}**
D	**EL molecules in 1 mL of 300 nM conjugate** *[=C*(3 x 10^{-7})]*	**7.77×10^{16}**
E	**EL molecules / NP** *[=D/A]*	**8.95×10^{5}**
F	**Cells in sample**	**2.7×10^{6}**
G	**NPs per cell by ICP-MS**	**9794**
H	**Total EL molecules in cells** *[=E*F*G]*	**2.37×10^{16}**
I	**Overall concentration of EL (M)** *[=H/Avogadro's Constant]*	**39×10^{-9}**

Moving forward, single particle ICP-MS (spICP-MS) experiments would establish whether the silver uptaken by cells is present in NP form, as ionic silver or a mixture of both. Furtheremore, it would yield information on the diameter and number concentration of the internalised NPs.

Determining silver ions present per cell *versus* the NPs would inform more on the toxicity effects of the bare NPs *versus* the conjugate form to the cell. This was achieved by using spICP-MS. The samples were prepared as before for ICP-MS on H1355 cells, but on this occasion, the HCC827 cells were used and only the trypsinisation detachment method was followed to harvest the cells.

spICP-MS quantifies the number and size of NPs. The frequency of the signal detection indicates particle number and the intensity of the signal is correlated with the size of the particle, due to amount of chemical element present.[172] This technique works well on spherical particles to calculate particle number and size present in a sample, which can be extended to particles per cell, if the cell number in a sample lysate is known.

The particles per cell were calculated and reported as predicted cell uptake from the NTA estimations in Table 19. These were 9.09×10^{6} and 2.38×10^{7} for AgHA NPs and conjugates respectively, which were several orders of magnitude greater than the previous experiment on H1355 cells. This could have been experimental error or that there appeared to be 20 times less cells than were present in the H1355 experiment therefore the estimated uptake appeared greater. On this occasion, the ICP-MS calculations were likely be more accurate than the NTA data as the total particles per cell were expected as hundreds of thousands not millions.

Table 19 NTA estimation of particles per HCC827 cell

Sample	Particles Total in Cells	Number of Cells Total	Particles per Cell
AgHA NP	7.72×10^{12}	8.50×10^{5}	9.09×10^{6}
300 nM EL on AgHA NP	1.07×10^{13}	4.50×10^{5}	2.38×10^{7}

LGC conducted the quantification of silver per sample by ICP-MS. In Table 20 the average content of the AgHA NP sample was 9.0 mg kg^{-1} and the AgHA conjugate was 8.9 mg kg^{-1}. This demonstrates equal uptake of the NPs and conjugates from total silver content.

Table 20 ICP-MS on HCC827 cells with AgHA NPs and EL-AgHA conjugates.

Type of sample	Customer name	Analyte	Unit	Mass fraction	Standard uncertainty	Expanded uncertainty (k=2)	Relative expanded uncertainty (%)	k
Control cells (trypsinised)	Cell Tryp (replicate 1)	Ag (total)	mg kg^{-1}	<LOQ*	N/A	N/A	N/A	N/A
	Cell Tryp (replicate 2)	Ag (total)	mg kg^{-1}	<LOQ*	N/A	N/A	N/A	N/A
	Cell Tryp (replicate 3)	Ag (total)	mg kg^{-1}	<LOQ*	N/A	N/A	N/A	N/A
Cells incubated with AgHA NPs (trypsinised)	Ag tryps (replicate 1)	Ag (total)	mg kg^{-1}	8.9	0.2	0.4	5	2
	Ag tryps (replicate 2)	Ag (total)	mg kg^{-1}	9.3	0.2	0.5	5	2
	Ag tryps (replicate 3)	Ag (total)	mg kg^{-1}	8.8	0.2	0.4	5	2
Cells incubated with conjugate (trypsinised)	Ag C tryps (replicate 1)	Ag (total)	mg kg^{-1}	8.8	0.2	0.4	5	2
	Ag C tryps (replicate 2)	Ag (total)	mg kg^{-1}	9.1	0.2	0.5	5	2
	Ag C tryps (replicate 3)	Ag (total)	mg kg^{-1}	8.9	0.2	0.4	5	2

*LOQ: 0.03 mg kg^{-1}

The total content of AgHA conjugates and NPs in the cell samples were calculated following Equation 8 with the data from Table 20 and the results are presented in Table 21.

$$\boldsymbol{Cp} = ((\mathbf{6} * \boldsymbol{Cm})/(\boldsymbol{dp}^{\mathbf{3}} * \boldsymbol{\pi} * \boldsymbol{\rho p})) * \mathbf{10}^{\mathbf{15}}$$

$\boldsymbol{Cp}$= particle number concentration (particles/mL)

$\boldsymbol{Cm}$= mass concentration of particle suspension (mg/kg)

$\boldsymbol{dp}$= spherical equivalent diameter of the particle (nm)

$\boldsymbol{\rho p}$= bulk density of the particle (g/mL)

Equation 8 Particle Number Concentration Calculation

To convert from the total content of silver (in mg kg^{-1}) to particles/mL, it was assumed the particles were spherical and the size was homogenously 40 nm. The

density of the silver was considered to be the same as the bulk (10.49 g/mL). The particles /mL values were calculated as 2.53 x 10^{10} for AgHA conjugates and 2.56 x 10^{10} for AgHA NPs samples, from the mass concentration values of silver at 8.9 mg kg^{-1} and 9.0 mg kg^{-1} respectively from Table 20. When factoring in the cell number counts (per mL) the final quantification was 52623 and 30121 particles in AgHA NPs and AgHA conjugates per cell respectively (Table 21). This is 1 order of magnitude greater than in the H1355 cell line and therefore, the HCC827 cells have a slightly greater uptake of particles. The caveat in these calculations, was that these figures assumed that all the silver content quantified is in NP form, and does not consider that a percentage of this could be ionic silver content.

spICP-MS can differentiate between the two forms of silver *i.e.* particulate and ionic; not only can it quantify particle number, it can also measure the size distribution of the particles.

Table 21 ICP-MS quantification of silver content per HCC827 cell.

Sample	*Cm* (mg/kg)	*dp* (nm)	*Pp* (g/mL)	*Cp* (particles/mL)	Cell No. (cells/mL)	Particles / cell
AgHA NPs	9.0	40	10.49	2.56 x 10^{10}	8.50 x 10^{5}	56263
AgHA Conjugates	8.9	40	10.49	2.53 x 10^{10}	4.50 x 10^{5}	30121

Further to this, the average particle size was estimated for the AgHA conjugate by spICP-MS in Figure 70. The frequency of < 50 nm particles were the greatest in number and those > 50 nm tailed off, it showed that the size was heterogeneous and not as monodispersed as expected. This conflicted with the SEM and TEM data presented previously and was thought to be procedural related. LGC carried out internal controls of aggregation studies with commercially available silver NP standards, which were resistant to any aggregation. This did not take into account that many pre-made NPs are surface capped for stability and that the surface chemistry would differ from the in-house synthesised AgHA NPs used for the preparation of the conjugates in this experiment. Additionally, the cell lysis buffer used during the cell sample preparation steps induced precipitation of NPs, due to a high salt content. In future, a sonication method is advisable to lyse the cells, avoiding any aggregation issues. Noteworthy to this discussion, is that previous studies in the field have indicated that aggregates can form within the cell before any lysis steps take place.[172] Perhaps the size distribution was useful information about the level of agglomeration that takes place within the cell. Next the ionic silver content of the cells was considered.

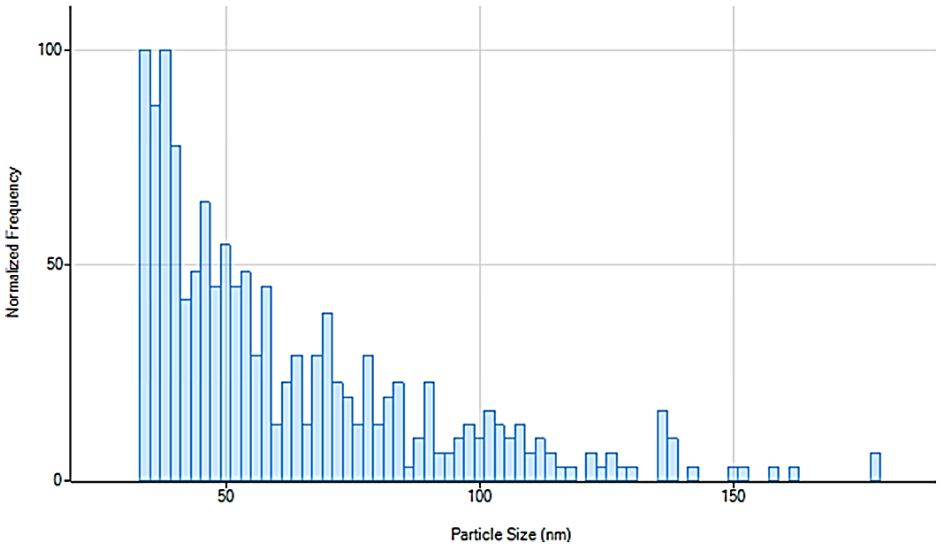

Figure 70 Particle size estimation from single particle Inductively Coupled Plasma-Mass Spectrometry (spICP-MS) of silver conjugates

Silver ions are known to be oxidising in their nature, which can cause toxicity to the cell if present in overwhelming quantities, such that antioxidants like GSH cannot counteract their effects.[138,174]

Table 22 summarises the NP content as NP kg^{-1} and the ionic content as mg kg^{-1}. The AgHA NPs were 5.3 x 10^{12} ± 3.8 x 10^{11} NP kg^{-1} and the AgHA conjugates were 5.3 x 10^{12} ± 4.4 x 10^{11} NP kg^{-1} but as mentioned earlier, the true NP per cell was difficult to estimate due to the aggregation effect. Table 23 uses the average Ag particles to calculate the number of particles / cell from the spICP-MS, which is exclusive of the silver ion values.

Table 22 spICP-MS on HCC827 cells with AgHA NPs and EL-AgHA NP conjugates, total silver and ionic silver content.

Type of sample	Customer name	Ag NPs (d>30 nm)			Ionic Ag		
		Mean (NP kg^{-1})	SD (NP kg^{-1})	RSD (%)	Mean (mg kg^{-1})	SD (mg kg^{-1})	RSD (%)
Control cells (trypsinised)	Cell Tryp	<LOQ*			<LOQ*		
Cells incubated with AgHA NPs (trypsinised)	Ag tryps	$5.3 \cdot 10^{12}$	$3.8 \cdot 10^{11}$	7	3.4	0.1	3
Cells incubated with conjugate (trypsinised)	Ag C tryps	$5.3 \cdot 10^{12}$	$4.4 \cdot 10^{11}$	8	4.8	0.6	12

*LOQ for ionic Ag was 0.65 mg kg^{-1} and LOQ for Ag NPs (d>30 nm) was $7.3 \cdot 10^{6}$ NP kg^{-1}

These final particles / cell results for AgHA NPs and AgHA conjugates samples were 11778 and 6235 respectively (Table 23). This quantified half the amount of particles

present in the conjugate sample in comparison to the bare AgHA NPs. Other valuable information derived from spICP-MS were the levels of ionic silver in the samples, which were found to be 3.4 ± 0.1 mg kg^{-1} and 4.8 ± 0.6 mg kg^{-1} for cells incubated with AgHA NPs and conjugate respectively. These levels of silver ions account for approximately 38% and 54% of the total silver found in cells incubated with AgHA NPs and conjugates (Table 23). In summary from spICP-MS, the ionic and particualte silver content was determined and from this it was established that the conjugates release more silver ions but the total silver (ionic plus particulate) uptaken by cells with AgHA NPs and conjugates are similar.

Table 23 spICP-MS quantification of silver content per HCC827 cell as ions and particles for AghA NPs and AgHA conjugates.

Sample	*Ag Particles (NP/kg)*	*Ionic Ag (mg/kg)*	Ionic Ag Content (%)	Cell No. (cells/mL)	Particles / cell
AgHA NPs	5.3 x 10^{12}	3.4	38	8.50 x 10^{5}	11778
AgHA Conjugates	5.3 x 10^{12}	4.8	54	4.50 x 10^{5}	6235

The underlying mechanisms for this result of different ionic content in AgHA NPs and conjguates are unclear. The functionalisation process may have displaced some of the ions present from colloidal synthesis. Subsequent release of the EL that replaced the surface ions from colloidal synthesis of the NP would leave the metal exposed to the cell environment and more vulnerable to oxidation and loss of silver ions. Equally at the point of functionalisation, perhaps during the wash step, the EL molecules act as a 'net' to hold ions that are otherwise allowed to be freely washed from the surface of the bare NPs. This would require further examination to conclude definitively why the conjugate released more silver ions.

5.7 Summary

Chapter 5 conclusions are shown in bullets per sub-section below for clarity:

- uptake of particles by 3D SERS showed internalisation starts from 0.5 hours onwards,
    - AgHA conjugates gave a greater signal than AuCt conjugates, even when interrogated at 633 nm,
    - label free-EL was observed being released from the particle intracellularly,
    - conjugates & NPs resulted in an intracellular distribution over time excluding the nucleus,

    - the same distribution and Raman signal was observed in live cells within a microfluidics platform and it was able to utilise 532 nm laser;
- correlative SEM and TEM demonstrated AgHA and AuCt particles were:
    - equivalent size and morphology of 40 nm spheres,
    - conjugates were settling on the surface and uptaken via microvilli,
    - AgHA conjugates and AuCt conjugates had different level of agglomeration inside the cell,
    - AgHA conjugates were observed more frequently within mitochondria,
    - conjugates were seen within and outwith membrane bound organelles (lysosomes, autophagoslysosomes, endosomes and mitophagosomes),
    - necrosis was observed more frequently in the H1355 cells than in HCC827 in response to AgHA conjugates;
- lysosomes immunofluorescence was inconclusive for co-localisation as staining was not substantial enough;
- DF and IFA mircoscopy with DAPI, ER and lysosome tracker showed some co-staining of lysosomes with NPs but had some artefactual fluorescence issues;
- pH and GSH release mechanism study demonstrated that both can cause a decrease in signal that could be correlated to EL desorption by the lysosomes or a digestive organelle environment;
- drug loading LC-MS study proved almost complete attachment of EL in 300 nM binds to the surface of AuCt conjugates and marginally less in AgHA conjugates, but only on the verge of the LOQ of 100 pM;
- ICP-MS quantified conjugates as inside the cell at ~9000 and estimates were made of 39 nM final concentration EL delivered to the cell population by AgHA conjugates;
- spICP-MS resulted in a lower ionic concentration of silver in the bare NP sample than the conjugate sample (38% compared with 54%);
- spICP-MS quantified double the number of particles in AgHA NPs sample cells than in AgHA conjugate cells (11778 compared with 6235 repectively).

This is the first known report to the author at the time of writing of spICP-MS quantitification of ionic and particulate AgHA NPs and drug conjugtes in cell samples, other reports have detected particle number from environmental waste contaminants in water samples only.[175-177] Combined these results prove that the conjugates were being internalised to deliver the EL, through desorption from the NP surface and that there was a greater affinity of EL towards AuCt than AgHA NP

surface, and that H1355 cells were more sensitive to the 'control' AgHA NPs. This helped explain the toxicity data from chapter 4, where AgHA conjugates were more effective against HCC827 cells than AuCt conjugates and the cell death from all silver samples in H1355 cells. A phospho-proteomic study would help to elucidate any difference between free-EL delivery and nanodelivery by AgHA and AuCt conjugates, to both the sensitive and insensitive cell lines, over time on the EGFR biomarker signalling and its downstream effects. RPPA was the ideal platform to analyse multiple treatment variables and signalling responses at once, in a high throughput approach.

Chapter 6 Targeted Proteomic Analysis

"Above all, don't fear difficult moments. The best comes from them."
Rita Levi-Montalcini, Nobel Prize for Physiology or Medicine 1986

6.1 Introduction to RPPA

RPPA is a high throughput proteomic analysis platform used in drug discovery pipelines to screen libraries of compounds in multiple cell lines at once. This can be to repurpose an existing treatment or to probe treatments that have not reached the clinic before. From this, both on and off target effects can be gauged by selecting 50-150 antibodies. To understand more about the mechanistic effects the treatments are having on the cells, post-translational modifications can be investigated.

Signal modulation can be assessed by activation or inhibition of certain signalling pathways. Here, the pathway of interest relates to the biomarker of the drug's target, EGFR. Moreover, the effects of introducing NPs into the nanodelivery system must be scrutinised to assess the biological impact that they may have, and to build a more complete picture of any gross signalling or mechanistic differences of delivering the EL in a different formulation. Therefore, stress pathways, cell-death mediators and apoptotic markers were included in the study design, alongside the proteins that are downstream of EGFR and the cell cycle arrest markers that should be influenced by effective EL treatment.

This detailed study hopes to explain further the reasons that the AuCt conjugate was not as effective as the AgHA conjugate in the EL-sensitive line, and why H1355 cell line was sensitive to AgHA NPs, by investigating signalling events other than just the on-target phosphorylation of EGFR, that previous studies using Western blots and immunofluorescence have focussed on. Targeted proteomic analysis was applied to compare insensitive and sensitive cell line responses to: EL delivery type (nano *cf* free-EL), NP type (AuCt *cf* AgHA) and duration of treatment incubation (4 hours *cf* 24 hours). RPPA was the approach used to investigate these multiple variables in the two cells lines.

6.2 Identification of Antibodies for Pathway Selection

6.2.1 Questions to Ask of NPs, Conjugates, EL, Insensitive and Sensitive Cell Lines

The questions which RPPA was employed to answer were:

1. Are AuCt and AgHA conjugates as effective as the free-EL?
    a. At both 4 hours and 24 hours *i.e.* is there a delay in effect owing to the additional time NPs take to enter the cells and release EL?
2. What are the differences in response to treatments in the EL-sensitive and EL-insensitive cell lines?
    a. Can the conjugates enhance any response to the treatment with the insensitive line?
3. Is there a difference in response to AgHA or AuCt NPs and/or conjugates in terms of stress and apoptotic pathways?

To resolve the above queries, many considerations were taken into account, for example EL is an anti-proliferative agent. Therefore, the cell cycle should be perturbed in respondent cells. AgHA NPs are known to leach silver ions, which elevate ROS in the cell, inducing stress response pathways and cell-death mediators. The form of cell-death from NPs and EL is also interesting as to whether it is programmed apoptosis or unprogrammed necrosis. Therefore, apoptotic signalling should be explored, as inhibited EGFR would result in less anti-apoptotic signalling from the downstream protein Akt's effects.

6.2.2 Hypothesis of Differential Responses from the Cell to Treatments

Figure 71 shows a schematic of the hypothesised relationships between the different treatments and the cells' signalling responses. This diagram gives insight into the experimental design and the logic behind the antibodies selected to explore the signalling events within the samples through RPPA.

In Figure 71 the Venn diagram highlights what was anticipated to be differentially affected per segment, or if they appear within the centre of the Venn diagram, it is thought the events or protein expression will be similar in all samples. Apoptosis and housekeeping proteins were expected to be present at similar levels in all treated samples, programmed cell death was expected in all as a response to either the NPs, the EL or the combination of both. It was anticipated that the stress pathways and cell death mediators would be elevated in the NP and conjugate samples, especially in the silver treatments as a response to the creation of ROS. Finally, it was hypothesised that inhibition of EGFR and cell cycle arrest would only

be seen within the EL and conjugate treated samples, as a specific response to the SM-TKI, it was not expected to be observed in the NPs alone.

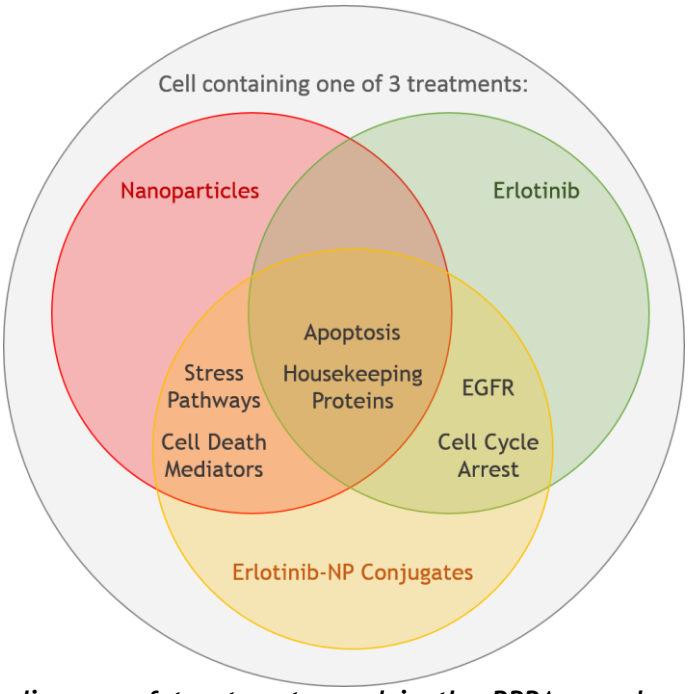

Figure 71 Venn diagram of treatments used in the RPPA samples and anticipated response to aid in antibody selection for the study. Those in the centre expected to be similar in all treated samples (EL, NPs and conjugates) with evidence of apoptosis and housekeeping proteins present, stress pathways and cell death mediators expected to be elevated in NPs and conjugates and inhibition of EGFR and cell cycle arrest anticipated to only be in the EL and conjugate treated samples.

6.2.3 EGFR Signalling Pathway

The first network explored with EL being an inhibitor of EGFR, was the ErbB (erythroblastosis oncogene B)/HER (human epidermal growth factor receptor) signalling pathways. Therefore, several key proteins were selected from downstream of EGFR in the signalling pathway of the receptor, as a basis to select antibodies. These antibodies were used during the RPPA study to investigate the cellular response to the treatments. These are summarised in Figure 72 which is adapted from Cell Signalling Technologies (CST) website. The two main players in the downstream signalling are Mitogen Activated Protein Kinase (MAPK) which promotes cell growth and Akt which regulates apoptosis and cell survival.[178]

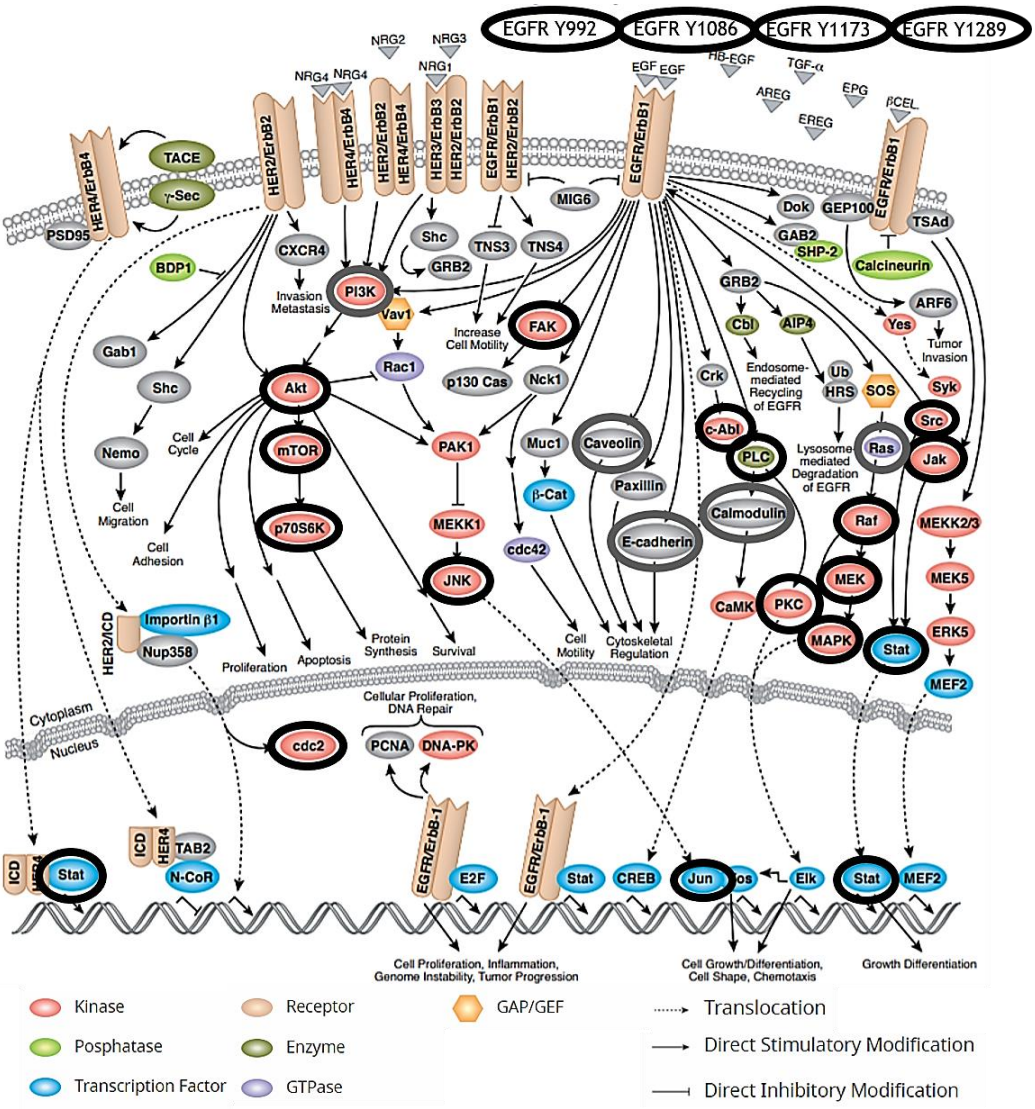

Figure 72 EGFR signalling pathway with proteins selected for RPPA, those in grey are either phospho or total proteins only, those in black are both phospho and total proteins selected. Illustration adapted and reproduced courtesy of Cell Signaling Technology, Inc. (www.cellsignal.com).

6.2.4 Other Pathways and the Proteins Selected

To understand the signalling events and changes in expression levels of proteins of interest, the respective phosphorylated protein pairs were also selected. This was to understand the activation and inhibition exerted by the various treatments. A summary of the 124 selected antibodies, their order numbers and suppliers are tabulated in Table 26 Appendix B page i. The antibodies are laid out in the slides and arrays in which they were incubated (first 2 columns of the table), there are also 3 rabbit Ab and 1 mouse Ab control arrays included for the purpose of background signal evaluation.

6.2.5 RPPA Experimental Process

The experimental process followed for the RPPA is seen in Figure 73, where it flows from plating cells, through to data normalisation, used to process data for heat maps and interactive networks.

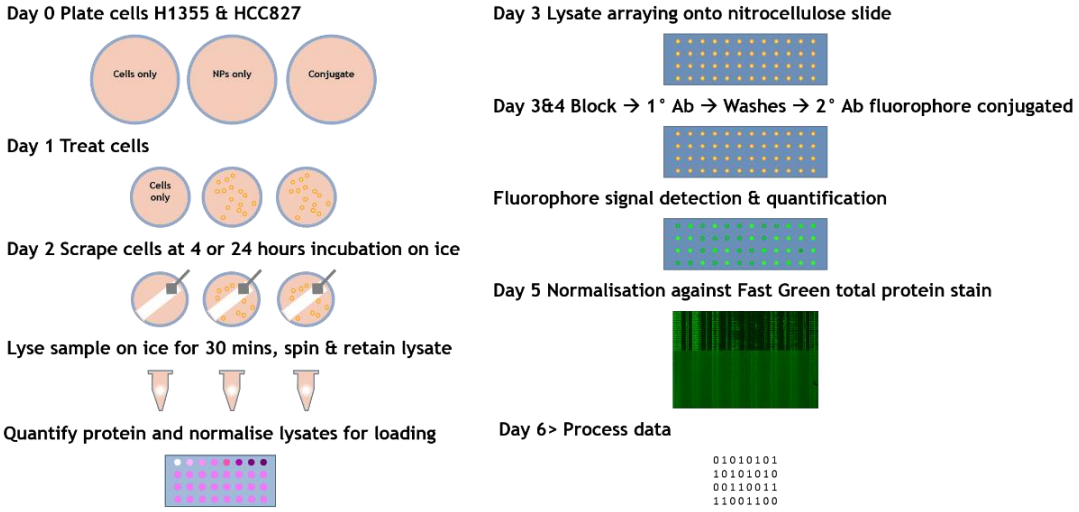

Figure 73 Schematic of the experimental work flow for RPPA analysis followed from plating cells through to harvesting lysates, BCA assay and normalising protein content of lysates, spotting samples onto array, probing with antibodies, signal detection and quantification, normalisation of signal against total protein loaded and finally, the data processing.

It was pertinent to make the RPPA experiment as biologically-relevant as possible. Slight changes are easily detected through inhibition of post-translational modifications at lower concentrations of EL than was used up to this point in the rest of this study (imaging experiments used 300 nM EL). Western blots were performed with different concentrations to determine the optimum concentration of EL to treat the cells to collect lysate to perform the RPPA with. The justification for altering the EL concentration from the SERS cell maps and other correlative studies, is that there needed to be enough cells present after 24 hours to collect sufficient protein from cell lysates. If the cells were treated with a higher level of EL and were on the whole a dying population, then the subtle responses to the free-EL and conjugate would be masked by death signalling. From Western blots such as Figure 31, it was determined that the IC_{50} level of EL would be most suitable, as 10 nM EL inhibited most of the pEGFR expression, but is not enough to have overwhelmed the whole cell population into apoptosis.

The cells were plated as per Western blot protocol 2.3.9, with conjugates prepared as per 2.1.2. The cells were incubated for 4 or 24 hours with each of the treatments; DMSO vehicle control, 10 nM EL, AgHA NP control, AgHA 10 nM EL conjugate, AuCt NP control and AuCt 10 nM EL conjugate. The cells were harvested and lysed as per the protocol in the RPPA section 2.3.10. The protein level was quantified per cell

lysate sample to allow normalisation to 2 mg/mL by following the BCA method in Western section 2.3.9. Thereafter, Kenny MacLeod from IGMM, University of Edinburgh arrayed the lysates, blocked, washed, incubated and probed for signal as per the RPPA protocol in 2.3.10.

To give an indication of treatment efficacy, bright field images were acquired for each treatment in two of the biological replicates, these are presented in Figure 74. It is clear that the H1355 cells are sensitive to both the AgHA treatments at 24 hours incubation and that the HCC827 cell line was responding to treatment from 10 nM EL and 10 nM EL-AgHA conjugates. Additionally, the HCC827 cell line was unaffected by 10 nM EL-AuCt conjugates and the DMSO control had affected the number of cells slightly in one replicate of the control. The bright field images reflect the data obtained in the cytotoxicity and efficacy Chapter 4.

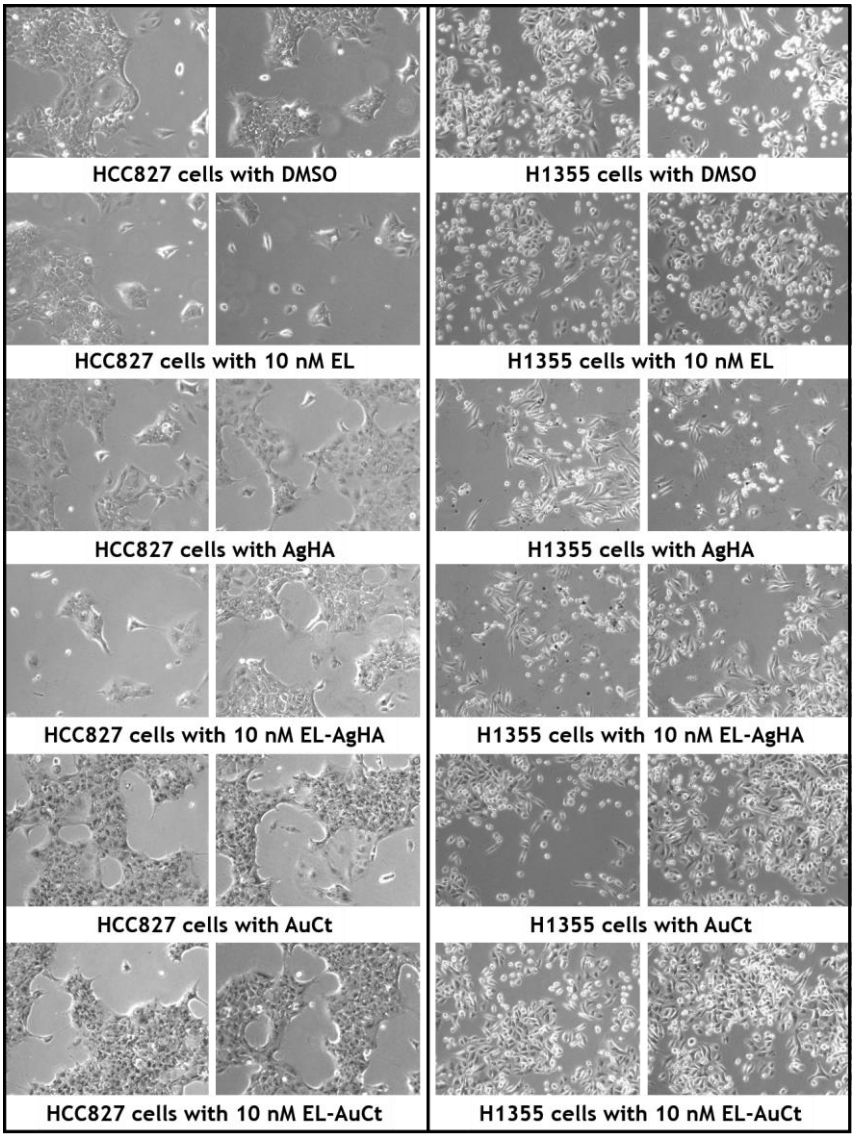

Figure 74 Bright field images of cells that were harvested at the 24 hour time point for the RPPA experiment. Left are HCC827 cells with treatments, right are H1355 cells. Two biological replicates are included per treatment: DMSO vehicle control, free 10 nM EL, AgHA NPs, 10 nM EL-AgHA conjugate, AuCt NPs and 10 nM EL-AuCt conjugate.

6.3 Data Processing Pipeline

RPPA experiments produce tens of thousands of data points that can be cumbersome to manually handle and produce a concise experimental readout. There are 3 main groups of processing techniques: unsupervised learning including PCA, to reduce dimensionality of data, and clustering techniques such as hierarchical clustering analysis (HCA); supervised learning, which predicts classes and requires a training data set for *e.g.* random forests; and finally, structured knowledge including network analysis, using interaction network integration, or functional enrichment and pathway exploration employing gene set enrichment analysis. Here, there were not enough data sets to train and use supervised learning. Hence, only unsupervised learning and structured knowledge will be used. Cluster analysis highlights class structures and overall changes, which are subsequently supplemented by the network analysis approach. This uses a structured protein knowledge to map the effects graphically on the pathways within a network.

The data processing pipeline used to reduce thousands of data points to an expression heat map is best described graphically as a workflow (Figure 75). First, the quality of the data must be validated for linearity across the 2-fold dilution series carried out per protein sample that results in 4 denatured cell lysate spots. The intensity of these 4 dilutions were plotted per sample and the R^2 value was calculated, from this a threshold was used to discard any samples that did not meet the standards pre-determined, *i.e.* a linearity score of <0.65 were removed from further analysis. All the samples which met this requirement were then normalised to the total protein loaded, which was quantified by Fast Green staining. From this point onwards, the data was treated as shown briefly in Figure 75. The raw data acquired were summarised into figures within the Appendix B from page xviii.

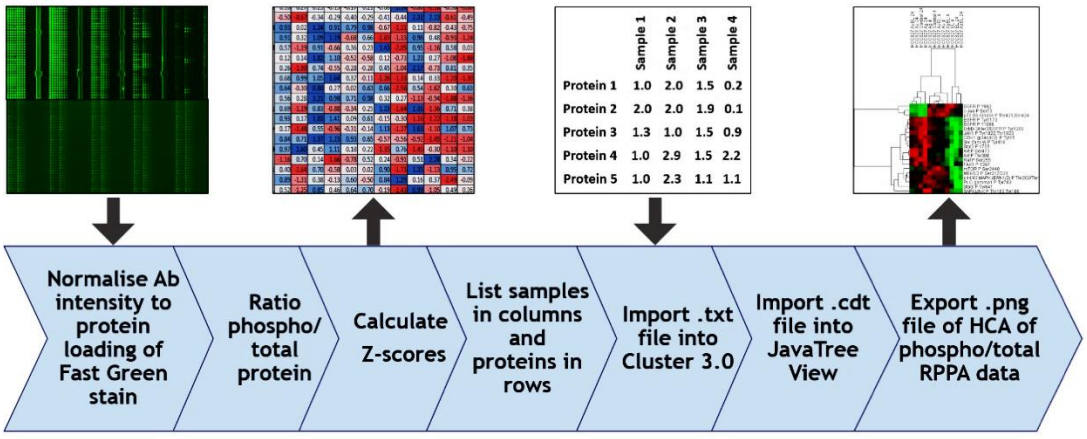

Figure 75 Data processing pipeline for RPPA intensities through to HCA heat map with clusters of similarly expressed proteins and/or their post-ranslational modifications against closest branched samples.

Normalised protein intensities for phosphorylated and total protein were converted into a ratio of phospho/total protein, to assess differences in activation or inhibition of any post-translational modifications and thus, induction or inhibition of any signal transduction pathways. To compare in a normalised fashion across the treatment conditions, a Z-score was calculated to normalise quantifications per phospho/total protein ratio. Z-scores were generated from: the sample value, minus the average of all samples, divided by the SD of all samples, or more simply- how many SDs above or below the mean value a sample resides. Essentially, this normalised the intensities between proteins, so that despite having different expression levels, they were all on the same scale. Therefore, any increase or reduction of relative expression levels were identified relatively across the samples per protein, additionally any trends were seen between associated proteins. This read out gave an indication of patterns and trends in the data but would have been time consuming to then sort the data into similarly affected proteins and sample groups. Employing HCA as an unsupervised learning technique for the purpose of streamlining the data mining process was invaluable.

A .txt file with protein names in the first column, sample names across the first row and the respective Z-values completing the data, was imported into Cluster 3.0 v.1.56 for cluster analysis. After this the .cdt file was imported into Java TreeView software v.1.1.6r4.[105,106]

In Java TreeView v.1.1.6r4, the proteins and samples were clustered with the similarity metric of Euclidian distance selected for the branches and the average linkage was calculated. The software nested the proteins, or sample elements, into branches of a hierarchical tree (dendrogram). The distances computed for each branched cluster indicated a similarity threshold. The nearer the branches were to the map, or the shorter the branches and closer to the 'trunk' they were, the stronger the relationship between the proteins or samples. The further away from the map or 'trunk' that the branches or clusters were, then the more divergent the relationship.

HCA heat maps are a simple way to present at-a-glance overall changes in protein expression across many proteins in one figure of a large phospho-proteomic study. However, it was pertinent to demonstrate the linkages between proteins and the post-translational modifications in a clear biological network, as a pairwise comparison between a control and treated sample, to better understand the biochemical interplays in effects on cell functions. Interactive network integration

was the chosen method for this deeper functional interpretation, or mechanistic exploration, of the biochemical results of the RPPA data.

To contextualise the relationships between proteins and post-translational modifications, the interactive network analysis software Cytsoscape v.3.6.1 was used with GeneMANIA v.3.5.0 algorithm plug-in application, to load the protein networks upon which, Cytoscape maps the data.[107,108] Now that an overview of the data handling approaches has been described, the results will be presented and discussed starting with the simpler HCA method.

6.4 Pathway Analyses by Hierarchical Cluster Analysis (HCA)

6.4.1 EL Insensitive and Sensitive Cell Line Comparisons

A comparison was drawn between the EL insensitive H1355 and sensitive HCC827 cell lines with regards to overall differences in response to treatments. These gross changes will reflect upon the general pathways selected for investigation by RPPA, illustrated in the Venn diagram in Figure 71. These were: stress pathways, cell death mediators, EGFR signalling, cell cycle arrest and some housekeeping proteins. The dividing factor here was that the insensitive line did not respond to EL and hence there were no changes in the EGFR and associated signalling pathways. Furthermore, the EL insensitive cell line was susceptible to the toxic effects of the AgHA NPs, whereas the EL sensitive cell line did not appear to be as vulnerable to the silver's toxicity.

Figure 76 displays an HCA heat map of all the samples tested, with all the phospho/total protein ratios. A differential response of cells to the length of incubation time, the NP type and whether the cell line was EL sensitive or not was detected. Down regulation is displayed in green and upregulation is shown in red, the scale bar demonstrates the fold change difference of the Z-score. At the longer 24 hour incubation with EL or AgHA conjugates in HCC827 cells there was down regulation in the EGFR phospho/total proteins and the associated downstream proteins in green. At 24 hours with AgHA NPs or conjugates on the H1355 cell line the death signalling and stress pathways were upregulated in red, such as PARP and caspase 3. However, the number of samples in general was too great to display concisely and the detail was explored in more detail within the next section.

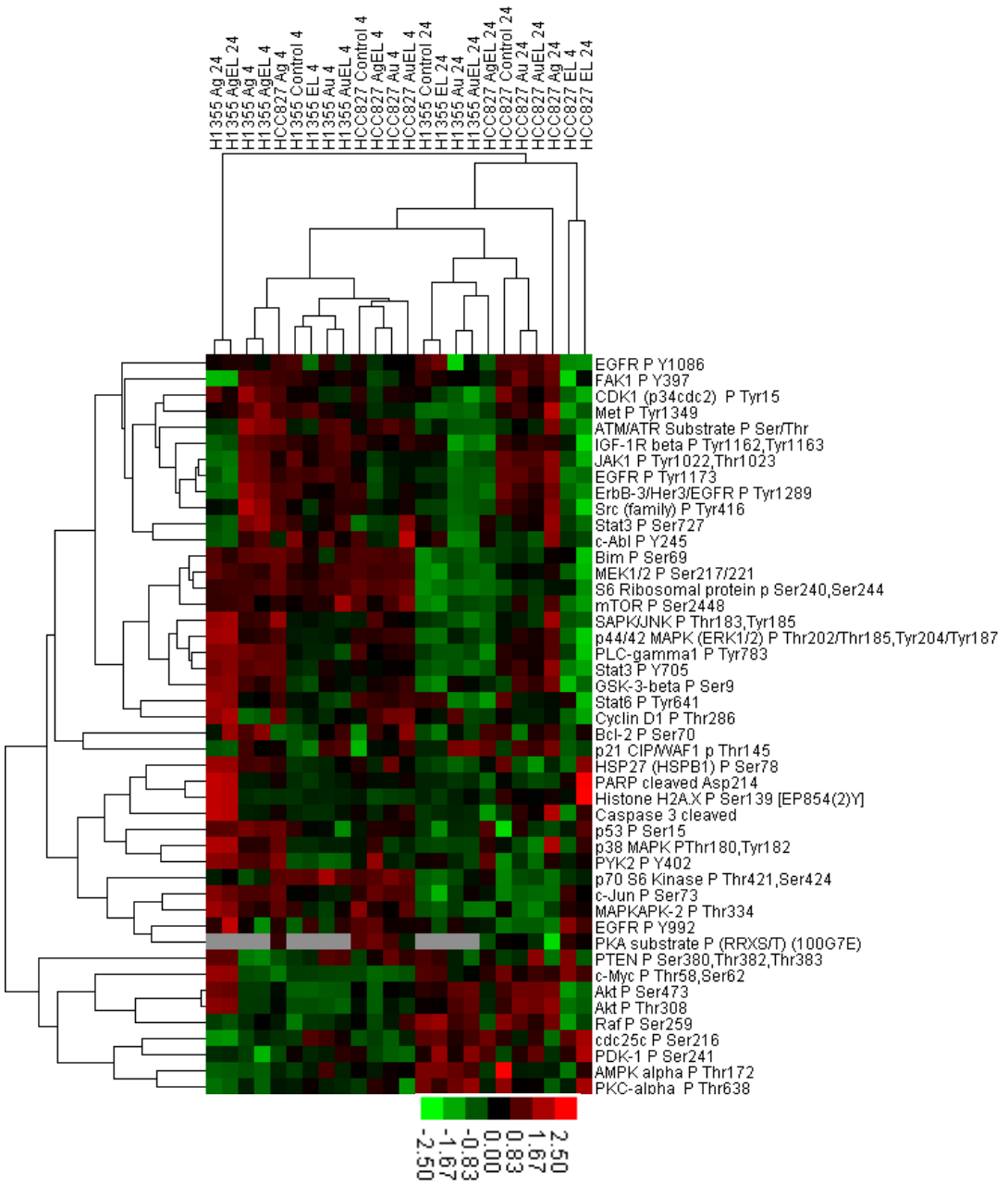

Figure 76 Pathway Analyses by HCA comparing response of all phospho/total protein ratios of all sample conditions. N=3 biological replicates. Timepoints 4 and 24 hours, cell lines were H1355 EL insensitive, HCC827 EL sensitive, treatments were: DMSO vehicle control, AgHA NP control, AuCt NP control, 10 nM EL, 10 nM EL- 0.34 nM AgHA conjugates, and 10 nM EL- 0.34 nM AuCt conjugates.

6.4.2 Time Point Incubation Comparison within Cell Lines

An evaluation of the alterations in expression levels of proteins was conducted between the 4 and 24 hour time points, with the EL-insensitive cells, and then the sensitive cell line. The key factor here was the delay in uptake of NPs into the cells and the release of the EL from the particles to exert its effect.

The noticeable consequence of treatments on the H1355 cells was the delineation between the 2 time points in Figure 77. Additionally, the silver treatments within the 24 hour time point respond almost in the opposite manner to the remainder of

the treatments. This is seen with the vertical split where the 24 hour control, EL, AuCt NPS and AuCt conjugates are in general downregulated, where as in the 4 hour silver samples they were greater in expression.The elevated expression (red) is observed in death related proteins such as, cleaved caspase 3, PARP and Histone H2A.X that is involved in DNA repair. At 24 hours, the AgHA NPs and the AgHA conjugates were upregulated for a majority of the proteins for these DNA repair and apoptotic markers and indicate dying cells. The fact that this is seen in both the bare AgHA NPs and the conjugate suggests that the response is to the metal itself as opposed to the EL. This is reinforced by the fact that the AuCt NPs and AuCt conjugates have a far lower expression (green) in relation to cleaved Caspsae 3, PARP and Histone H2A.X.

In terms of reponse of the H1355 cells to EL treatment, there is no difference in EGFR and associated downstream protein expression levels between the 24 hour control and free-EL samples (columns 7 and 8 from the left respectively). Furthermore, these 2 samples are paired to have the closest relationship, in terms of overall response to treatments, as seen by the closest bootstrapping to the HCA heatmap in Figure 77.

The AuCt NPs and conjugates appear to have less phosphrylated EGFR protein than the control and EL treated samples at 24 hours, indicated by the green heat points. However this can be disregarded as overall at the 24 hour timepoint there seems to be less EGFR expression than the 4 hour time point and this may be skewing the result. Looking at the rest of the data from p70 s6 kinase downwards the expression of proteins between the gold samples and the control and EL are seen to match. This is confirmed by by these 2 sets of samples being paired in a relationship at the top of the heat map. This again reinforces the difference in response to treatment by the 24 hour silver samples are these a bootstrapped in a relationship of their own, separate to all other samples.

From Figure 77, it is concluded that H1355 cells are not responsive to EL given the similar response of the control at 24 hours. The H1355 cells are detrimentally affected by the concentration of AgHA NPs used in this study, due to their separate branching and DNA repair and apoptotic markers being elevated. Therefore, no judgement can be made of the efficacy of the AgHA conjguates. Furthermore, the AuCt conjugates do not offer any beneft over free-EL on the *EGFRwt* EL-insensitive H1355 cell line. Efforts to analyse further results were therefore focussed on the EL-sensitive HCC827 cell line.

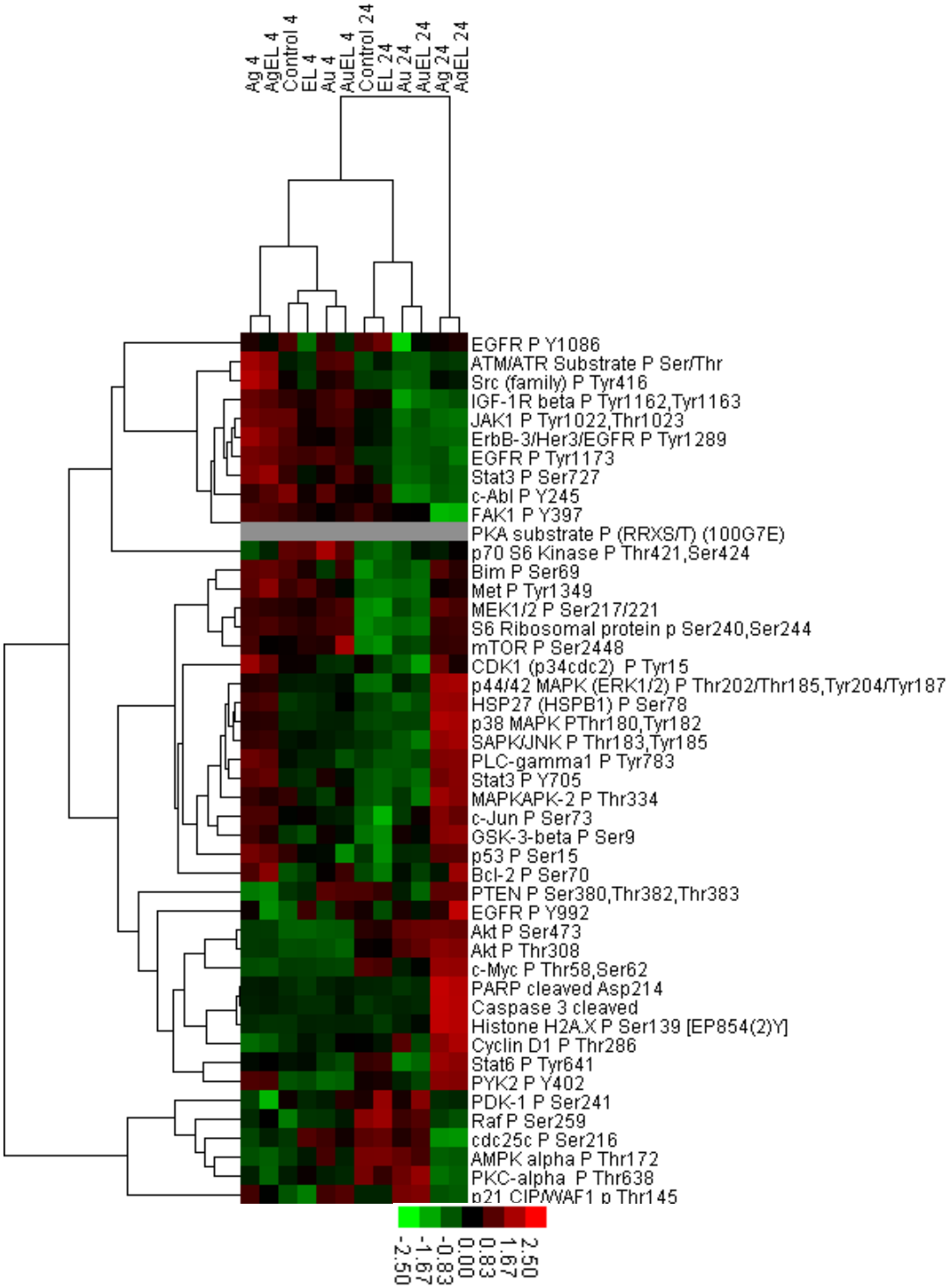

Figure 77 Pathway Analyses by HCA comparing response of all phospho/total protein ratios of all sample conditions. N=3 biological replicates. Timepoints 4 and 24 hours, H1355 EL insensitive cells only, treatments were: DMSO vehicle control, AgHA NP control, AuCt NP control, 10 nM EL, 10 nM EL- 0.34 nM AgHA conjugates, and 10 nM EL-0.34 nM AuCt conjugates.

Figure 78 with the EL-sensitive HCC827 cells at 4 and 24 hours has a different response than H1355 to treatments. Firstly, there is no difference in protein signalling response between the 2 types of metal NPs, therefore, no toxicity is exerted by either of the bare NPs themselves. This was an initial concern highlighted during the initial hypothesis of this chapter which is rejected given these data. Free-

EL and EL-AgHA conjugates also responded differently than in H1355 cells. This can be seen with the both the 4 and 24 hour time points with EL and AgHA EL conjugates grouping on the right hand side of the HCA heatmap. The concentration of heat points with lower phosphorylated over total protein expression are clusted within all the samples for free-EL and AgHA conjugates, seen in green on the top right hand side of Figure 78. Interestingly, this separation within the phsospho/total protein ratios is within the EGFR related protein ratios that group together strongly in the respondent cells. This is seen with the short Euclidean distances of the pairing between protein bars on the left hand side of the map that relate to the EGFR proteins at the top of the HCA map from FAK1 to Stat 3. Therefore, an HCA was created to zone in on these important signalling events.

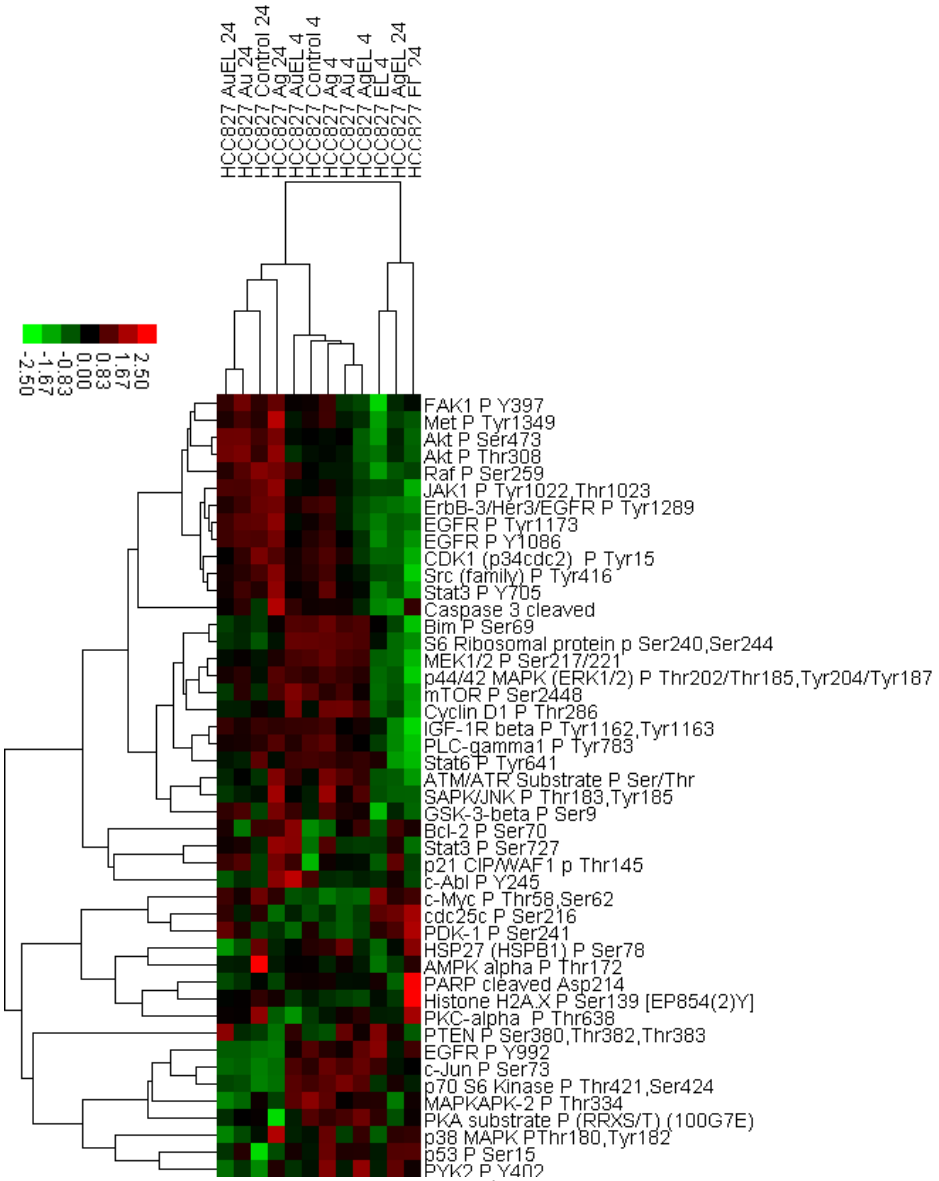

Figure 78 Pathway Analyses by HCA comparing response of all phospho/total protein ratios of all sample conditions. N=3 biological replicates. Timepoints 4 and 24 hours, HCC827 EL sensitive cells only, treatments were: DMSO vehicle control, AgHA NP control, AuCt NP control, 10 nM EL, 10 nM EL- 0.34 nM AgHA conjugates, and 10 nM EL-0.34 nM AuCt conjugates.

Figure 79 shows a strong relationship within the responding cells to EL and EL-AgHA conjugate treatments within the EGFR signalling pathway. Overall, the 24 hour EL exerts the greatest down regulation of EGFR signalling. The strongest relationship within the respondent cells was between 24 hour free-EL and AgHA conjugate, which pair on the top right hand side of the map. It is seen that although the 4 hour AgHA conjugate is adjacent to the 4 hour EL, 24 hour EL and 24 hour AgHA EL conjugate, that it is not paired by a bracket to them; thus it is further away in its relationship to those 3 other treatments. This could be due to a delayed uptake and consequently the onset of the EL release into the cells, and that by 24 hours the cells that have uptaken conjugates have had time to respond to the treatment. The response at 48 hours would be interesting to determine whether the nanodelivery has had time to reach an equivalent effect to the free-EL, after 2 cell cycles. However, this would be practically difficult to assess due to the drop in cell numbers caused by the successful treatment (reduction in cell growth and induction of apoptosis) by both the free and conjugate delivery. Instead, closer attention is paid to the 24 hour time point of the HCC827 cells to explore the response in more detail as an interactive network analysis.

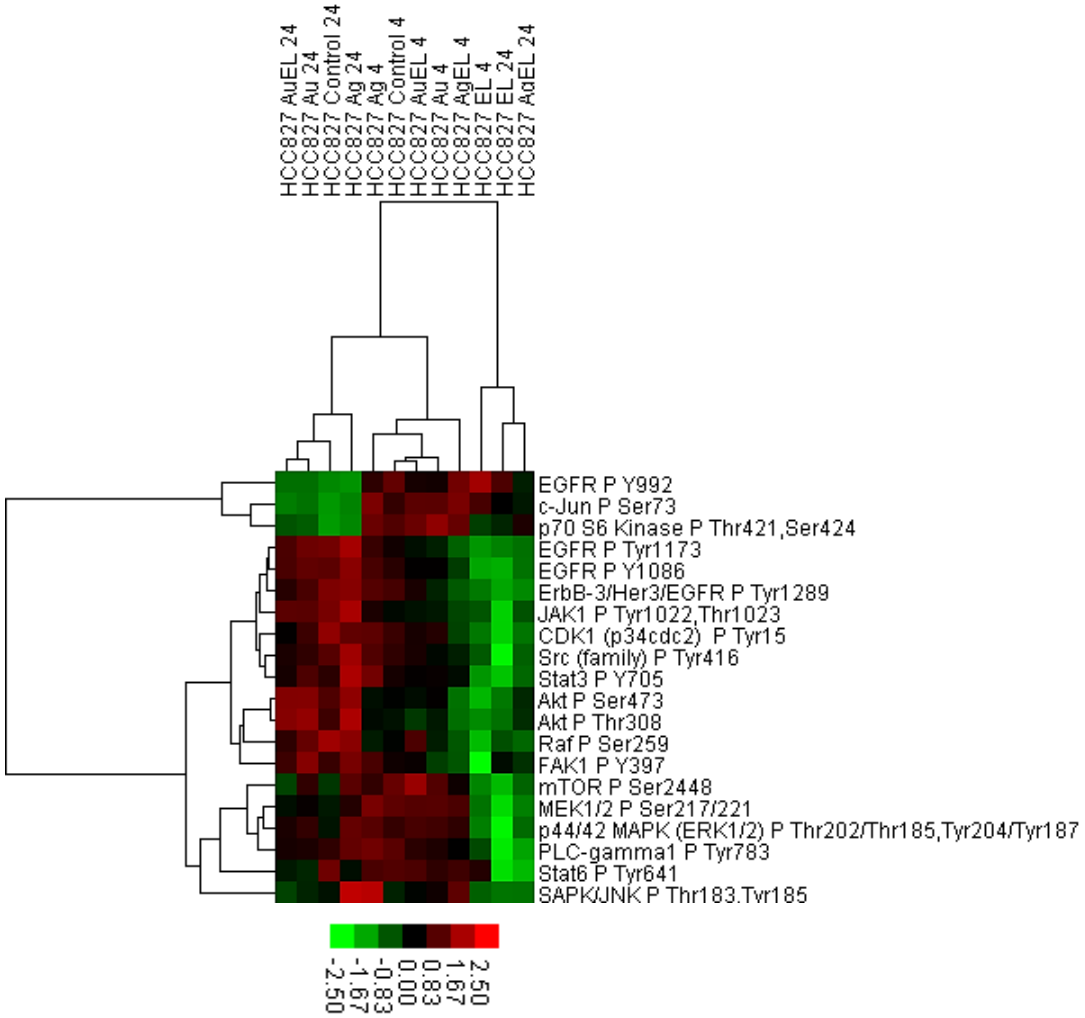

Figure 79 HCA heat map of HCC827 cells treated with DMSO control, AuCt NP control, AgHA NP control, free-EL 10 nM, 10 nM EL-AuCt conjugate and 10 nM EL-AgHA conjugate for either 4 or 24 hours. Scale bar is -2.5 to +2.5 relative intensity values of phospho/total protein Z-scores. Most similar responses are branch closest to the map and have a higher associated probability.

6.4.3 Comparison of Treatments of the 24 Hour Incubations of the HCC827 Sensitive Cell Line EL and EL conjugates

The emphasis here is on drawing a final comparison between the efficacies of free-EL with that of the NP-bound EL. Hence, there is a focus on the EGFR and downstream signalling pathways.

To ascertain the granular similarities and differences it is prudent to conduct a pairwise analysis of treatments. This is done through interactive network analysis which highlights connected proteins that are activated or inhibited by a phospho-protein in comparison to a control. Unlike HCA heat maps, the network is constructed from online gene databases to link the proteins into pathways or related functions in a supervised manner, instead of grouping only by similar expression levels as in the HCA graphics. Ultimately, interactive network analysis can provide mechanistic details through known and published relationships between associated proteins. It could also help to highlight outliers in terms of response to different

treatments, due to the way it is visualised, these could lead to new information on the function of a singular or group of proteins.

6.5 Interactive Network Pathway Analysis

Various comparisons are drawn between controls and samples, these are 3 pairwise comparisons within 3 groupings, which is summarised in Table 24. Being compared were controls (including bare NPs), treatments *vs* respective controls, and finally the most biologically relevant was a comparison of the 2 conjugates agaianst the free-EL. The table provides a matrix for easy comprehension of the pairwise comparisons within the groupings discussed for analysis, which are expanded on in this section. A baseline has been established for the effects amongst the controls and if they alter the EGFR signalling protein levels in any way i.e.: DMSO *vs* AgNPs, DMSO *vs* AuNPs and AgNPs *vs* AuNPs. It was seen in Figure 79 that the DMSO control, AuCt NP control and AgHA NP control were all grouped together on the left hand side of the HCA heatmap with short Euclidian distances. Therefore, these pairwise comparisons would be superfluous, and although they are described in Table 24 for clarity, they were deemed unceccesary to probe by interactive network analysis.

Table 24 Pairwise Comparisons for 24 hr Treatments on HCC827 adenocarcinoma cell line

	DMSO	EL	Ag	AgEL	Au
EL					
Ag					
AgEL					
Au					
AuEL					

	Controls / metal comparisons
	Treatments Vs respective controls comparisons
	Treatment comparisons
	Comparisons avaialble but not reported here

1. An evaluation was carried out to address any changes within each treatment and control group *i.e.:* DMSO *vs* EL, AgNPs *vs* Ag conjugates, AuNPs *vs* Au conjugates.
2. The most biologically relevant assessment conducted was on the effectiveness of the treatments and whether the conjugates were as efficacious as the free-EL and which metallic conjugate performs best *i.e.:* EL *vs* AgEL, EL *vs* AuEL and AgEL *vs* AuEL.

Interactive network maps utilised the significance levels of relationships to emphasise each node within the pairwise comparison *e.g.* non-significant was the smallest and as the p-value decreased the node size and significance increased. To

create the p-values, much like the cytotoxicity studies in chapter 4, a one-way ANOVA was used to test the null hypothesis of no difference in the mean values. This was done for each phospho/total protein ratio to compare all the treatments. Table 25 shows the protein ratiod p-values for the one-way ANOVA, within these, each pair was assigned a significance level of: non-significant (ns), $p<0.05$ (*), $p<0.01$ (**) or $p<0.001$ (***). They were sorted from most significant to least significant and the respective individual pairwise p-values are seen within the appendix on page xxxviii to deteremine where the significant differences arose from.

The top 14 proteins from the one-way ANOVA analysis in Table 25 had a $p<0.001$. That is to say, there is great statistical confidence in their significance, with only a 0.1% chance of being incorrectly classified as significant. In fact, a majority are actually $p<0.0001$, which would mean only 0.01% chance of an incorrect rejection of the null hypothesis. It is a strong indication that there is a difference in the mean values of those samples. These values were assessed in conjunction with the HCA heatmaps and individual pairwise p-values in the appendix starting on page xxxviii, to observe what the significant differences meant biologcially.

Interestingly, insulin-like growth factor 1 receptor (IGF-1R) was in this group, cancer immunotherapy studies have found that targeted IGF-1R therapies can suffer from EGFR compensating for IGF-1.[179] It would seem that in this case the opposite is true and that IGF-1 is also downregulated as EGFR levels decrease (Figure 78).

Two of the DNA repair proteins are present in Table 25 and upon closer inspection of Figure 78 it is seen that this significance is due to a distinct upregulation within the 24 hour free-EL treatment, in comparison to the rest of the treatments. Elevated expression of Histone H2A.X (H2AFX) would suggest an attempt by the cells to repair double stranded DNA breaks.[180] However, the protein upstream that would cascade this signal, ATM/ATR, was not elevated. PARP is the other DNA repair protein that was upregulated in free-EL at 24 hours.

Janus Kinase (JAK)/ Signal Transducer and Activator of Transcription proteins (STATs), or JAK/STAT for short, is another signalling pathway perturbed by the EL treatments, it is seen in Figure 79 that they have reduced expression levels, especially in the 24 hour EL and AgHA EL conjugate. STAT 6 is more adversely affected at 24 hours than STAT 3, although it was unaffected at 4 hours. On the other hand, STAT3 was down regulated at both 4 and 24 hours for EL but only 24 hours for EL-AgHA. STATs are known to affect immunity, cell division, cell death

and tumour formation. Mechanistically the ligand binding results in dimerising of the cell surface receptors, which brings the JAKs into close proximity enabling phosphorylation and activation. In turn, the signalling cascades and induces STAT activity by dimersisation of STATs. These STAT dimers translocate into the nucleus resulting in target gene trsnscription. Since these proteins are downregulated the cells divide less, in line with the anti-proliferative effects of EL. JAK-STAT signalling can also interconnect with MAPK/ERK and PI3K/AKT/mTOR signalling pathways (Figure 80).

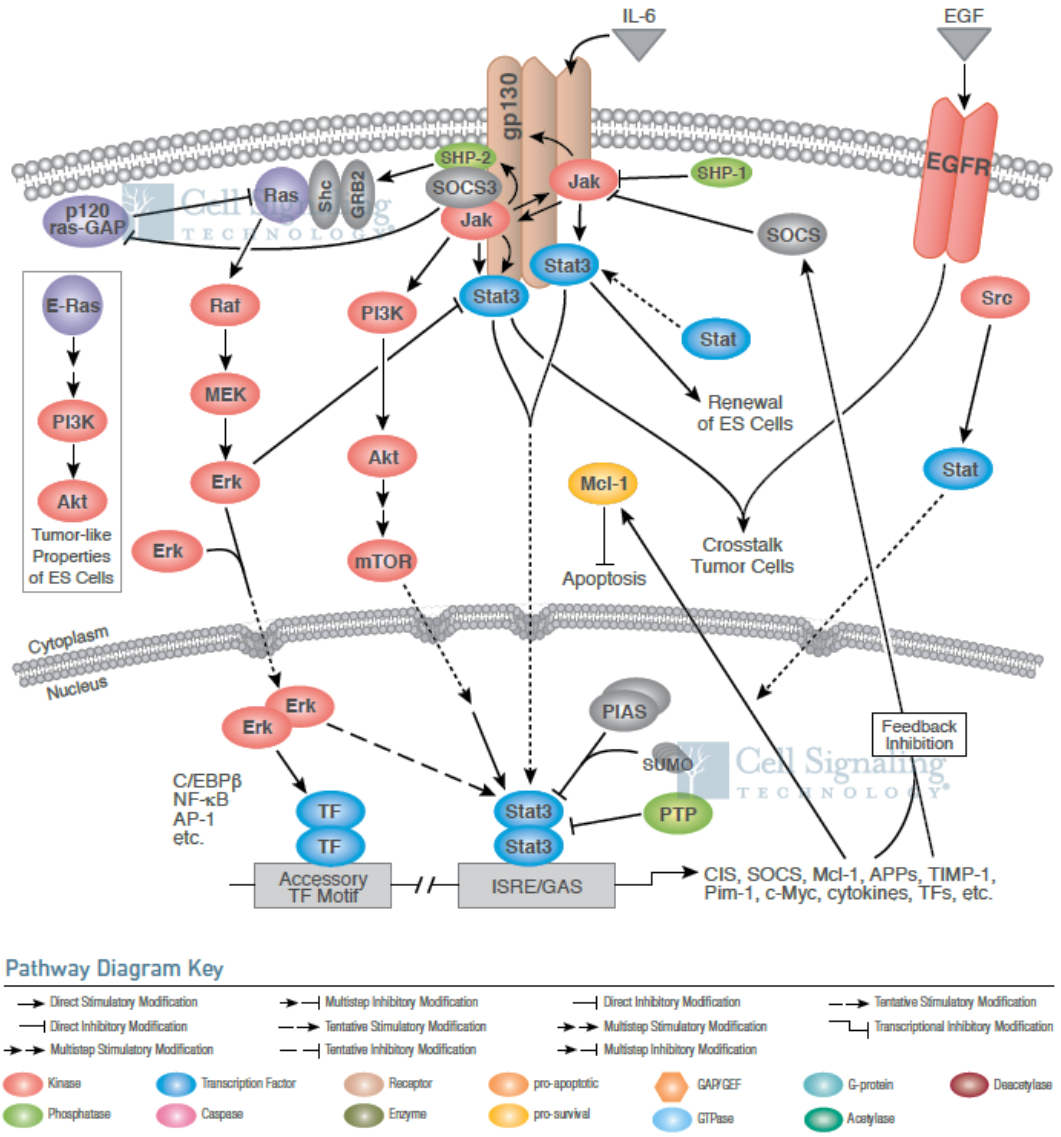

Figure 80 JAK/STAT signalling pathway map. Illustration adapted and reproduced courtesy of Cell Signaling Technology, Inc. (www.cellsignal.com).

p38 MAPK was slightly less significantly different at $p<0.01$ and is not affected by the treatments as much as the p44/42 extracellular signal-regulated kinases (ERK) signal is affected by EL treatment ($p<0.001$). An overview of the MAPK/ERK pathway, also known as the wider Ras/Raf/MEK/ERK signalling pathway, which occurs as a direct result of EGF ligand binding to EGFR (and other stimulations), is

illustrated in Figure 81. MAPK activates the translation of mRNA to proteins and also regulates several transcription factors. Overall, MAPK induces the progression of the cell from G1 to S phase and causes proliferaton, from mitogens such as EGF, promoting growth. It is seen in Figure 79 that there is downregulation of all of these components that were included in the RPPA experiment, namely: Raf, MEK and ERK 1/2. Whilst Raf does not hold a statistical signicance in Table 25, it is clear that the EL treatments are all downregulated. MEK ($p<0.01$) and ERK 1/2 ($p<0.001$) are also evidently expressed at far lower levels in 4 hour EL, 24 hour EL and 24 hour EL-AgHA conjugate. It would seem that the 4 hour EL-AgHA conjugate did not affect the expression levels of these as much. As such, there is a greater anti-proliefrative effect on the 4 hour EL, 24 hour EL and 24 hour EL-AgHA conjugate than other cell treatments on HCC827, as seen by the down regulation of the components in the MAPK/ERK signalling pathway. The down regulation of MAPK/ERK signalling causes less transcription and halts progression from G1 to S phase in the cell cycle, hence cell growth stops.

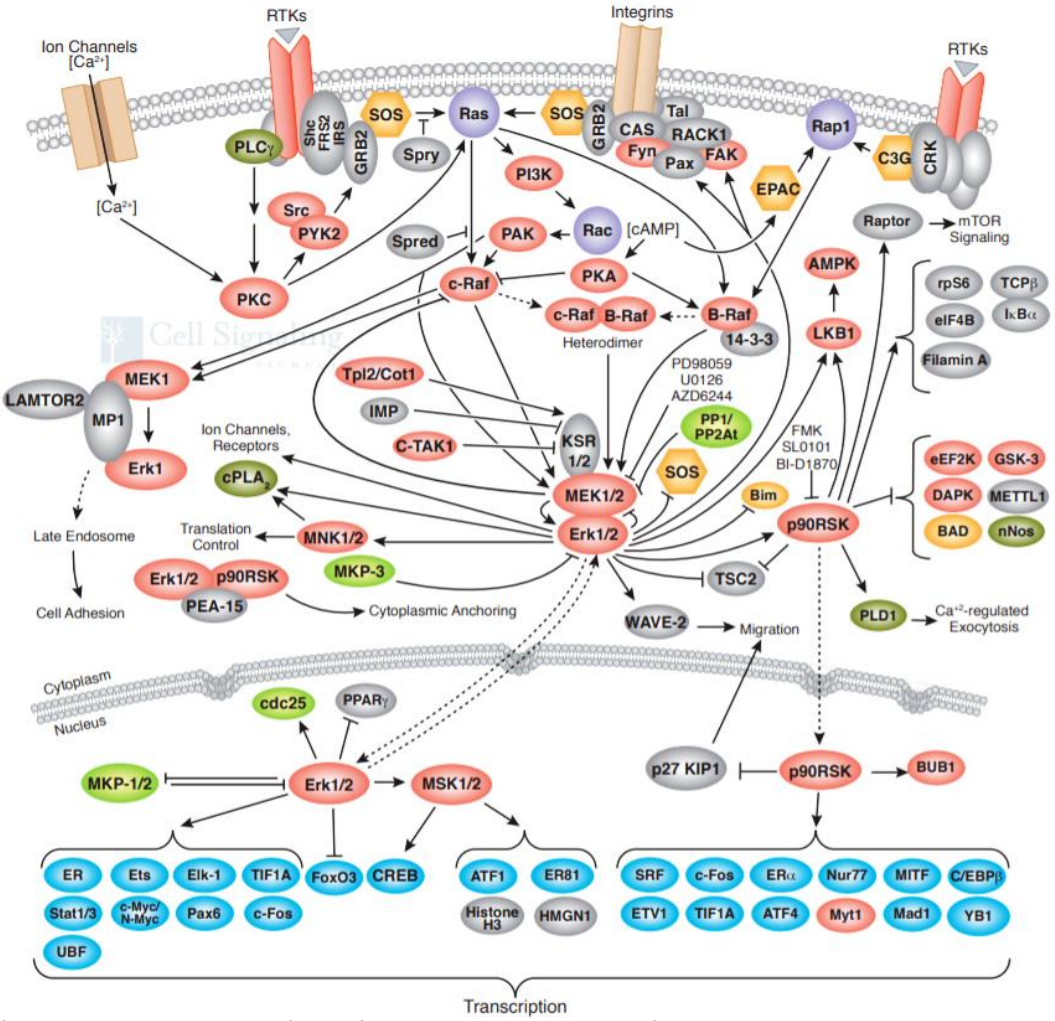

Figure 81 MAPK/ERK signalling pathway. Illustration reproduced courtesy of Cell Signaling Technology, Inc. (www.cellsignal.com).

Table 25 One-way ANOVA p-values for HCC827 cells of p/t ratios. Green= p<0.001, orange= p<0.01, red= p<0.05 and white is non-significant.

P-Value	Protein ratios	HUGO Gene ID
< 0.0001	PARP cleaved Asp214 / PARP	PARP1
< 0.0001	Met P Tyr1349 / Met	MET
< 0.0001	IGF-1R beta P Tyr1162,Tyr1163 / IGF-1R beta	IGF1R
< 0.0001	EGFR P Tyr1173 / ErbB-1/EGFR	EGFR
< 0.0001	EGFR P Y1086 / ErbB-1/EGFR	EGFR
< 0.0001	p44/42 MAPK (ERK1/2) P Thr202/Thr185,Tyr204/Tyr187 / p44/42 MAPK (ERK1/2)	MAPK1 & 3
< 0.0001	Src (family) P Tyr416 / Src	SRC
< 0.0001	SAPK/JNK P Thr183,Tyr185 / SAPK/JNK (JNK2)	MAPK9
< 0.0001	PLC-gamma1 P Tyr783 / PLC-gamma1	PLCG1
< 0.0001	Stat3 P Y705 / Stat3	STAT3
< 0.0001	Histone H2A.X P Ser139 [EP854(2)Y] / Histone H2A.X	H2AFX
0.0001	ErbB-3/Her3/EGFR P Tyr1289 / ErbB-1/EGFR	EGFR
0.0001	Stat6 P Tyr641 / Stat6	STAT6
0.0004	JAK1 P Tyr1022,Thr1023 / JAK1	JAK1
0.0019	GSK-3-beta P Ser9 / GSK-3-beta	GSK3B
0.0056	Caspase 3 cleaved / Caspase 3	CASP3
0.0057	mTOR P Ser2448 / mTOR	MTOR
0.0063	MEK1/2 P Ser217/221 / MEK1/2	MAP2K1 & 2
0.0068	p38 MAPK PThr180,Tyr182 / p38 MAPK	MAPK11, 12 & 14
0.0129	Akt P Ser473 / Akt	AKT1 AKT2 AKT3
0.0157	S6 Ribosomal prot p Ser240,Ser244 / S6 Ribosomal prot	RPS6
0.0159	cdc25c P Ser216 / cdc25A	CDC25C
0.018	CDK1 (p34cdc2) P Tyr15 / CDK1 (cdc2)	CDK1
0.0186	p53 P Ser15 / p53	MTAP
0.0202	PKC-alpha P Thr638 / PKC-alpha	PRKCA
0.0298	EGFR P Y992 / ErbB-1/EGFR	EGFR
0.0375	p21 CIP/WAF1 p Thr145 / p21 CIP/WAF1	CDKN1A
0.0394	Akt P Thr308 / Akt	AKT1, 2 & 3
0.0622	Bim P Ser69 / Bim	BCL2L11
0.1366	SP27 (HSPB1) P Ser78 / HSP27 (HSPB1)	HSPB1
0.1507	PYK2 P Y402 / PYK2 [EP206Y]	PYK2B
0.1592	p70 S6 Kinase P Thr421,Ser424 / p70 S6 Kinase	RPS6KB1
0.2504	c-Jun P Ser73 / c-Jun N-term	JUN
0.2799	FAK1 P Y397 / FAK1	PTK2
0.2906	PDK-1 P Ser241 / PDK-1	PDPK1
0.2992	c-Myc P Thr58,Ser62 / c-Myc	MYC
0.3853	Cyclin D1 P Thr286 / Cyclin D1	CCND1
0.4539	ATM/ATR Substrate P Ser/Thr / ATM	ATM ATR
0.5014	PTEN P Ser380,Thr382,Thr383 / PTEN	PTEN
0.5148	MAPKAPK-2 P Thr334 / MAPKAPK-2	MAPKAPK2
0.516	c-Abl P Y245 / c-Abl	ABL1
0.5417	AMPK alpha P Thr172 / AMPK alpha	PRKAA1 & 2
0.5893	Stat3 P Ser727 / Stat3	STAT3
0.6662	Raf P Ser259 / Raf1 (C-12)	RAF1
0.8049	Bcl-2 P Ser70 / Bcl-2	BCL2

6.5.1 Treatments *versus* Respective Controls Comparisons

It is important to use the correct controls as a baseline for signalling events respectively for treatments. In this instance it was key to understand this before comparing all the treatments directly, as otherwise any changes in treatments could have been due to the presence of the metals, rather than the treatment itself. It was previously confirmed in Figure 78 that the presence of metals did not exert any toxicity on the cells, since there were no elevated apotptotic or DNA signalling events. However, this does not mean that the presence of NPs did not somehow alter the complex downstream EGFR signals. This section aims to investigate this closely.

Figure 82 shows interactive network analysis maps for free-EL vs DMSO vehicle control, EL-AgHA conjugate against AgHA NP control and EL-AuCt conjugate compared to AuCt NP control. It is seen that the top two maps are very similar and the bottom map differs, the bottom map is AuCt NP control vs 10 nM EL-AuCt conjugate. The three maps will be discussed individually.

The DMSO vehicle control *versus* the free-EL shows many changes in protein expression levels (Figure 82). These are predominantly that EGFR and associated proteins are expressed at a greater level in the control than in the EL treated samples, seen by the strong red colour (near the maximum value 1.4 on the scale bar) and large node sizes. More specifically, these include: AKT1, ERK1/2 (MAPK1), PLCG1, JAK1, SRC and to a slightly lesser degree, STAT3,6 and MEK1/2 (MAP2K1) and MET. These proteins are all associated with the EGFR or JAK/STAT or MAPK/ERK pathways which are linked. This confirms that at 24 hours post-treamtent with EL, the sensitive cells respond phosphoproteomically as would be expected in reponse to the treatment. EGFR signalling and associated pathways are inhibited by the anti-proliferative drug EL. There were two proteins (in blue on the DMSO *vs* EL network in Figure 82) that show a lower expression level, which were Cdc25a and H2AFX. The DNA repair protein Histone H2A variant H2AX was downregualted in the control sample compared to the EL treated sample; in otherwords, the phosphorylation was stimulated in the EL treated sample to mend the DNA double strand breaks. This protein is also associated with DNA replication, present during apoptosis and found connected with residual damaged DNA.[181] Therefore, the kinetics, morphology, number and size of H2AFX-associated foci should be explored in future. CDC25a is a cell cycle protein phosphatase that is stabilised by CHK1 a kinase which regulates S phase of the cell cycle. In conclusion EL halts the cell cycle progression as a result of inhibiting the EGFR target.

The AgHA NP control *versus* EL-AgHA conjugate treatment interactive network map displays similar results to the DMSO vs free-EL treatment pairwise comparison (Figure 82). These overall changes would be seen if PCA was conducted. However, the interactive network maps highlight greater detail and better represent the relationship information gained from existing protein databases. Additonally the p-values can be added alongside the protein fold change in expression levels. Namely, the phosphorylation of EGFR, MAPK1, STATs, SRC, MET, PLG1, MAP2K1, AKT and IGF1R is greater in the control than the drug treated sample. The difference was not quite as marked as in the other map as the red clour was less intense. The reason for this could be due to a delayed uptake and therefore release of EL into the cells, less EL delivered overall, or the silver NP alone causing a slight inhibiton in phosphorylation. The main difference between the AgHA NP control *versus* EL-AgHA conjugate map (Figure 82) and the EL treatment without NPs was that the H2AFX was slightly elevated in AgHA *cf* EL-AgHA conjugate as indicated by the pale pink colour of the node rather than the blue seen in DMSO *cf* EL. Overall the effect of EL conjugated on AgHA NPs is one that mimics the free-EL but it is slightly less intense effects in terms of inhibition of protein-phosphorylation levels.

Finally, the AuCt NP control *versus* the EL-AuCt conjugate map was completely different from the other two interactive network maps, as seen in Figure 82. All of the nodes are neutal in colour (close 0 fold change on scale bar) compared to the other 2 network maps. This indicates that the phosphorylation levels were equivalent in both the control and EL-AuCt conjugate treated sample.

In summary of the controls *versus* treatments results, these RPPA data are supported by the Western blots and viability assay experiments from Chapter 4. Overall the AgHA conjugate was found to be effective, if slightly less so than the free-EL, and the AuCt conjugate was completely ineffective at perturbing the phosphorylation of EGFR and its associated downstream effector signalling, or at preventing proliferation or promoting cell death.

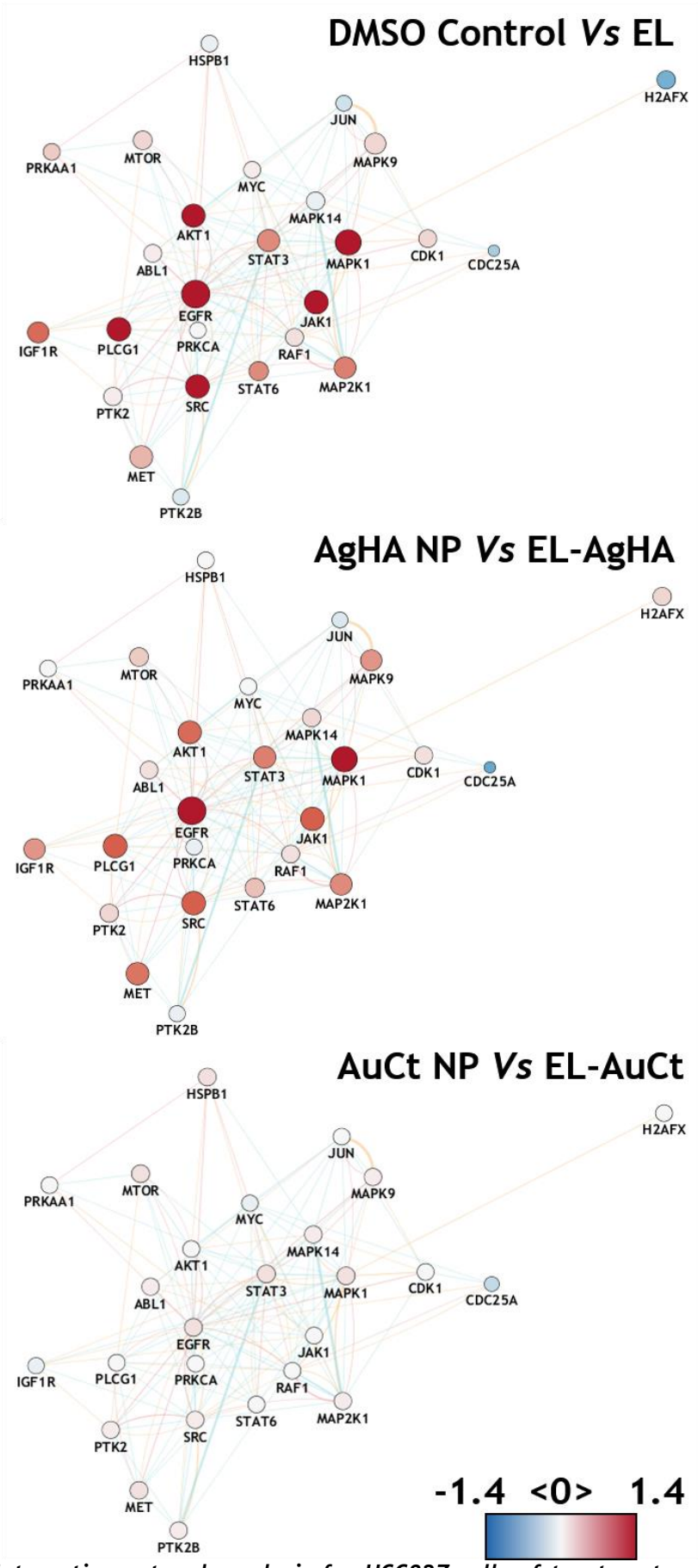

Figure 82 Interactive network analysis for HCC827 cells of treatments compared to control, with log_2 fold change per pairing. Node size relates to fold change log_2 transformed phospho/total protein ranging from -1.4 to 1.4. Key for protein names found within Table 25. Blue is down regulation, red is upregulation.

6.5.2 Treatment Comparisons

The final and most pertinent comparisons drawn in this thesis, were in the analyses between free-EL and the EL-AgHA and EL-AuCt conjugate test treatments. This was to test the effectiveness of supressing the EL target, EGFR and associated signalling pathways downstream. The comparison of free-EL and the AgHA conjugate's phosphoproteomic signalling profiles by RPPA, culminate the extensive characterisations on efficacy and toxicity conducted throughout this project. The importance of this test cannot be understated in determining the results of this study. The aims were: to characterise the conjugates, to image intracellularly by 3D SERS without the use of dyes and establish uptake profiles, and to determine the efficacy of the two metal particle conjugates, when compared to free-EL.

Figure 83 draws comparisons between the 2 metal conjugates and the free-EL using the interactive network analysis mapping method. From the EL compared with EL-AgHA conjugate interactive analysis network map (Figure 83) it can be seen that they are very similar with relatively neutral coloured nodes, close to 0 on the scale bar, that are all of equivalent size to one another, indicating similar expression profiles. The main difference was in the H2AFX protein, which is a known DNA repair protein discussed earlier in this chapter. The H2AFX signal was far higher in the 24 hour free-EL than in the 24 hour EL-AgHA conjugate or 24 hour EL-AuCt conjugate and this was also seen in PARP from the HCA heatmaps (Figure 79). This would be interesting to pursue further to understand why these are elevated in free-EL but not in the EL-AgHA conjugate samples that also exert the effects of the drug on all other the other relevant signalling pathways tested.

The EL *versus* EL-AuCt conjugate interactive network map of Figure 83 revealed a difference from the EL-AgHA conjugate comparison, although one similarity was the overexpression of H2AFX in the free-EL sample (indicated by strong red (approaching maximum of 1.4 on the scale bar) large node). There were numerous proteins whose expression levels were lower in EL than EL-AuCt-treated cells, including: EGFR, ERK1/2 (MAPK1), JAK1, MEK1/2 (MAP2K1), SRC, PLCG1, AKT1 and IGF1R and these are visualised as small blue nodes symbolising inhibition of phosphorylation by the EL treatment. Ultimately this means that the EL-AuCt-treated cells were not affected by the drug, as there is such a disparity in the level of phosphorylated proteins compared to the EL-treated-cells that showed a reduced level of phosphorylation in response to the treatment.

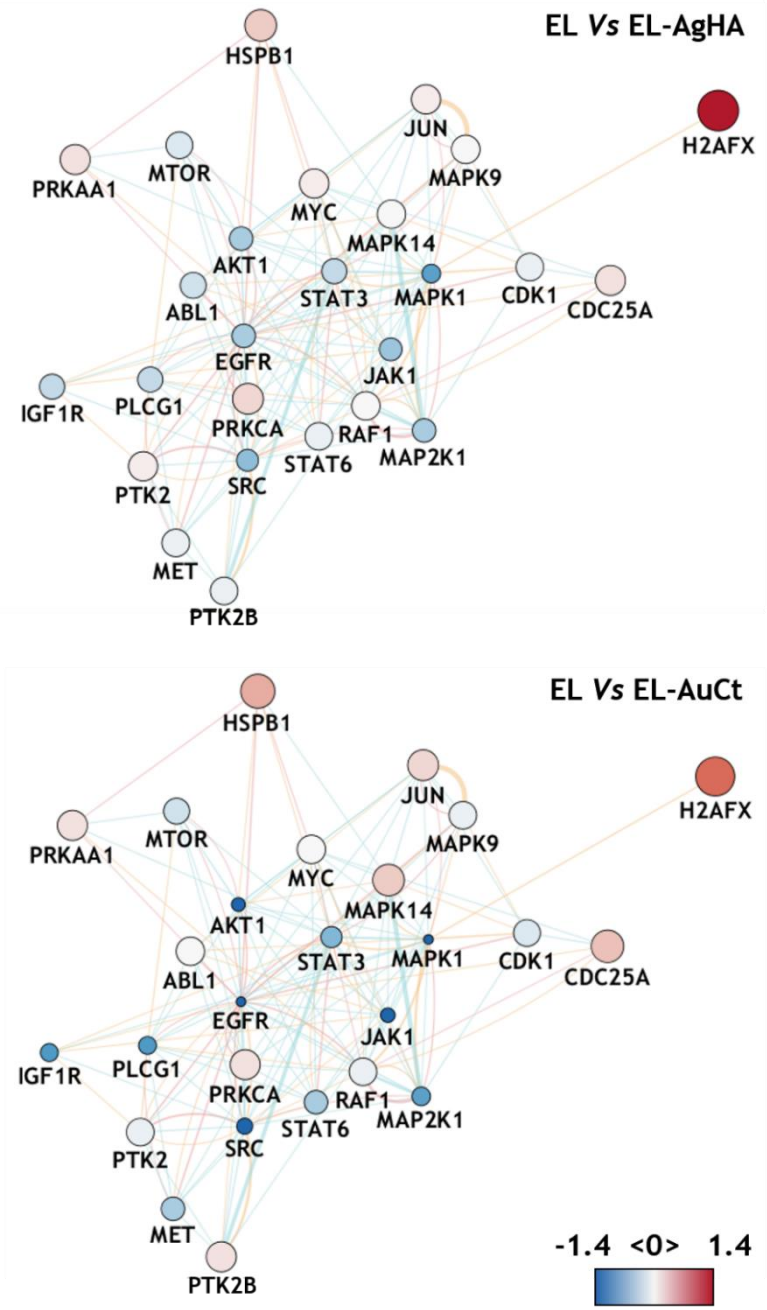

Figure 83 Interactive network analysis for HCC827 cells of free-EL compared to El-AgHA and EL-AuCt conjugatetreatments, with log2 fold change per pairing. Node size relates to fold change log2 transformed phospho/total protein ranging from -1.4 to 1.4. Key for protein names found within Table 24Table 25. Blue is down regulation, red is upregulation.

6.6 Summary

The RPPA study yielded information rich large data sets, care was taken to focus on the relevant treatment comparisons and protein relationships. To do so, HCA heat maps and interactive analysis network maps, were created and one-way ANOVA statistical analysis was employed to highlight differential responses.

In summary, H1355 EL-insensitive cells responded differently to treatments than HCC827 EL-sensitive cells. H1355 cells were sensitive to the toxicity of silver NPs, did not respond to EL treatment and AuCt conjugates did not offer a better efficacy

of EGFR inhibition than free-EL. HCC827 EL-sensitive cells were unaffected by the presence of either bare AuCt or AgHA NPs, which is different from the H1355 cell response. HCC827 cells treated with EL demonstrated inhibition of EGFR and the associated signal transduction pathways found downstream of the receptor. Successful inhibition of EGFR was also seen in the AgHA conjugates, which also displayed less phosphorylation of the EGFR biomarker and its downstream proteins. Covnersely, the AuCt conjugates had no effect on preventing the activation of EGFR and were unsuccessful in delivering the anti-proliferative efficacy of the conjugated EL.

These results highlight the importance of empirical testing of nanoparticle type and concentration on various cell lines for them to be deemed safe for use in patients. However, the killing effect of silver has been exploited in topical applications in an anti-microbial capacity and if the particles were to be targeted in the case of cancer, this could enhance therapeutic effect of tumour shrinkage. Future work could involve investigating safe metal NPs that can be dual purpose by acting as targeted drug delivery vehicles and enabling photothermal ablation of tumour cells.

The EL-sensitive cells EGFR pathway responded to treatment with free-EL and AgHA conjugates but not AuCt conjugates by inhibiting the phosphorylation events. AuCt conjugates require further investigation as to why the EL did not exert its inhibitory effects on the EGFR target. Experiments earlier in this project concluded that perhaps the binding of the drug moiety to the surface of gold was stronger than on silver, or that the surface chemistry of citrate reduced instead of hydroxylamine reduced affected the binding affinity and subsequent release of the drug intracellularly.

Ultimately, the EGFR signalling was focussed upon within this chapter as being most relevant to the research question. However, future work could include PCA to data mine and evaluate the differences between cell line response at the different time periods to each treatment and control. This could result in a deeper understanding of e.g. the cells responses over time to coping with silver toxicity or generally the burden of particles within the cell and how this impacts the structure and motility of the cell. The structure and motility proteins were not topics in the scope of this study, nonetheless this data rich RPPA study could yield the answers to complex mechanistic responses to a nanomedicine drug payload. This is the first study reporting high throughput targeted phosphoproteomic analysis of NP treated cells by RPPA. The protocol outlined hear could be utilised widely to gain mechanistic details illucidating phenotypic responses to cell treatments in other studies.

Chapter 7 Conclusions

"We ignore public understanding of science at our peril"
Eugenie Clark (The Shark Lady), ichthyologist.

This study set out to understand the localisation and efficacy of nano-delivered EL on cells that are both sensitive and insensitive to this drug; these were delivered on two types of metallic NPs- AgHA and AuCt NPs. This was to elucidate fundamentally why cells may not respond to EL treatments by exploring the uptake and localisation and to help inform future repurposing of drugs in a nano-formulation. That formulation may, in turn, lead to an enhanced efficacy with less systemic toxicity. SERS imaging is a non-destructive method that could be used on *ex vivo* biopsies, and in the future, fibre optic SERS could be used to observe the delivery and release of the drug from the NP in a theranostic approach *in vivo*.

In brief, the areas explored were; conjugate characterisations, NP uptake and localisation, EL release by SERS, efficacy of EL and the conjugates on the EGFR biomarker, the toxicity of all the treatments and finally a targeted phospho-proteomic study of cell signalling pathways by RPPA. To do so, various scientific disciplines and techniques were employed to carry out a study that would be accepted as reasonable proof of the findings in the biological, chemical and spectroscopic research communities. The correlative studies used various techniques: analytical chemistry, optical imaging, electron microscopy, and other proteomic techniques used in drug-discovery pipelines to support the SERS imaging data. These experiments were summarised in more detail in a contextual map illustrating the relationships of these experiments at the end of chapter 1. This was to introduce an overview of what would be conducted in each results chapter to explain the thought process followed in this interdisciplinary PhD project (Figure 17). All the research aims and motivations are now addressed in turn, to report on the conclusions and future work resulting from this explorative project.

7.1 Conclusions to the Characterisation of Erlotinib-Nanopaticle Conjugates

Aim- "Chapter 3: to characterise the NPs and conjugates to determine the optimum concentrations for the cell based studies."

Initially, 4 particle types were selected for characterisation, these were all negatively charged NPs reduced by hydroxylamine or citrate methods in gold and silver. Two were found to be stable and produce a reliable SERS signal, these were AgHA and AuCt NPs. The monodispersity and spherical shape was confirmed by various means, to lay the foundation for EL loading calculations. A self-assembly method was used to functionalise the particles as per the literature that had set a precedent for this approach to load EL onto NPs. The SERS signal was acquired using various laser wavelengths and the 633 nm HeNe laser source was chosen to limit the potentially damaging irradiative heating effects within the cells experienced with the higher energy 532 nm Nd:YAG laser. A series of different concentrations of EL was tested on NPs in both gold and silver metal NPs. This was to determine the optimum concentration for both conjugate's stability and intracellular SERS signal detection, given that no dye or aggregating agent was being used and that large clusters are not beneficial for cell uptake. This phase of the study established that 300 nM EL in 0.34 nM NPs was the ideal set of conditions, as approaching monolayer NP coverage of 1 μM EL caused self-aggregation that could hinder cellular uptake.

It was found that EL-AgHA conjugates propagated a greater SERS singal intensity than the equivalent concentration of EL-AuCt conjugates. Furthermore, the Raman shift was characterised as 2111 cm^{-1} for free-EL, 2010 cm^{-1} for EL-AuCt conjugates and 1985 cm^{-1} for EL-AgHA conjugates. Interestingly the AuCt conjugates showed multiple alkyne vibrations presenting as a 'shoulder' or secondary smaller peak that can be explained by alkynes sensitivity to the environment. This was only seen in the silver conjugate once it was within the cell, but was observed in the solution based SERS of the colloidal AuCt conjugte.

Understanding the SERS signals of both AuCt and AgHA conjugates in solution laid the foundations, to test the efficacy of the nanodelivery of the EL in conjugate formulation *versus* free-EL, in its anti-proliferative and apoptotic activity.

7.2 Conclusions to Cytotoxicity and Efficacy of Conjugate *versus* Free Erlotinib…

Aim- "Chapter 4: to characterise the cell lines and determine whether EL-NP conjugates can improve the efficacy and toxicity of in vitro cancer cell treatment compared to free-EL."

Most of the research aims set out were answered to a degree; however, certain areas require further extensive efforts and were difficult to explore with my time costraints as I came to the end of practicacl work, in part, due to the delay in obtaining the correct cell line. The main example of this was the toxicity, or viability, studies to directly compare NP-bound to free-EL. Ideally, one assay would allow high-throughput quantification of cell viability and proliferation. Due to the light-based artefacts of having NPs present in a plate-based assay, these were not suitable for this study. Alternatively, fluorescent imaging-based techniques were used to directly compare viability and cell number but this was low throughput. It required manual post-acquisition quantification for each image, although it did allow qualitative analysis, since the morphology of the cells were also recorded along with the cell number and area. Trypan blue exclusion was a quick method to quantify cell number and viability; however it was very labour intensive to manually repeat the cell number counts.The Live Dead fluorescent cell viability method was slightly higher throughput, with a trusted audit trail of images, which were counted by a semi-automated approach in ImageJ software.

Characterisations showed that HCC827 cells expressed greater levels of EGFR, than the H1355 cells, from immunofluorescence assays. However both cell lines possess contitutivley active EGFR. The cells were authenticated with HCC827 harboring the activating mutation *EGFRm+* and the H1355 cells being *EGFRwt*, both were mycoplasma infection-free.

Finally, Alamar blue metabolic assay was used to determine the IC_{50} of the HCC827 EL-sensitive cell line as ~10 nM and the H1355 EL-insensitive cell line as ~350 nM. Within the sensitive cells, free-EL was the most effective treatment at preventing proliferation and inducing apoptosis, closely followed by EL-AgHA conjugate and the EL-AuCt conjugates had no effect on the viability or cell growth rate. It was noted that the H1355 cells were more sensitive to silver NP's toxicity at the concentration used during this study, than the HCC827 cells, which were unaffected by the bare silver or gold NPs.

The key points are that AgHA conjugate retains the potential of EL to deliver an effective treatment to the cells, whereas for gold despite being less toxic to all cell lines, does not allow the delivery of EL to the active site of the drug target. These cell characterisations and efficacy studies allowed the detailed SERS localisation and correlative uptake experiments to be conducted.

7.3 Conclusions to 3D SERS Characterisation & Correlative Uptake Studies…

Aim- "Chapter 5: to characterise the spatio-temporal distribution of EL within in vitro fixed cells and live cells within a microfluidic device by Surface Enhanced Raman Spectroscopy and correlative uptake studies."

The 3D SERS maps were created for NP and conjugates from 0.5, 2, 4 and 24 hours in H1355 and HCC827 cells with both gold and silver particles. The distribution was observed in both space and time addressing the aim in both *in vitro* fixed cells and confirmed *in vitro* in live cells. This was the first reported observation of drug being delivered and released intracellularly without the need for a Raman reporter, fluorescent dye or being inferred from a secondary enzymatic reaction. The release of the drug ensured that the active moiety could act upon the target site of the EGFR ATP-binding pocket.

A work flow was developed to process tens of samples as 3D SERS maps. This enabled a standardised system to acquire the cell maps, pre-process the data, conduct spectral quality checks, qualitatively assess the distribution in 2D slices and in 3D and finally, quantifying the volume of the cell occupied by the SERS signal. This builds upon the initial 3D SERS work pioneered by McAughtrie *et al.*[47] Here, a reproducible method was created to assess conjugate uptake by cells in a spatio-temporal manner. This produced the spectral detail expected of any SERS study, the images to understand the intracellular localisation of the conjugates and volume of the cell percentages occupied by each molecular vibration of interest. From these a bar chart and table showed at a glance a comparsion of experimental variables. Here, the bare NPs and conjguates were compared against each other and between AgHA and AuCt particle type for HCC827. These results were also produced for both cell lines although for brevity only the EL-sensitive details were included as distribution appeared to be similar.

Correlative SEM and TEM confirmed that NPs were endocytosed and resided within various ultrastructural compartments of cells as single particles and agglomerations. At 4 hours there was evidence of necrosis in the H1355 cells, which were sensitive to the AgHA NPs. The distribution of AuCt conjugates was more clustered and tended to be within vesicles or other membrane bound organelles, where as the silver was more freely distributed but did appear to localise more frequently in the mitochondria.

To determine the structure that the conjugates were observed within from the TEM studies, several theories were tested. Lysosome staining was inconclusive due to artefactual fluorescing of the NPs themselves, but also that the stains operate in a pH dependant manner and should not be solely relied upon for organelle identification. Further to this, a pH release study showed that the colloidal SERS signal reduced from pH 4 and below, this was likely due to the release of EL from the conjugate. Since the lysosomes have a lower pH, that may be the mechanism for EL release that resulted in the efficacy of the AgHA conjugate on the sensitive cells. The AuCt conjugate was not effective on the cells which led to the drug loading studies to establish if there was a difference between those and the AgHA conjugates.

LC-MS studies established almost complete loading efficacy of EL onto both AgHA and AuCt conjugates of the 300 nM EL. The wash supernatant conained trace amounts in AuCt samples and 100 pM which was around LOQ for AgHA conjugates. From this it was determined that there was a higher affinity of EL for AuCt than the AgHA NPs, but that despite being loaded with the drug, the AuCt conjugate was ineffective as it was not releasing the EL within the cell or it was trapped within organelles that prevented delivery to the drug target.

The number of particles delivering EL to the cells were quantified by ICP-MS as ~9000 per cell and therefore a final concentration equivalent to ~39 nM was delivered to the cells. Further to this the ionic and particulate silver was determined by spICP-MS. The particle number per cell was ~12000 and ~6000 for AgHA NPs and AgHA conjugates respectively. The ionic siver was calculated to be 38% of the total silver content for AgHA NP sample and 54% of the AgHA conjugate sample. This shows that more of the silver from the conjugates is ionised within the cells. This may be due to the EL functionalisation displacing the surface chemistry from the synthesis and thereafter the release of the EL from the conjugates exposing the surface of the metal to greater oxidisation within the cell.

The SERS data and correlative studies provide evidence that the particles were internalised by the cells and that EL is delivered from the conjugates. The final section of this project was to analyse the signalling events that occurred after the nanodelivery of the conjugates and how the efficacy compared to the free-EL as a function of EGFR inhibition of the EGFR drug target.

7.4 Conclusions to Targeted Proteomic Analysis…

Aim- "Chapter 6: to explore the mechanisms of action of conjugated EL on NPs and whether they alter from free-EL. Furthemore, cellular stress, cell death or toxicity signalling associated with bare NPs is investigated by Reverse Phase Protein Arrays."

The phopsphoproteomic study of the cell response to treatment was carried out by RPPA on both the sensitive and insensitive cells lines with free-EL, AgHA NPs, AuCt NPs, AgHA conjugates and AuCt conjugates at 4 and 24 hour time points. This was to compare early signalling events against those after one cell cycle and if there was a delay observed in the conjugate delivered EL's activity.

HCA heat maps were utilised for overall trends and the interactive network analysis maps gave a more detailed insight into the relationships between protein pathways and the comparisons of free-EL, AgHA conjugate and AuCt conjugate. Comparing both cell lines revealed the importance of empiricial testing of cell lines and NP type when investigating toxicity, since the H1355 EL-insensitive cell line was vulnerable to AgHA NPs, which induced apoptosis and necrosis. This cell line did not respond to 10 nM EL or any of the conjugated EL as there was no inhibitory effects on the phosphorylation of the EGFR.

The inhibitory effects on HCC827 EL-sensitive cells EGFR signalling pathway were clear from 10 nM free-EL and the AgHA conjugate but they were unaffected by the AuCt conjugate. The main difference between the free-EL and AgHA conjugate signalling events were that there was a slight delay in some down regulations of phospho/total expression ratios. This was anticipated due to earlier studies showing that the clear presence of intracellular conjugates was from 2-4 hours onwards and the first time point coinciding with this.

Overall, the free-EL appeared to have the greatest inhibitory effect on the EGFR and downstream signalling, closely followed by AgHA conjugates, with AuCt conjugates having no effect.

This study has explored many avenues to understand the loading and release of EL from NPs within the cell by SERS imaging and other correative studies. Furthermore the signalling events behind the conjugate's effects have been investigated.

"The important thing is to never stop questioning." Albert Einstein.

7.5 Future Work

There were 4 key areas discussed in the results chapters: the conjugate characterisations, the cell characterisations with the toxicity and efficacy effects of NPs and EL on those cells, the SERS imaging and correlative uptake studies, followed by the proteomic analysis. It is important to view the bigger picture before dealing with specific aspects of future works for each of these areas.

7.5.1 Refine the Model

This study was conducted on two cell lines with two types of NPs in comparison to free-EL. The model used in a study is the first consideration and here an EL-sensitive and EL-insensitive lung adenocarcinoma cell line was selected. The next step to address all the aims in this thesis, is to reassess the model. It is suggested that for all research questions the future work should consider the model used. Here, is it proposed that the next model would be to grow 3D cell cultures to mimic the tumour microenvironment. The cells used in this study were tested briefly for this prupose and appeared to naturally form spheres in U bottomed 96-well plates and this would be recommended for the next set of experiments. Spheroids bring with them a fresh set of challenges and much optimisation would be required in terms of handling for SERS imaging, the types of viability assays that would be appropriate and before any of these steps, determining the required NP concentrations and EL dose. To repeat all the experiments carried out during this PhD in 3D culture would prove to be a whole new PhD in itself, however the results would be interesting and rewarding, it is a step towards the *in vivo* model. It would perhaps deliver insights into more complex cell to cell interactions and signalling events from the RPPA study alone.

Attempts were made to acquire *ex vivo* samples through the network of clinicians associated with the Optima PhD programme. The reason for this was to assess whether the drug accumulated in membrane bound bodies within cells or if there was a different distribution of EL in the tumours of respondant *versus* non-respondant patients. A more attainable source of *in vivo* or *ex vivo* samples would be to create a *Xenopus* (zebra fish) with the cells used in this study. It is possible to breed optically transparent fish that could be imaged using Raman within environmental chambers for the ADME response of the free-EL and conjugates over time in various organs.

7.5.2 Reassess the Nanodelivery Method

In terms of future work on conjugate characterisations, it is suggested that one reduction method is used to compare gold and silver conjugate efficacies. More time

should be spent on making reproducible 40 nm spheres of both metals by citrate or hydroxylamine reduced methods. This would remove any doubt over the lack of efficacy being due to the synthesis method producing a different surface chemistry or whether it is the inherent property of the metal surface itself. Gold is the safer option biologically, should these proof of concept studies be continued into an *in vivo* scenario. Another option would be to consider delivering EL in a nanocage structured gold particle. Nanocages may release the drug more readily, however they may prove harder to image and would require interrogation source optimisation. Nanocages are also more amenable to photothermal ablation, which could be used to release the drug payload with an energy source that is safe to use *in vivo*, such as near infrared wavelengths.

7.5.3 Replicate with a Library of Alkyne Moieties or Small Molecule Inhibitors

This is the first report of tracking the release of a drug directly from a NP without the use of dyes or inferring this action through secondary tests. This proof of concept leads the way to replicate the study with other drugs that contain alkyne moieties to track their delivery. There is currently a heightened interest in the inclusion of alkynes and polyynes during the development of imaging agents for their inobtrusive qualities. They are less likely to perturb a system than a chromophore, fluorophore, *etc*. There are studies which utilise poly-ynes for Raman imaging purposes to create a library of dyes which are organelle specific to rival the multiplexing capabilities already available within fluorescent imaging. Combining these organelle targeting polyynes with NPs for delivery could reveal fundamental physical characteristics of using metal NPs to target delivery of drugs and localise photothermal ablation within cells or tissue.

7.5.4 Refine the Methods used for Efficacy and Toxicity Assessment

During the toxicity and efficacy studies various techniques were used to compare the effects of controls, free-EL, NPs, and conjugates. This is an area for future work that could be easily refined for a catch all viability assay and IC_{50} estimation for all the treatments. It is suggested that flow cytometry is explored further for live cell numbers to calculate the IC_{50} across varying concentrations of EL, NPs and EL concentrations on a fixed NP concentration. This would enable a full statement of IC_{50} to be made as a direct comparison of free-EL *versus* conjugated-EL from one experimental method. This would provide closure on whether AgHA conjugates are as effective as free-EL or not. Similarly the clonogenic assays or scratch wound healing assays could be repeated more extensively to optimise the correct cell number to be plated at day 0 of these experiments. Otherwise it would be advisable

to continue with the live/dead fluorescent area counts or trypan blue cell exclusion counts if the full range of treatment concentrations are included to obtain the IC_{50} data for comparison and comment.

7.5.5 Repeat the Correlative Uptake Studies in Gold

The results obtained frm the spICP-MS and ICP-MS for the AgHA NPs and conjugates produced informative results in terms of quantitation of the number of particles taken up by the cells and silver ions present. Despite the AuCt NP and conjugate samples also being prepared and sent to the collaborator, these were not processed. These could be tested once the relevant protocols have been validated for used with gold.

It would be interesting to repeat the silver samples for testing with spICP-MS with the exception of using sonication to lyse the cells to release the silver content for testing. This is recommended as some aggregation was detected during this test and it was unclear of it was due to the high salt content of the cell lysis buffer or, whether agglomeration had already taken place intracellularly. To repeat this experiment with the suggested change, would deliver details on the intracellular processing of the particles, although in the silver appeared to cluster less in cells than gold. The one organelle that appeared to have a higher concentration of NPs was the mitochondria. To explore the aggregation status within this organelle it is suggested that a mitochondrial isolation is performed on these cells and sent for analysis.

7.5.6 Review the RPPA Phosphoproteomic Data

The data generated from the RPPA assay was extensive. Through intial pre-processing when assessing the quality of the output created, 120 bar charts with averaged data for 12 treatment variables were plotted to view the quality of replicates, that's 4320 data points plotted. The EGFR signalling and some apoptotic and DNA repair proteins were focussed upon during this study. However, this data-rich experiment could yield far more interesting signalling events given the time to review it more thoroughly. It is recommended that PCA be employed to highlight differences in cell responses to treatments in a less targeted approach. This would open up explorative projects to investigate any differences highlighted by further Western blots or immunofluorescence studies.

There were antibodies available that were not candidates in this study and and it would be interesting to explore more cell death markers, cell skeleton and motility proteins. The samples could be screened with the remainder of the antibody library,

to understand more about the release of the drug from the NPs and the different effects on the cell from the AgHA and AuCt particles.

Ultimately there are several biological and chemistry questions that were raised during this study to explore further. It has created several standard work flows to follow when 3D Raman mapping, assessing cytotoxicity of NPs to cells and analysing the phosphoproteomic response of cells to NPs and conjugates by RPPA. Using these as an explorative foundation, many of the future works suggested could be achieved.

"Science knows no country, because knowledge belongs to humanity, and it is the torch, which illuminates the world." Louis Pasteur, biologist and chemist, 1822-95.

Chapter 8 References

"I didn't want to just know names of things. I remember really wanting to know how it all worked." Elizabeth Blackburn, Nobel Prize Physiology or Medicine 2009.

1. Wang, H. *et al*. Global, regional, and national life expectancy, all-cause mortality, and cause-specific mortality for 249 causes of death, 1980–2015: a systematic analysis for the Global Burden of Disease Study 2015. *Lancet* **388,** 1459–1544 (2016).

2. Hanahan, D. & Weinberg, R. A. A. Hallmarks of Cancer:The Next Generation. *Cell* **100,** 646–674 (2011).

3. Ferlay, J. *et al*. Cancer incidence and mortality worldwide: Sources, methods and major patterns in GLOBOCAN 2012. *Int. J. Cancer* **136,** E359–E386 (2015).

4. Hanahan, D. Rethinking the war on cancer. *Lancet* **383,** 558–563 (2014).

5. Stewart, B. W. & Wild, C. P. *World Cancer Report 2014. World Health Organization: Geneva* (IARC, 2014). doi:9283204298

6. Sharma, S. V., Bell, D. W., Settleman, J. & Haber, D. A. Epidermal growth factor receptor mutations in lung cancer. *Nat. Rev. Cancer* **7,** 169–181 (2007).

7. Chen, Z., Fillmore, C. M., Hammerman, P. S., Kim, C. F. & Wong, K. K. Non-small-cell lung cancers: A heterogeneous set of diseases. *Nat. Rev. Cancer* **14,** 535–546 (2014).

8. McLaughlin, C., MacMillan, D., McCardle, C. & Smith, W. E. Quantitative analysis of mitoxantrone by surface-enhanced resonance Raman scattering. *Anal.Chem.* **74,** 3160–3167 (2002).

9. Dowell, J., Minna, J. D. & Kirkpatrick, P. Erlotinib hydrochloride. *Nat. Rev. Drug Discov.* **4,** 13–14 (2005).

10. Chial, H. Proto-oncogenes to oncogenes to cancer. *Nat. Educ.* **1,** 33 (2008).

11. Magkou, C. *et al*. Expression of the epidermal growth factor receptor (EGFR) and the phosphorylated EGFR in invasive breast carcinomas. *Breast Cancer Res.* **10,** 1–8 (2008).

12. Socinski, M. A. The emerging role of biomarkers in advanced non-small-cell lung cancer. *Clin. Lung Cancer* **11,** 149–159 (2010).

13. Yasuda, H., Park, E., Yun, C.-H., Sng, N. & Lucena-Araujo, A. Structural, biochemical and clinical charactereization of Epidermal growth factor receptor(EGFR) exon 20 insertions mutations in lung cancer. *Sci. Transl. Med.* **5,** (2014).

14. Toporkiewicz, M., Meissner, J., Matusewicz, L., Czogalla, A. & Sikorski, A. F. Toward a magic or imaginary bullet? Ligands for drug targeting to cancer cells: Principles, hopes, and challenges. *Int. J. Nanomedicine* **10,** 1399–1414 (2015).

15. Grodsinski, P. *et al*. NCI Cancer Nanotechnology Plan. *NCI Rep.* 1–76 (2010). at <http://nano.cancer.gov/objects/pdfs/CaNanoPlan.pdf>

16. Lindeman, N. I. *et al*. Molecular Testing Guideline for Selection of Lung Cancer Patients for EGFR and ALK Tyrosine Kinase Inhibitors. *J. Thorac. Oncol*. **8,** 823–859 (2013).

17. FDA. In Vitro Companion Diagnostic Devices: Guidance for Industry and Food and Drug Administration Staff. *Fed. Regist*. 12 (2014).

18. Roskoski, R. The ErbB/HER receptor protein-tyrosine kinases and cancer. *Biochem. Biphysical Res. Commun*. **319,** 1–11 (2004).

19. Stamos, J., Sliwkowski, M. X. & Eigenbrot, C. Structure of the epidermal growth factor receptor kinase domain alone and in complex with a 4-anilinoquinazoline inhibitor. *J. Biol. Chem*. **277,** 46265–46272 (2002).

20. Park, J. H., Liu, Y., Lemmon, M. A. & Radhakrishnan, R. Erlotinib binds both inactive and active conformations of the EGFR tyrosine kinase domain. *Biochem. J*. **448,** 417–423 (2012).

21. Remko, M. Acidity, lipophilicity, solubility, absorption, and polar surface area of some ACE inhibitors. *Chem. Pap*. **61,** 133–141 (2007).

22. Lam, A. T. N. *et al*. Adsorption and desorption of tyrosine kinase inhibitor erlotinib on gold nanoparticles. *J. Colloid Interface Sci*. **425,** 96–101 (2014).

23. Fleischmann, M., Hendra, P. J. & McQuillan, A. J. Raman spectra of pyridine adsorbed at a silver electrode. *Chem. Phys. Lett*. **26,** 163–166 (1974).

24. Jeanmaire, D. L. & Van Duyne, R. P. Surface raman spectroelectrochemistry. *J. Electroanal. Chem. Interfacial Electrochem*. **84,** 1–20 (1977).

25. Raman, C.V.; Krishnan, K. S. A New Type of Secondary Radiation. *Nature* **3048,** 501–502 (1928).

26. Smith, E. & Dent, G. *Modern Raman Spectroscopy—A Practical Approach*. *Journal of Raman Spectroscopy* **36,** (2005).

27. Palonpon, A. F. *et al*. Raman and SERS microscopy for molecular imaging of live cells. *Nat. Protoc*. **8,** 677–692 (2013).

28. Sanchez-Dominguez, C. N., Gallardo-Blanco, H. L., Rodriguez-Rodriguez, A. A., Vela-Gonzalez, A. V & Sanchez-Dominguez, M. Nanoparticles vs cancer: a multifuncional tool. *Curr. Top. Med. Chem*. **14,** 664–75 (2014).

29. Jerjes, W. K. *et al*. The future of medical diagnostics: review paper. *Head Neck Oncol*. **3,** 38 (2011).

30. Egusquiaguirre, S. P., Igartua, M., Hernández, R. M. & Pedraz, J. L. Nanoparticle delivery systems for cancer therapy: Advances in clinical and preclinical research. *Clin. Transl. Oncol*. **14,** 83–93 (2012).

31. Barth, A., Haris, P. I. *Biological and Biomedical Infrared Spectroscopy*. (IOP Press, 2009). at <https://www.iospress.nl/book/biological-and-biomedical-infrared-spectroscopy/>

32. Atkins, P. DePaula, P. Keeler, J. *Atkins' Physical Chemistry*. (Oxford University Press, 2016). at <https://global.oup.com/ukhe/product/atkins-physical-chemistry-9780198769866?cc=gb&lang=en&>

33. Smith, E. & Dent, G. *Modern Raman Spectrocopy: A Practical Approach*. *Modern Raman Spectroscopy - A Practical Approach* (2005). doi:10.1002/0470011831

34. Albrecht, M. G. & Creighton, J. A. Anomalously Intense Raman Spectra of Pyridine at a Silver Electrode. *J. Am. Chem. Soc.* **99,** 5215–5217 (1977).

35. Le Ru, E. C. & Etchegoin, P. G. *Principles of Surface Enhanced Raman Spectroscopy and related plasmonic effects*. (Elsevier, 2009).

36. McAughtrie, S., Faulds, K. & Graham, D. Surface enhanced Raman spectroscopy (SERS): Potential applications for disease detection and treatment. *J. Photochem. Photobiol. C Photochem. Rev.* **21,** 40–53 (2014).

37. Aili, D. & Stevens, M. M. Bioresponsive peptide–inorganic hybrid nanomaterials. *Chem. Soc. Rev.* **39,** 3358 (2010).

38. Ritchie, R. H. Plasma Losses by Fast Electrons in Thin Films. *Phys. Rev.* **106,** 874–881 (1957).

39. Hammond, J. L., Bhalla, N., Rafiee, S. D. & Estrela, P. Localized surface plasmon resonance as a biosensing platform for developing countries. *Biosensors* **4,** 172–188 (2014).

40. Larmour, I. A. & Graham, D. Surface enhanced optical spectroscopies for bioanalysis. *Analyst* **136,** 3831–3853 (2011).

41. Freestone, I., Meeks, N., Sax, M. & Higgitt, C. *The Lycurgus Cup-A Roman Nanotechnology*. at <http://master-mcn.u-strasbg.fr/wp-content/uploads/2015/09/lycurgus.pdf>

42. Demtroeder, W. *Laser Spectroscopy: Basic Concepts and Instrumentation*. (Springer-Verlag Berlin Heidelberg GmbH, 2003). doi:10.1007/978-3-662-08260-7

43. Weber, D. Nanomedicine. *Health Forum J.* **42,** 36–37 (1999).

44. Sorg, C. *Scientific Forward Look on Nanomedicine*. *European Science Foundation Policy Briefing* **23,** (2005).

45. Craig, D. *et al.* Confocal SERS mapping of glycan expression for the identification of cancerous cells. *Anal. Chem.* **86,** 4775–4782 (2014).

46. Gajjar, Siddharth K.; Sailor, G. U.; Seth, A. K.; Patel, P. B. A Review on Targeted Drug Delivery: Magnetic Drug Delivery System. *J. Pharm. Sci. Biosci. Res.* **1,** 125–133 (2011).

47. McAughtrie, S., Lau, K., Faulds, K. & Graham, D. 3D optical imaging of multiple SERS nanotags in cells. *Chem. Sci.* **4,** 3566–3572 (2013).

48. Belsey, N. A. *et al.* Evaluation of drug delivery to intact and porated skin by coherent Raman scattering and fluorescence microscopies. *J. Control. Release* **174,** 37–42 (2014).

49. Misak, H. E. *et al.* Albumin-based nanocomposite spheres for advanced drug delivery systems. *Biotechnol. J.* **9,** 163–70 (2014).

50. Luo, J. *et al.* Well-defined, size-tunable, multifunctional micelles for efficient paclitaxel delivery for cancer treatment. *Bioconjug. Chem.* **21,** 1216–1224 (2010).

51. Fang, W. *et al.* PH-controllable drug carrier with SERS activity for targeting cancer cells. *Biosens. Bioelectron.* **57,** 10–15 (2014).

52. Du, J. Z., Du, X. J., Mao, C. Q. & Wang, J. Tailor-Made dual pH-sensitive polymer-doxorubicin nanoparticles for efficient anticancer drug delivery. *J.*

Am. Chem. Soc. **133,** 17560–17563 (2011).

53. Mclaughlin, C., Macmillan, D., Mccardle, C. & Smith, W. E. Quantitative Analysis of Mitoxantrone by Surface-Enhanced Resonance Raman Scattering important to know the concentration in blood during. *Anal. Chem.* **74,** 3160–3167 (2002).

54. Ramasamy, T. *et al.* Layer-by-layer assembly of liposomal nanoparticles with PEGylated polyelectrolytes enhances systemic delivery of multiple anticancer drugs. *Acta Biomater.* **10,** 5116–5127 (2014).

55. Brown, S. D. *et al.* Gold Nanoparticles for the Improved Anticancer Drug Delivery of the Active Component of Oxaliplatin. *J. Am. Chem. Soc.* **132,** 4678–4684 (2010).

56. Pijanka, J. K. *et al.* Identification of different subsets of lung cells using Raman microspectroscopy and whole cell nucleus isolation. *Analyst* **138,** 5052–5058 (2013).

57. Schut, T. B., Vincent, A., Kros, J. M. & Puppels, G. J. Detection of Meningioma in Dura Mater by Raman Spectroscopy. *In Vivo (Brooklyn).* **77,** 7958–7965 (2005).

58. Crow, P. *et al.* The use of Raman spectroscopy to differentiate between different prostatic adenocarcinoma cell lines. *Br. J. Cancer* **92,** 2166–70 (2005).

59. El-Mashtoly, S. F. *et al.* Label-free imaging of drug distribution and metabolism in colon cancer cells by Raman microscopy. *Analyst* **139,** 1155–1161 (2014).

60. Jamieson, L. E., Wetherill, C., Faulds, K. & Graham, D. Ratiometric Raman imaging reveals the new anti-cancer potential of lipid targeting drugs. *Chem. Sci.* (2018). doi:10.1039/C8SC02312C

61. Schiff, R. I. & Gennaro, J. F. The role of the buffer in the fixation of biological specimens for transmission and scanning electron microscopy. *Scanning* **2,** 135–148 (1979).

62. Ma, Y.-H. V., Middleton, K., You, L. & Sun, Y. A review of microfluidic approaches for investigating cancer extravasation during metastasis. *Microsystems Nanoeng.* **4,** 17104 (2018).

63. Sackmann, E. K., Fulton, A. L. & Beebe, D. J. The present and future role of microfluidics in biomedical research. *Nature* **507,** 181–189 (2014).

64. Zhang, X., Yin, H., Cooper, J. M. & Haswell, S. J. Characterization of cellular chemical dynamics using combined microfluidic and Raman techniques. *Anal. Bioanal. Chem.* **390,** 833–840 (2008).

65. Cristobal, G., Arbouet, L., Sarrazin, F., Talaga, D. & Bruneel, J. On-line laser Raman spectroscopic probing of droplets engineered in microfluidic devices. *Lab a Ch* **6,** 1140–1146 (2006).

66. Ackermann, K. R., Henkel, T. & Popp, J. Quantitative Online Detection of Low- Concentrated Drugs via a SERS Microfluidic System. *Chem Phys Chem* **8,** 2665–2670 (2007).

67. Yamakoshi, H. *et al.* Imaging of EdU, an alkyne-tagged cell proliferation probe, by Raman microscopy. *J. Am. Chem. Soc.* **133,** 6102–6105 (2011).

68. Yamakoshi, H. *et al*. Alkyne-tag Raman imaging for visualization of mobile small molecules in live cells. *J. Am. Chem. Soc.* **134,** 20681–20689 (2012).

69. Palonpon, A. F., Sodeoka, M. & Fujita, K. Molecular imaging of live cells by Raman microscopy. *Curr. Opin. Chem. Biol.* **17,** 708–715 (2013).

70. Hu, F. *et al*. Supermultiplexed optical imaging and barcoding with engineered polyynes. *Nat. Methods* **15,** 194–200 (2018).

71. Elsaesser, A. & Howard, C. V. Toxicology of nanoparticles. *Adv. Drug Deliv. Rev.* **64,** 129–137 (2012).

72. Love, S. A., Maurer-Jones, M. A., Thompson, J. W., Lin, Y.-S. & Haynes, C. L. Assessing Nanoparticle Toxicity. *Annu. Rev. Anal. Chem.* **5,** 181–205 (2012).

73. Etheridge, M. L. *et al*. The big picture on nanomedicine: The state of investigational and approved nanomedicine products. *Nanomedicine Nanotechnology, Biol. Med.* **9,** 1–14 (2013).

74. Juliano, R. Nanomedicine: Is the wave cresting? *Nat. Rev. Drug Discov.* **12,** 171–172 (2013).

75. Vert, M. *et al*. Terminology for biorelated polymers and applications (IUPAC Recommendations 2012). *Pure Appl. Chem.* **84,** 377–410 (2012).

76. Conde, J. *et al*. Revisiting 30 years of biofunctionalization and surface chemistry of inorganic nanoparticles for nanomedicine. *Front. Chem.* **2,** 1–27 (2014).

77. Qian, X. *et al*. In vivo tumor targeting and spectroscopic detection with surface-enhanced Raman nanoparticle tags. *Nat. Biotechnol.* **26,** 83–90 (2008).

78. Barenholz, Y. Doxil® - The first FDA-approved nano-drug: Lessons learned. *J. Control. Release* **160,** 117–134 (2012).

79. Pillai, G. Nanomedicines for Cancer Therapy : An Update of FDA Approved and Those under Various Stages of Development. *SOJ Pharm Pharm Sci* **1,** 1–13 (2014).

80. Song, S. *et al*. Novel peptide ligand directs liposomes toward EGF-R high-expressing cancer cells in vitro and in vivo. *FASEB J.* **23,** 1396–1404 (2009).

81. Honary, S. & Zahir, F. Effect of zeta potential on the properties of nano-drug delivery systems - A review (Part 1). *Trop. J. Pharm. Res.* **12,** 255–264 (2013).

82. Li, Y. *et al*. A smart and versatile theranostic nanomedicine platform based on nanoporphyrin. *Nat. Commun.* **5,** (2014).

83. Dreaden, E. C., Alkilany, A. M., Huang, X., Murphy, C. J. & El-Sayed, M. A. The golden age: Gold nanoparticles for biomedicine. *Chem. Soc. Rev.* **41,** 2740–2779 (2012).

84. Marslin, G. *et al*. Poly(D,L-lactic-co-glycolic acid) nanoencapsulation reduces Erlotinib-induced subacute toxicity in rat. *J. Biomed. Nanotechnol.* **5,** 464–71 (2009).

85. Barghi, L., Asgari, D., Barar, J., Nakhlband, A. & Valizadeh, H. Synthesis, characterization and in vitro anti-tumoral evaluation of erlotinib-PCEC nanoparticles. *Asian Pacific J. Cancer Prev.* **15,** 10281–10287 (2014).

86. Han, G. *et al*. Label-Free Surface-Enhanced Raman Scattering Imaging to

Monitor the Metabolism of Antitumor Drug 6 - Mercaptopurine in Living Cells. *Anal. Chem.* **86,** 11503–11507 (2014).

87. McLintock, A., Cunha-Matos, C. A., Zagnoni, M., Millington, O. R. & Wark, A. W. Universal surface-enhanced Raman tags: Individual nanorods for measurements from the visible to the infrared (514-1064 nm). *ACS Nano* **8,** 8600–8609 (2014).

88. Reifarth, M., Hoeppener, S. & Schubert, U. S. Uptake and Intracellular Fate of Engineered Nanoparticles in Mammalian Cells: Capabilities and Limitations of Transmission Electron Microscopy—Polymer-Based Nanoparticles. *Adv. Mater.* **30,** 1–28 (2018).

89. Ong, K. J. *et al.* Widespread nanoparticle-assay interference: Implications for nanotoxicity testing. *PLoS One* **9,** (2014).

90. Hoskins, C., Wang, L., Cheng, W. P. & Cuschieri, A. Dilemmas in the reliable estimation of the in-vitro cell viability in magnetic nanoparticle engineering : which tests and what protocols ? *Nanoscale Res. Lett.* **7,** 1–12 (2012).

91. Paweletz, C. P. *et al.* Reverse phase protein microarrays which capture disease progression show activation of pro-survival pathways at the cancer invasion front. *Oncogene* **20,** 1981–1989 (2001).

92. Nishizuka, S. S. & Mills, G. B. New era of integrated cancer biomarker discovery using reverse-phase protein arrays. *Drug Metab. Pharmacokinet.* **31,** 34–45 (2016).

93. Septiadi, D., Crippa, F., Moore, T. L., Rothen-Rutishauser, B. & Petri-Fink, A. Nanoparticle–Cell Interaction: A Cell Mechanics Perspective. *Adv. Mater.* **30,** 1–30 (2018).

94. Waris, G. & Ahsan, H. Reactive oxygen species: Role in the development of cancer and various chronic conditions. *J. Carcinog.* **5,** 1–8 (2006).

95. Orcutt, K. P. *et al.* Erlotinib-mediated inhibition of EGFR signaling induces metabolic oxidative stress through NOX4. *Cancer Res.* **71,** 3932–3940 (2011).

96. Leopold, N. & Lendl, B. A New Method for Fast Preparation of Highly Surface-Enhanced Raman Scattering (SERS) Active Silver Colloids at Room Temperature by Reduction of Silver Nitrate with Hydroxylamine Hydrochloride. *J. Phys. Chem. B* **107,** 5723–5727 (2003).

97. Turkevich, J. Colloidal gold. Part II. *Gold Bull.* **18,** 125–131 (1985).

98. The MathWorks Inc. MATLAB. (2014).

99. Haiss, W., Thanh, N. T. K., Aveyard, J. & Fernig, D. G. Determination of Size and Concentration of Gold Nanoparticles from UV - Vis Spectra. **79,** 4215–4221 (2007).

100. Yguerabide, J. & Yguerabide, E. E. Light-scattering submicroscopic particles as highly fluorescent analogs and their use as tracer labels in clinical and biological applications. *Anal. Biochem.* **262,** 157–176 (1998).

101. Rasband, W. S. ImageJ. (1997).

102. Schindelin, J. *et al.* Fiji: An open-source platform for biological-image analysis. *Nat. Methods* **9,** 676–682 (2012).

103. Schindelin, J., Rueden, C. T., Hiner, M. C. & Eliceiri, K. W. The ImageJ ecosystem: An open platform for biomedical image analysis. *Mol. Reprod.*

Dev. **82,** 518–529 (2015).

104. Wills, J., Edwards-hicks, J. & Finch, A. J. AssayR: A Simple Mass Spectrometry Software Tool for Targeted Metabolic and Stable Isotope Tracer Analyses. *Anal. Chem.* **89,** 9616–9619 (2017).

105. Eisen, M. B., Spellman, P. T., Brown, P. O. & Botstein, D. Cluster analysis and display of genome-wide expression patterns. *Proc. Natl. Acad. Sci.* **95,** 14863–14868 (1998).

106. Saldanha, A. J. Java Treeview - Extensible visualization of microarray data. *Bioinformatics* **20,** 3246–3248 (2004).

107. Shannon, P. *et al.* Cytoscape: a software environment for integrated models of biomolecular interaction networks. *Genome Res.* 2498–2504 (2003). doi:10.1101/gr.1239303.metabolite

108. Warde-Farley, D. *et al.* The GeneMANIA prediction server: Biological network integration for gene prioritization and predicting gene function. *Nucleic Acids Res.* **38,** 214–220 (2010).

109. Willner, M. R., Mcmillan, K. S., Graham, D., Vikesland, P. J. & Zagnoni, M. Surface-Enhanced Raman Scattering Based Microfluidics for Single-Cell Analysis. *Anal. Chem.* **90,** 12004–12010 (2018).

110. McMillan, K. S., McCluskey, A. G., Sorensen, A., Boyd, M. & Zagnoni, M. Emulsion technologies for multicellular tumour spheroid radiation assays. *Analyst* **141,** 100–110 (2016).

111. Fleger, Y. & Rosenbluh, M. Surface Plasmons and Surface Enhanced Raman Spectra of Aggregated and Alloyed Gold-Silver Nanoparticles. **2009,** (2009).

112. El-Dessouky, R., Georges, M. & Azzazy, H. M. E. in *Functional Nanoparticles for Bioanalysis, Nanoemdicine and Bioelectronic Devices* (eds. Hepel, M. & Zhong, C.-J.) 359–404 (American Chemical Socirty (Oxford Universuty Press), 2012).

113. Mott, D. & Maenosono, S. in *Functional Nanparticles for Bioanalysis, Nanomedicine, and Bioelectronic Devices* (eds. Hepel, M. & Zhong, C.-J.) 327–358 (American Chemical Society (Oxford University Press), 2012).

114. Schindelin, J. *et al.* Fiji: an open-source platform for biological-image analysis. *Nat. Methods* **9,** 676 (2012).

115. Fu, D., Holtom, G., Freudiger, C., Zhang, X. & Xie, X. S. Hyperspectral imaging with stimulated Raman scattering by chirped femtosecond lasers. *J Phys Chem B* **117,** 4634–4640 (2013).

116. Joo, S. W. & Kim, K. Adsorption of phenylacetylene on gold nanoparticle surfaces investigated by surface-enhanced Raman scattering. *J. Raman Spectrosc.* **35,** 549–554 (2004).

117. Wang, Y. & Wang, E. in *Surface Enhanced Raman Spectroscopy: Analytical, Biophysical and Life Science Applications* (ed. Schlucker, S.) 39–69 (Wiley VCH, 2011).

118. Kustner, B. *et al.* SERS labels for red laser excitation: silica-encapsulated SAMs on tunable gold/silver nanoshells. *Angew Chem Int* **48,** 1950–1953 (2009).

119. Todor, I. ., Szabo, L., Marisca, O. T., Chis, V. & Leopold, N. Gold nanoparticle

assemblies of controllable size obtained by hydroxylamine reduction at room temperature. *J. Nanoparticle Res.* **16,** 2740–2744 (2014).

120. Lee, P. C. & Meisel, D. Adsorption and surface-enhanced Raman of dyes on silver and gold sols. *J. Phys. Chem.* **86,** 3391–3395 (1982).

121. Hare, J. I. *et al.* Challenges and strategies in anti-cancer nanomedicine development: An industry perspective. *Adv. Drug Deliv. Rev.* **108,** 25–38 (2017).

122. TARCEVA. Prescribing Information TARCEVA. *Astellas Pharma US Inc Genentech Inc.* 1–18 (2004). at <https://www.accessdata.fda.gov/drugsatfda_docs/label/2009/021743s015lbl.pdf>

123. Phelps, R. *et al.* NCI-Navy Medical Oncology Branch cell line data base. *J. Cell. Biochem.* **24,** 32–91 (1996).

124. Rottem, S. & Barile, M. F. Beware of Mycoplasma. *Trends Biotechnol.* **11,** 143–151 (1993).

125. Olarerin-george, A. O. & Hogenesch, J. B. Assessing the prevalence of mycoplasma contamination in cell culture via a survey of NCBI ' s RNA-seq archive. *Nucleic Acids Res.* **43,** 2535–2542 (2015).

126. Coronato, S. & Coto, C. E. [Prevalence of Mycoplasma orale as a contaminant of cell cultures in Argentina]. *Rev Argent Microbiol* **23,** 166–171 (1991).

127. Drexler, H. G. & Uphoff, C. C. Mycoplasma contamination of cell cultures : Incidence , sources , effects , detection , elimination , prevention. *Cytotechnology* **39,** 75–90 (2002).

128. Miller, C. J. *et al.* Mycoplasma infection significantly alters microarray gene expression profiles. *Biotechniques* **35,** 812–814 (2003).

129. Korch, C., Vaughan, L., Gl, W. & Capes-davis, A. Widespread Use of Misidentified Cell Line KB (HeLa): Incorrect Attribution and Its Impact Revealed through Mining the Scientific Literature. *Cancer Res.* **77,** 2784–2789 (2017).

130. Capes-davis, A. *et al.* Match criteria for human cell line authentication : Where do we draw the line ? *Int. J. Cancer* **132,** 2510–2519 (2013).

131. Fotakis, G. & Timbrell, J. A. In vitro cytotoxicity assays: Comparison of LDH, neutral red, MTT and protein assay in hepatoma cell lines following exposure to cadmium chloride. *Toxicol. Lett.* **160,** 171–177 (2006).

132. Stoddart, M. J. *Cell viability assays: introduction. Methods in molecular biology (Clifton, N.J.)* **740,** (2011).

133. Barth, S., Glick, D. & Macleod, K. F. Autophagy : assays and artifacts. *J. Pathol.* **221,** 117–124 (2010).

134. Riss, T. L., Niles, A. L. & Minor, L. Cell Viability Assays Assay Guidance Manual. *Assay Guid. Man.* 1–23 (2004). doi:10.1016/j.acthis.2012.01.006

135. Gliga, A. R., Skoglund, S., Odnevall Wallinder, I., Fadeel, B. & Karlsson, H. L. Size-dependent cytotoxicity of silver nanoparticles in human lung cells: The role of cellular uptake, agglomeration and Ag release. *Part. Fibre Toxicol.* **11,** 1–17 (2014).

136. McKeating, K. S., Sloan-Dennison, S., Graham, D. & Faulds, K. An

investigation into the simultaneous enzymatic and SERRS properties of silver nanoparticles. *Analyst* **138,** 6347–6353 (2013).

137. Saquib, Q., Faisal, M. & Abdulrahman, A. A. A. *Cellular and Molecular Toxicology of Nanoparticles*. (Springer International Publishing, 2018).

138. Joris, F. *et al*. Assessing nanoparticle toxicity in cell-based assays: Influence of cell culture parameters and optimized models for bridging the in vitro-in vivo gap. *Chem. Soc. Rev.* **42,** 8339–8359 (2013).

139. Kim, M., Ock, K., Cho, K., Joo, S. W. & Lee, S. Y. Live-cell monitoring of the glutathione-triggered release of the anticancer drug topotecan on gold nanoparticles in serum-containing media. *Chem. Commun.* **48,** 4205–4207 (2012).

140. Yeo, W. *et al*. Erlotinib at a dose of 25 mg daily for non-small-cell lung cancers with EGFR mutations. *J. Thorac. Oncol.* **5,** 1048–1053 (2011).

141. Kim, J. *et al*. PEGylated polypeptide lipid nanocapsules to enhance the anticancer efficacy of erlotinib in non-small cell lung cancer. *Colloids Surfaces B Biointerfaces* **150,** 393–401 (2017).

142. Ono, N. *et al*. Enhanced antitumor activity of erlotinib in combination with the Hsp90 inhibitor CH5164840 against non-small-cell lung cancer. *Cancer Sci.* **104,** 1346–1352 (2013).

143. Sos, M. L. *et al*. Priority Report PTEN Loss Contributes to Erlotinib Resistance in EGFR-Mutant Lung Cancer by Activation of Akt and EGFR. (2009). doi:10.1158/0008-5472.CAN-08-4055

144. Hirano, T. *et al*. In vitro modeling to determine mutation specificity of EGFR tyrosine kinase inhibitors against clinically relevant EGFR mutants in non-small-cell lung cancer. *Oncotarget* **6,** 38789–38803 (2015).

145. Beer, C., Foldbjerg, R., Hayashi, Y., Sutherland, D. S. & Autrup, H. Toxicity of silver nanoparticles-Nanoparticle or silver ion? *Toxicol. Lett.* **208,** 286–292 (2012).

146. Matthaus, C. *et al*. in *Biophysical Tools for Biologists: In Vivo Techniques* (eds. Correia, J. J. & Detrich, H. W.) 275–308 (Academic Press (Elsevier Science Imprint), 2009). at <https://books.google.co.uk/books?id=mD76YWQu-xIC>

147. Ota, C., Furukawa, T., Shima, K., Sano, S. & Kuramochi, K. Alkyne Tagged Raman Probes for Protein by Chemical Modification Approach. *Chem. Sel. Commun.* **2,** 1267–1270 (2017).

148. Blasiak, B., Londergan, C. H., Webb, L. J. & Cho, M. Vibrational Probes: From Small Molecule Solvatochromism Theory and Experiments to Applications in Complex Systems. *Acc. Chem. Res.* **50,** 968–976 (2017).

149. Kennedy, D. C., McKay, C. S., Tay, L. L., Rouleau, Y. & Pezacki, J. P. Carbon-bonded silver nanoparticles: Alkyne-functionalized ligands for SERS imaging of mammalian cells. *Chem. Commun.* **47,** 3156–3158 (2011).

150. Joo, S. W. Adsorption of bipyridine compounds on gold nanoparticle surfaces investigated by UV-vis absorbance spectroscopy and surface enhanced Raman scattering. *Spectrosc. Lett.* **39,** 85–96 (2006).

151. Schlucker, S. in *Surface Enhanced Raman Spectroscopy: Analytical, Biophysical and Life Science Applications* (ed. Schlucker, S.) 263–281 (Wiley-

VCH, 2011).

152. Balvan, J., Krizova, A., Gumulec, J. & Raudenska, M. Multimodal Holographic Microscopy : Distinction between Apoptosis and Multimodal Holographic Microscopy : Distinction between Apoptosis and Oncosis. (2015). doi:10.1371/journal.pone.0121674

153. Akter, M. *et al*. A systematic review on silver nanoparticles-induced cytotoxicity: Physicochemical properties and perspectives. *J. Adv. Res.* **9,** 1–16 (2018).

154. Xue, Y. *et al*. Cytotoxicity and apoptosis induced by silver nanoparticles in human liver HepG2 cells in different dispersion media. *J. Appl. Toxicol.* **36,** 352–360 (2016).

155. Gandhi, J. *et al*. Alterations in Genes of the EGFR Signaling Pathway and Their Relationship to EGFR Tyrosine Kinase Inhibitor Sensitivity in Lung Cancer Cell Lines. **4,** (2009).

156. Fu, D. *et al*. Imaging the intracellular distribution of tyrosine kinase inhibitors in living cells with quantitative hyperspectral stimulated Raman scattering. *Nat. Chem.* **6,** 614–622 (2014).

157. Abcam. *CytoPainter: Lysosome, ER, Nuclear Stain*. (2012). at <www.abcam.com>

158. Stevenson, R. *et al*. Analysis of intracellular enzyme activity by surface enhanced Raman scattering. *Analyst* **138,** 6331 (2013).

159. Traverso, N. *et al*. Role of Glutathione in Cancer Progression and Chemoresisstance. *Oxid. Med. Cell. Longev.* **2013,** (2013).

160. Gomez-cabrera, M. C. *et al*. Mitochondria as sources and targets of damage in cellular aging. (2012). doi:10.1515/cclm-2011-0795

161. Marzetti, E. *et al*. Role of mitochondrial dysfunction and altered autophagy in cardiovascular aging and disease : from mechanisms to therapeutics. (2018). doi:10.1152/ajpheart.00936.2012

162. Li, Y. & Ju, D. in *Cellular and Molecular Toxicology of Nanoparticles* (eds. Alatar, A., Al-Khedhairy, A., Faisal, M. & Saquib, Q.) 71–84 (Springer International Publishing, 2018).

163. Cameron, S. J., Hosseinian, F. & Willmore, W. G. A Current Overview of the Biological and Cellular Effects of Nanosilver. 1–40 (2018). doi:10.3390/ijms19072030

164. Natale, G. *et al*. Compartment-dependent mitochondrial alterations in experimental ALS , the effects of mitophagy and mitochondriogenesis. *Front. Cell. Neurosci.* **9,** 1–25 (2015).

165. Kurzątkowska, K., Santiago, T. & Hepel, M. Plasmonic nanocarrier grid-enhanced Raman sensor for studies of anticancer drug delivery. *Biosens. Bioelectron.* **91,** 780–787 (2017).

166. Jeong, C. & Joo, S. H. Downregulation of Reactive Oxygen Species in Apoptosis. *J. Cancer Prev.* **21,** 13–20 (2016).

167. Traverso, N. *et al*. Role of Glutathione in Cancer Progression and Chemoresisstance. *Oxid. Med. Cell. Longev.* **2013,** 1–10 (2013).

168. Wang, S. *et al*. Smart pH- and reduction-dual-responsive folate– PEG-coated

polymeric lipid vesicles for tumor- triggered targeted drug delivery. *Nanoscale* **6,** 7635–7642 (2014).

169. Lam, A. T. N. *et al*. Colloidal gold nanoparticle conjugates of gefitinib. *Colloids Surfaces B Biointerfaces* **123,** 61–67 (2014).

170. Annapurna, M. M., Venkatesh, B. & Chaitanya, R. K. Analytical Techniques for the Determination of Erlotinib HCl in Pharmaceutical Dosage Forms by Spectrophotometry. *Chem. Sci. Trans.* **3,** 840–846 (2014).

171. McKenzie, F., Steven, V., Ingram, A. & Graham, D. Quantitation of biomolecules conjugated to nanoparticles by enzyme hydrolysis. *Chem. Commun.* 2872–2874 (2009). doi:10.1039/b823057a

172. Hsiao, I. L. *et al*. Quantification and visualization of cellular uptake of TiO 2 and Ag nanoparticles : comparison of different ICP - MS techniques. *J. Nanobiotechnology* 1–13 (2016). doi:10.1186/s12951-016-0203-z

173. Rosman, C., Pierrat, S., Henkel, A. & Tarantola, M. A New Approach to Assess Gold Nanoparticle Uptake by Mammalian Cells : Combining Optical Dark-Field and Transmission Electron Microscopy. 3683–3690 (2012). doi:10.1002/smll.201200853

174. Rosarin, F. S. & Mirunalini, S. Nobel Metallic Nanoparticles with Novel Biomedical Properties. *J. Bioanal. Biomed.* **03,** 85–91 (2011).

175. Huynh, K. A., Siska, E., Heithmar, E., Tadjiki, S. & Pergantis, S. A. Detection and Quantification of Silver Nanoparticles at Environmentally Relevant Concentrations Using Asymmetric Flow Field − Flow Fractionation Online with Single Particle Inductively Coupled Plasma Mass Spectrometry. *Anal. Chem.* **88,** 4909–4616 (2016).

176. Aznar, R. *et al*. Quantification and size characterisation of silver nanoparticles in environmental aqueous samples and consumer products by single particle- ICPMS. *Talanta* **175,** 200–208 (2017).

177. Vidmar, J., Milacic, R. & Scancar, J. Sizing and simultaneous quantification of nanoscale titanium dioxide and a dissolved titanium form by single particle inductively coupled plasma mass spectrometry. *Microchem. J.* **132,** 391–400 (2017).

178. Perez-Soler, R. Oncologist HER1 / EGFR Targeting : Refining the Strategy. *Oncologist* **9,** 58–67 (2004).

179. Liefers-visser, J. A. L., Meijering, R. A. M., Reyners, A. K. L., Zee, A. G. J. Van Der & Jong, S. De. IGF system targeted therapy : Therapeutic opportunities for ovarian cancer. *Cancer Treat. Rev.* **60,** 90–99 (2017).

180. Podhorecka, M., Skladanowski, A. & Bozko, P. H2AX Phosphorylation : Its Role in DNA Damage Response and Cancer Therapy. *J. ofNucleic Acids* **2010,** 1–9 (2010).

181. Sharma, A. M., Singh, K. & Almasan, A. in *Methods in Molecular Biology: DNA Repair Protocols* (ed. Bjergbaek, L.) 613–626 (Springer, 2012).

Appendices

"That's all folks!"
Looney Tunes.

A. ICP-MS and spICP-MS Reports by LGC on Silver Content

Report by LGC on ICP-MS of AgHA and AgHA conjugates in H1355 cell samples.

Total content of silver in cell lysates
Results Report

NAME : Heidi Goenaga-Infante
INSTITUTE : LGC Limited
DEPARTMENT : Inorganic Analysis, Science and Innovation
ADDRESS : Queens Road, Teddington, Middlesex, TW11 0LY

COUNTRY : United Kingdom
TEL : +44(0)208 943 7555
FAX : +44(0)208 943 2767
E-MAIL : Heidi.Goenaga-Infante@lgcgroup.com

Results completed, checked and authorised by:

Lead Analysts Susana Nunez 31/01/2018

Approved
and authorised Heidi Goenaga-Infante 31/01/2018

Sample receipt and storage

Cell lysates samples were received from University of Strathclyde in 1.5 mL Eppendorf tubes containing approximately 300 µL of sample which were stored at 4°C until analysis.

Sample Preparation

Sample tubes were gently shaken to mix the solution thoroughly prior to opening. Approximately 0.05 g of sample was accurately weighed into PTFE microwave digestion vessels, followed by the addition of 0.1 g of 2 mg kg^{-1} of Indium (In), which will be used as an internal standard to correct for any instrumental drift or ionisation effects.

1.4 g of HNO_3 (UpA grade, Romil Ltd., Cambride, UK) and 0.45 g of ultrapure water (>18.2 MΩcm^{-1}, Elga Maxima, UK) were added to each vessel which was subjected to the following conditions:

1) 10 minutes ramp to 180°C at 800 W
2) 10 minutes hold at 180°C at 800 W
3) 15 minutes at 0 W

After digestion, the digest solutions were made up to 20 g with ultrapure water (>18.2 MΩcm^{-1}, Elga Maxima, UK) (to achieve a final acid concentration of 7%) and analysed without further dilution.

Calibration standards

Quantification of the samples was performed *via* external calibration using a silver standard (Table 1) from an accredited supplier (VHG, Manchester, USA). The working standards were prepared daily by gravimetric dilution in 7% HNO_3 to match the acid concentration in the samples. The working range was 0 to 60 µg kg^{-1}. Calibration curves achieved correlation coefficients of at least 0.995. Indium was added to all the calibration points, as an internal standard, with a final concentration of 10 µg kg^{-1}, matching the concentration in the samples.

Table 1: Details of the calibration standard

Analyte	Supplier	Source of traceability	Lot/Batch Number	Mass fraction	Expiry
Ag	LGC Standards	SRM 3151	127001-5	998 ± 3 mg kg^{-1}	31 Jan 2019

Instrumentation

The analysis was carried out using an Agilent 8900 ICP-QQQ-MS. The samples were introduced into the plasma *via* a micromist nebuliser, operating at a pumping mode of 0.1 rpm, and using a Scott type double pass spray chamber cooled to 2°C.

The ^{107,109}Ag and ^{113,115}In isotopes were measured in no gas mode. The instrument was tuned daily for optimum signal intensity and stability with typical operating parameters provided in Table 2.

Table 2: Typical operating parameters for total Ag by ICP-MS

Parameter	Agilent 7700
Isotopes measured	$^{107,109}Ag$, $^{113,115}In$
Integration Time (s)	0.3
Points per spectral peak	3
RF Power (W)	1550
Carrier gas (l min^{-1})	1.09
Make up gas (l min^{-1})	0
Spray Chamber (°C)	2

Quality Control

To ensure the quality of results a reference material was submitted to the same sample treatment as the samples:

Table 3: Details of the reference material (source of traceability)

Analyte	Supplier	Source of traceability	Lot/Batch Number	Mass fraction	Expiry
Ag	NIST	NIST RM 8017	Not specified	2.162 ± 0.020 mg	5 days after sample reconstitution

During analysis, up to 8 samples were bracketed by a 'check' standard, typically the middle calibration standard, to ensure there was no drift in the signal. Additionally, spike experiments were performed by adding RM8017 to the cell lysates followed by the same microwave digestion as the samples (see sample preparation section), to check for possible matrix effects.

Results

Calculations

The limit of detection (LOD) and limit of quantification (LOQ) was calculated using at least 6 blanks in each analytical run. The measurement uncertainty was estimated by combining the following components:

- the short-term precision (6 replicate measurements of 2 samples)
- the average recovery of reference materials and spiked samples
- the specificity obtained by comparing the two Ag isotopes

All sample results are corrected for the individual dilution factors. Concentrations over the LOQ and corresponding uncertainties are reported in mg kg^{-1} in the liquid samples as received (Table 4). Although two silver isotopes were measured, only results for the most abundant isotope (^{107}Ag) are reported throughout since the concentration data between isotopes agreed well.

Results overview

A total of 3 replicates per sample and 2 replicates per control cells were measured for total silver. The results of the individual replicates are presented in Table 4 with their associated uncertainty calculated in accordance with ISO 17025 and Eurachem/CITAC guidelines.

Table 4: Silver mass fraction in the cell lysates

Type of sample	Customer name	Analyte	Unit	Mass fraction	Standard uncertainty	Expanded uncertainty (k=2)	Relative expanded uncertainty (%)	k
Control cells (trypsinised)	1A tryps **(replicate 1)**	Ag (total)	mg kg^{-1}	<LOQ*	N/A	N/A	N/A	N/A
	1A tryps **(replicate 2)**	Ag (total)	mg kg^{-1}	<LOQ*	N/A	N/A	N/A	N/A
Cells incubated with AgHA NPs (trypsinised)	1B tryps **(replicate 1)**	Ag (total)	mg kg^{-1}	12.5	0.3	0.6	5	2
	1B tryps **(replicate 2)**	Ag (total)	mg kg^{-1}	12.4	0.3	0.6	5	2
	1B tryps **(replicate 3)**	Ag (total)	mg kg^{-1}	12.1	0.3	0.6	5	2
Cells incubated with conjugate (trypsinised)	1C tryps **(replicate 1)**	Ag (total)	mg kg^{-1}	13.4	0.3	0.7	5	2
	1C tryps **(replicate 2)**	Ag (total)	mg kg^{-1}	13.1	0.3	0.7	5	2
	1C tryps **(replicate 3)**	Ag (total)	mg kg^{-1}	13.2	0.3	0.7	5	2
Control cells (scraped)	3A scrape **(replicate 1)**	Ag (total)	mg kg^{-1}	<LOQ*	N/A	N/A	N/A	N/A
	3A scrape **(replicate 2)**	Ag (total)	mg kg^{-1}	<LOQ*	N/A	N/A	N/A	N/A
Cells incubated with AgHA NPs (scraped)	3B scrape **(replicate 1)**	Ag (total)	mg kg^{-1}	4.8	0.1	0.2	5	2
	3B scrape **(replicate 2)**	Ag (total)	mg kg^{-1}	5.2	0.1	0.3	5	2
	3B scrape **(replicate 3)**	Ag (total)	mg kg^{-1}	5.1	0.1	0.3	5	2
Cells incubated with conjugate (scraped)	3C scrape **(replicate 1)**	Ag (total)	mg kg^{-1}	8.2	0.2	0.4	5	2
	3C scrape **(replicate 2)**	Ag (total)	mg kg^{-1}	9.3	0.2	0.5	5	2
	3C scrape **(replicate 2)**	Ag (total)	mg kg^{-1}	8.2	0.2	0.4	5	2

***LOQ: 0.014 mg kg^{-1}**

The obtained data suggest that the silver content in cells collected by scraping is overall lower than the content of silver of trysinised cells. Comparing the incubation of cells with AgHA NPs and with conjugate, the absorption of silver seems higher in cells exposed to the conjugate. The recoveries from the analysis of NIST RM 8017 and samples spiked with NIST RM 8017 were between 98-103%.

For future work, we would suggest performing single particle ICPMS experiments in order to know if the silver uptaken by cells is present in nanoparticle form or as ionic silver or a mixture of both, and also to obtain information about the diameter and number concentration of the internalised nanoparticles.

Report by LGC on ICP-MS of AgHA and AgHA conjugates in HCC827 cell samples.

Total content of silver in cell lysates
Results Report

Customer details:

INSTITUTE	: University of Strathclyde
DEPARTMENT	: Pure and Applied Chemistry
ADDRESS	: 99 George Street, Glasgow, G1 1XQ
COUNTRY	: United Kingdom
TEL	: +44 (0)141 548 4701
E-MAIL	: duncan.graham@strath.ac.uk

Results completed, checked and authorised by:

Senior researcher Susana Cuello-Nunez 05/06/2018

Approved and authorised
by team leader Heidi Goenaga-Infante 05/06/2018

Sample receipt and storage

Cell lysates samples were received from University of Strathclyde in 1.5 mL Eppendorf tubes containing approximately 300 µL of sample which were stored at 4°C until analysis.

Sample Preparation

Sample tubes were gently shaken to mix the solution thoroughly prior to opening. Approximately 0.05 g of sample was accurately weighed into PTFE microwave digestion vessels, followed by the addition of 0.1 g of 2 mg kg^{-1} of Indium (In), which will be used as an internal standard to correct for any instrumental drift or ionisation effects.

1.4 g of HNO_3 (UpA grade, Romil Ltd., Cambride, UK) and 0.45 g of ultrapure water (>18.2 MΩcm^{-1}, Elga Maxima, UK) were added to each vessel which was subjected to the following conditions:

1) 10 minutes ramp to 180°C at 800 W
2) 10 minutes hold at 180°C at 800 W
3) 15 minutes at 0 W

After digestion, the digest solutions were made up to 20 g with ultrapure water (>18.2 MΩcm^{-1}, Elga Maxima, UK) (to achieve a final acid concentration of 7%) and analysed without further dilution.

Calibration standards

Quantification of the samples was performed *via* external calibration using a silver standard (**Table 1**) from an accredited supplier (VHG, Manchester, USA). The working standards were prepared daily by gravimetric dilution in 7% HNO_3 to match the acid concentration in the samples. The working range was 0 to 60 µg kg^{-1}. Calibration curves achieved correlation coefficients of at least 0.995. Indium was added to all the calibration points, as an internal standard, with a final concentration of 10 µg kg^{-1}, matching the concentration in the samples.

Table 1: Details of the calibration standard

Analyte	Supplier	Source of traceability	Lot/Batch Number	Mass fraction	Expiry
Ag	LGC Standards	SRM 3151	127001-5	998 ± 3 mg kg^{-1}	31 Jan 2019

Instrumentation

The analysis was carried out using an Agilent 8900 ICP-QQQ-MS. The samples were introduced into the plasma *via* a micromist nebuliser, operating at a pumping mode of 0.1 rpm, and using a Scott type double pass spray chamber cooled to 2°C.

The ^{107,109}Ag and ^{113,115}In isotopes were measured in no gas mode. The instrument was tuned daily for optimum signal intensity and stability with typical operating parameters provided in **Table 2**.

Table 2: Typical operating parameters for total Ag by ICP-MS

Parameter	Agilent 7700
Isotopes measured	$^{107,109}Ag$, $^{113,115}In$
Integration Time (s)	0.3
Points per spectral peak	3
RF Power (W)	1550
Carrier gas (l min^{-1})	1.09
Make up gas (l min^{-1})	0
Spray Chamber (°C)	2

Quality Control

To ensure the quality of results a reference material was submitted to the same sample treatment as the samples:

Table 3: Details of the reference material (source of traceability)

Analyte	Supplier	Source of traceability	Lot/Batch Number	Mass fraction	Expiry
Ag	NIST	NIST RM 8017	Not specified	2.162 ± 0.020 mg	5 days after sample reconstitution

During analysis, up to 8 samples were bracketed by a 'check' standard, typically the middle calibration standard, to ensure there was no drift in the signal. Spike experiments were not performed this time as it was proven in the previous analysis (January 2018) the lack of matrix effects for this type of samples.

Results

Calculations

The limit of detection (LOD) and limit of quantification (LOQ) was calculated using at least 6 blanks in each analytical run. The measurement uncertainty was estimated by combining the following components:

- the short-term precision (6 replicate measurements of 2 samples)
- the average recovery of reference materials
- the specificity obtained by comparing the two Ag isotopes

All sample results are corrected for the individual dilution factors. Concentrations over the LOQ and corresponding uncertainties are reported in mg kg^{-1} in the liquid samples as received (Table 4). Although two silver isotopes were measured, only results for the most abundant isotope (^{107}Ag) are reported throughout since the concentration data between isotopes agreed well.

Results overview

A total of 3 replicates per sample were measured for total silver. The results of the individual replicates are presented in Table 4 with their associated uncertainty calculated in accordance with ISO 17025 and Eurachem/CITAC guidelines.

Table 4: Silver mass fraction in the cell lysates

Type of sample	Customer name	Analyte	Unit	Mass fraction	Standard uncertainty	Expanded uncertainty (k=2)	Relative expanded uncertainty (%)	k
Control cells (trypsinised)	Cell Tryp **(replicate 1)**	Ag (total)	mg kg^{-1}	<LOQ*	N/A	N/A	N/A	N/A
	Cell Tryp **(replicate 2)**	Ag (total)	mg kg^{-1}	<LOQ*	N/A	N/A	N/A	N/A
	Cell Tryp **(replicate 3)**	Ag (total)	mg kg^{-1}	<LOQ*	N/A	N/A	N/A	N/A
Cells incubated with AgHA NPs (trypsinised)	Ag tryps **(replicate 1)**	Ag (total)	mg kg^{-1}	8.9	0.2	0.4	5	2
	Ag tryps **(replicate 2)**	Ag (total)	mg kg^{-1}	9.3	0.2	0.5	5	2
	Ag tryps **(replicate 3)**	Ag (total)	mg kg^{-1}	8.8	0.2	0.4	5	2
Cells incubated with conjugate (trypsinised)	Ag C tryps **(replicate 1)**	Ag (total)	mg kg^{-1}	8.8	0.2	0.4	5	2
	Ag C tryps **(replicate 2)**	Ag (total)	mg kg^{-1}	9.1	0.2	0.5	5	2
	Ag C tryps **(replicate 3)**	Ag (total)	mg kg^{-1}	8.9	0.2	0.4	5	2

***LOQ: 0.03 mg kg^{-1}**

The obtained data suggest that the incubation of cells with AgHA NPs and with conjugate does not affect the silver uptake differently. The recoveries from the analysis of NIST RM 8017 were between 99-101 %.

Report by LGC on AgHA and AgHA conjugates in HCC827 cell samples by spICP-MS.

Measurements of ionic silver and AgNPs in cell lysates by spICP-MS
Results Report

Customer details:

INSTITUTE : University of Strathclyde
DEPARTMENT : Pure and Applied Chemistry
ADDRESS : 99 George Street, Glasgow, G1 1XQ

COUNTRY : United Kingdom
TEL : +44 (0)141 548 4701
E-MAIL : duncan.graham@strath.ac.uk

Results completed, checked and authorised by:

Senior researcher Susana Cuello-Nunez 05/06/2018

Approved and authorised
by team leader Heidi Goenaga-Infante 05/06/2018

Sample receipt and storage

Cell lysates samples were received from University of Strathclyde in 1.5 mL Eppendorf tubes containing approximately 300 µL of sample which were stored at 4°C until analysis.

Calibration standards

NanoXact™ PEG coated Ag NPs from Nanocomposix, Inc with the mean diameter of 40 nm (lot: PTM0006) were *in-house* characterised using a reference method and consequently used for spiking experiments and for the determination of the transport efficiency, a key parameter that influences the accuracy of number concentration data.
Ionic Ag standard from VHG Labs, Inc. (lot: 127001-5) was used in spiking experiments and also to determine the detector's response.

Sample Preparation

NanoComposix was diluted to the required concentration in 0 2.5% TMAH (Tetramethylammonium hydroxide), 0.1% Triton-X solution in order to calculate the transportation efficiency. Ionic Ag standard was diluted in 2.5% TMAH, 0.1% Triton-X prior to detector's response determination. All dilutions were prepared gravimetrically.

Sample preparation was undertaken using a method previously developed *in-house,* in which samples were digested using basic hydrolysis to keep the integrity of nanoparticles. Briefly, upon arrival, cell samples were digested by mixing with 50 µL of 15% TMAH per 25 µL of cell lysate followed by 1 h sonication in an ultrasonic bath and 24 h incubation at room temperature in the dark. Once the incubation time was finalized, digested samples were diluted approximately 20-fold with 0.1% Triton-X100. Further dilutions were prepared in 2.5% TMAH + 0.1% Triton X-100.

Instrumentation

spICP-MS measurements were performed using an Agilent 8900 ICP-QQQ-MS. The samples were introduced into the plasma *via* a micromist nebuliser, operating at a pumping mode of 0.1 rpm, and using a Scott type double pass spray chamber cooled to 2°C. The instrument was equipped with the MassHunter4.3 (version: G72dC C.01.03) software and microsecond detection capability, allowing the analysis in single particle mode.

The instrument performance was verified daily with 1 µg L^{-1} tuning solution (1 µg L^{-1} of Ce, Co, Li, Tl and Y in 2% HNO_3). After the daily performance check, the ICP-MS conditions were optimized to obtain maximum ^{107}Ag sensitivity with a minimum background contribution using 1 µg L^{-1} ionic silver solution. Analyses in fast transient analysis (TRA) mode were performed with 'No Gas' using a dwell time of 0.1 ms per point, with no settling time between the measurements and using the newly developed Single Particle Application Module of ICP-MS MassHunter software. The general settings of the ICP-MS are given in **Table 1**. After each sample run the instrument was cleaned with 1% HNO3 0.1% Triton X-100 solution followed by ultrapure water after each sample. Each sample was measured 2-3 times under repeatability conditions.

Table 1: Typical operating parameters for spICP-MS measurements

Parameter	Agilent 7700
RF Power (W)	1550
Sampling depth (mm)	7
Carrier gas (L min^{-1})	1.09
Make up gas (L min^{-1})	0
Sample/skimmer cones	Ni/Ni
Sample uptake rate (mL min^{-1})	0.35
Spray Chamber (°C)	2
Dwell time (ms)	0.1
Acquisition time (s)	60
Isotopes measured	^{107}Ag

Results

The summary of the obtained results is shown in **Table 2.** The stated LOQs (limits of quantification), in terms of the particle number concentration and the level of ionic silver in the original cell lysates, were both calculated as the average readouts from 6 blanks (2.5% TMAH + 0.1% Triton X-100) samples multiplied by 10 times the standard deviation value from these readouts. For the number concentration of particles the calculated LOQ was $7.3 \cdot 10^6$ NP kg^{-1} and for the ionic Ag LOQ was 0.65 mg kg^{-1}. Also here, only particles larger than 30 nm were detected over the background signal and quantified, whilst smaller particles might have been present in the sample, since the particle size distribution shown in **Figure 1** is not a typically Gaussian shape distribution typically observed for nanomaterials. This distribution also indicates particle aggregation as the original size of the particles, determined by SEM, were around 52.9 nm, and the size distribution obtained by spICP-MS shows particle sizes between 30-150 nm

Table 2: Particle number concentration values (dimeter larger than 30 nm) and levels of ionic Ag measured in the cell lysates

Type of sample	Customer name	Ag NPs (d>30 nm)			Ionic Ag		
		Mean (NP kg^{-1})	SD (NP kg^{-1})	RSD (%)	Mean (mg kg^{-1})	SD (mg kg^{-1})	RSD (%)
Control cells (trypsinised)	Cell Tryp	<LOQ*			<LOQ*		
Cells incubated with AgHA NPs (trypsinised)	Ag tryps	$5.3 \cdot 10^{12}$	$3.8 \cdot 10^{11}$	7	3.4	0.1	3
Cells incubated with conjugate (trypsinised)	Ag C tryps	$5.3 \cdot 10^{12}$	$4.4 \cdot 10^{11}$	8	4.8	0.6	12

***LOQ for ionic Ag was 0.65 mg kg^{-1} and LOQ for Ag NPs (d>30 nm) was $7.3 \cdot 10^6$ NP kg^{-1}**

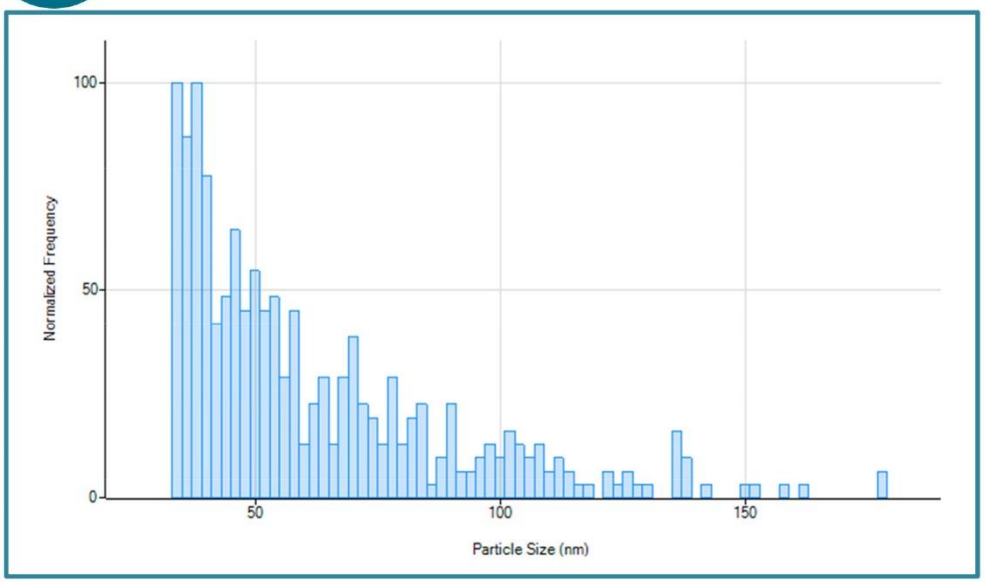

Figure 1. Representative particle size distribution histogram obtained from cells incubated with the conjugate

In order to find out if the aforementioned aggregation is due to the digestion with TMAH, control cells were spiked with 40 nanocomposix at a level of $5.55 \cdot 10^7$ NP kg^{-1} and the obtained recoveries were around 89% and also the size distribution (**Figure 2**) was not affected by the digestion with TMAH, indicating that the aggregation is not caused by the digestion process.

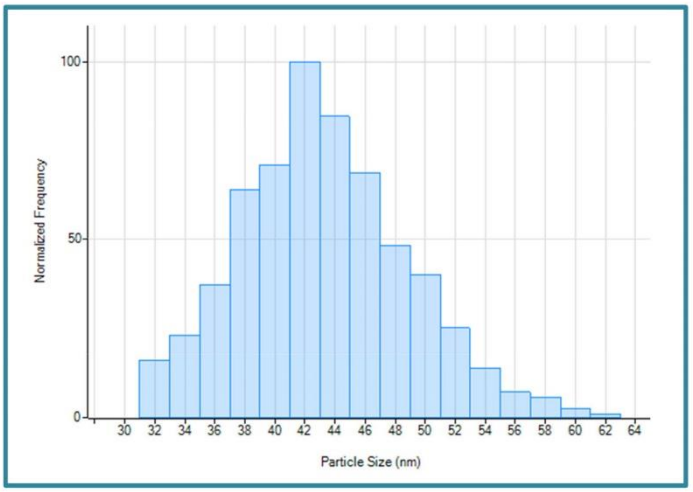

Figure 2. Representative particle size distribution histogram obtained from control cells spiked with 40 nm nanocomposix

In terms of the ionic content of silver found in the samples, those cells incubated with the conjugate have slightly higher concentration of ionic Ag in compare with the samples incubated with AgHA NPs, whereas the levels of silver in the control cells were below the LOQ. Spike experiments, of the

control cell with ionic silver, at the same level than those found in the digested samples (0.1 µg kg^{-1}), gave recoveries of around 99%.

Summary

Number based concentration could not be determined accurately due to nanoparticle aggregation, therefore the only valuable information derived from spICP-MS are the levels of ionic silver in the samples, which were found to be 3.4 ± 0.1 mg kg^{-1} and 4.8 ± 0.6 mg kg^{-1} for cells incubated with AgHA NPs and conjugate, respectively. These levels of silver account for approximately 38 and 54% of the total silver (see total content of silver report) found in cells incubated with AgHA NPs and conjugate, respectively.

B. RPPA Antibody List, Raw Fluorescent Outputs & Statistical Outputs

Table 26 Antibodies for RPPA with Supplier, Order No. and Type

Slide	Array	Antibody	Supplier	Order No.	Type
1	1	FAK1	CST	3285	rabbit
	2	FAK1 P Y397	CST	3283	rabbit
	3	ATM/ATR Substrate P Ser/Thr	CST	2851	rabbit
	4	Aurora A/B/C P Thr288/Thr232/Thr198	CST	2914	rabbit
	5	Bad P Ser136	CST	9295	rabbit
	6	Bad P Ser112	CST	9291	rabbit
	7	HSP27 (HSPB1) P Ser78	CST	2405	rabbit
	8	rabbit Ab control			
Slide	**Array**	**Antibody**	**Supplier**	**Order No.**	**Type**
2	1	JAK1	CST	3332	rabbit
	2	MEK1/2	CST	9122	rabbit
	3	MEK1/2 P Ser217/221	CST	9154	rabbit
	4	PARP	CST	9542	rabbit
	5	PI3 Kinase p110-alpha	CST	4249	rabbit
	6	Bim	Epitomics	1036	rabbit
	7	CDK1 (cdc2)	CST	9112	rabbit
	8	rabbit Ab control			
Slide	**Array**	**Antibody**	**Supplier**	**Order No.**	**Type**
3	1	Met P Tyr1349	Signalway	11238	rabbit
	2	IGF-1R beta P Tyr1162,Tyr1163	Invitrogen (Biosource)	44-804G	rabbit
	3	ErbB-1/EGFR	CST	2232	rabbit
	4	ErbB-3/Her3/EGFR P Tyr1289	CST	4791	rabbit
	5	EGFR P Tyr1173	CST	4407	rabbit
	6	Akt P Thr308	CST	2965	rabbit
	7	Met	CST	4560	rabbit
	8	p44/42 MAPK (ERK1/2)	CST	9102	rabbit
Slide	**Array**	**Antibody**	**Supplier**	**Order No.**	**Type**
4	1	p44/42 MAPK (ERK1/2) P Thr202/Thr185,Tyr204/Tyr187	CST	4370	rabbit
	2	Src	CST	2109	rabbit
	3	Akt	CST	9272	rabbit
	4	Akt P Ser473	CST	4060	rabbit
	5	PARP cleaved Asp214	CST	9541	rabbit
	6	beta-actin	CST	4970	rabbit
	7	cdc25c P Ser216	CST	4901	rabbit
	8	Chk1 P Ser345	CST	2348	rabbit
Slide	**Array**	**Antibody**	**Supplier**	**Order No.**	**Type**
5	1	Chk2 P Thr68	CST	2661	rabbit
	2	c-Jun P Ser73	CST	9164	rabbit
	3	c-Myc	CST	5605	rabbit
	4	E-Cadherin	CST	3195	rabbit
	5	cdc25A	CST	3652	rabbit
	6	PTEN	CST	9552	rabbit
	7	PTEN P Ser380,Thr382,Thr383	CST	9554	rabbit
	8	SAPK/JNK (JNK2)	CST	9258	rabbit
Slide	**Array**	**Antibody**	**Supplier**	**Order No.**	**Type**
6	1	p70 S6 Kinase P Thr421,Ser424	CST	9204	rabbit
	2	LKB1	CST	3047	rabbit
	3	Stat6 P Tyr641	CST	9361	rabbit
	4	p53 P Ser15	CST	9284	rabbit
	5	p38 MAPK PThr180,Tyr182	CST	9211	rabbit

	6	p38 MAPK	CST	9212	rabbit
	7	mTOR P Ser2448	CST	2971	rabbit
	8	mTOR	CST	2972	rabbit
Slide	**Array**	**Antibody**	**Supplier**	**Order No.**	**Type**
7	1	Raf P Ser259	CST	9421	rabbit
	2	PLC-gamma1 P Tyr783	CST	2821	rabbit
	3	PDK-1 P Ser241	CST	3061	rabbit
	4	PDK-1	CST	3062	rabbit
	5	p70 S6 Kinase	CST	9202	rabbit
	6	JAK1 P Tyr1022,Thr1023	Invitrogen (Biosource)	44-422G	rabbit
	7	c-Myc P Thr58,Ser62	Epitomics	1203-1	rabbit
	8	SAPK/JNK P Thr183,Tyr185	CST	4668	rabbit
Slide	**Array**	**Antibody**	**Supplier**	**Order No.**	**Type**
8	1	S6 Ribosomal protein p Ser240,Ser244	CST	2215	rabbit
	2	S6 Ribosomal Protein	CST	2217	rabbit
	3	MAPKAPK-2 P Thr334	CST	3041	rabbit
	4	Stat6	CST	9362	rabbit
	5	Src (family) P Tyr416	CST	2101	rabbit
	6	Cyclin D1 P Thr286	CST	3300	rabbit
	7	AMPK alpha	CST	2532	rabbit
	8	AMPK alpha P Thr172	CST	2535	rabbit
Slide	**Array**	**Antibody**	**Supplier**	**Order No.**	**Type**
9	1	Bcl-2	Epitomics	1017-1	rabbit
	2	Bim P Ser69	CST	4585	rabbit
	3	c-Jun N-term	Epitomics	1254-1	rabbit
	4	Caspase 3	CST	9662	rabbit
	5	Caspase 3 cleaved	CST	9664	rabbit
	6	CDK1 (p34cdc2) P Tyr15	CST	9111	rabbit
	7	p53	CST	9282	rabbit
	8	GSK-3-beta P Ser9	CST	9336	rabbit
Slide	**Array**	**Antibody**	**Supplier**	**Order No.**	**Type**
10	1	GSK-3-beta	CST	9315	rabbit
	2	SQSTM1 (p62)	CST	8025	rabbit
	3	PLC-gamma1	CST	2822	rabbit
	4	CDK2	Abcam/Epitomics	ab32147	rabbit
	5	MAPKAPK-2	Epitomics	1497-1	rabbit
	6	Stat3	CST	12640	rabbit
	7	PDGFR P Tyr1021	CST	2227	rabbit
	8	PDGFR P Tyr751	CST	4549	rabbit
Slide	**Array**	**Antibody**	**Supplier**	**Order No.**	**Type**
11	1	Bcl-2 P Ser70	CST	2827	rabbit
	2	IGF-1R beta	CST	3027	rabbit
	3	Profilin (C56B8)	CST	3246	rabbit
	4	PYK2 P Y402	CST	3291	rabbit
	5	Rock1 (C8F7)	CST	4035	rabbit
	6	Mena (D33C1)	CST	6921	rabbit
	7	EGFR P Y992	CST	2235	rabbit
	8	EGFR P Y1086	CST	2234	rabbit
Slide	**Array**	**Antibody**	**Supplier**	**Order No.**	**Type**
12	1	B-Raf [EP152Y]	Abcam	ab33899	rabbit
	2	Fibronectin [F14]	Abcam	ab45688	rabbit
	3	MMP21 [EP1277Y]	Abcam	ab52817	rabbit
	4	MEK6 [EP558Y]	Abcam	ab52937	rabbit
	5	Integrin Beta 1 [EP1041Y]	abcam	ab52971	rabbit
	6	PYK2 [EP206Y]	abcam	ab81266	rabbit
	7	Histone H2A.X P Ser139 [EP854(2)Y]	abcam	ab81299	rabbit

	8	Stat3 P Y705	CST	9131	rabbit
Slide	**Array**	**Antibody**	**Supplier**	**Order No.**	**Type**
13	1	Lamin A/C	CST	2032	rabbit
	2	Histone H2A.X	CST	2595	rabbit
	3	Ezrin P T567/Radixin T564/Moesin T588	CST	3141	rabbit
	4	Caveolin-1 (D46G3) XP R	CST	3267	rabbit
	5	Cofilin P Ser3 (C77G2)	CST	3313	rabbit
	6	Cortactin (H222)	CST	3503	rabbit
	7	TIF1 Beta (C42G12)	CST	4124	rabbit
	8	Integrin alpha 4	CST	4600	rabbit
Slide	**Array**	**Antibody**	**Supplier**	**Order No.**	**Type**
14	1	Integrin beta3	CST	4702	rabbit
	2	Integrin beta4	CST	4707	rabbit
	3	Clathrin (D3C6) XP ®	CST	4796	rabbit
	4	Slug (C19G7	CST	9585	rabbit
	5	Stat3 P Ser727	CST	9134	rabbit
	6	TGF beta (56E4)	CST	3709	rabbit
	7	PKA substrate P (RRXS/T) (100G7E)	CST	9624	rabbit
	8	c-Abl P Y245	CST	2868	rabbit
Slide	**Array**	**Antibody**	**Supplier**	**Order No.**	**Type**
15	1	c-Abl	CST	2862	rabbit
	2	ATM	Merck (Calbiochem)	PC116	rabbit
	3	PKA	Abcam	ab26322	rabbit
	4	beta-Tubulin	Abcam	ab6046	rabbit
	5	PKC-alpha P Thr638	Abcam	ab32502	rabbit
	6	Raf1 (C-12)	Santa Cruz	sc-133	rabbit
	7	p21 CIP/WAF1 p Thr145	Santa Cruz	sc-20220-R	rabbit
	8	Rabbit Ab control			
Slide	**Array**	**Antibody**	**Supplier**	**Order No.**	**Type**
16	1	Cyclin D1	CST	2926	mouseIgG2a
	2	p21 CIP/WAF1	CST	2946	mouseIgG2a
	3	HSP27 (HSPB1)	CST	2402	mouseIgG1
	4	PKC-alpha	Beckton Dickinson	610108	mouseIgG2b
	5	Ras	Beckton Dickinson	610001	mouseIgG1
	6	Calmodulin	Calbiochem	NB12	mouseIgG1
	7	GAPDH	Abcam	ab9484	mouseIgG2b
	8	mouse Ab control			

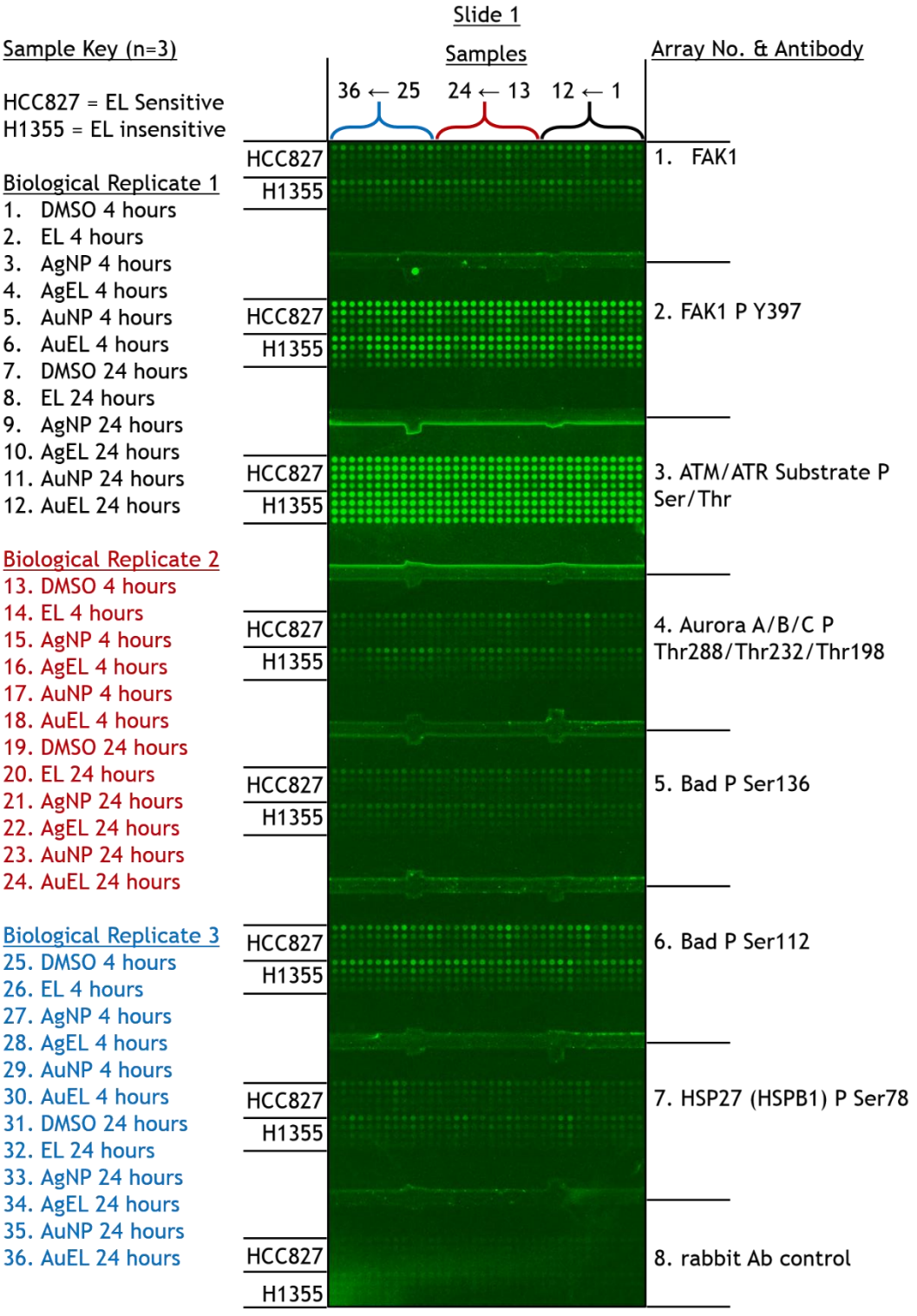

Figure 84 RPPA Antibody stained slide 1 labelled with 8 antibodies used (including rabbit Ab background control), to probe HCC827 EL sensitive & H1355 EL insensitive cell lines treated with: DMSO control, 10 nM EL, 0.34 nM AgNP, AgNP EL conjugate, 0.34 nM AuNP & AuNP EL conjugate for 4 & 24 hour incubations in biological triplicate.

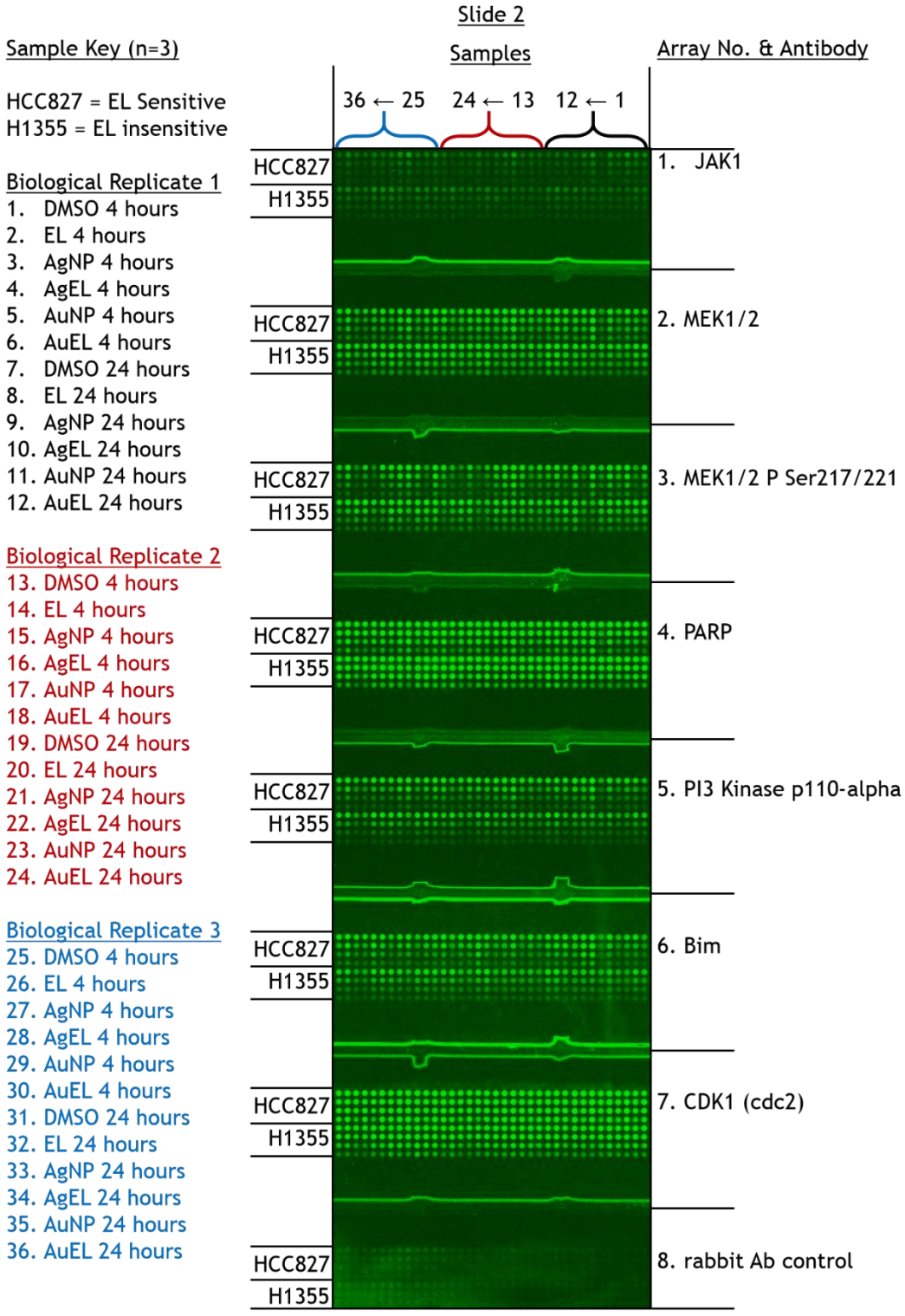

Figure 85 RPPA Antibody stained slide 2 labelled with 8 antibodies used (including rabbit Ab background control), to probe HCC827 EL sensitive & H1355 EL insensitive cell lines treated with: DMSO control, 10 nM EL, 0.34 nM AgNP, AgNP EL conjugate, 0.34 nM AuNP & AuNP EL conjugate for 4 & 24 hour incubations in biological triplicate

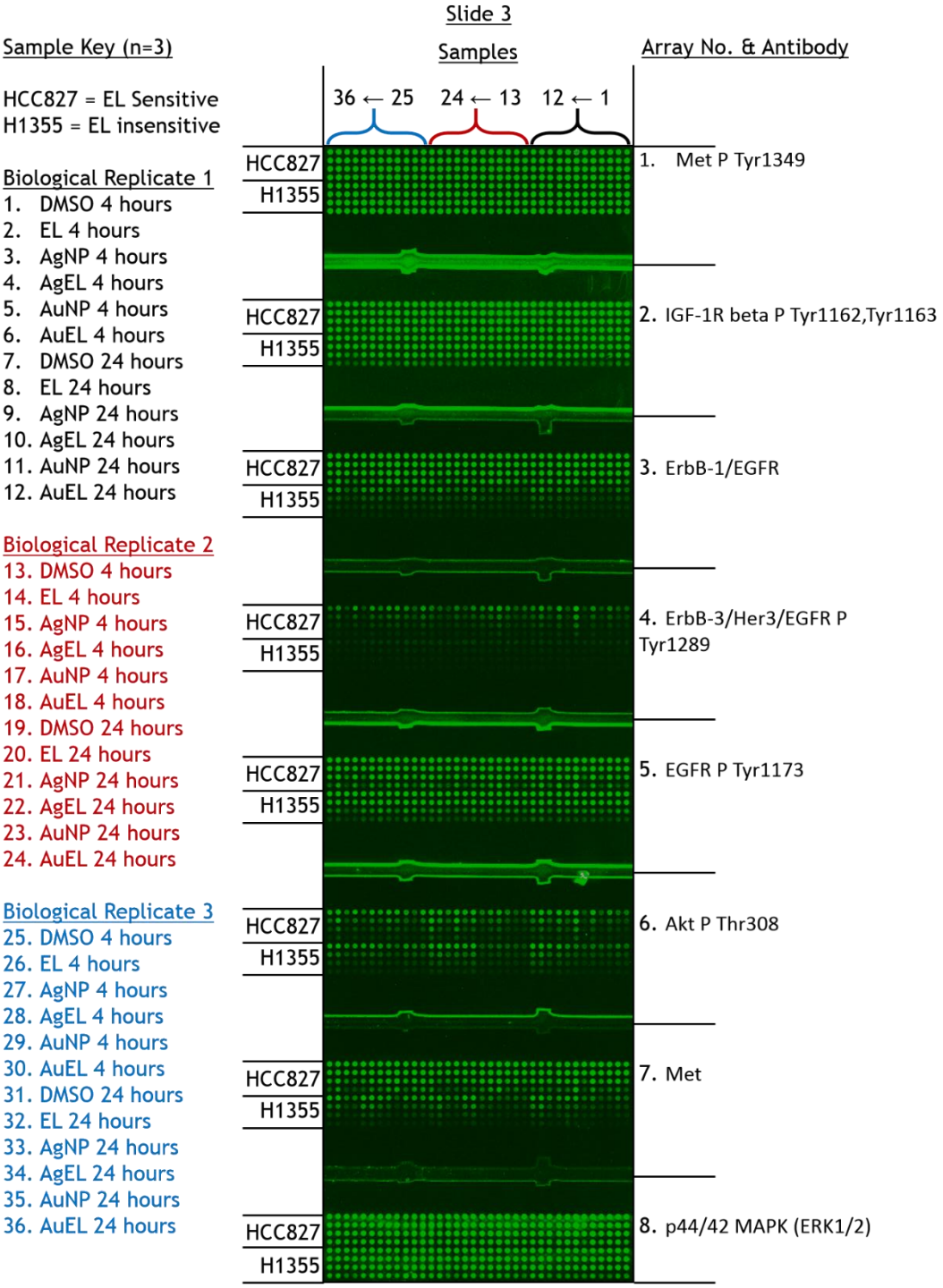

Figure 86 RPPA Antibody stained slide 3 labelled with 8 antibodies used, to probe HCC827 EL sensitive & H1355 EL insensitive cell lines treated with: DMSO control, 10 nM EL, 0.34 nM AgNP, AgNP EL conjugate, 0.34 nM AuNP & AuNP EL conjugate for 4 & 24 hour incubations in biological triplicate

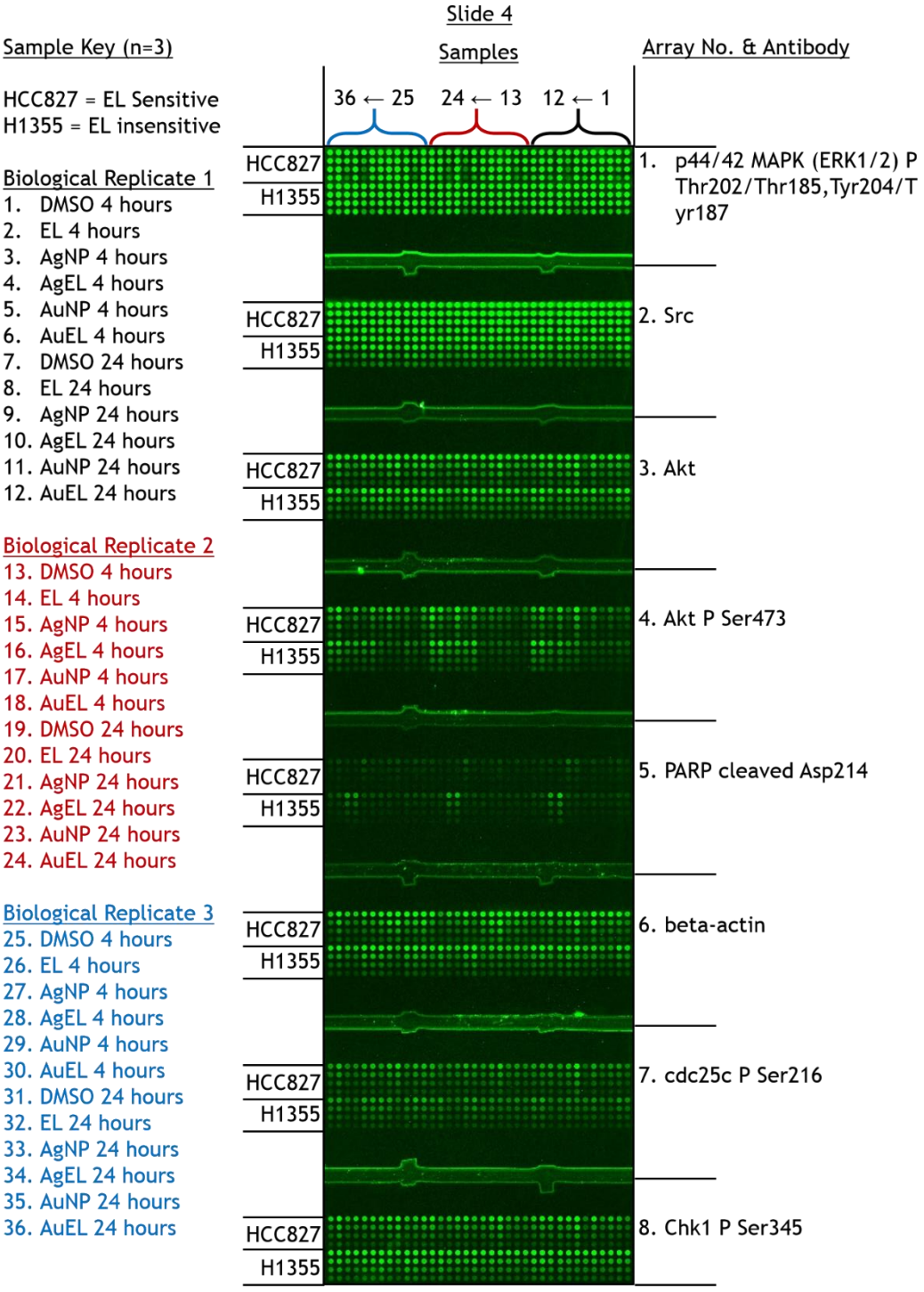

Figure 87 RPPA Antibody stained slide 4 labelled with 8 antibodies used, to probe HCC827 EL sensitive & H1355 EL insensitive cell lines treated with: DMSO control, 10 nM EL, 0.34 nM AgNP, AgNP EL conjugate, 0.34 nM AuNP & AuNP EL conjugate for 4 & 24 hour incubations in biological triplicate

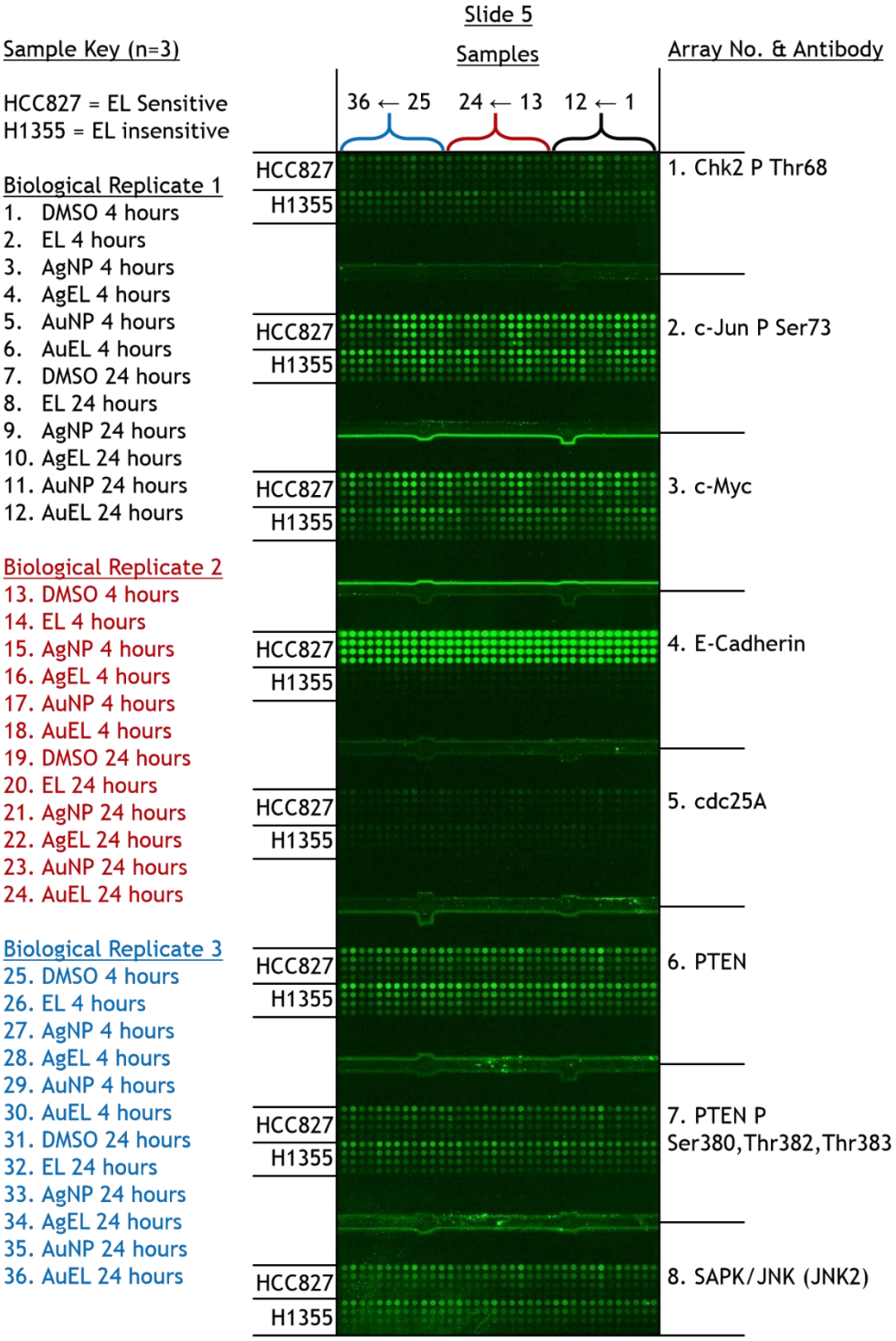

Figure 88 RPPA Antibody stained slide 5 labelled with 8 antibodies used, to probe HCC827 EL sensitive & H1355 EL insensitive cell lines treated with: DMSO control, 10 nM EL, 0.34 nM AgNP, AgNP EL conjugate, 0.34 nM AuNP & AuNP EL conjugate for 4 & 24 hour incubations in biological triplicate

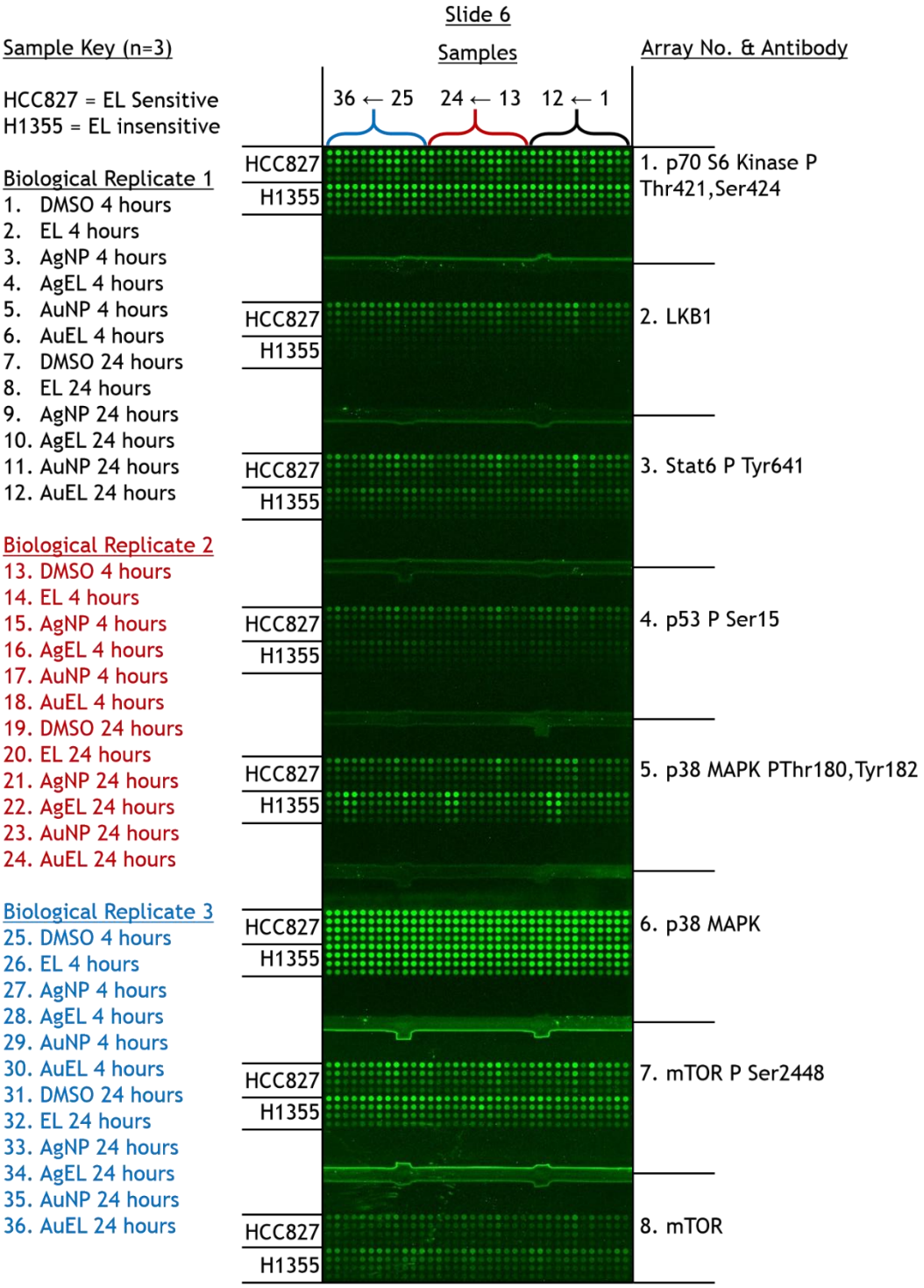

Figure 89 RPPA Antibody stained slide 6 labelled with 8 antibodies used, to probe HCC827 EL sensitive & H1355 EL insensitive cell lines treated with: DMSO control, 10 nM EL, 0.34 nM AgNP, AgNP EL conjugate, 0.34 nM AuNP & AuNP EL conjugate for 4 & 24 hour incubations in biological triplicate

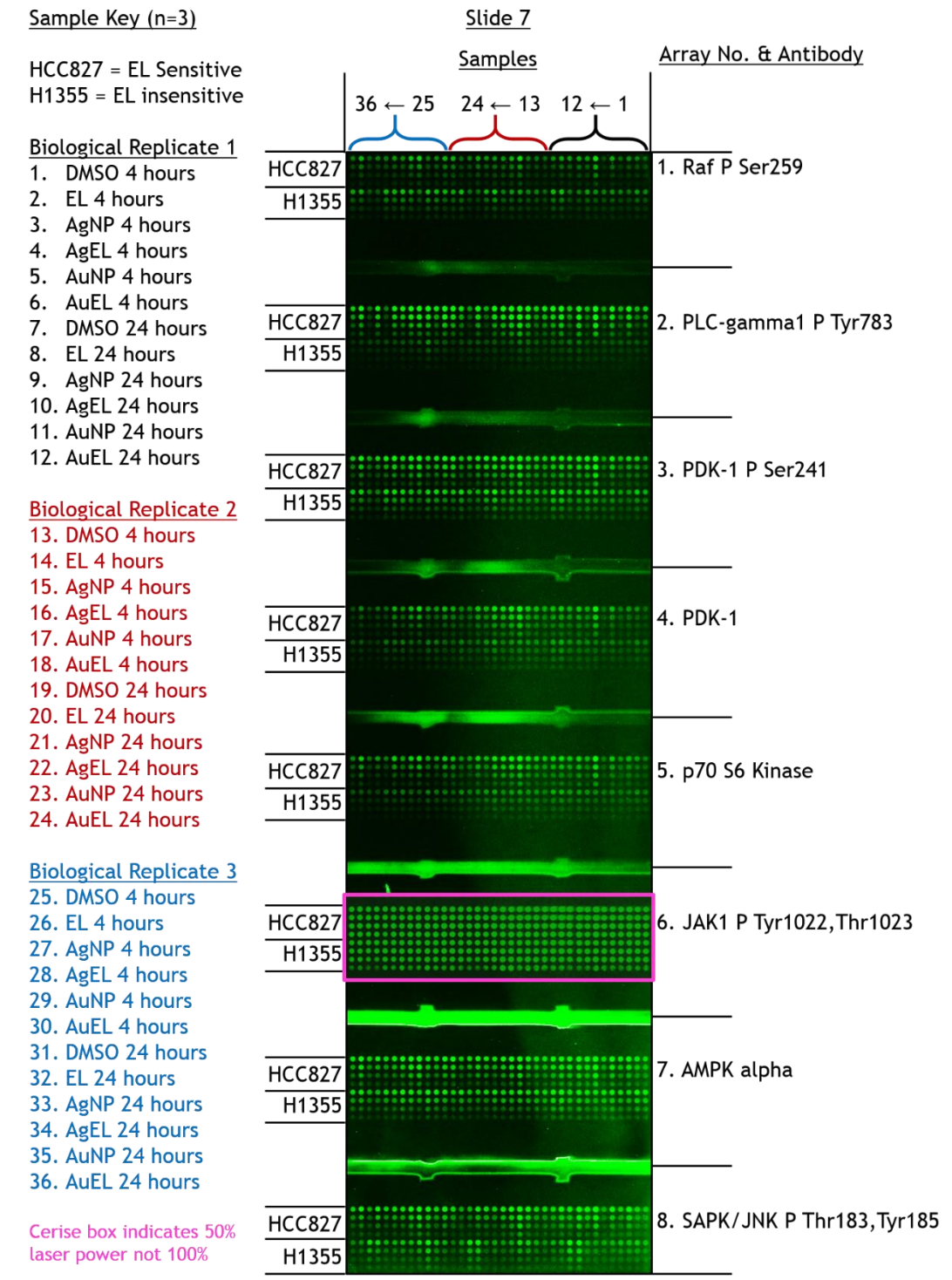

Figure 90 RPPA Antibody stained slide 7 labelled with 8 antibodies used, to probe HCC827 EL sensitive & H1355 EL insensitive cell lines treated with: DMSO control, 10 nM EL, 0.34 nM AgNP, AgNP EL conjugate, 0.34 nM AuNP & AuNP EL conjugate for 4 & 24 hour incubations in biological triplicate

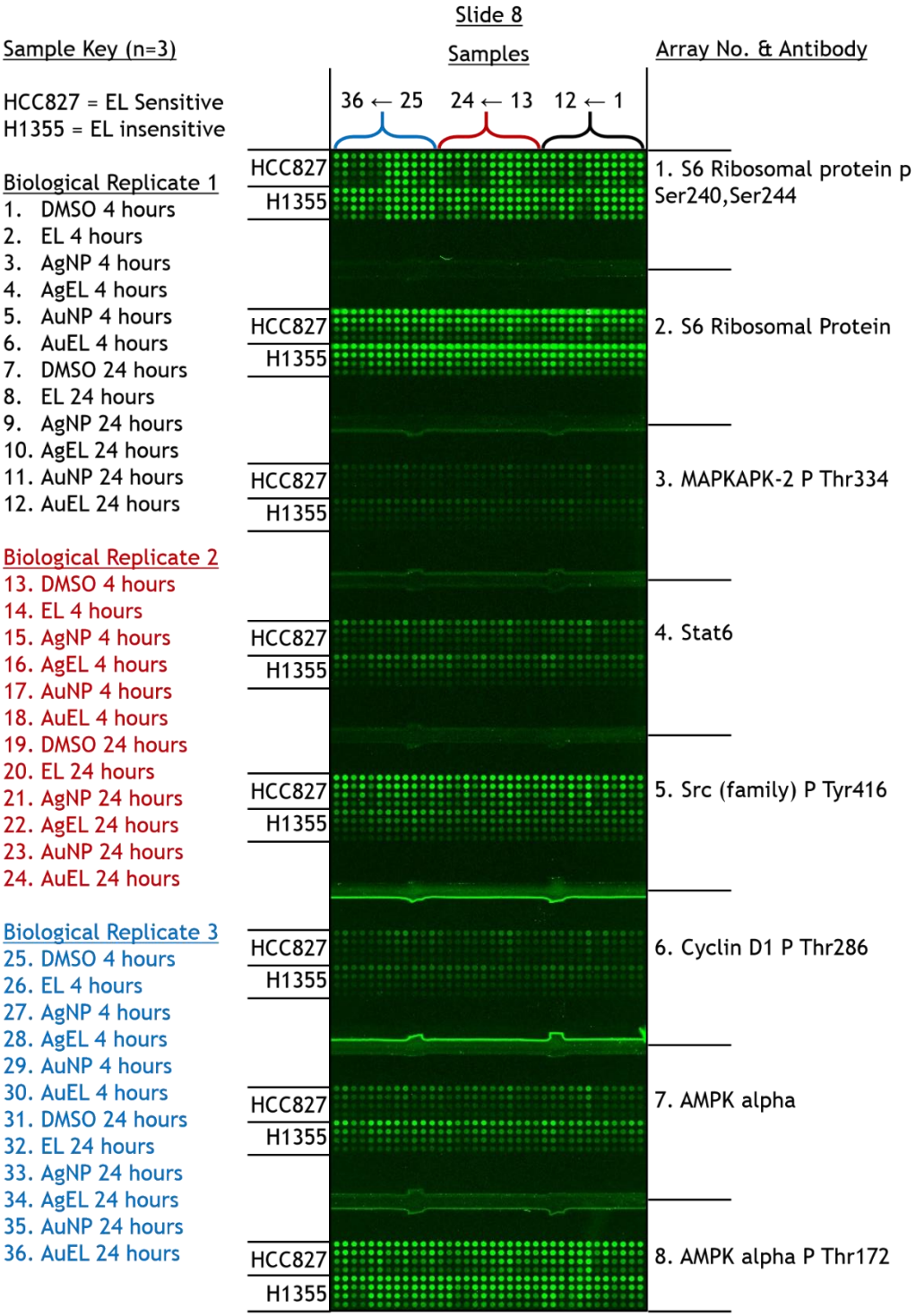

Figure 91 RPPA Antibody stained slide 8 labelled with 8 antibodies used, to probe HCC827 EL sensitive & H1355 EL insensitive cell lines treated with: DMSO control, 10 nM EL, 0.34 nM AgNP, AgNP EL conjugate, 0.34 nM AuNP & AuNP EL conjugate for 4 & 24 hour incubations in biological triplicate

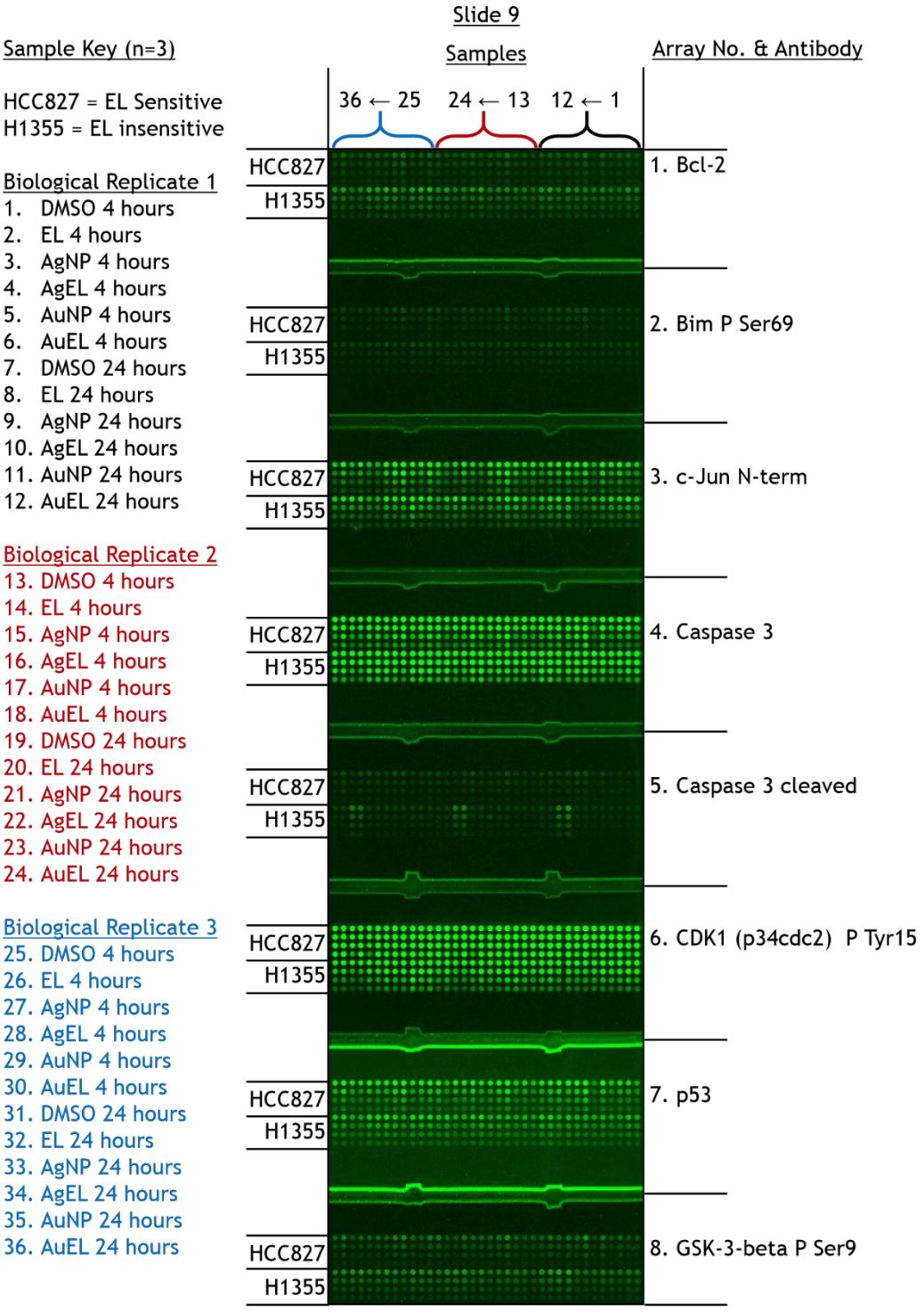

Figure 92 RPPA Antibody stained slide 9 labelled with 8 antibodies used, to probe HCC827 EL sensitive & H1355 EL insensitive cell lines treated with: DMSO control, 10 nM EL, 0.34 nM AgNP, AgNP EL conjugate, 0.34 nM AuNP & AuNP EL conjugate for 4 & 24 hour incubations in biological triplicate

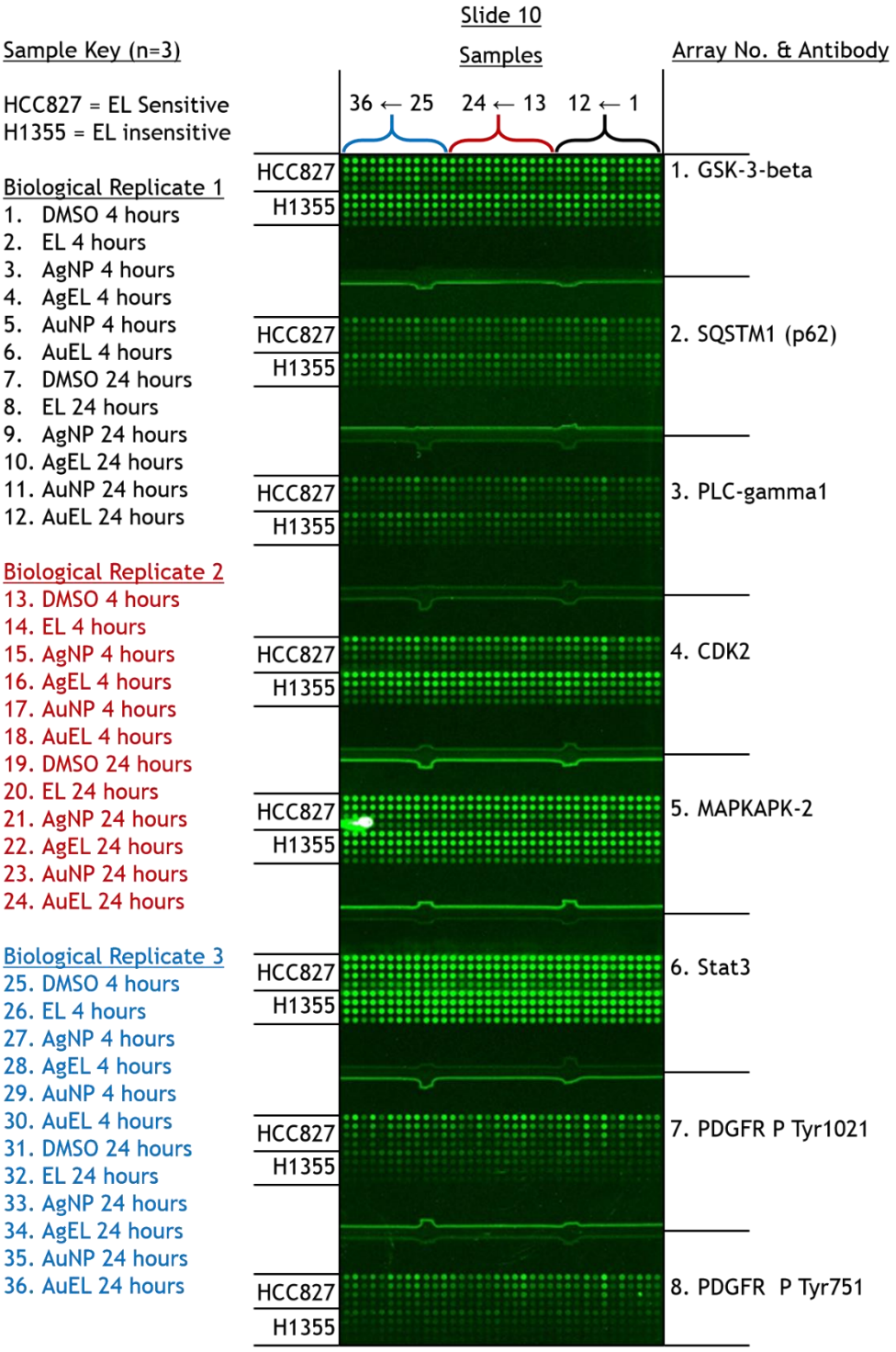

Figure 93 RPPA Antibody stained slide 10 labelled with 8 antibodies used, to probe HCC827 EL sensitive & H1355 EL insensitive cell lines treated with: DMSO control, 10 nM EL, 0.34 nM AgNP, AgNP EL conjugate, 0.34 nM AuNP & AuNP EL conjugate for 4 & 24 hour incubations in biological triplicate

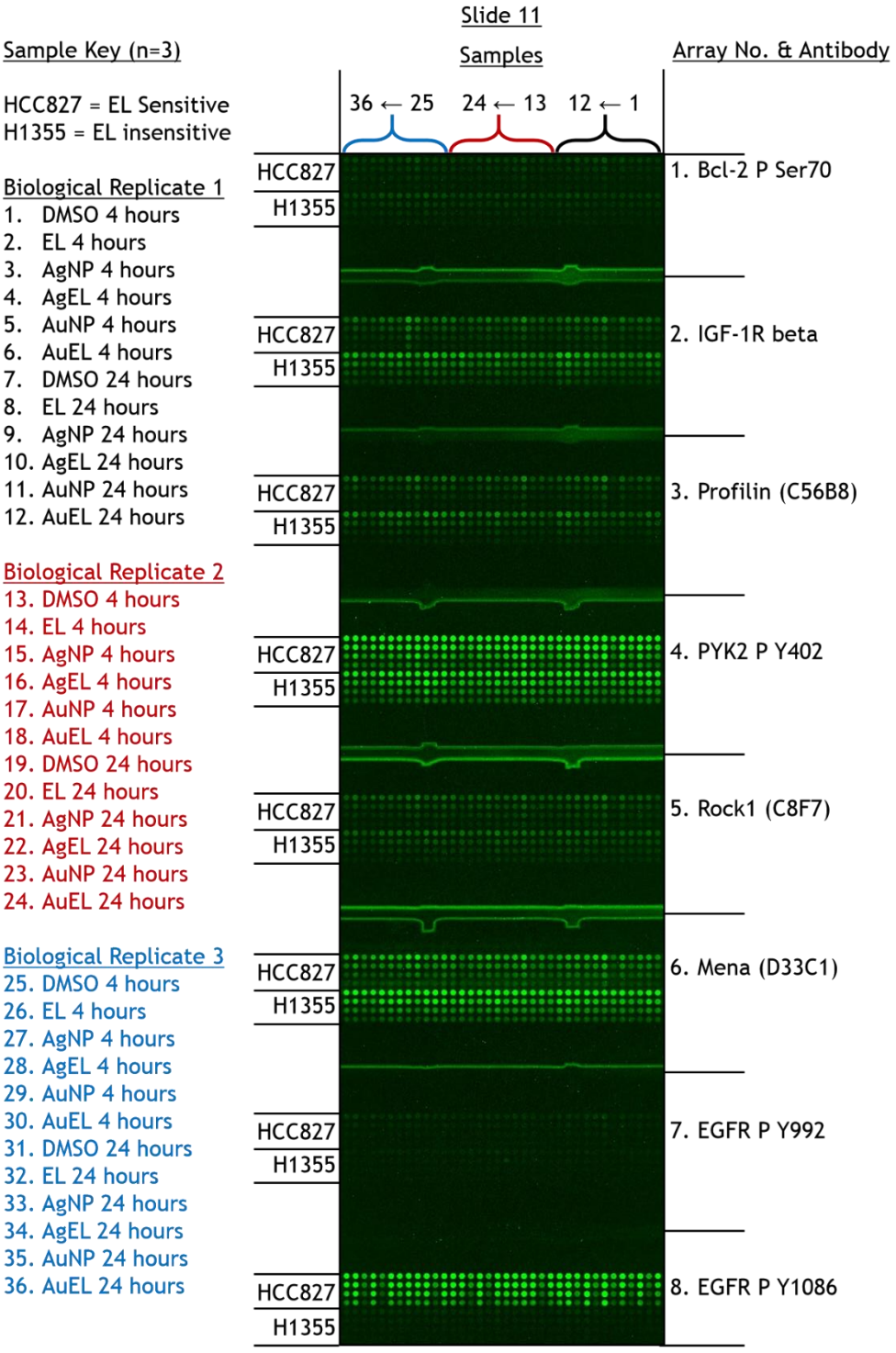

Figure 94 RPPA Antibody stained slide 11 labelled with 8 antibodies used, to probe HCC827 EL sensitive & H1355 EL insensitive cell lines treated with: DMSO control, 10 nM EL, 0.34 nM AgNP, AgNP EL conjugate, 0.34 nM AuNP & AuNP EL conjugate for 4 & 24 hour incubations in biological triplicate

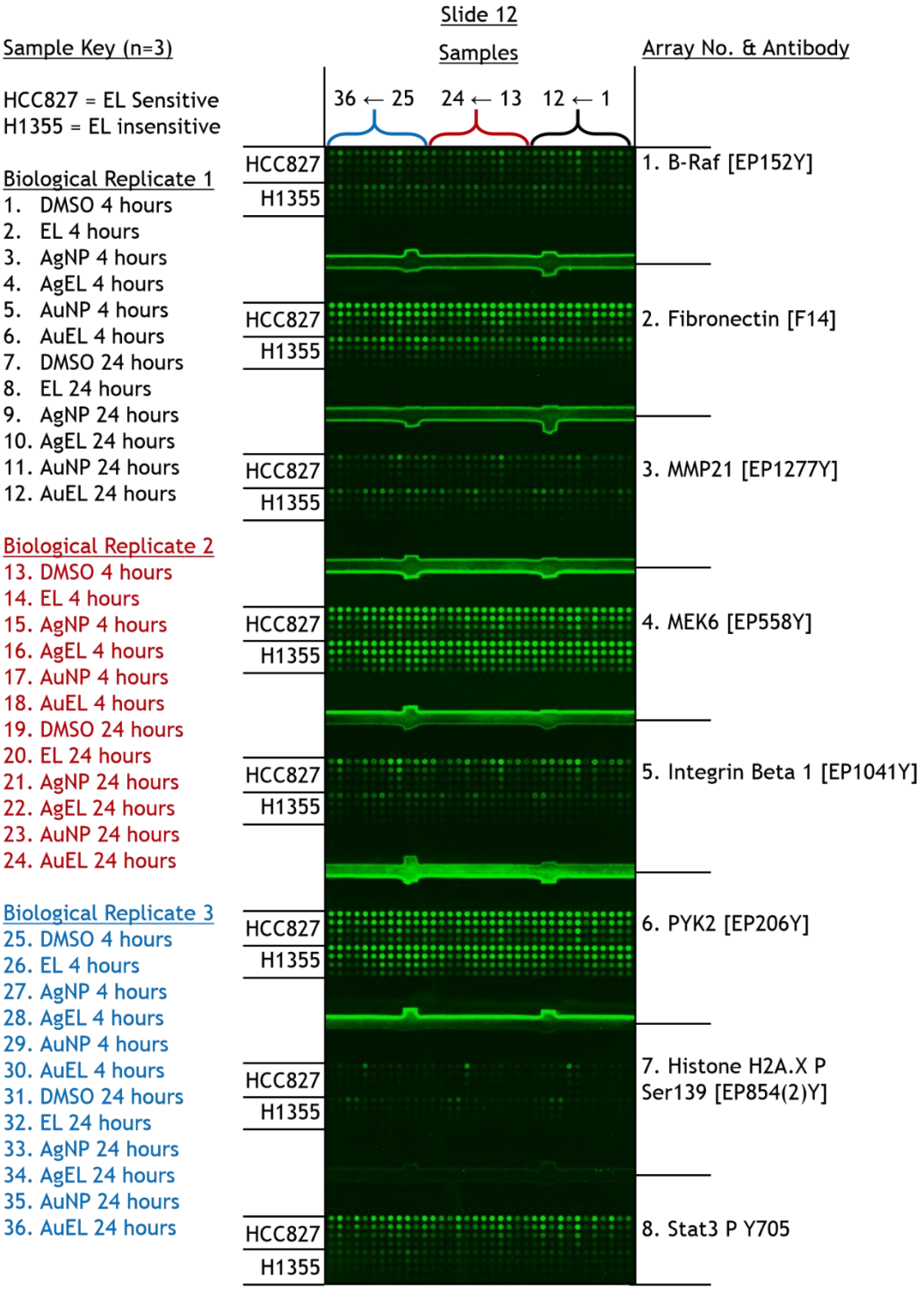

Figure 95 RPPA Antibody stained slide 12 labelled with 8 antibodies used, to probe HCC827 EL sensitive & H1355 EL insensitive cell lines treated with: DMSO control, 10 nM EL, 0.34 nM AgNP, AgNP EL conjugate, 0.34 nM AuNP & AuNP EL conjugate for 4 & 24 hour incubations in biological triplicate

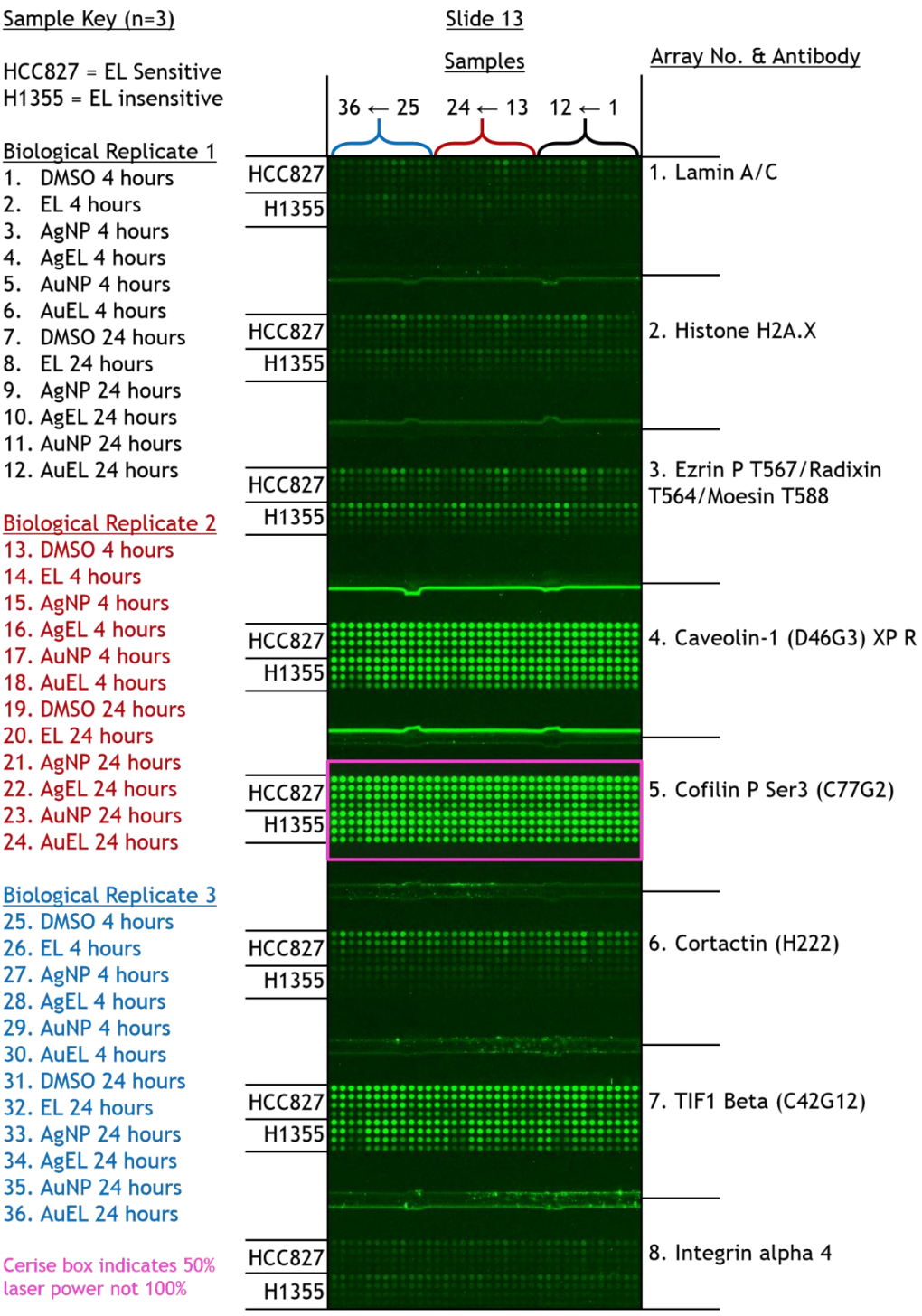

Figure 96 RPPA Antibody stained slide 13 labelled with 8 antibodies used, to probe HCC827 EL sensitive & H1355 EL insensitive cell lines treated with: DMSO control, 10 nM EL, 0.34 nM AgNP, AgNP EL conjugate, 0.34 nM AuNP & AuNP EL conjugate for 4 & 24 hour incubations in biological triplicate

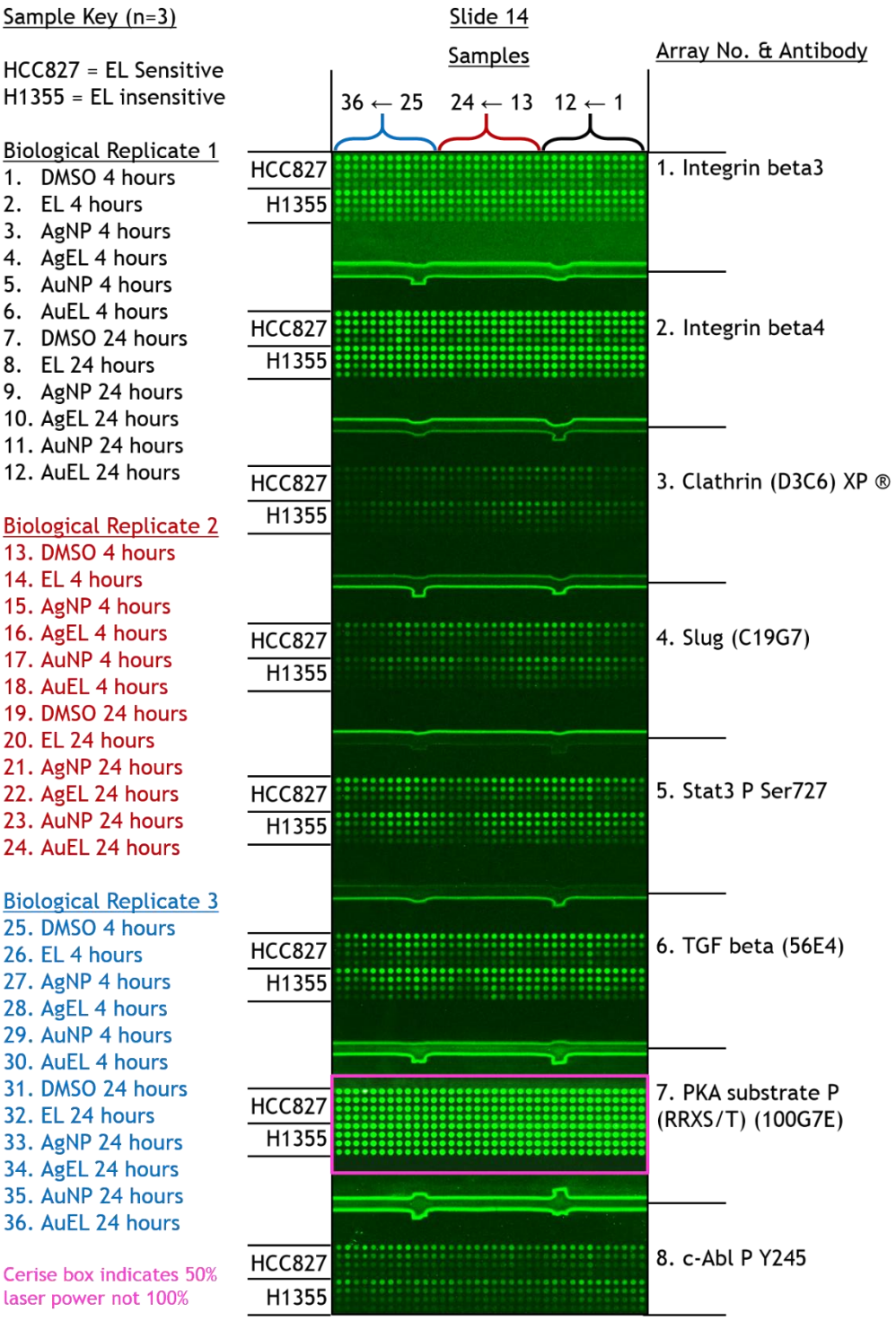

Figure 97 RPPA Antibody stained slide 14 labelled with 8 antibodies used, to probe HCC827 EL sensitive & H1355 EL insensitive cell lines treated with: DMSO control, 10 nM EL, 0.34 nM AgNP, AgNP EL conjugate, 0.34 nM AuNP & AuNP EL conjugate for 4 & 24 hour incubations in biological triplicate

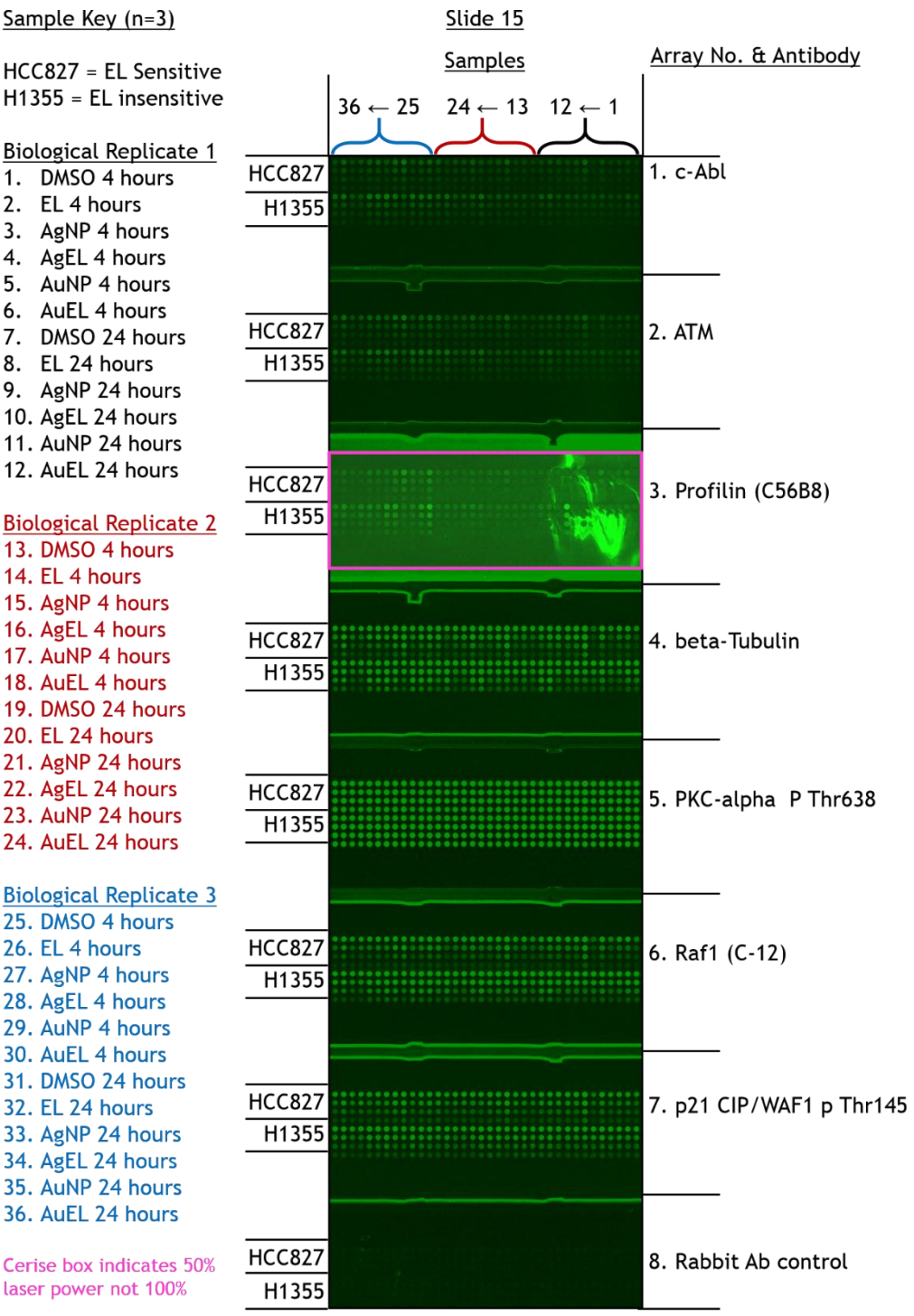

Figure 98 RPPA Antibody stained slide 15 labelled with 8 antibodies used (including rabbit Ab background control), to probe HCC827 EL sensitive & H1355 EL insensitive cell lines treated with: DMSO control, 10 nM EL, 0.34 nM AgNP, AgNP EL conjugate, 0.34 nM AuNP & AuNP EL conjugate for 4 & 24 hour incubations in biological triplicate

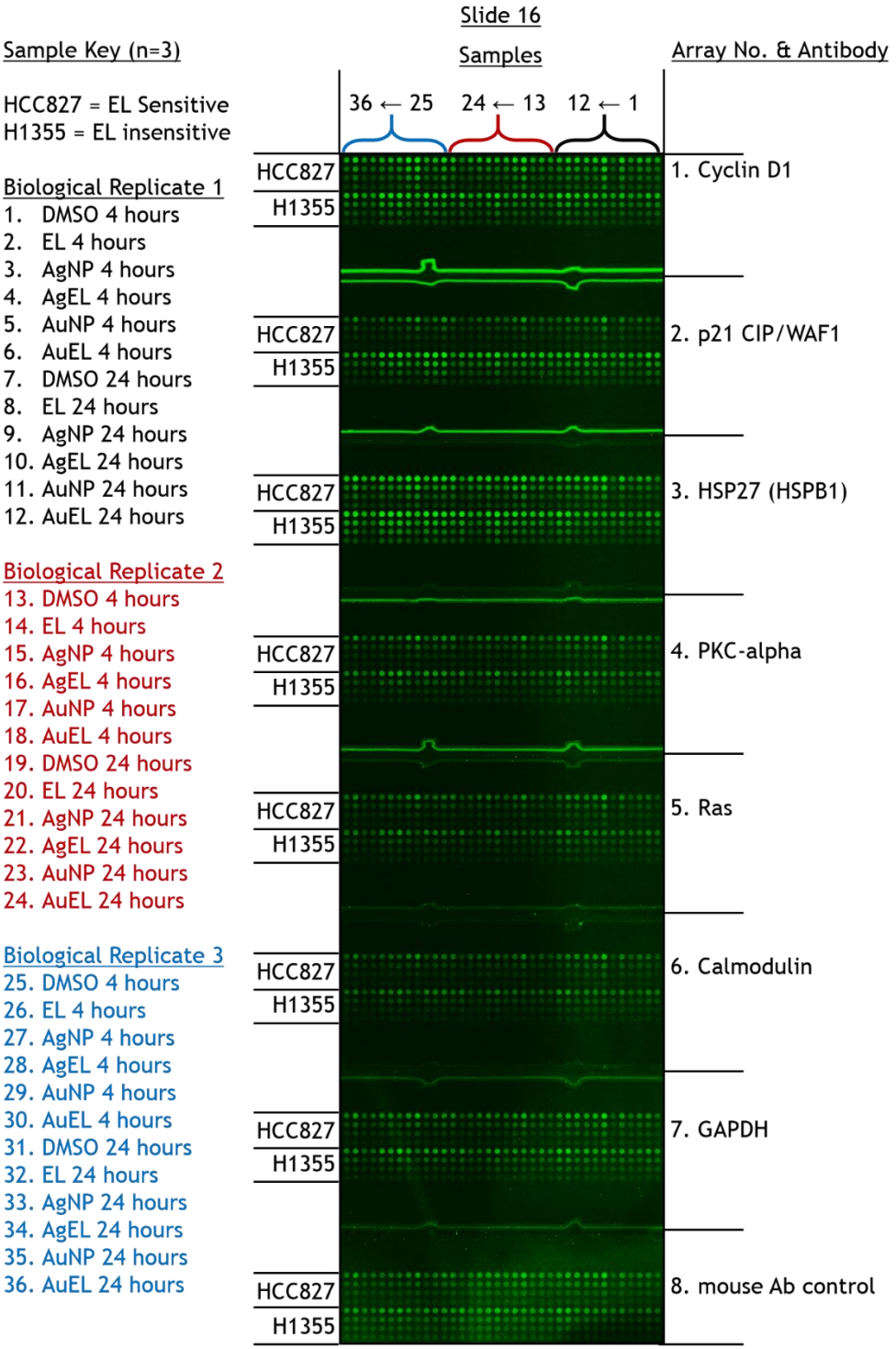

Figure 99 RPPA Antibody stained slide 16 labelled with 8 antibodies used (including mouse Ab control for background), to probe HCC827 EL sensitive & H1355 EL insensitive cell lines treated with: DMSO control, 10 nM EL, 0.34 nM AgNP, AgNP EL conjugate, 0.34 nM AuNP & AuNP EL conjugate for 4 & 24 hour incubations in biological triplicate

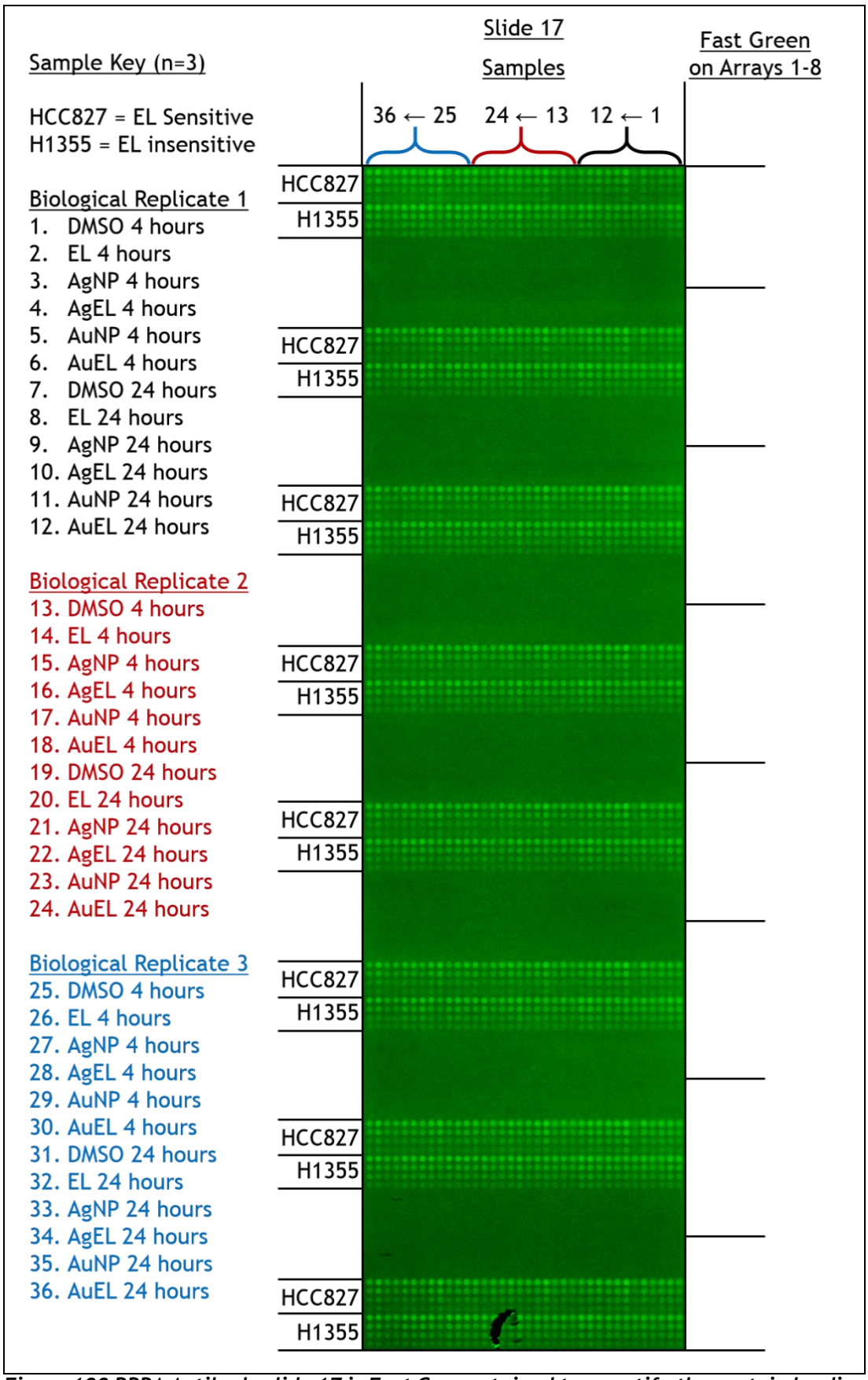

Figure 100 RPPA Antibody slide 17 is Fast Green stained to quantify the protein loading as a control.

Table 27 Protein names key for HUGO Gene Nomenclature used in Interactive Networks

Protein Name From Antibody List of RPPA	HUGO Gene Nomenclature		
FAK1	PTK2		
FAK1 P Y397	PTK2		
ATM/ATR Substrate P Ser/Thr	ATM	ATR	
Aurora A/B/C P Thr288/Thr232/Thr198	AURKA	AURKB	AURKC
Bad P Ser136	BAD		
Bad P Ser112	BAD		
HSP27 (HSPB1) P Ser78	HSPB1		
JAK1	JAK1		
MEK1/2	MAP2K1	MAP2K2	
MEK1/2 P Ser217/221	MAP2K1	MAP2K2	
PARP	PARP1		
PI3 Kinase p110-alpha	PIK3CA		
Bim	BCL2L11		
CDK1 (cdc2)	CDK1		
Met P Tyr1349	MET		
IGF-1R beta P Tyr1162,Tyr1163	IGF1R		
ErbB-1/EGFR	EGFR		
ErbB-3/Her3/EGFR P Tyr1289	EGFR		
EGFR P Tyr1173	EGFR		
Akt P Thr308	AKT1	AKT2	AKT3
Met	MET		
p44/42 MAPK (ERK1/2)	MAPK3	MAPK1	
p44/42 MAPK (ERK1/2) P Thr202/Thr185,Tyr204/Tyr187	MAPK3	MAPK1	
Src	SRC		
Akt	AKT1	AKT2	AKT3
Akt P Ser473	AKT1	AKT2	AKT3
PARP cleaved Asp214	PARP1		
beta-actin	ACTB		
cdc25c P Ser216	CDC25C		
Chk1 P Ser345	CHEK1		
Chk2 P Thr68	CHEK2		
c-Jun P Ser73	JUN		
c-Myc	MYC		
E-Cadherin	CDH1		
cdc25A	CDC25A		
PTEN	PTEN		
PTEN P Ser380,Thr382,Thr383	PTEN		
SAPK/JNK (JNK2)	MAPK9		
p70 S6 Kinase P Thr421,Ser424	RPS6KB1		
LKB1	STK11		
Stat6 P Tyr641	STAT6		

p53 P Ser15	MTAP		
p38 MAPK PThr180,Tyr182			
p38 MAPK	MAPK14	MAPK11	MAPK12
mTOR P Ser2448	MTOR		
mTOR	MTOR		
Raf P Ser259	RAF1		
PLC-gamma1 P Tyr783	PLCG1		
PDK-1 P Ser241	PDPK1		
PDK-1	PDPK1		
p70 S6 Kinase	RPS6KB1		
JAK1 P Tyr1022,Thr1023	JAK1		
c-Myc P Thr58,Ser62	MYC		
SAPK/JNK P Thr183,Tyr185	MAPK9		
S6 Ribosomal protein p Ser240,Ser244	RPS6		
S6 Ribosomal Protein	RPS6		
MAPKAPK-2 P Thr334	MAPKAPK2		
Stat6	STAT6		
Src (family) P Tyr416	SRC		
Cyclin D1 P Thr286	CCND1		
AMPK alpha	PRKAA1	PRKAA2	
AMPK alpha P Thr172	PRKAA1	PRKAA2	
Bcl-2	BCL2		
Bim P Ser69	BCL2L11		
c-Jun N-term	JUN		
Caspase 3	CASP3		
Caspase 3 cleaved	CASP3		
CDK1 (p34cdc2) P Tyr15	CDK1		
p53	MTAP		
GSK-3-beta P Ser9	GSK3B		
GSK-3-beta	GSK3B		
SQSTM1 (p62)	SQSTM1		
PLC-gamma1	PLCG1		
CDK2	CDK2		
MAPKAPK-2	MAPKAPK2		
Stat3	STAT3		
PDGFR P Tyr1021	PDGFRB		
PDGFR P Tyr751	PDGFRB		
Bcl-2 P Ser70	BCL2		
IGF-1R beta	IGF1R		
Profilin (C56B8)	PFN1		
PYK2 P Y402	PTK2B		
Rock1 (C8F7)	ROCK1		
Mena (D33C1)	ENAH		

EGFR P Y992	EGFR		
EGFR P Y1086	EGFR		
B-Raf [EP152Y]	BRAF		
Fibronectin [F14]	FN1		
MMP21 [EP1277Y]	MMP21		
MEK6 [EP558Y]	MAP2K6		
Integrin Beta 1 [EP1041Y]	ITGB1		
PYK2 [EP206Y]	PTK2B		
Histone H2A.X P Ser139 [EP854(2)Y]	H2AFX		
Stat3 P Y705	STAT3		
Lamin A/C	LMNA		
Histone H2A.X	H2AFX		
Ezrin P T567/Radixin T564/Moesin T588	EZR	MSN	RDX
Caveolin-1 (D46G3) XP R	CAV1		
Cofilin P Ser3 (C77G2)	CFL1		
Cortactin (H222)	CTTN		
TIF1 Beta (C42G12)	TRIM28		
Integrin alpha 4	ITGA4		
Integrin beta3	ITGB3		
Integrin beta4	ITGB4		
Clathrin (D3C6) XP ®	CLTC		
Slug (C19G7	SNAI2		
Stat3 P Ser727	STAT3		
TGF beta (56E4)	TGFB1	TGFB2	TGFB3
PKA substrate P (RRXS/T) (100G7E)	AKAP10		
c-Abl P Y245	ABL1		
c-Abl	ABL1		
ATM	ATM		
PKA	AKAP10		
beta-Tubulin	TUBB		
PKC-alpha P Thr638	PRKCA		
Raf1 (C-12)	RAF1		
p21 CIP/WAF1 p Thr145	CDKN1A		
Cyclin D1	CCND1		
p21 CIP/WAF1	CDKN1A		
HSP27 (HSPB1)	HSPB1		
PKC-alpha	PRKCA		
Ras	HRAS		
Calmodulin	CALM1		
GAPDH	GAPDH		

Table 28 Individual pairwise p-values from one-way ANOVA of p/t ratios for HCC827 cells. In order from greatest significance to no significance (p<0.001, p<0.01, p<0.05, no significance (ns)).

p<0.001

PARP Copy of One-way ANOVA data

P value **< 0.0001**

	Control	300 nM EL	AgHA	AgHA Conj	AuCt	AuCt conj
Control						
300 nM EL	***					
AgHA	ns	***				
AgHA Conj	ns	***	ns			
AuCt	ns	***	ns	ns		
AuCt conj	ns	***	ns	ns	ns	
P-value key						
*** p<0.001			** p<0.010		* p<0.050	

Met One-way ANOVA data

P value **< 0.0001**

	Control	300 nM EL	AgHA	AgHA Conj	AuCt	AuCt conj
Control						
300 nM EL	ns					
AgHA	**	***				
AgHA Conj	ns	ns	***			
AuCt	ns	*	**	*		
AuCt conj	ns	ns	**	ns	ns	
P-value key						
*** p<0.001			** p<0.010		* p<0.050	

IGF 1R beta One-way ANOVA data

P value **< 0.0001**

	Control	300 nM EL	AgHA	AgHA Conj	AuCt	AuCt conj
Control						
300 nM EL	***					
AgHA	ns	***				
AgHA Conj	***	ns	***			
AuCt	ns	***	ns	**		
AuCt conj	ns	***	ns	***	ns	
P-value key						
*** p<0.001			** p<0.010		* p<0.050	

EGFR p Tyr1173 One-way ANOVA data

P value **< 0.0001**

	Control	300 nM EL	AgHA	AgHA Conj	AuCt	AuCt conj
Control						
300 nM EL	***					
AgHA	ns	***				
AgHA Conj	**	ns	***			
AuCt	ns	***	ns	**		
AuCt conj	ns	**	ns	**	ns	
P-value key						
*** p<0.001			** p<0.010		* p<0.050	

EGFR p Y1086 One-way ANOVA data

P value < 0.0001

	Control	300 nM EL	AgHA	AgHA Conj	AuCt	AuCt conj
Control						
300 nM EL	***					
AgHA	ns	***				
AgHA Conj	***	ns	***			
AuCt	ns	***	ns	***		
AuCt conj	ns	***	*	**	ns	
P-value key						
*** p<0.001			** p<0.010		* p<0.050	

p44/42 (ERK1/2) One-way ANOVA data

P value < 0.0001

	Control	300 nM EL	AgHA	AgHA Conj	AuCt	AuCt conj
Control						
300 nM EL	***					
AgHA	***	***				
AgHA Conj	**	**	***			
AuCt	***	***	***	***		
AuCt conj	*	***	***	**	***	
P-value key						
*** p<0.001			** p<0.010		* p<0.050	

Src One-way ANOVA data

P value < 0.0001

	Control	300 nM EL	AgHA	AgHA Conj	AuCt	AuCt conj
Control						
300 nM EL	***					
AgHA	ns	***				
AgHA Conj	*	ns	***			

AuCt	ns	**	*	ns		
AuCt conj	ns	*	**	ns	ns	
P-value key						
*** p<0.001			** p<0.010		* p<0.050	

SAPK/JNK One-way ANOVA data

P value < 0.0001

	Control	300 nM EL	AgHA	AgHA Conj	AuCt	AuCt conj
Control						
300 nM EL	ns					
AgHA	***	***				
AgHA Conj	ns	ns	***			
AuCt	ns	ns	***	ns		
AuCt conj	ns	ns	***	ns	ns	
P-value key						
*** p<0.001			** p<0.010		* p<0.050	

PLC gamma 1 One-way ANOVA data

P value < 0.0001

	Control	300 nM EL	AgHA	AgHA Conj	AuCt	AuCt conj
Control						
300 nM EL	**					
AgHA	ns	***				
AgHA Conj	**	ns	***			
AuCt	ns	**	ns	*		
AuCt conj	ns	**	ns	*	ns	
P-value key						
*** p<0.001			** p<0.010		* p<0.050	

Stat3 p Y705 One-way ANOVA data

P value < 0.0001

	Control	300 nM EL	AgHA	AgHA Conj	AuCt	AuCt conj
Control						
300 nM EL	**					
AgHA	*	***				
AgHA Conj	ns	ns	***			
AuCt	ns	**	ns	*		
AuCt conj	ns	*	**	ns	ns	
P-value key						
*** p<0.001			** p<0.010		* p<0.050	

Histone H2A.X One-way ANOVA data

P value < 0.0001

	Control	300 nM EL	AgHA	AgHA Conj	AuCt	AuCt conj
Control						
300 nM EL	***					
AgHA	ns	***				
AgHA Conj	ns	***	ns			
AuCt	ns	***	ns	ns		
AuCt conj	ns	***	ns	ns	ns	
P-value key						
*** p<0.001			** p<0.010		* p<0.050	

Stat6 One-way ANOVA data

P value 0.0001

	Control	300 nM EL	AgHA	AgHA Conj	AuCt	AuCt conj
Control						
300 nM EL	***					
AgHA	ns	*				
AgHA Conj	***	ns	*			
AuCt	*	*	ns	ns		
AuCt conj	*	*	ns	ns	ns	
P-value key						
*** p<0.001			** p<0.010		* p<0.050	

EGFR p Tyr 1289 One-way ANOVA data

P value 0.0001

	Control	300 nM EL	AgHA	AgHA Conj	AuCt	AuCt conj
Control						
300 nM EL	***					
AgHA	ns	***				
AgHA Conj	**	ns	**			
AuCt	ns	**	ns	*		
AuCt conj	ns	*	ns	ns	ns	
P-value key						
*** p<0.001			** p<0.010		* p<0.050	

JAK1 One-way ANOVA data

P value 0.0004

	Control	300 nM EL	AgHA	AgHA Conj	AuCt	AuCt conj
Control						
300 nM EL	**					
AgHA	ns	***				
AgHA Conj	*	ns	**			

AuCt	ns	*	ns	ns		
AuCt conj	ns	*	ns	ns	ns	
P-value key						
*** p<0.001			** p<0.010		* p<0.050	

p<0.010

GSK 3 beta One-way ANOVA data

P value 0.0019

	Control	300 nM EL	AgHA	AgHA Conj	AuCt	AuCt conj
Control						
300 nM EL	ns					
AgHA	*	**				
AgHA Conj	ns	ns	*			
AuCt	ns	*	ns	ns		
AuCt conj	ns	ns	ns	ns	ns	
P-value key						
*** p<0.001			** p<0.010		* p<0.050	

Caspase 3 One-way ANOVA data

P value 0.0056

	Control	300 nM EL	AgHA	AgHA Conj	AuCt	AuCt conj
Control						
300 nM EL	ns					
AgHA	*	ns				
AgHA Conj	ns	ns	**			
AuCt	ns	ns	ns	ns		
AuCt conj	ns	ns	ns	ns	ns	
P-value key						
*** p<0.001			** p<0.010		* p<0.050	

mTOR One-way ANOVA data

P value 0.0057

	Control	300 nM EL	AgHA	AgHA Conj	AuCt	AuCt conj
Control						
300 nM EL	ns					
AgHA	ns	**				
AgHA Conj	ns	ns	*			
AuCt	ns	*	ns	ns		
AuCt conj	ns	ns	ns	ns	ns	
P-value key						

*** p<0.001	** p<0.010	* p<0.050

MEK1/2 One-way ANOVA data

P value **0.0063**

	Control	300 nM EL	AgHA	AgHA Conj	AuCt	AuCt conj
Control						
300 nM EL	ns					
AgHA	ns	**				
AgHA Conj	ns	ns	*			
AuCt	ns	*	ns	ns		
AuCt conj	ns	ns	ns	ns	ns	

P-value key		
*** p<0.001	** p<0.010	* p<0.050

p38 MAPK One-way ANOVA data

P value **0.0068**

	Control	300 nM EL	AgHA	AgHA Conj	AuCt	AuCt conj
Control						
300 nM EL	ns					
AgHA	ns	ns				
AgHA Conj	ns	ns	ns			
AuCt	ns	ns	*	ns		
AuCt conj	ns	ns	**	ns	ns	

P-value key		
*** p<0.001	** p<0.010	* p<0.050

p<0.050

Akt p Ser 473 One-way ANOVA data

P value **0.0129**

	Control	300 nM EL	AgHA	AgHA Conj	AuCt	AuCt conj
Control						
300 nM EL	ns					
AgHA	ns	*				
AgHA Conj	ns	ns	ns			
AuCt	ns	ns	ns	ns		
AuCt conj	ns	ns	ns	ns	ns	

P-value key		
*** p<0.001	** p<0.010	* p<0.050

S6 Ribosomal protein One-way ANOVA data

P value **0.0157**

	Control	300 nM EL	AgHA	AgHA Conj	AuCt	AuCt conj
Control						

300 nM EL	ns					
AgHA	ns	*				
AgHA Conj	ns	ns	ns			
AuCt	ns	ns	ns	ns		
AuCt conj	ns	ns	ns	ns	ns	
P-value key						
*** p<0.001			** p<0.010		* p<0.050	

cdc25 One-way ANOVA data

P value 0.0159

	Control	300 nM EL	AgHA	AgHA Conj	AuCt	AuCt conj
Control						
300 nM EL	ns					
AgHA	ns	*				
AgHA Conj	ns	ns	ns			
AuCt	ns	ns	ns	ns		
AuCt conj	ns	ns	ns	ns	ns	
P-value key						
*** p<0.001			** p<0.010		* p<0.050	

CDK1 One-way ANOVA data

P value 0.018

	Control	300 nM EL	AgHA	AgHA Conj	AuCt	AuCt conj
Control						
300 nM EL	*					
AgHA	ns	ns				
AgHA Conj	ns	ns	ns			
AuCt	ns	ns	ns	ns		
AuCt conj	ns	ns	ns	ns	ns	
P-value key						
*** p<0.001			** p<0.010		* p<0.050	

p53 One-way ANOVA data

P value 0.0186

	Control	300 nM EL	AgHA	AgHA Conj	AuCt	AuCt conj
Control						
300 nM EL	*					
AgHA	ns	ns				
AgHA Conj	*	ns	ns			
AuCt	ns	ns	ns	ns		
AuCt conj	ns	ns	ns	ns	ns	
P-value key						
*** p<0.001			** p<0.010		* p<0.050	

PKC alpha One-way ANOVA data

P value 0.0202

	Control	300 nM EL	AgHA	AgHA Conj	AuCt	AuCt conj
Control						
300 nM EL	ns					
AgHA	ns	*				
AgHA Conj	ns	ns	ns			
AuCt	ns	ns	ns	ns		
AuCt conj	ns	ns	ns	ns	ns	
P-value key						
*** p<0.001			** p<0.010		* p<0.050	

EGFR p Y992 One-way ANOVA data

P value 0.0298

	Control	300 nM EL	AgHA	AgHA Conj	AuCt	AuCt conj
Control						
300 nM EL	ns					
AgHA	ns	*				
AgHA Conj	ns	ns	ns			
AuCt	ns	ns	ns	ns		
AuCt conj	ns	ns	ns	ns	ns	
P-value key						
*** p<0.001			** p<0.010		* p<0.050	

Akt p Thr 308 One-way ANOVA data

P value 0.0394

	Control	300 nM EL	AgHA	AgHA Conj	AuCt	AuCt conj
Control						
300 nM EL	ns					
AgHA	ns	ns				
AgHA Conj	ns	ns	ns			
AuCt	ns	ns	ns	ns		
AuCt conj	ns	ns	ns	ns	ns	
P-value key						
*** p<0.001			** p<0.010		* p<0.050	

p21 CIP/WAP One-way ANOVA data

P value 0.0375

	Control	300 nM EL	AgHA	AgHA Conj	AuCt	AuCt conj
Control						
300 nM EL	ns					
AgHA	ns	ns				
AgHA Conj	ns	ns	ns			
AuCt	ns	ns	ns	ns		

AuCt conj	ns	ns	ns	ns	ns	
P-value key						
*** p<0.001			** p<0.010		* p<0.050	

Non-significant

Bim One-way ANOVA data

P value 0.0622

	Control	300 nM EL	AgHA	AgHA Conj	AuCt	AuCt conj
Control						
300 nM EL	ns					
AgHA	ns	*				
AgHA Conj	ns	ns	ns			
AuCt	ns	ns	ns	ns		
AuCt conj	ns	ns	ns	ns	ns	
P-value key						
*** p<0.001			** p<0.010		* p<0.050	

HSP27 One-way ANOVA data

P value 0.1366

	Control	300 nM EL	AgHA	AgHA Conj	AuCt	AuCt conj
Control						
300 nM EL	ns					
AgHA	ns	ns				
AgHA Conj	ns	ns	ns			
AuCt	ns	ns	ns	ns		
AuCt conj	ns	ns	ns	ns	ns	
P-value key						
*** p<0.001			** p<0.010		* p<0.050	

PYK2 One-way ANOVA data

P value 0.1507

	Control	300 nM EL	AgHA	AgHA Conj	AuCt	AuCt conj
Control						
300 nM EL	ns					
AgHA	ns	ns				
AgHA Conj	ns	ns	ns			
AuCt	ns	ns	ns	ns		
AuCt conj	ns	ns	ns	ns	ns	
P-value key						
*** p<0.001			** p<0.010		* p<0.050	

p70 s6 kinase One-way ANOVA data

P value 0.1592

	Control	300 nM EL	AgHA	AgHA Conj	AuCt	AuCt conj

Control						
300 nM EL	ns					
AgHA	ns	ns				
AgHA Conj	ns	ns	ns			
AuCt	ns	ns	ns	ns		
AuCt conj	ns	ns	ns	ns	ns	
P-value key						
*** p<0.001			** p<0.010		* p<0.050	

c-Jun p Ser73 One-way ANOVA data

P value 0.2504

	Control	300 nM EL	AgHA	AgHA Conj	AuCt	AuCt conj
Control						
300 nM EL	ns					
AgHA	ns	ns				
AgHA Conj	ns	ns	ns			
AuCt	ns	ns	ns	ns		
AuCt conj	ns	ns	ns	ns	ns	
P-value key						
*** p<0.001			** p<0.010		* p<0.050	

FAK1 One-way ANOVA data

P value 0.2799

	Control	300 nM EL	AgHA	AgHA Conj	AuCt	AuCt conj
Control						
300 nM EL	ns					
AgHA	ns	ns				
AgHA Conj	ns	ns	ns			
AuCt	ns	ns	ns	ns		
AuCt conj	ns	ns	ns	ns	ns	
P-value key						
*** p<0.001			** p<0.010		* p<0.050	

PDK-1 protein One-way ANOVA data

P value 0.2906

	Control	300 nM EL	AgHA	AgHA Conj	AuCt	AuCt conj
Control						
300 nM EL	ns					
AgHA	ns	ns				
AgHA Conj	ns	ns	ns			
AuCt	ns	ns	ns	ns		
AuCt conj	ns	ns	ns	ns	ns	
P-value key						
*** p<0.001			** p<0.010		* p<0.050	

c-Myc One-way ANOVA data

P value **0.2992**

	Control	300 nM EL	AgHA	AgHA Conj	AuCt	AuCt conj
Control						
300 nM EL	ns					
AgHA	ns	ns				
AgHA Conj	ns	ns	ns			
AuCt	ns	ns	ns	ns		
AuCt conj	ns	ns	ns	ns	ns	

P-value key		
*** p<0.001	** p<0.010	* p<0.050

Cyclin D-1 One-way ANOVA data

P value **0.3853**

	Control	300 nM EL	AgHA	AgHA Conj	AuCt	AuCt conj
Control						
300 nM EL	ns					
AgHA	ns	ns				
AgHA Conj	ns	ns	ns			
AuCt	ns	ns	ns	ns		
AuCt conj	ns	ns	ns	ns	ns	

P-value key		
*** p<0.001	** p<0.010	* p<0.050

ATM/ATR One-way ANOVA data

P value **0.4539**

	Control	300 nM EL	AgHA	AgHA Conj	AuCt	AuCt conj
Control						
300 nM EL	ns					
AgHA	ns	ns				
AgHA Conj	ns	ns	ns			
AuCt	ns	ns	ns	ns		
AuCt conj	ns	ns	ns	ns	ns	

P-value key		
*** p<0.001	** p<0.010	* p<0.050

PTEN One-way ANOVA data

P value **0.5014**

	Control	300 nM EL	AgHA	AgHA Conj	AuCt	AuCt conj
Control						
300 nM EL	ns					
AgHA	ns	ns				
AgHA Conj	ns	ns	ns			

AuCt	ns	ns	ns	ns		
AuCt conj	ns	ns	ns	ns	ns	
P-value key						
*** p<0.001			** p<0.010		* p<0.050	

MAPKAPK-2 One-way ANOVA data

P value 0.5148

	Control	300 nM EL	AgHA	AgHA Conj	AuCt	AuCt conj
Control						
300 nM EL	ns					
AgHA	ns	ns				
AgHA Conj	ns	ns	ns			
AuCt	ns	ns	ns	ns		
AuCt conj	ns	ns	ns	ns	ns	
P-value key						
*** p<0.001			** p<0.010		* p<0.050	

c-Abl One-way ANOVA data

P value 0.516

	Control	300 nM EL	AgHA	AgHA Conj	AuCt	AuCt conj
Control						
300 nM EL	ns					
AgHA	ns	ns				
AgHA Conj	ns	ns	ns			
AuCt	ns	ns	ns	ns		
AuCt conj	ns	ns	ns	ns	ns	
P-value key						
*** p<0.001			** p<0.010		* p<0.050	

AMPK alpha One-way ANOVA data

P value 0.5417

	Control	300 nM EL	AgHA	AgHA Conj	AuCt	AuCt conj
Control						
300 nM EL	ns					
AgHA	ns	ns				
AgHA Conj	ns	ns	ns			
AuCt	ns	ns	ns	ns		
AuCt conj	ns	ns	ns	ns	ns	
P-value key						
*** p<0.001			** p<0.010		* p<0.050	

Stat 3 p Ser 727 One-way ANOVA data

P value 0.5893

	Control	300 nM EL	AgHA	AgHA Conj	AuCt	AuCt conj

Control						
300 nM EL	ns					
AgHA	ns	ns				
AgHA Conj	ns	ns	ns			
AuCt	ns	ns	ns	ns		
AuCt conj	ns	ns	ns	ns	ns	
P-value key						
*** p<0.001			** p<0.010		* p<0.050	

Raf One-way ANOVA data

P value 0.6662

	Control	300 nM EL	AgHA	AgHA Conj	AuCt	AuCt conj
Control						
300 nM EL	ns					
AgHA	ns	ns				
AgHA Conj	ns	ns	ns			
AuCt	ns	ns	ns	ns		
AuCt conj	ns	ns	ns	ns	ns	
P-value key						
*** p<0.001			** p<0.010		* p<0.050	

Bcl-2 One-way ANOVA data

P value 0.8049

	Control	300 nM EL	AgHA	AgHA Conj	AuCt	AuCt conj
Control						
300 nM EL	ns					
AgHA	ns	ns				
AgHA Conj	ns	ns	ns			
AuCt	ns	ns	ns	ns		
AuCt conj	ns	ns	ns	ns	ns	
P-value key						
*** p<0.001			** p<0.010		* p<0.050	